



LANCASTER UNIVERSITY ENGINEERING

DEPARTMENT

DOCTORAL THESIS

---

**X-Band LLRF Developments for High  
Power CLIC Test Stands and Waveguide  
Interferometry for Phase Stabilisation**

---

*Author:*

Amelia EDWARDS

*Supervisor:*

Dr. Amos DEXTER & Dr.  
Nuria CATALAN LASHERAS

*A thesis submitted in fulfillment of the requirements  
for the degree of Doctor of Philosophy*

October 12, 2022

## Declaration of Authorship

I, Amelia EDWARDS, declare that this thesis titled, X-Band LLRF Developments for High Power CLIC Test Stands and Waveguide Interferometry for Phase Stabilisation and the work presented in it are my own. I confirm that:

- This work was done wholly or mainly while in candidature for a research degree at this University.
- Where any part of this thesis has previously been submitted for a degree or any other qualification at this University or any other institution, this has been clearly stated.
- Where I have consulted the published work of others, this is always clearly attributed.
- Where I have quoted from the work of others, the source is always given. With the exception of such quotations, this thesis is entirely my own work.
- I have acknowledged all main sources of help.
- Where the thesis is based on work done by myself jointly with others, I have made clear exactly what was done by others and what I have contributed myself.

Signed:

---

Date:

---

# Abstract

This thesis describes the upgrade of the first high power X-band RF test for high gradient accelerating structures at CERN, as required for the  $e^+ e^-$  collider research program; Compact Linear Collider, CLIC.

Significant improvements to the control system and operation of the first test stand, Xbox-1, are implemented. The design and commissioning of the new Low Level Radio Frequency, LLRF, system is described in detail. The upgrade also encompasses software, interlock systems, timing, safety and control. The new LLRF requires an up-converter to convert an input signal at 187.4 MHz to 11.806 GHz. The most common method is a phase locked loop, PLL, an alternative method was envisioned which uses single side-band up-converter. This necessitated the design and manufacture of a custom cavity filter. The up-converter and PLL are compared and both are implemented in the new LLRF.

The new LLRF system is implemented at Xbox1 and used to RF condition a 50 MW CPI klystron, the final output power was 45 MW for a 50 ns RF pulse length. The phase and amplitude of the LLRF, TWT and klystron are characterised with both the PLL and up-converter. The klystron phase stability was studied using a sensitivity analysis.

The waveguide network between the klystron and the accelerating structures is approximately 30 m. This network is subject to environmental phase changes which affect the phase stability of the RF arriving at the structures. A single path interferometer was designed which will allow a phase measurement pulse at a secondary frequency to be injected into the waveguide network interleaved with klystron pulses. The interferometer is commissioned in the lab and low power measurements validate its operation. The system is then integrated into the high power network at Xbox1 and used to measure phase shifts in the waveguide network which are correlated with temperature.

# Acknowledgements

I would like to thank Amos Dexter for his supervision, advice and care. I would also like to thank Graeme Burt for his continued guidance and support. Thank-you both for allowing me the opportunity to partake in this fantastic opportunity and for continually supporting me ever since the start of my undergraduate degree.

My special thanks go to Nuria Catalan Lasheras for her supervision during my time at CERN, your guidance, support and ideas were invaluable to me.

Also thanks to everyone who helped teach me to operate the test stands and helped with my thesis work including Gerard, Stephane, Alan, Sergio, Ben, Joseph, Pedro, Jan, Alex, Lee and especially the provider of chocolate, Ruth Peacock. I would also like to thank everybody at the Cockcroft Institute and Daresbury Laboratory, you welcomed me during my first days as a PhD student and I made some friends for life.

I would like to especially mention four very special people who I met during my time in the Xbox group. Thankyou to Sam Pitman, Veronica Del Pozo Romano, Matteo Volpi, Marca Boronat Arvelo. You four are some of my favourite people and you helped me more than you can possibly know. I have been so lucky to meet you all, you all helped me immeasurably during my PhD and in my darkest times. You were each an inspiration to me. When I grow up I want to be like you guys!

Finally, I would like to thank my family and friends for their love and support throughout this whole process. My family have had unwavering faith in me ever since I was a young girl and I started saying 'one day I will work at CERN'. Finally, I would like to thank Mo Saffaf for always reminding me I could do this even when I felt I couldn't keep going.

# Contents

<b>Declaration of Authorship</b>	<b>i</b>
<b>Abstract</b>	<b>ii</b>
<b>Acknowledgements</b>	<b>iii</b>
<b>List of Figures</b>	<b>ix</b>
<b>List of Tables</b>	<b>xxiv</b>
<b>Glossary</b>	<b>xxvii</b>
<b>1 Literature Review</b>	<b>1</b>
1.1 The CLIC Study - A Future Linear Collider . . . . .	1
1.1.1 Physics after the Large Hadron Collider . . . . .	1
Luminosity . . . . .	2
1.1.2 A Future Collider . . . . .	3
1.1.3 Hadron vs Lepton Colliders . . . . .	3
1.1.4 Circular and Linear Colliders . . . . .	4
1.2 The Compact Linear Collider Project . . . . .	6
1.2.1 The CLIC Design . . . . .	8
1.2.2 CLIC - Main Beam . . . . .	9
1.2.3 CLIC - Drive Beam . . . . .	10
1.2.4 Klystron Based CLIC . . . . .	12
1.2.5 CLIC Test Facility . . . . .	13
1.2.6 CLEAR Linear Accelerator in CTF3 . . . . .	14
1.3 RF Accelerating Structures for the Main Beam . . . . .	15
1.3.1 CLIC Modules . . . . .	15
1.3.2 CLIC RF Frequency . . . . .	16
1.3.3 CLIC RF Pulse Length . . . . .	17
1.3.4 Travelling Wave RF Cavities . . . . .	17

	v
1.3.5	<i>Normal Conducting vs Superconducting RF Cavities</i> . . . . . 18
1.3.6	12GHz Accelerating Structures for the CLIC Main Beam . . . . . 19
1.3.7	Manufacture of Accelerating Structures . . . . . 20
1.4	High Gradient Testing and Conditioning . . . . . 21
1.4.1	Breakdown Studies . . . . . 21
1.4.2	X-band Test Stands at CERN . . . . . 23
1.4.3	RF Conditioning . . . . . 24
1.4.4	Breakdown Localisation . . . . . 25
1.4.5	X-Band Power Sources . . . . . 26
1.4.6	RF Pulse Compression . . . . . 27
<b>2</b>	<b>Low Level RF Systems</b> . . . . . <b>28</b>
2.1	Introduction . . . . . 28
2.2	RF Systems . . . . . 29
2.3	Frequency Conversion Techniques . . . . . 29
2.3.1	Frequency Mixers . . . . . 29
2.3.2	Single Sideband Up-Conversion . . . . . 31
2.3.3	Phase Locked Loops . . . . . 32
2.4	RF Measurements . . . . . 34
2.4.1	Phase and Amplitude Detection . . . . . 35
	Analog IQ Demodulation . . . . . 37
	Digital IQ Demodulation . . . . . 37
2.5	Sources of Errors and Instability in RF Systems . . . . . 40
2.5.1	Thermal Noise . . . . . 41
2.5.2	Phase Noise in RF Systems . . . . . 42
2.5.3	Phase Noise in Frequency conversion . . . . . 44
2.5.4	Phase Noise in PLLs . . . . . 45
2.5.5	Phase Noise to Jitter . . . . . 46
2.6	RF Reflections . . . . . 48
2.6.1	Reflection Coefficient . . . . . 48
2.6.2	Phase of Reflected Signal . . . . . 49
2.7	Visual Programming Languages . . . . . 50
2.7.1	Labview . . . . . 50
	Graphical Programming in Labview . . . . . 51
	PXI Chassis . . . . . 52

	vi
2.8	Diagnostics and RF Control in Particle Accelerators using Labview . . . 53
	Timing And Synchronisation using PXI Chassis . . . . . 55
<b>3</b>	<b>Xbox1 LLRF: Design and Commissioning . . . . . 56</b>
3.1	Introduction . . . . . 56
3.2	Design of the X-Band Pulse Forming Network . . . . . 58
3.2.1	Requirements . . . . . 59
3.2.2	Managing Phase Noise in Chains of RF Components . . . . . 60
3.2.3	Models for Predicting Phase Noise in RF Components . . . . . 62
	Amplifier . . . . . 62
	Passive Components . . . . . 63
	Frequency Multiplier . . . . . 64
	The Effect of Frequency Multiplication on Phase Noise . . . . . 64
	Mixer . . . . . 65
3.2.4	Predicting Phase Noise of RF Generation Schemes . . . . . 66
3.2.5	Converting Phase Noise to Jitter . . . . . 69
3.2.6	Commissioning the X-Band Pulse Generation System . . . . . 71
3.3	Design of the LLRF Receiving End . . . . . 77
3.3.1	PXI Acquisition Cards . . . . . 79
3.3.2	Generating the Local Oscillator Frequency . . . . . 81
3.3.3	Generating the Sampling Clock . . . . . 84
3.3.4	Frequency Up-Conversion to produce the Local Oscillator . . . . . 86
3.3.5	Commissioning the Receiver/Down-Conversion . . . . . 98
3.4	DC Power Supply Stability . . . . . 100
3.5	Conclusion . . . . . 102
<b>4</b>	<b>Design of a Narrow-band Cavity Filter at 11.806GHz . . . . . 103</b>
4.1	Introduction . . . . . 103
4.2	Design Specification . . . . . 103
4.3	Equivalent Lumped Circuit Model . . . . . 105
4.3.1	Determining Filter Order . . . . . 107
4.3.2	Low-Pass Prototype Element Values . . . . . 108
4.3.3	Low-Pass to Band-Pass Transformation . . . . . 109
4.3.4	Verifying Prototype Circuits . . . . . 110
4.4	Conversion to Physical Dimensions . . . . . 114
4.4.1	Determining Diameter of Cavity and Resonators . . . . . 115

4.4.2	Calculating Iris Parameters	116
4.4.3	Adjusting Resonant Frequencies due to Irises	121
4.4.4	Final Design Dimensions	122
4.5	Simulations in CST	124
4.5.1	Initial Optimisation	124
4.5.2	Manufacturing Material	127
4.5.3	Manufacturing Tolerances, Bend Radii and Mechanical Design	127
4.5.4	Tuning Pins	130
4.6	Manufacture and Test	133
4.6.1	Thermal Dependence	136
4.7	Conclusion	136
<b>5</b>	<b>High Power X-Band Measurements at Xbox1</b>	<b>138</b>
5.1	Introduction	138
5.2	Xbox1	138
5.2.1	High Power Network	139
5.2.2	Klystron	140
5.2.3	Modulator	142
5.2.4	Low Power Network	145
5.2.5	Control and Acquisition	147
5.3	High Power Testing	150
5.3.1	Intra-Pulse Stability	151
	Amplitude Stability	152
	Phase Stability	155
5.3.2	Pulse-to-Pulse Stability	158
	Amplitude Stability	158
	Phase Stability	160
5.4	Klystron Phase Stability Study	161
5.4.1	RF Power Scan	161
5.4.2	Pulse Length Scan	164
5.4.3	Modulator Voltage Scan	166
5.4.4	Sensitivity Analysis - Summary	171
	Klystron Phase Shift	171
	Klystron Phase Stability	174
5.4.5	Modulator Voltage Ripple	176

5.5	Conclusion . . . . .	179
<b>6</b>	<b>Single Path Inteferometry for High Precision Phase Measurements of Phase Shifts in X-Band Waveguide Networks</b>	<b>181</b>
6.1	Introduction . . . . .	181
6.2	Theory of Operation . . . . .	182
6.3	Determining TWT Frequency and Path Length . . . . .	189
6.4	Phase Changes in the Waveguide due to Temperature . . . . .	193
6.5	System Simulations . . . . .	195
6.5.1	Dependence on Difference in Path Length . . . . .	201
6.5.2	Dependence on Frequency . . . . .	203
6.5.3	Dependence on Length to Load . . . . .	204
6.6	Low Power Tests . . . . .	207
6.6.1	Loaded Output . . . . .	210
6.6.2	Shorted Output . . . . .	213
6.6.3	Thermal Effects . . . . .	216
6.7	High Power Implementation . . . . .	219
6.7.1	Klystron Pulses . . . . .	220
6.7.2	TWT Pulses . . . . .	223
6.8	Conclusion . . . . .	229
6.8.1	Low Power Tests . . . . .	229
6.8.2	High Power Results . . . . .	229
<b>7</b>	<b>Conclusion</b>	<b>231</b>
	Relevance . . . . .	231
	Summary of Results . . . . .	232
	Future Work . . . . .	233
	<b>Bibliography</b>	<b>237</b>
<b>A</b>	<b>Simulation Results from Two Cavity Tuning</b>	<b>248</b>
<b>B</b>	<b>Full Calibration Results for NI5162A and NI5162B</b>	<b>249</b>
<b>C</b>	<b>Explicitly Changing Phase Shifts on the Hybrid</b>	<b>251</b>
<b>D</b>	<b>Code for System Simulation</b>	<b>253</b>

# List of Figures

1.1	The Compact Linear Collider (CLIC) shown overlaid over its proposed location at CERN. The final tunnel will be 50km long and is positioned in front of the Jura mountain range . . . . .	6
1.2	Production cross section (measured in $\text{fb}$ ) as a function of centre-of-mass energy for the main Higgs boson production processes. A larger production cross section indicates an increased likelihood of the specific interaction occurring. The design energy of the linear collider is driven by the desire to observe different Higgs boson production processes which occur more often at different centre-of-mass collision energies. For example, the Higgsstrahlung process (yellow) dominated up to $\approx 500 \text{ GeV}$ . . . . .	7
1.3	The Higgs-strahlung (left) is the dominant process up to $\approx 500 \text{ GeV}$ , though its cross section decreases with centre-of-mass energy increases. The WW-fusion process (right) dominates at higher energies, as its cross section increases with centre-of-mass energy. . . . .	8
1.4	Functional diagram of the CLIC accelerator. Each Drive Beam complex generates a beam which is decelerated in order to supply RF power to 2984 accelerating structures in the Main Beam over the length of one sector. The main beams collide in the central interaction point (IP) . . . . .	9
1.5	Principle of the two-beam acceleration scheme: The beam power in the Drive Beam is converted to RF power in PETS, each feeding two accelerating structures in the Main Beam . . . . .	10
1.6	Bunch train combination by injection with RF deflectors for a multiplication factor 4. The images show the injection region of the ring for four successive turns of injected bunches and the corresponding bunch distribution on the RF field of the deflectors [17]. . . . .	11

1.7	Full Drive Beam Complex of CLIC. The drive beam is generated, compressed in the time domain and frequency multiplied using three loops of increasing diameter. Finally, the power is extracted and fed to the main beam (which is shown in the lower half of the diagram) . . . . .	12
1.8	Photo of the TBTS test area with vacuum tanks for the PETS (right) and accelerating structure (left). [20] . . . . .	13
1.9	Electric field plot in the CLIC two-beam accelerator unit. Here the PETS (shown left) is driven by the steady state drive beam current [23]	14
1.10	Layout of the 3 GHz CLEAR Beamline with CALIFES gun as of November 2016, no major upgrades have taken place since this time. The beamline operates mainly at 2.998 554 GHz with one X-band acceleration section in the centre. The X-band station was previously used to test the PETS power extraction scheme with a CLIC accelerating structure . . . . .	15
1.11	CLIC Module Type 1 integration layout [6]. The modules contain four main accelerating structures which are fed by two PETS structures. The integration also contains vacuum, water cooling and a movable girder for alignment . . . . .	16
1.12	Internal Volume of the CLIC Main Beam Structure . . . . .	19
1.13	Proposed Pulse Shape of the CLIC Main Beam RF Structure Input Pulse	20
1.14	Internal Cell geometry for the CLIC Main Beam Accelerating Structures. All of the main features are limited to one side of the disk and the reverse is flat for ease of bonding . . . . .	20
1.15	Cross Sectional view of a CLIC Main LINAC Accelerating Structure . .	21
1.16	Data showing the processing history of a TD24R05 CLIC prototype structure tested at KEK [37]. The red and green points show the accelerating gradient and the pulse width respectively . . . . .	24
1.17	RF signal time delays in a traveling-wave structure. The round-trip time $\tau_{RT}$ is used to localize the breakdown. In practice, $\tau_d$ ,REF is first estimated using the TDOA approach on REF and TRA or REF and INC	26

2.1	Diagram of Frequency Conversion using Mixing where the input and output signal frequencies are represented by 'F'. The central mixer effectively performs an arithmetic multiplication of the two input signals. Where $\varphi_{RF}$ is the phase of the RF signal and $\varphi_{LO}$ is the frequency of the LO signal . . . . .	30
2.2	Example output frequency spectrum of a real, non-ideal mixer, this is showing the production of unwanted harmonics and sidebands at harmonic frequencies of the input signals. The amplitude of these unwanted signals (usually measured in dBm) is typically lower than the IF (which is the desired signal) [50] . . . . .	31
2.3	Single Sideband Mixer Configuration [51]. The introduction of the two hybrids enables the trigonometric cancellation of the unwanted sideband . . . . .	32
2.4	Simplified block diagram of a Phase-Locked-Loop [52]. The error signal from the phase detector is passed to the loop filter and then filtered signal is applied to the voltage controlled oscillator to produce the locked output signal . . . . .	33
2.5	Three commonly used methods for Amplitude and Phase Detection [50]. All three methods use a combination of analog and digital components. In scheme <i>a</i> , the LO is the same frequency as the RF such that the output is a DC voltage which is proportional to the phase difference between the LO and RF. In schemes <i>b</i> and <i>c</i> , The LO frequency is usually at least an order of magnitude lower than the RF frequency in order to achieve down conversion to produce an AC signal containing both phase and amplitude information . . . . .	36
2.6	Phasor Representation of RF signal on a complex plane [50]. Using basic mathematical relations the I and Q values can be converted to phase and amplitude and vice versa . . . . .	38
2.7	Aliased Harmonic Frequencies shown as a function of the chosen sample rate [60] . . . . .	39
2.8	Pictorial representation of an LO signal with phase noise (Blue), and an RF signal close in frequency to the LO (Green). . . . .	44

2.9	Pictorial representation of phase noise issues in communications systems. LO signal with phase noise (Blue), RF signal (Green). In this figure, we note that if the phase noise of the LO is too high, then the noise will be converted into adjacent channels of the baseband data, thereby ruining the integrity of the information. . . . .	45
2.10	Example of Spreading of the Fundamental Frequency due to Phase Noise Sidebands and Spurious Signals. Ideally the difference between $P_s$ and $P_{SBB}$ should be maximised to ensure the cleanest signal [52] . . .	46
2.11	Diagram showing the individual phase noise contribution of each component in the PLL loop and how the sum of these sources creates the total PLL Phase Noise . . . . .	46
2.12	Calculating Jitter from Phase Noise by integrating the phase noise contribution from individual sections [66]. The phase noise profile is often separated into decades along the x-axis (Frequency offset) . . .	47
2.13	Reflections and VSWR on a Transmission Line . . . . .	49
2.14	An example of a basic piece of code in LabVIEW. The block diagram (white background) is used to send instructions to the front panel (grey background). The instructions can be used for control, data collection, data viewing or indication of status . . . . .	51
2.15	A PXI Chassis similar to those used at the X-band Test Stands. The controller is the left-most unit which controls the other modules. There are up to 18 slots in a PXI crate of this size, these can be filled by a variety of cards such as: ADC's, DAC's, voltage probes, digital multi meters, and timing cards . . . . .	53
3.1	Scheme 1: Proposed LLRF layout for the generation of a modulated 11.9942 GHz signal using a the CLEAR local oscillator source. This generation scheme uses a x4 Multiplier to produce sidebands close to 15 GHz and 9 GHz, of which the 9 GHz will be used . . . . .	60
3.2	Scheme 2: Proposed LLRF layout for the generation of a modulated 11.9942 GHz signal using a the CLEAR local oscillator source. This scheme differs from the previous (Scheme 1) only in the use of a x2 multiplier (instead of a x4 multiplier) . . . . .	60

3.3	Example of Single Sideband Oscillator Phase Noise measured in dBc/Hz vs Offset Frequency. The spectral purity of the carrier is affected by the device generated flicker noise at frequencies close to the carrier and shows a 1/f component with a corner frequency known as $f_c$ . . .	61
3.4	Scheme 1 Annotated: This is the same scheme as was shown previously in Figure 3.1 for 12 GHz Generation using x4 Multiplier. This diagram contains all of the available gains, corner frequencies, noise figures and input powers which can be collected from the component data-sheets . . . . .	66
3.5	Scheme 2 Annotated: similarly, This is the same scheme as was shown previously in Figure 3.2 for 12 GHz Generation using x2 Multiplier plus additional annotations . . . . .	67
3.6	Measured Phase noise of 2.998 554 GHz Master Oscillator and 11.9942 GHz produced by frequency multiplication by a factor 4 (followed by amplification and filtering) . . . . .	67
3.7	Predicted Single Sideband Phase Noise for the Quadrupler (blue) and Doubler (purple) Schemes (from Figures 3.4 and 3.5) with respect to the 3GHz Master Oscillator (yellow) which is the source for both schemes. So the additional phase noise above the level of the master oscillator is added by the components in the chain . . . . .	68
3.8	Phase Noise of the NI5793 PXI RF Generation Card taken from the component datasheet. The phase noise profile is dependent on the programmed output frequency of the card, in this case the frequency will be 2.998 554 GHz . . . . .	69
3.9	Single Sideband Phase Noise at 11.9942 GHz for the Quadrupler and Doubler Schemes with respect to the NI5793 PXI Card (left) and at 8.995 GHz before being mixed with the modulated pulse from the NI5793 (right) . . . . .	70
3.10	X-Band Pulse Generation Schematic. The S-Band master oscillator is shown in the top left and is the source for all the signals in the LLRF crate. This is used to create the 11.9942 GHz modulated pulse and is sent to the receiver (bottom left) to produce the local oscillator for down-conversion . . . . .	72

3.11 Proposed X-Band Pulse Generation during Commissioning. During commissioning additional components (amplifiers and filters) were added in order to ensure all components are operating within their desired range . . . . .	72
3.12 Final implementation of the X-band LLRF Transmitter system. This schematic contains the power levels measured throughout the system. The output power from the master oscillator (SMC100A) IS +15dBm which is then transported over to the LLRF at Xbox1. . . . .	73
3.13 ZX05-24MH Mixer Measured Conversion Loss - IF Input Power (dBm) vs RF Output Power (dBm) with 11.9942 GHz LO at 10.78dBm . . . . .	75
3.14 Expected Mixer Conversion Loss as a function of both Input RF Frequency and LO Power Level as taken from the ZX05-24MH+ Datasheet	75
3.15 ZX05-24MH Measured Power Scan - 2.9985 GHz Pulse Input Power provided be the NI5793 (dBm) vs 11.9942 GHz Output Power (dBm) with constant LO power of 10.86 dBm at 8.995 GHz . . . . .	76
3.16 Expected Phase Noise vs Temperature Performance of the HMC705 Programmable Divider as taken from the datasheet . . . . .	83
3.17 Simplified Diagram of the operation of a DDS showing the main blocks and a visual representation of the conversion from digital values to analog sine wave . . . . .	83
3.18 Measured Phase Noise of each of the 187.409 MHz signals which were generated by dividing the 2.998 554 GHz by 16 using the divider (Blue) and DDS (Purple) . . . . .	85
3.19 Measured Phase Noise profile of two versions of the 1.499 GHz Sampling Clock which were which were generated by multiplication of the output signal from the divider (Blue) and DDS (Purple) . . . . .	85
3.20 Measured Phase Noise at 11.8068 GHz generated by using the AD5355 PLL. Two versions of the signal are shown which compare the output of the PLL when using the Divider (Blue) and DDS (Purple) as the input	87
3.21 Expected Closed Loop Phase Noise of the PLL for an output frequency of $RF_{Out} = 13.6$ GHz taken from the ADF5355 datasheet . . . . .	88
3.22 ADI SimPLL Simulation of the Phase Noise of the PLL output at 11.8068 GHz and the individual contributions to the total Phase Noise of the major components inside the PLL. It can be seen that the phase noise is dominated by the quality of the VCO . . . . .	89

	xv
3.23 Schematic of Single Side-band Up-Conversion . . . . .	89
3.24 Predicted Phase Noise of the Up-Convertor . . . . .	90
3.25 ADRF6780 Side-band Suppression at Three Gain Settings and Tem- peratures (Left) and spectral output (right) . . . . .	91
3.26 Initial Phase Noise results at 11.8068 GHz from the ADRF6780 Up- Convertor . . . . .	91
3.27 Up-Convertor Schematic . . . . .	92
3.28 Board Outline for Balancing IQ Inputs . . . . .	93
3.29 Prototype Boards for Balancing IQ Inputs . . . . .	93
3.30 Added phase noise due to signal conditioning of the 187.4 MHz in- puts. The input to the up-convertor crate is shown in yellow, this is produced by dividing the master oscillator by 16. The input to the up-convertor is shown in purple, this is after all the stages of splitting, amplifying, filtering and biasing . . . . .	94
3.31 Up-Convertor after Commissioning . . . . .	95
3.32 Measured Frequency Spectrum at the output of Up-Convertor. The rejection of the carrier and upper side-band is below the noise floor of the measurement . . . . .	96
3.33 Measured phase noise spectrum after Commissioning: comparison of the phase noise of the LO when produced with the PLL and the Up- Convertor. The master oscillator is included for reference . . . . .	97
3.34 Measured phase noise spectrum after down-mixing the PLL and the Up-convertor with an X-Band signal at 11.9942 GHz to produce two versions of the IF at 187.4 MHz . . . . .	97
3.35 Schematic for the LLRF Down-Conversion with the PLL. The PLL can be replaced by the single side-band up-convertor . . . . .	98
3.36 Down-Conversion section of the LLRF Crate during Commissioning . . . . .	98
3.37 Measured Power at the Output of the Mixer at 187.4 MHz vs Input 2.998 554 GHz Pulse Power provided by the NI5793 RF Generation card . . . . .	99
3.38 Schematic for the LLRF Down-Conversion using Up-Convertor in place of the PLL . . . . .	100
3.39 Measured Stability of the 5 V (Top) and 12 V (Bottom) DC Power Sup- plies to the LLRF Crate vs a NGE103B DC Power Supply over 50 Hours during February 2021 . . . . .	101

4.1	Iris Coupled Cavity Filter . . . . .	104
4.2	Simulated Scattering Parameters of Low-Pass Lumped Element Prototype Filter . . . . .	112
4.3	Band Pass Lumped Element Prototype Filter . . . . .	113
4.4	Scattering Parameters of Band Pass Lumped Element Prototype Filter . . . . .	113
4.5	Chord Length of a Circle . . . . .	117
4.6	The iris length ( $L$ ) is a chord of the cavity and can be calculated from the expression (shown in the bottom left corner) using the cavity radius ( $r$ ) and the distance between the centres of the two cavities ( $2 \cdot d$ ). In the successive calculations the diameter of the cavity is referred to as $a$ as shown on the right . . . . .	117
4.7	Empirical measurements which describe the relationships between Iris shape, Dimensions and Magnetic Polarizability [53]. These relationships are used to calculate dimensions for a given iris shape . . . . .	118
4.8	The Empirical Relationship between Iris Dimensions and Magnetic Polarizability for a Rectangular Iris which was shown in Figure [53] has been converted to a linear equation for the region where $w/L$ is between 0 and 1. . . . .	121
4.9	SMA Probe which will be used to couple into the Input and Output Cavities. The radius and length of the coax probe is fixed . . . . .	122
4.10	CST Model of Two Cavity Filter (Left) and Scattering Parameters of Two Cavity Iris Coupled Filter (Right). The resonant frequencies of the two cavities can be seen clearly from the $S_{21}$ . . . . .	124
4.11	CST Model of Three Cavity Filter (Left) and Scattering Parameters of Three Cavity Iris Coupled Filter (Right) . . . . .	125
4.12	CST Model of Five Cavity Filter (Left) and Scattering Parameters of Five Cavity Iris Coupled Filter (Right). The resonant frequencies of the individual cavities are no longer clearly defined but the rejection outside the pass band is significantly improved . . . . .	125
4.13	CST Model of Seven Cavity Filter (Left) and Scattering Parameters of Seven Cavity Iris Coupled Filter (Right). The rejection outside the pass-band far surpasses the specification . . . . .	126
4.14	Comparison of $S_{21}$ for the Seven Cavity Filter when the background material is changed from PEC to Cooper C109 (left) and Aluminium AL6082 (right) . . . . .	127

4.15	Final Results from CST Frequency Doamin Simulations. The Seven Cavity Filter will be Manufactured in AL6082 and the simulated results include all Tolerances and Radii on internal corners . . . . .	128
4.16	3D Model of Seven Cavity Band Pass Filter without the lid. The internal structure of the cavities with central resonators is shown as well as tapped holes for attaching the lid and SMA connectors . . . . .	129
4.17	CST Simulation of Filter with Tuning Screws, a single pin is entered into the centre of each cavity, it would also be possible to add tuning pins into the irises to alter the coupling between cavities but the space is limited and the tuning would become overly complicated . . . . .	130
4.18	Interior and Lid of one of the Manufactured Cavity Filters, the SMA connector can be seen on the left. . . . .	134
4.19	Measured transmission (S21) and reflection 9S11) of the 1st filter after tuning . . . . .	134
4.20	S11 and S21 of the 2nd Filter after Tuning . . . . .	135
4.21	Variation of the reflection and transmission at 11.806 GHz with temperature measured with an RTD probe placed onto the cavity surface and external air heating . . . . .	136
5.1	Xbox1 functional diagram of the high power network. The position of seven high power RF signals are shown. The low power section has been simplified and ancillary systems are not included . . . . .	140
5.2	Two functional representations of a multiple cavity klystron. Modern klystrons usually have additional bunching cavities but only three are shown. On the left is a circuit diagram and the physical model is shown on the right . . . . .	141
5.3	Xbox1 ScandiNova K-3 Modulator with the XL5 Klystron Functional Diagram, the model is extracted from the klystron datasheet [37] . . .	143
5.4	Measured klystron output power vs LLRF output power (%) vs modulator voltage setting (kV). The klystron output power is monitored directly using a power meter . . . . .	145
5.5	Xbox1 low power functional diagram showing the LLRF, timing and control. The PXI is also included with the internal cards shown [73] . .	146

5.6	A sample Phase and Amplitude Profile collected using IQ sampling on CH0 OF the NI5162A and NI5162B. The source is produced using a Signal Generator at 187.46 MHz . . . . .	149
5.7	Diagram of the method which will be used for calculating the intra-pulse and pulse-to-pulse stability. The same method applies for both the amplitude and phase measurements hence the y-axis can either the phase (°) or the amplitude (MW) across the flat top of a pulse. Gradient of the flat top is not considered here . . . . .	152
5.8	Example of a measured data which shows the amplitude of the Reference, TWT and Klystron channels for the same pulse. This is a 150 ns RF Pulse collected on 30.07.2021 . . . . .	152
5.9	Calibration of the PXI NI5162 ADC cards which will measure the RF channels. The raw ADC Counts are converted to Output Power for TWT and Klystron respectively . . . . .	153
5.10	Normalized standard deviation of the intra-pulse amplitude stability at the output of the LLRF crate. The data shown here compares the LLRF output when the LO is produced by the up-Convertor (blue) and PLL (orange) for a 150 ns RF Pulse . . . . .	154
5.11	Normalized intra-pulse stability of the reference, TWT and klystron output amplitude for 150 ns RF pulse . . . . .	155
5.12	Measured data showing an example of the flat-top region of the phase of the RF pulses from the reference channel, TWT Output and klystron output. The data is measured on the same pulse for all three channels .	155
5.13	Deviation of the phase from the average across the flat top region (20 ns to 120 ns) for three channels, reference (blue), TWT output (orange) and klystron output (yellow), for the same pulse (pulses are the same as were shown in Figure 5.12) . . . . .	156
5.14	The intra-pulse phase stability for both the PLL and the Up-converter LLRF systems. This is the standard deviation across the flat top region taken from 7000 pulses. . . . .	157
5.15	Normalized standard deviation of intra-pulse stability for the reference, TWT output and klystron output channels. In the plot on the left the PLL is used as the LO source. On the right the up-convertor is used as the LO and the measurement is repeated . . . . .	157

5.16	Measured Pulse-to-Pulse Phase stability on the Reference, TWT and Klystron channels. The data is taken from 7000 RF pulses with an RF pulse length of 250ns RF Pulses collected on 10.09.2021 . . . . .	158
5.17	Normalized standard deviation of the pulse-to-pulse amplitude stability for the reference, TWT and klystron output pulses for a 150 ns RF Pulse . . . . .	159
5.18	Measured pulse-to-pulse phase stability of the TWT (left) and klystron (right) output signals. The data has been normalised in order to be centred around zero . . . . .	160
5.19	Measured LLRF output power vs klystron output power. The output power is varied by the user via a LabVIEW GUI and the klystron power is measured using a power meter. . . . .	162
5.20	Klystron Pulse-to-Pulse Phase stability vs LLRF Power for 150 ns RF Pulse Length for 330 kV and 360 kV Modulator Voltages . . . . .	163
5.21	Measured phase shift across the klystron vs klystron output power for 150ns RF Pulse. The modulator voltage was manually set to 330kV (left) and 360kV (right) . . . . .	164
5.22	Standard Deviation of the Klystron Pulse-to-Pulse Phase stability vs RF Pulse Length for 8.7 MW Klystron Output Power and 330 kV Modulator Voltage . . . . .	165
5.23	Phase Shift across the Klystron vs RF Pulse Length for 8.7 MW Klystron Output Power and 300 kV Modulator Voltage. . . . .	165
5.24	Diagram of an ideal voltage pulse (purple) and a real voltage pulse (red) [36]. After the initial ripple has decayed the stability across the flat top can be measured (FTS). The ripple can be reduced by increasing the rise time. . . . .	166
5.25	Relationship between Modulator Voltage and Klystron Output Power (Left) and measured modulator voltage at the PXI (Right) for a Klystron Input Power of 748.2kW (80% of the full TWT Output Power). . . . .	167
5.26	Normalized Standard Deviation of the Pulse-to-Pulse Modulator Voltage stability at 330 kV. The stability is taken by averaging across 1 us region of the flat-top of each pulse and comparing between pulses . . .	168

5.27	Klystron Output Phase vs Modulator Voltage Setpoint for 250 ns RF pulse at 80% of the Full TWT Output Power, the vertical and horizontal error bars are calculated as one standard deviation of the phase and modulator voltage stability respectively. The modulator voltage was swept twice starting at 330 kV (Left) and 360 kV (Right) . . . . .	169
5.28	Relationship between the measured change in modulator voltage (jitter) and the klystron phase shift for a modulator voltage setting of 338 kV . . . . .	170
5.29	Measured modulator voltage (kV) vs pulse-to-pulse stability of the measured klystron phase ( $^{\circ}$ ). The modulator voltage was swept twice starting at 330 kV (Left) and 360 kV (Right) . . . . .	171
5.30	Calculation of the gain, $a$ (Left), and the intercept, $b$ (Right), with respect to each range of modulator voltage (330 kV and 360 kV). The gains and intercept are used to define how the phase shifts with RF power level using a logarithmic fit of the form: $y = a \cdot \ln(x) + b$ . . . . .	172
5.31	Predicted Klystron Phase Shift ( $^{\circ}$ ) with respect to changing RF power Levels (%) and Modulator Voltages (kV) . . . . .	173
5.32	Predicted change in the phase shift across the klystron ( $^{\circ}$ ) when changing the RF power level (%) . . . . .	174
5.33	First Derivative of the Pulse-to-Pulse Phase Stability with respect to RF Power Level (%) and Modulator Voltage (kV) . . . . .	176
5.34	Measured modulator voltage ripple across the flat top region at for a modulator voltage setting of 330 kV . . . . .	176
5.35	Normalized Standard Deviation of the Ripple across the Flat Top of the Modulator Voltage Pulse measuring the difference between the maximum and minimum across each flat top . . . . .	177
5.36	Correlation between the Modulator Voltage Ripple and the Deviation in Phase of Pulses exiting the Klystron, 250ns RF Pulse Length and 330kV Modulator Voltage Set-point . . . . .	178
5.37	Klystron Output Pulse-to-Pulse Phase Stability Normalized around zero, before (Blue) and after (Orange) the ripple correction was applied in post-processing . . . . .	179
6.1	The Electric Field Profile of the Jog Mode Convertor which converts rectangular WR90 to Circular Waveguide [121] . . . . .	185

6.2	Schematic showing the proposed integration of the inteferometer at Xbox1 . . . . .	185
6.3	Inteferometer Schematic demonstrating the required phase shift at both the Klystron Frequency and the TWT Frequency . . . . .	187
6.4	Diagram defining variable for the additional length calculation. Note lack of symmetry in interchange of input ports (F1 and F4) . . . . .	190
6.5	Diagram of the inteferometer as used in the simulation. The matrix elements correspond to the forward and reflected signals at different point in the system as indicated here . . . . .	195
6.6	Hybrid during S-parameter Measurement in the RF Lab at CERN . . .	197
6.7	Measured Magnitude S-Parameters of High Power X-Band Hybrid produced by CINEL . . . . .	199
6.8	Measured S-Parameters: Phase (°) Response of the Hybrid . . . . .	199
6.9	Measured S-Parameters: Magnitude (dB) Response of the H-Plane Tee	200
6.10	Measured S-Parameters: Phase (°) Response of the H-Plane Tee . . . .	200
6.11	Measured S-Parameters: Magnitude (dB) and Phase (°) Response of a Low Power X-band Load . . . . .	200
6.12	Simulation of Transmitted Amplitude at Port 5, and Reflected Amplitude at both Hybrid Input ports (Port 1 and Port 4) when pulsing into Port 1 at the klystron frequency (F1) with respect to Length 3 . . . . .	202
6.13	Simulation of Transmitted Amplitude at Port 5, and Reflected Amplitude at both Hybrid Input ports (Port 1 and Port 4) when pulsing into Port 4 at the Frequency 4 with varying Length 3 . . . . .	203
6.14	Simulation of Transmitted Amplitude at Port 5 and Reflected Amplitude at both Hybrid Input ports (Port 1 and Port 4) when pulsing into Port 1 as a function of Frequency 1 . . . . .	203
6.15	Simulation of Transmitted Amplitude at Port 5 and Reflected Amplitude at both Hybrid Input ports (Port 1 and Port 4) when pulsing into Port 4 as a function of Frequency 4 . . . . .	204
6.16	Simulation of Reflected Amplitude at Port 1 and Port 4 when the length of Line 5 is changed, input signal is injected into Port 4 at Frequency 4 . . . . .	205
6.17	Simulation of Reflected Phase at Port 1 and Port 4 when the length of Line 5 is changed, input signal is injected into Port 4 at Frequency 2 . . .	205

6.18 Simulation of Phase of the Reflection at Port 4 of the Hybrid vs the Phase of the Reflection from Line 5 with changing Path Difference of the Inteferometer Arms (length of L3). The ideal length of L3 is 2.276 097 m . . . . .	206
6.19 Schematic showing the inteferometer with the position of the RTD (resistance temperature detector) temperature probes, heating tapes and cooling blocks . . . . .	208
6.20 Waveguide Surface Temperatures measured using PT100 probes when the heating systems is set at 20% Duty Cycle (Right). The probes 1-4 are placed on the heated arms and probe 5 is placed on the short arm which is stabilised using a water cooling system . . . . .	209
6.21 The Upper and Lower Temperatures of the Waveguide vs Heater Duty Cycle. The upper temperature is taken from the two probes placed at the start of the heating tapes (close to the power source) and the lower temperature is taken from the two probes placed at the opposite end of the arm ( 1 m away from the power source) . . . . .	209
6.22 Measured Transmission (S51) and Reflection (S11) taken from the VNA when pulsing into port 1 vs Injection Frequency. The temperature of the arms is set at 40°(% duty cycle) . . . . .	210
6.23 Simulated transmission (S51) and Reflection (S11) when pulsing into port 1 at vs Injection Frequency . . . . .	211
6.24 Measured transmission (S41) and Reflection (S44) when pulsing into port 4 vs Injection Frequency. Temperature of the long arm is set at 40°	212
6.25 Simulated transmission (S41) and Reflection (S44) when pulsing into port 4 vs Injection Frequency . . . . .	213
6.26 Measure change in phase detected at Port 1 (S11) with respect to the phase of the reflection from the short on the output controlled by the positon of the moveable short . . . . .	214
6.27 Measured change in phase at port 4 (S44) with respect to the phase of the reflection from the short on the output . . . . .	215
6.28 Measured change in amplitude when pulsing into Port 1, (Left, S11) and pulsing into port 4, (Right, S44) with respect to the phase of the reflection from the short which is connected to Port 5 (Output port) . .	215

6.29	For injection on port 4, Measured Phase (Top) and Amplitude (Bottom) Response at when pulsing into port 4 vs Reflected Phase at Load at 40° . . . . .	216
6.30	Measured reflected amplitude at Port 1 (Left) and Port 4 (Right) when injecting into port 4 with a short on line 5, vs varying duty cycle . . . . .	217
6.31	Measurement of the reflected phase at port 4 when injecting into port 4 with a short on line 5, vs varying duty cycle . . . . .	218
6.32	Reflected Phase at port 4 when injecting into port 4 with shorted on line 5, with 20% Duty Cycle (approximately 40°) with Error Bars . . . . .	218
6.33	A photograph of the inteferometer installation at Xbox1 with all electronics, cooling circuits and insulation . . . . .	219
6.34	Inteferometer WG installation at Xbox1 in the CTF2 Klystron Gallery (Left) and the 3D Design for the installation (Right) . . . . .	220
6.35	The waveguide loop is thermally stabilised at 84°C, the stabilisation of the waveguide loop was measured over 50 hours. RTD's 1-4 are plotted on the scale on the left (Blue) and RTD5 is plotted on the scale on the right (Orange) . . . . .	221
6.36	Left: Reflected Power at the Klystron Port and the TWT Port vs Temperature when pulsing into Port 1 (Klystron Port) at 11.9942 GHz. . . . .	222
6.37	Forward Power at the load vs Temperature when pulsing into the Klystron Port at 11.9942 GHz . . . . .	223
6.38	Left: Reflected Power at the Klystron Port and the TWT Port vs Temperature when pulsing into port 4 at 11.9364 GHz . . . . .	224
6.39	Normalized Standard Deviation of the Reflected Phase of the TWT pulses . . . . .	225
6.40	Air Temperatures in the CTF2 Klystron Gallery where the Xbox1 Klystron and Inteferometer is located . . . . .	226
6.41	Oscillations with a short time period (on the order of 2 minutes, compared with 24 hour oscillation) in CTF2 Air Temperature and Reflected Phase and the fitted function for each . . . . .	227
6.42	Reflected Phase, WR90 Copper Surface Temperature and Stabilised Temperatures vs Time from 08.10.2021 . . . . .	227
6.43	Correlation between change in reflected phase measured using the PXI and change in copper surface temperature measured using a PT100 probe on the bare copper in the gallery . . . . .	228

# List of Tables

3.1	Stability in Different Accelerators [13], [33], [82]. The stability is specified in peak to peak rather than in rms in proton machine due to beam velocity is dependent on energy gain. . . . .	57
3.2	Comparison of phase and amplitude stability targets at the output of the LLRF system from a variety of particle accelerator facilities operative at or below X-band frequencies [5], [14], [37], [58], [83], [84]. X-band is in the range of 12 GHz (in these specific cases, in actuality X-band can extend down to 9 GHz) , S-Band is 3 GHz and L-band is 1.5 GHz . . . . .	58
3.3	Definition and Units of the parameters used in Phase Noise Estimation calculations in Section 3.2.3 . . . . .	63
3.4	Predicted RMS Phase Jitter and RMS Timing Jitter . . . . .	70
3.5	Required and Measured Power levels for each of the four 2 99855GHz Channels from the Master Oscillator . . . . .	74
3.6	Mean and Standard Deviation of the Stability of the 5V and 12V DC Power Supplies . . . . .	101
4.1	Specification for 11.806 GHz Band Pass Filter . . . . .	104
4.2	Specification for 11.806 GHz Band Pass Filter . . . . .	110
4.3	Comparison of Tabulated and Computed 'g-values' . . . . .	111
4.4	Element Values for the 7 Element Chebyshev Low-Pass Prototype Filter	111
4.5	Calculated Element Values for Lumped Element Band-pass Prototype	112
4.6	Calculated Coupling Coefficient between Adjacent Resonators, the values calculates can only ever be approximate . . . . .	119
4.7	Coupling between Cavities, the resulting Magnetic Polarizability of Irises and Iris Length before and after adjustment . . . . .	122
4.8	Final Calculated Design Dimensions for the Seven Cavity filter with SMA connections . . . . .	123

4.9	Simulated Performance of Seven Cavity Filter Manufactured in AL6082 with Tolerances . . . . .	128
4.10	Final Dimensions of Seven Cavity Filter Manufactured in AL6082 with Tolerances . . . . .	129
4.11	Tuning Optimisation Goals for the filter, these will be monitored by observing the S11 and S21 while the tuning pin positons is changed . .	132
4.12	Tuning Results from Individual Cavity Tuning . . . . .	132
4.13	Tuning Results from Two Cavity Tuning . . . . .	133
4.14	Final S-Parameters of Two Manufactured Filters Before and After Tuning . . . . .	134
5.1	Nominal Parameters Used for the Klystron Phase Stability Study . . .	150
5.2	Intra-Pulse Amplitude Stability for the Reference, TWT and Klystron Output for a 150 ns RF Pulse using the Up-Convertor as the LO . . . .	154
5.3	Intra-Pulse Phase stability of the Reference, TWT output and Klystron Output for a 150 ns RF Pulse . . . . .	158
5.4	Pulse-to-Pulse Amplitude Stability of the Reference, TWT and Klystron Pulses using different lengths of Averaging Filter . . . . .	159
5.5	Pulse-to-Pulse Phase Stability of the Reference, TWT and Klystron Pulses using different lengths of Averaging Filter . . . . .	161
5.6	Pulse-to-Pulse Mean and Standard Deviation of the Measured Modulator Voltage vs Modulator Voltage Setpoint . . . . .	169
6.1	RF Measurement Settings Setup . . . . .	198
6.2	Parameters used for high power simulations of the interferometer Network presented in Figures 6.12 and 6.14 . . . . .	201
6.3	Parameters used for Low Power Simulations of the Interferometer Network vs Injection Frequency . . . . .	211
6.4	Mean Temperature and Standard Deviation of the Thermal Stabilisation of the Waveguide Loop . . . . .	220
A.1	Tuning Results from Two Cavity Tuning . . . . .	248
B.1	Corrections for NI5162A and NI5162B where $x$ is the measured voltage on the channel (ADC Counts) and $y$ is the adjusted voltage (ADC Counts) . . . . .	249

B.2 Error for each Channel with respect to the Reference Channel (NI5162A	
CH0) ( $mV_{rms}$ ) . . . . .	250

# Glossary

CLIC	Compact Linear Collider
LHC	Large Hadron Collider
HL-LHC	High Luminosity LHC
RF	Radio Frequency
LINAC	Linear Accelerator
FCC	Future Circular Collider
LEP	Large Electron Positron Collider
ILC	International Linear Collider
PETS	Power Extraction Transfer Structures
CTF3	CLIC Test Facility
TBTS	Two Beam Test Stand
CLEAR	CERN Linear Electron Accelerator for Research
WFM	Wake Field Monitor
BDR	Break Down Rate
SLAC	Stanford Linear ACcelerator
KEK	High Energy Accelerator Research Organization KEK
SLED	Stanford Linear Accelerator Pulse Compressor (SLED)
FEL	Free Electron Laser
LLRF	Low Level Radio Frequency
AM	Frequency Modulation
FM	Amplitude Modulation
DC	Direct Current
TWT	Travelling Wave Tube
SSA	Solid State Amplifier
LO	Local Oscillator
IF	Intermediate Frequency
SSB	Single Side Band
PLL	Phase Locked Loop
PD	Phase Detector
CP	Charge Pump
VCO	Voltage Controlled Oscillator
IQ	In-phase Quadrature
ADC	Analog Digital Convertor

<b>LMS</b>	<b>Least Mean Square</b>
<b>RMS</b>	<b>Root Mean Square</b>
<b>PN</b>	<b>Phase Noise</b>
<b>SNR</b>	<b>Signal Noise Ratio</b>
<b>BW</b>	<b>Band Width</b>
<b>VSWR</b>	<b>Voltage Standing Wave Ratio</b>
<b>VPL</b>	<b>Visual Programming Language</b>
<b>PLC</b>	<b>Programmable Logic Controller</b>
<b>NI</b>	<b>National Instruments</b>
<b>GPIB</b>	<b>General Purpose Interface Bus</b>
<b>VI</b>	<b>Virtual Instrument</b>
<b>GUI</b>	<b>Graphical User Interface</b>
<b>PXI</b>	<b>PCI eXtensions for Instrumentation</b>
<b>FPGA</b>	<b>Field Programmable Gate Array</b>
<b>PPM</b>	<b>Parts Per Million</b>
<b>CST</b>	<b>Computer Simulation Technology</b>
<b>TE</b>	<b>Transverse Electric</b>
<b>TM</b>	<b>Transverse Magnetic</b>
<b>SMA</b>	<b>Sub Miniature A</b>
<b>RTD</b>	<b>Resistance Temperature Detector</b>
<b>Speed of Light</b>	$c_0 = 2.997\,924\,58 \times 10^8 \text{ m s}^{-1}$
<b>Vacuum Permittivity</b>	$\epsilon_0 = 8.8541 \times 10^{-12} \text{ Fm}^{-1}$
<b>Air Permittivity</b>	$\epsilon_r = 1.000 \text{ Fm}^{-1}$
<b>Vacuum Permeability</b>	$\mu_0 = 1.2566 \times 10^{-6} \text{ Hm}^{-1}$

## Chapter 1

# Literature Review

### 1.1 The CLIC Study - A Future Linear Collider

The Compact Linear Collider, CLIC, is a design for a future linear accelerator that will reach unprecedented energies for lepton collisions. CLIC would offer significant fundamental physics insight beyond that available from the Large Hadron Collider, LHC. The particle beams will use a novel two beam acceleration scheme in two opposing linear accelerators and the beams will collide in a central physics detector. CLIC is an international collaboration based at CERN which is also the proposed site for the accelerator.

#### 1.1.1 Physics after the Large Hadron Collider

The Large Hadron Collider, LHC, based at CERN, is the largest and highest-energy particle collider in the world today [1]. The LHC provided thorough exploration of the TeV energy range which led to the discovery of the Higgs Boson. The knowledge attained from the LHC will be used to determine the nature of its successor. The successor will likely be used to search for dark matter candidates and to produce more understanding of the Higgs mass.

The second operational run of the LHC began on the 5th April 2015, the LHC restarted after a two-year break and achieved collisions at 6.5 TeV per beam, 13 TeV total. In 2016, the machine operation focused on increasing the luminosity for proton-proton collisions. Technological improvements increased the collision rate to 40% above the design value. In 2017 the luminosity was increased further and reached twice the design value. After some years of running any particle physics experiment typically begins to suffer from diminishing returns, as the key results reachable by the device begin to be completed, later years of operation discover proportionately less than earlier years. In particular at the LHC there is a lack of direct evidence

for new physics beyond the Higgs boson discovery [2]. A common response is to upgrade the devices involved, typically in collision energy, luminosity, or with more advanced detectors [3].

The High Luminosity LHC, HL-LHC, is an upgrade of the LHC to achieve instantaneous luminosities a factor of five larger than the LHC nominal value.

The second long shutdown of the LHC started 10 December 2018. The LHC and the whole CERN accelerator complex is being maintained and upgraded in order to implement the HL-LHC. The timeline of the project is dictated by the fact that, at the beginning of the next decade, many critical components of the accelerator will reach the end of their lifetime due to radiation damage and will need to be replaced. The upgrade is crucial to enable operation of the collider beyond 2025 [3].

### **Luminosity**

Luminosity is one of the most important parameters of an accelerator [4]. Luminosity, which is the measure of the number of potential collisions per surface unit over a given period of time, is an essential indicator of an accelerator's performance. Integrated luminosity is measured in inverse femtobarns (fb<sup>-1</sup>); one inverse femtobarn equates to 100 million million collisions [1].

In particle physics experiments the energy available for the production of new phenomena is also an important parameter. The required large centre-of-mass energy, the energy available for a collision, can only be provided by colliding beams where little or no energy is lost in the motion of the centre of mass system [3]. Besides the energy, the number of useful interactions is also an important parameter. This is especially true when rare events with a small production cross sections are to be studied [4].

Higher luminosity produces more collisions thus increasing the likelihood of observing rare processes and continuing the study of known physics mechanisms in greater detail [3].

The luminosity that can be achieved in a linear collider strongly depends on the emittance of the beams at the interaction point. In order to produce beam with high luminosity and repeatability, the beam parameters should be stabilized rigorously. By using beam-dynamic calculations and simulations, the stability targets for RF system can be proposed on basis of analyzing the influence of RF jitter on emittance growth in the main beam [5], [6].

In calculations, when the RF amplitude and phase, jitter increases the beam parameters gradually deviate from the optimal values [7].

Respectively, the amplitude jitter has a significant impact on the beam energy, and the phase jitter mainly leads to a higher energy spread and emittance [5]. From this is clear that the RF quality in the main can be directly correlated with the CLIC luminosity.

### 1.1.2 A Future Collider

Future accelerator experiments are being developed which will allow precision investigation of the Higgs boson and the top quark. In addition, they should offer discovery potential for 'new physics' complementing the possibilities which have been afforded by the LHC. CERN in collaboration with international partners, is conducting various R&D programs for the next generation of machines [8].

There are two main pathways envisioned for continuing to make progress in high energy physics. Firstly, increase the achievable precision of the measurements of the discovered Higgs boson and of particles that carry the imprint of the Higgs particle, such as  $W$  and  $Z$  bosons or the top quark. Secondly, operation at higher centre-of-mass energies to access states of new physics [9].

### 1.1.3 Hadron vs Lepton Colliders

Conventionally, particle colliders handle two types of fundamental particles, hadrons or leptons, which can either be collided with itself or with each other. Each type of collision can produce different particle interactions and can study physics phenomena at new collision energies.

In particle physics, a hadron is a subatomic composite particle made of two or more quarks held together by the strong force, protons and neutrons are hadrons. Hadrons are composite objects with the total energy carried by the particle shared in a probabilistic way among its gluons and quarks [9].

A lepton is an elementary particle of half-integer spin that does not undergo strong interactions. The electron and positron are examples of leptons. They appear to be point-like particles without discernible internal structure.

The additional level of complexity in hadrons, with respect to leptons, increases the number of possible outputs hadron collisions. The centre of mass energy of collisions will be distributed over the internal constituents of the baryons involved

in the interaction. Baryons are heavy subatomic particles that are made up of three quarks. Both protons and neutrons, as well as other particles, are baryons.

Therefore, hadron colliders allow for sweeping over a large energy range exploring a large phase space for discoveries [9].

Leptons are point-like fundamental particles. When leptons are collided the centre of mass energy is concentrated into a fundamental particle, hence, the leptons retains higher energy at the interaction point. By colliding point-like particles, physicists will gain access to decays that are difficult to identify at the LHC.

### 1.1.4 Circular and Linear Colliders

High energy particle accelerators are also divided roughly into linear and circular devices. Linear colliders accelerate two beams into a central interaction point, thereby the particles pass through each component once (magnets, RF units, focusing devices). In a circular machine, particles are accelerated around the same orbit by using magnetic fields. this allows the RF units to be 'recycled' meaning the particles will pass through the same RF units multiple times. Furthermore, in a circular collider the RF systems must compensate the energy loss due to synchrotron radiation and thus maintain the energy of the experiment constant after initial acceleration.

A main advantage of circular colliders of sufficiently large size is to offer a higher luminosity than a linear one due to the particles passing through the loop many times to gain additional energy. Also, a circular collider can accommodate more than one interaction point.

The Future Circular Collider, FCC, project proposes a circular hadron collider with a centre-of-mass energy of 100 TeV that would reside in a circular tunnel of about 100 km in circumference [10]. The biggest technological challenge of the FCC is the realisation of high-field dipole magnets. For the FCC these magnets will have to provide a magnetic field of 16 T over a length of about 13.5 m (the final value being dependent on the beam optics) [11].

Several examples of circular lepton colliders have been built and operated in the past five decades, for example LEP at CERN. The technology is mature and there is technological experience. However, to meet the required energy and luminosity of a 'Higgs factory,' several new major technical challenges need to be met. The main limitation of a circular  $e + e^-$  collider is that its energy is limited by synchrotron radiation and thus has no potential for an energy upgrade [12].

The energy loss per turn can be expressed as shown in Equation 1.1 for a particle with mass,  $m$ , measured in atomic mass units, and an energy,  $E$ , measured in GeV. The mass and energy are combined into one parameter:  $\gamma = \frac{E}{m}$ . Finally,  $r$  is the radius of the circular accelerator or storage ring [9].

$$\frac{\Delta E}{Turn} \propto \frac{\gamma^4}{r^2} \quad (1.1)$$

Synchrotron radiation is emitted when charged particles are forced into a circular orbit by transverse acceleration. The radiated power is related to the fourth power of the particle velocity, which is proportional to  $\gamma$ , and inversely proportional to the square of the radius of the particle path. Electrons in the LHC have been able to reach 209 GeV before synchrotron radiation losses became insurmountable at 3.6 GeV per turn [11].

The energy loss per turn in these machines is on the order of 10 GeV, where the radiated power which must be replenished by the RF system. The major concerns are the RF power coupler, radiation shielding, radio activation and the required wall plug power. The total site power, including cryogenics, magnets, water cooling and injectors would be even higher [9]. In addition, the hardware must be capable of withstanding the power emitted by the synchrotron radiation without being damaged [12]. These factors render TeV range circular colliders unfeasible.

An alternative method for reaching TeV energies in a circular lepton collider is acceleration of muons. Muons are a species of lepton which have a mass of approximately 207 times that of an electron. They are produced through secondary interactions when proton beams are fired at a stationary target and the resulting pions decay to produce muons. The increased mass would be able to reduce radiative losses in the collider by as much as 9 orders of magnitude. In addition, muons are able to achieve smaller energy distributions at the interaction point compared to electron beams due to their higher mass. The barrier is that muons will decay into electrons within approximately 2  $\mu$ s (in the muon rest frame) and that the muon production yield is relatively small with a large energy and directional spread [13]. Without considerable research effort it is unlikely that muon beams will be able to reach the luminosity requirement of the LHC successor.

Many studies have shown that a linear collider can add significant value to exploration of the TeV scale, notably in detailed studies of the Higgs boson and of any accessible new physics appearing at the electroweak scale (approximately 250 GeV,



FIGURE 1.1: The Compact Linear Collider (CLIC) shown overlaid over its proposed location at CERN. The final tunnel will be 50km long and is positioned in front of the Jura mountain range

such as super-symmetry [8].

The Stanford Linear Accelerator, SLAC, was the first linear collider ever built. Since then, extensive studies on linear colliders have been carried out, CLIC and the ILC are two flagship programs [14] [5]. The former uses two-beam acceleration while the latter one is based on, superconducting RF technology. A significant research and development program has been carried out for both proposals. Linear colliders are extremely challenging and complex machines, but the key technologies are in hand and well-organized international collaborations exist.

## 1.2 The Compact Linear Collider Project

CLIC is an international collaboration based at CERN. The CLIC design will collide two opposing beams of electrons and positrons in a central interaction point, as shown in Figure 1.1. The CLIC production is proposed to take place in stages. The construction of the first CLIC energy stage could start as early as 2026 and first beams would be available by 2035, marking the beginning of a physics program spanning 25–30 years [5].

The feasibility of CLIC has been demonstrated and documented for both the accelerator and the detector. This current design is the result of a comprehensive study addressing the performance, cost and power of the CLIC accelerator complex as a function of centre-of-mass energy and optimal physics output. The proposed location of CLIC and a rendering of the machine is shown in Figure 1.1.

A key component of the CLIC physics program studies the production and decay properties of the known standard model particles. The experimental conditions

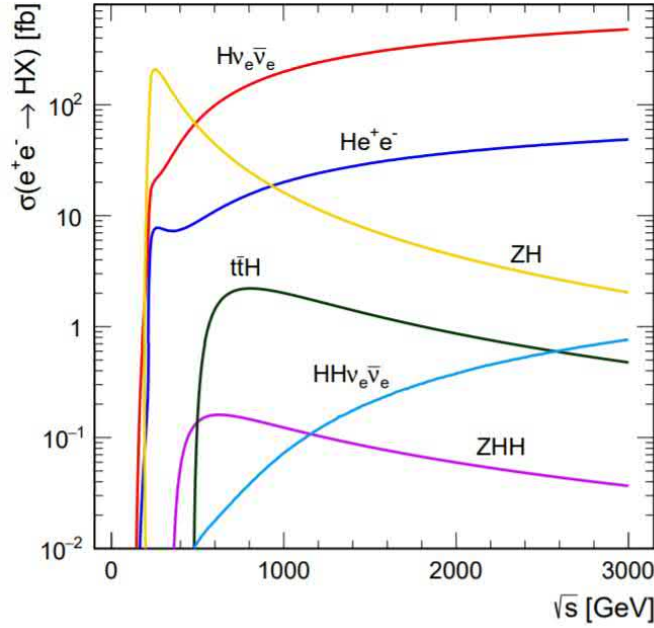


FIGURE 1.2: Production cross section (measured in fb) as a function of centre-of-mass energy for the main Higgs boson production processes. A larger production cross section indicates an increased likelihood of the specific interaction occurring. The design energy of the linear collider is driven by the desire to observe different Higgs boson production processes which occur more often at different centre-of-mass collision energies. For example, the Higgsstrahlung process (yellow) dominated up to  $\approx 500$  GeV

at CLIC allow the study of many relevant final states after interaction with high efficiency while keeping the background contributions at a low level. The CLIC study has potential for Higgs boson and top-quark physics, as well as two-fermion and multi-boson production processes [15].

At CLIC, the properties of the colliding electrons and positrons are known with high precision and so resulting Z particle can be measured with matching precision. Thus, physicists would be able to deduce the Higgs mass and its coupling to other particles. If an unknown particle were to enter into the equation, for example a candidate for dark matter, it would be easily and accurately spotted.

Figure 1.2 shows the centre-of-mass energy dependence of the relevant Higgs boson production processes in  $e^+e^-$  interactions. The CLIC project has designed a collision experiment with a luminosity of  $5.9 \cdot 10^{34} \text{ cm}^{-2} \text{ s}^{-1}$  and a centre-of-mass collision energy of 3 TeV. The CLIC project has evaluated a range of scenarios in order to minimise accelerator length and cost in parallel with the overarching goal of reaching design luminosity and collision energy [5].

The intermediate energies for the CLIC stages were selected for optimal Higgs characterisation. At 380 GeV Higgs are primarily produced via the ‘Higgsstrahlung’

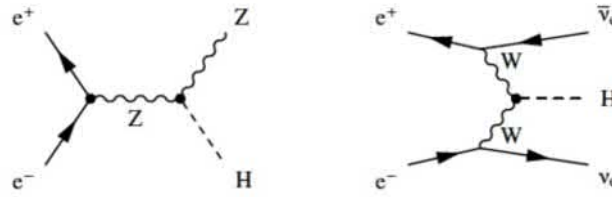


FIGURE 1.3: The Higgs-strahlung (left) is the dominant process up to  $\approx 500$  GeV, though its cross section decreases with centre-of-mass energy increases. The WW-fusion process (right) dominates at higher energies, as its cross section increases with centre-of-mass energy.

interaction, shown as a Feynman diagram in Figure 1.3. At the 1.4 TeV stage many more Higgs interactions will take place than in the LHC so this will allow for more statistics for describing the interactions. Above 1.4 TeV the WW fusion and ZZ interactions begin to dominate. The full CLIC baseline scenario provides about 4.5 million Higgs boson decays over the lifetime of the machine [15].

### 1.2.1 The CLIC Design

There are currently two CLIC designs under consideration. The primary CLIC design uses a novel two beam acceleration scheme. A low energy, high current drive beam is decelerated providing RF power into the low current, high intensity main beam. The power from the drive beam is extracted via power extraction and transfer structures, PETS [5]. This scheme differentiates the CLIC design from its competitor, the International Linear Collider, ILC, and from superconducting RF technologies which are gradient limited around 55 MV/m. A functional diagram of the CLIC layout is shown in Figure 1.4

The CERN study for a high energy linear collider began in 1985, around the same time the long range planning committee examined the potential of linear colliders and their technical feasibility. It was recommended to proceed with CLIC studies based on the two beam acceleration scheme [16]

Central to the entire complex will be the interaction point which will bring together two main beams after a scheme of collimation and focusing. It is proposed that the interaction point will be constructed in existing CERN territory while the peripheral elements would be in the surrounding Swiss and French area. All of the components will be housed in the same tunnel.

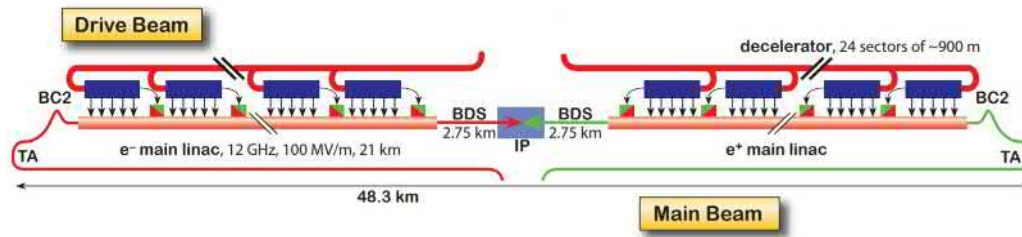


FIGURE 1.4: Functional diagram of the CLIC accelerator. Each Drive Beam complex generates a beam which is decelerated in order to supply RF power to 2984 accelerating structures in the Main Beam over the length of one sector. The main beams collide in the central interaction point (IP)

## 1.2.2 CLIC - Main Beam

This section explains in more detail the CLIC two-beam acceleration scheme. The two main accelerators will accelerate electrons and positrons from 9 GeV to 1.4 TeV in a single pass.

For the main beam, two lepton beams will be created and pre-accelerated using standard injector LINACS. The injector LINAC accelerates both positrons and electrons from 200 MeV to 2.86 GeV. The beams will be fed into damping rings to reduce transverse and longitudinal beam emittance.

In the main beam sections, the accelerating field must be as high as possible to limit the length of the machine. The RF frequency of the main beam accelerating cavities is 11.9942 GHz. This allows for 100 MV/m gradients in the accelerating structures using input powers of around 50 MW, short bunch lengths and small intervals between bunches. All of these factors are favourable for increasing luminosity.

The machine operation will be pulsed because such high power levels cannot possibly be maintained constantly. The RF pulse length will be 244 ns with 156 ns flat top and repetition rate of 50 Hz [5].

The RF power for acceleration is provided by a second electron beam. The Drive Beam runs parallel to the Main Beam. Beam power is extracted from this beam and converted to RF power in special RF devices called PETS (Power Extraction and Transfer Structures). The PETS are large aperture high group velocity and overmoded periodic structures [5]. The power is then injected into the accelerating structures in the Main Beam. One PETS provides RF power for two accelerating structures.

Emittance of a particle bunch is a representation of the volume of phase space occupied by the particles in the bunch. The emittance targets for the beam upon

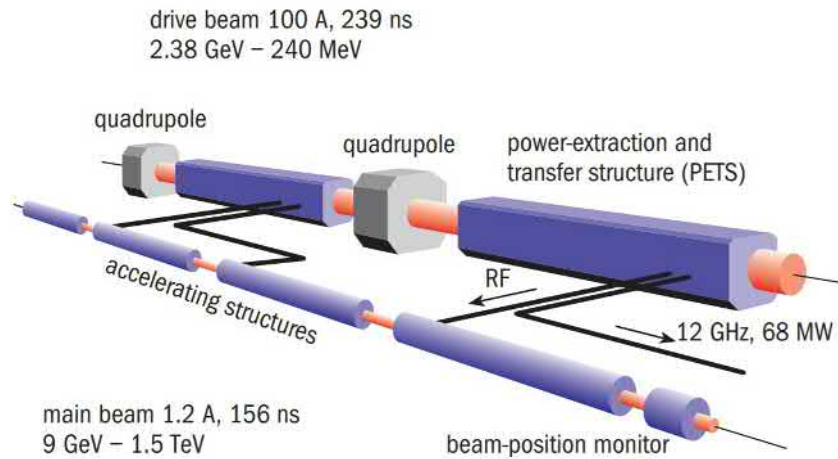


FIGURE 1.5: Principle of the two-beam acceleration scheme: The beam power in the Drive Beam is converted to RF power in PETS, each feeding two accelerating structures in the Main Beam

exiting the damping rings are 500 nm horizontally and 5 nm vertically. Further acceleration of the low emittance beams will follow in a booster LINAC to replace the energy lost by the beam during emittance damping. The beam is transported to the main accelerating complex in two semi-circular turnarounds. The main accelerating complex is where acceleration gradients of 100 MV/m will be achieved [5].

### 1.2.3 CLIC - Drive Beam

The Drive Beam is generated at the central campus of the CLIC complex. The drive beam LINAC will be divided into sections each containing a bunch train which will supply one corresponding section of the main beam LINAC with RF power. Each section of the drive beam will be 878 m long and contain 3,000 structures.

One major challenge of the CLIC two-beam acceleration scheme is the generation of the drive beam pulses with the required high-current (150 A) and high frequency bunch structures needed for 12 GHz RF power production. The required drive beam cannot be obtained directly from an electron source with the present technology, in particular, in terms of bunch repetition frequency and beam pulse length. Furthermore, a highly efficient drive beam acceleration is required [17].

Therefore, a long electron pulse is accelerated by low frequency (937 MHz), normal conducting traveling-wave cavities, working with strong beam loading. The structures are relatively short to minimize RF losses in the copper [17].

The long drive beam pulse is then subdivided into sub-pulses by means of transverse RF deflectors, working at half the bunch repetition frequency. The sub-pulses are then recombined in stages, multiplying the current and the bunch frequency at

the same time, this process is shown in the time domain in the diagram in Figure 1.6. The main manipulation for bunch frequency multiplication consists of sending the beam through an isochronous combiner ring using RF deflectors to inject and combine the electron bunch trains [17].

The energy of the bunches in the drive beam is only 2.4 GeV but the bunches current will be 100 A. This configuration will provide 62 GeV of acceleration to the main beam.

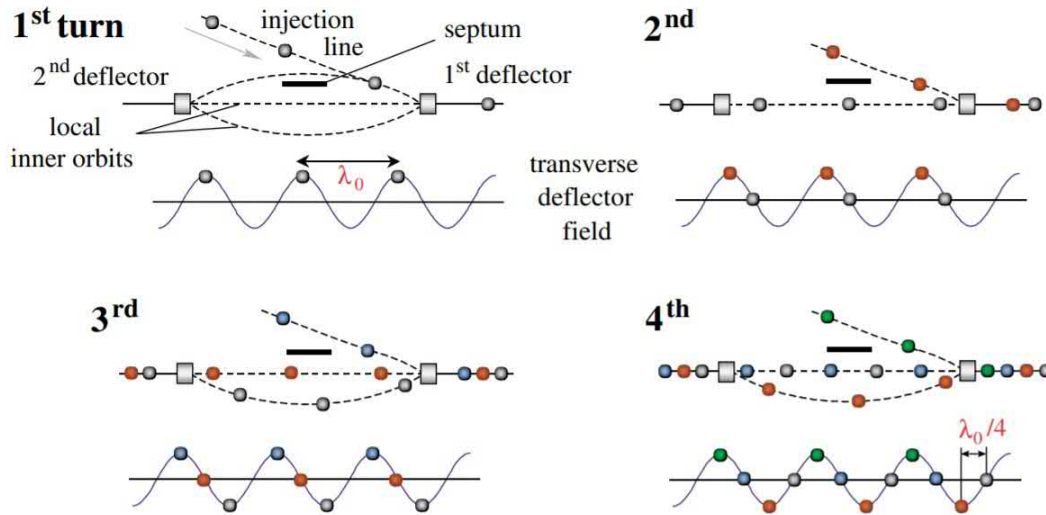


FIGURE 1.6: Bunch train combination by injection with RF deflectors for a multiplication factor 4. The images show the injection region of the ring for four successive turns of injected bunches and the corresponding bunch distribution on the RF field of the deflectors [17].

The relative impedance levels of the two systems creates a high transformer ratio. Low impedance for the PETS and high impedance at the accelerating structures. Each section of the drive beam will need to convert 84% of its stored energy into RF in the main beam. After which the drive beam will be dumped and a consecutive bunch will arrive at the successive section of the main beam line [5].

The CLIC baseline design for Drive Beam production consists of a thermionic gun, followed by a sub-harmonic bunching system. A potential alternative scheme makes use of a photo-injector RF gun. The overall performance of the Drive Beam injector has been demonstrated fully in CTF3, with parameters very similar to the ones required in CLIC.

The drive beam will be produced in two opposing LINACs running parallel to the main beam lines. The drive beam will be passed through combiner rings and delay loops in order to compress the beam in the time domain before entering the decelerating sections. The first bunch will travel the furthest distance to the lowest

energy section of the main beam. Sequential bunches will travel progressively diminishing distances which ensures correct timing of the arrival of the drive bunch trains at the PETS. This scheme is shown spatially in the diagram in Figure 1.7.

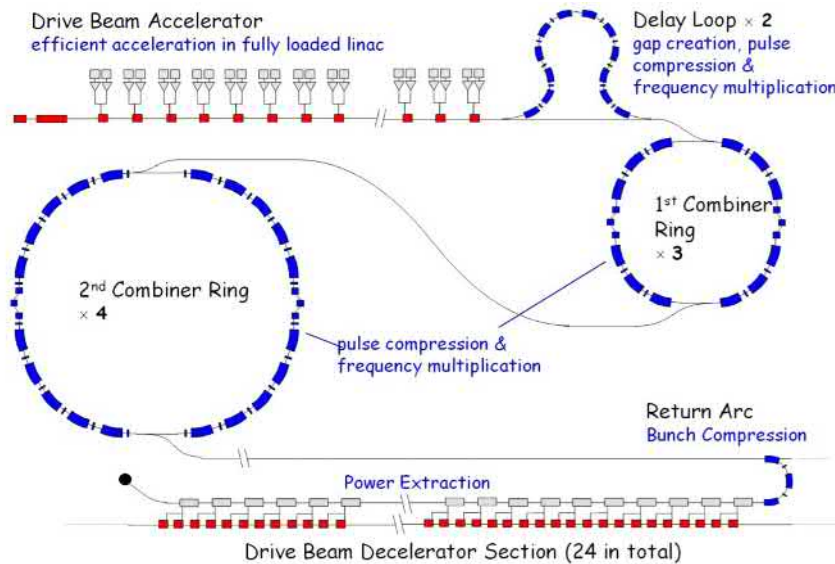


FIGURE 1.7: Full Drive Beam Complex of CLIC. The drive beam is generated, compressed in the time domain and frequency multiplied using three loops of increasing diameter. Finally, the power is extracted and fed to the main beam (which is shown in the lower half of the diagram)

### 1.2.4 Klystron Based CLIC

For the first 380 GeV stage of CLIC the main beams could be accelerated by powering the X-band accelerating structures using klystrons instead of the two-beam scheme. A clear advantage of a klystron-based design over a two-beam design at low energy is that the technical development of full RF unit prototypes is essentially complete so they can be tested easily. The production of the high-current drive beam for two-beam power generation is relatively costly but is the better option for the high energy stages of CLIC [18].

The design uses the same accelerating structure as the 3 TeV stage of CLIC and achieves the same luminosity and power consumption as an equivalent drive-beam based first stage. The costs of klystron and drive beam machines are also equivalent around 380 GeV. A klystron-based first stage could be followed by a drive beam-based energy upgrade by increasing the LINAC length using the same accelerating structures but changing the RF power source [18].

### 1.2.5 CLIC Test Facility

CERN built the CLIC Test Facility, CTF, as a machine for linear collider studies. Once the CTF facility had achieved all of its objectives the facility was converted into its second phase, CTF2. The goals of CTF2 were to further the CLIC study:

- Feasibility of the two beam test scheme
- Design and construct fully-engineered test sections
- Develop the drive beam technology

The design parameters for CLIC with a nominal energy of 3 TeV were derived from the successful tests and experience accumulated at CTF2 [19]. The two-beam acceleration scheme has been extensively studied in the Two-beam Test-stand (TBTS) shown in Figure 1.8, part of the third generation of the CLIC Test Facility, CTF3. CTF3 is primarily a scaled version of the CLIC drive beam complex.

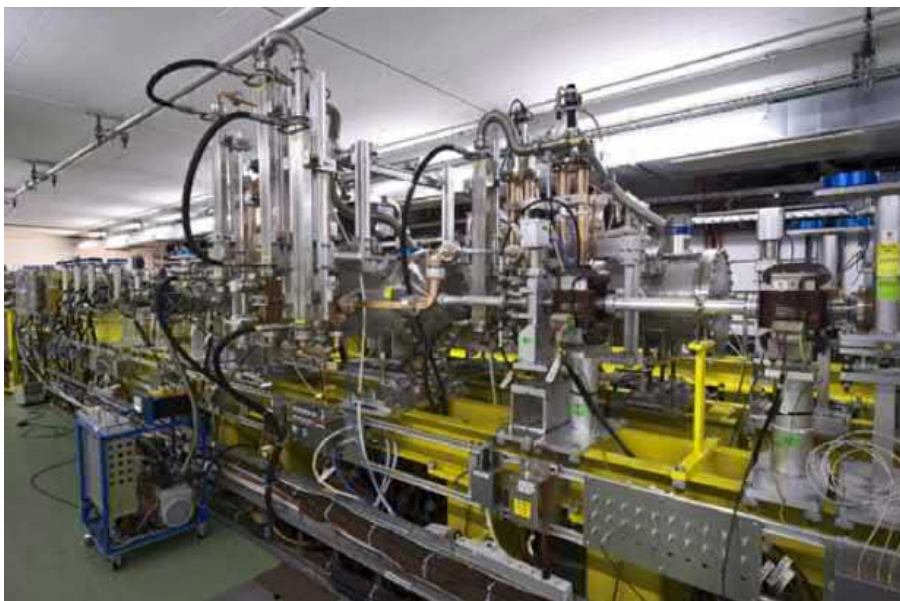


FIGURE 1.8: Photo of the TBTS test area with vacuum tanks for the PETS (right) and accelerating structure (left). [20]

The LINAC in CTF3 uses S-Band, 3 GHz, accelerating structures to produce the high-current drive beam that generates the 12 GHz RF power for the CLIC accelerating structures. The original purpose of this beam is to test the power extraction capability of the PETS structures. The PETS transfer the extracted beam energy into an RF structure where it is used to accelerate the main beam, the simulated electric field of the two structures is shown in Figure 1.9. CTF3 has successfully demonstrated drive beam generation, the production of the CLIC RF power, and two-beam

acceleration up to a gradient of 145 MeV/m, well above the 100 MeV/m nominal for CLIC [21], [22].

The CLIC PETS is a low impedance, high group velocity iris loaded 0.213 m long structure with a relatively large beam aperture. Each PETS is comprised of eight octants separated by damping slots. Each slot is equipped with damping loads in order to provide the strong damping of the transverse higher order modes [5], [23]. In operation, the high peak power RF pulses ( $135 \text{ MW} \times 240 \text{ ns}$ ) are generated in the PETS via interaction with a high current (100 A) bunched (12 GHz) drive beam. These pulses are extracted at the downstream end of the PETS using a special high power coupler and are distributed to the two CLIC accelerating structures using an RF waveguide network [23].

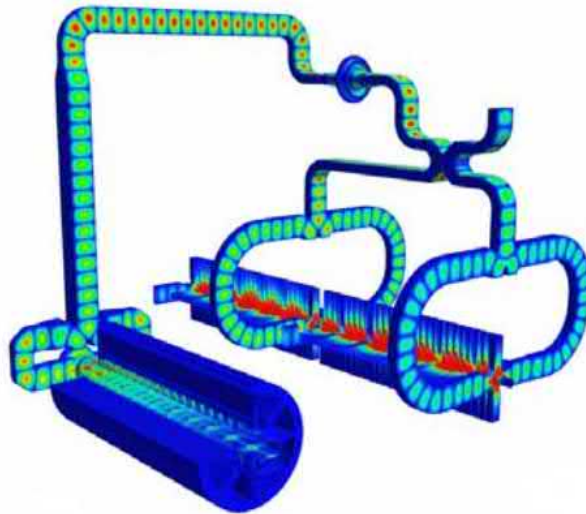


FIGURE 1.9: Electric field plot in the CLIC two-beam accelerator unit. Here the PETS (shown left) is driven by the steady state drive beam current [23]

Beam stability, beam loss issues as well as PETS and RF structures were studied in this set-up. CTF3 stopped its operation at the end of 2016 after successfully completing its program [21].

### 1.2.6 CLEAR Linear Accelerator in CTF3

CLEAR is a facility which repurposed the previous electron LINAC located in CTF3. Today, the CLEAR LINAC is capable of producing an electron beam with great flexibility in the parameters. The wide range of adjustable beam parameters is ideal for a user-orientated facility.

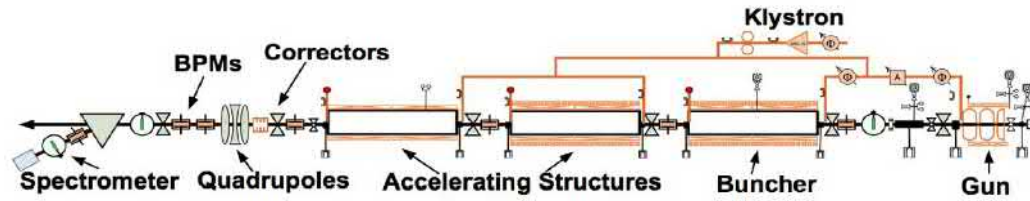


FIGURE 1.10: Layout of the 3 GHz CLEAR Beamline with CALIFES gun as of November 2016, no major upgrades have taken place since this time. The beamline operates mainly at 2.998 554 GHz with one X-band acceleration section in the centre. The X-band station was previously used to test the PETS power extraction scheme with a CLIC accelerating structure

The European Strategy for Particle Physics has named one of its top priorities as studies of high-gradient acceleration methods so the CLEAR facility serves this priority [8]. The CTF3 accelerating hall in 42 m in length and the layout of the CLEAR beamline is shown in Figure 1.10.

### 1.3 RF Accelerating Structures for the Main Beam

The parameters of the CLIC Main LINAC accelerating structure have been obtained through optimization of high-gradient limits, wakefield-related beam dynamics constraints, and performance and cost of CLIC at 3 TeV [5]. The optimum RF acceleration scheme must provide the highest ratio of the luminosity to the main LINAC input power. The parameter optimisation led to the selection of 12 GHz, normal-conducting, travelling wave structures with a design accelerating gradient of 100 MV/m [5].

#### 1.3.1 CLIC Modules

The CLIC accelerator complex involves the design and integration of many different technical systems. For the construction of two main LINACs it has been decided to proceed with a modular design and repetitive two-beam modules. There are just a few different module types depending on the type of magnets required. The modules consist of micro-precision components operating under ultra-high vacuum as required by the beam physics [6].

It has been proven that the drive beam is able to power two accelerating structures from one PETS structure. Each module might contain up to four PETS, feeding two accelerating structures each, and two drive-beam quadrupoles. A very dense

lattice is required for the low-energy drive beam [6]. The proposed CLIC module is shown in Figure 1.11.

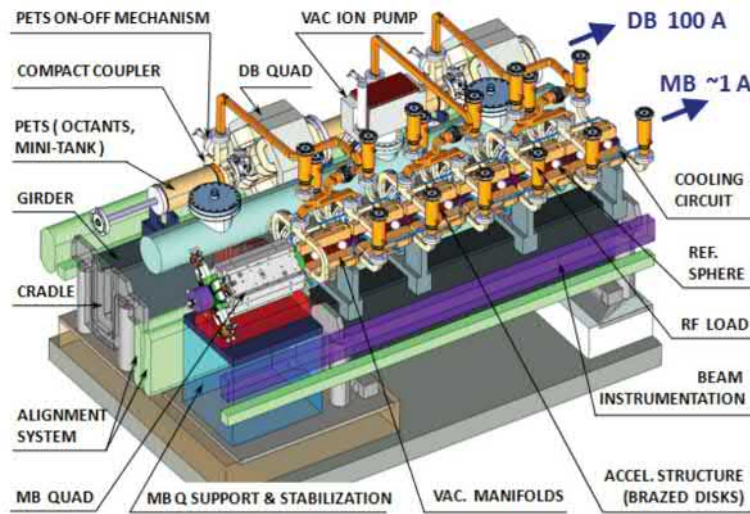


FIGURE 1.11: CLIC Module Type 1 integration layout [6]. The modules contain four main accelerating structures which are fed by two PETS structures. The integration also contains vacuum, water cooling and a movable girder for alignment

### 1.3.2 CLIC RF Frequency

Originally it was assumed that the increase of obtainable accelerating fields observed in the frequency range up to 12 GHz continues for even higher frequencies. This assumption was not confirmed experimentally, which indicate rather a saturation of the attainable field for an electric surface field-strength of about 300 MV/m independent of frequency.

Another important limitation comes from cavity surface damage due to pulsed surface heating by the magnetic RF surface field. RF pulsed heating is a process by which a metal is heated from magnetic fields on its surface due to high-power pulsed RF. When the thermal stresses induced are larger than the elastic limit, microcracks and surface roughening will occur due to cyclic fatigue [24]. Recent measurements indicate that the pulsed heating must be limited somewhere in the range of 40 K to 120 K for copper cavities.

Higher frequency brings higher gradient, lower dimensions and less input power to the structures. Small dimensions also bring smaller aperture and higher wake-fields. Frequency choice based also on available technology and available machining tolerances.

Based on this information, the optimum RF frequency and accelerating gradient is 12 GHz and 100 MV/m respectively [25]. The final choice of parameters has been driven by the results of a main LINAC cost and performance optimization [26].

### 1.3.3 CLIC RF Pulse Length

Pulsed surface heating is proportional to square root of pulse length and square of peak magnetic field. Pulse surface heating also limits operation due to vacuum arcs. The relationship between the pulsed heating and pulse length limits the maximum magnetic field on the surface and through it the maximum achievable accelerating gradient in a normal conducting accelerator structure [24].

### 1.3.4 Travelling Wave RF Cavities

The CLIC accelerating structures are travelling wave which means the accelerating field will propagate through the structure. A portion of the RF power will be dissipated, a portion will be consumed by the beam and the remaining at the output will be dissipated in a resistive load [27].

Travelling wave structures can be simply described as a cylindrical waveguide into which obstacles are placed to slow down the phase velocity below the speed of light to synchronize with the beam. Conventional travelling wave structures use round disk-loaded waveguide. Usually the phase shift per cell in the disk-loaded waveguide is  $2\pi/3$ . Coupling between the cells is executed by the electric field through an central iris in the disks on the axis [28].

In contrast, conventional standing wave accelerating structures usually include a bi-periodic structure of cavities with  $\pi/2$  mode of operation. Accelerating cavities of optimal shape alternate with coupling cavities, phase shift between adjacent cavities is  $\pi/2$  and between the accelerating cavities is  $\pi$ . The cavity-to-cavity coupling is executed by the magnetic field via off-center windows, and the dispersion is negative [28].

In physics and engineering, the quality factor or Q factor is a dimensionless parameter that describes how under-damped an oscillator or resonator is. Q factor is alternatively defined as the ratio of a resonator's centre frequency to its bandwidth when subject to an oscillating driving force.

for very short beam pulses (less than  $\mu s$ ), there is a clear power efficiency advantage for travelling wave structures. For longer pulses (in the  $\mu s$  range) both structure

types can be optimised to similar efficiencies and cost. Depending on the specific parameters standing wave structures can be more cost efficient from the microsecond range onwards. Due to the extremely short RF pulse lengths required, travelling wave structures can typically sustain much higher peak fields than any standing wave structure (CLIC advantage over ILC).

High Q resonant cavities reflect a large fraction of the incident power when the accelerating structure is filling. Reflections from standing wave accelerating cavities are a significant problem as it can result in damage to the klystron. For high power, high frequency applications isolators and circulators do not currently exist [29]. A standing wave cavity is also difficult to match, a higher or lower input current will result in reflected power from the structure [29].

The principal difference between the two types of cavity is how quickly the cavities are filled with RF power. Travelling wave structures are filled spatially, which means that longitudinally cell-after-cell is filled with power. The filling of a travelling wave structure typically takes place with a speed of approximately 1–3% of the speed of light and results in total filling times in the sub-microsecond range. Standing wave structures on the other hand are filled temporally, the electromagnetic waves are reflected at the end-walls of the cavity and slowly build up a standing wave pattern at the desired amplitude [30]. The filling process is typically in the range of 10s of microseconds. This means that for applications that require very short beam pulses, such a CLIC, travelling wave structures are much more power efficient [30].

### 1.3.5 Normal Conducting vs Superconducting RF Cavities

Superconducting cavities excel in applications requiring continuous wave or long-pulse accelerating fields above a few MV/m. Superconducting cavities have a fundamental gradient limitation and must use long RF pulses  $E_{acc} \leq 50$  MV/m limited by field emission and peak magnetic fields that produce quenches

The traditional arguments against superconductor technology in linear colliders have been the low accelerating fields achieved in super conducting cavities and the high cost of cryogenic equipment. Superconducting cavities face a strong physical limitation: the microwave magnetic field must stay below the critical field of the superconductor. For the best superconducting cavities, niobium, this corresponds to a maximum accelerating field of about 55 MV/m while normal-conducting cavities operating at high frequency (above 5 GHz) should in principle be able to reach

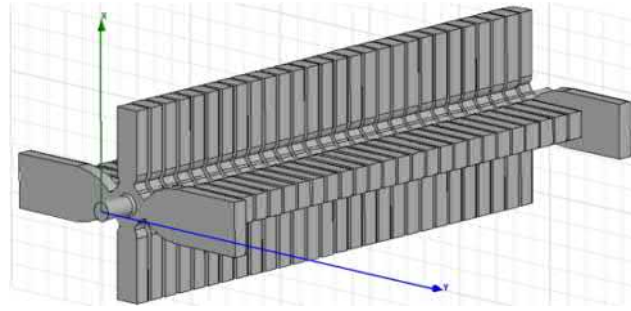


FIGURE 1.12: Internal Volume of the CLIC Main Beam Structure

100 MV/m or more. In practice, however, superconducting cavities were often found to be limited at much lower fields of some 5 MV/m and hence were totally non-competitive for a linear collider [31].

Although normal conducting copper cavities are less efficient, they are the natural choice for the CLIC design due to the high accelerating gradient and short pulse lengths.

### 1.3.6 12GHz Accelerating Structures for the CLIC Main Beam

The final design parameters of the accelerating structures were determined based upon systematic variation of the following parameters: iris diameter, iris thickness, RF phase advance per cell, RF frequency and average loaded accelerating gradient. Although a different choice of optimization criteria is possible, the main goal is to reach the design luminosity at a given energy in the shortest design length. The final design also satisfies RF factors. These are dominated by, but not limited to; surface electric fields, pulsed surface heating and scaled power density.

The internal RF geometry of the CLIC prototype structure is shown in Figure 1.12. It has 26 regular cells, which are tapered along the length of the structure, plus input and output coupler cells.

The group velocity in the last cell is 0.83%  $v_g/c$ , at this rather low group velocity, the bandwidth of the structure sets a lower limit to the rise time of the field level in a cell. The consequence of the limited bandwidth is that two ramps are necessary at the beginning of the pulse to simultaneously compensate for the structure bandwidth and for the beam loading-induced bunch-to-bunch energy spread. The input pulse shape is shown in Figure 1.13.

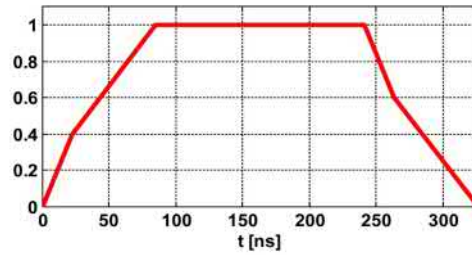


FIGURE 1.13: Proposed Pulse Shape of the CLIC Main Beam RF Structure Input Pulse

### 1.3.7 Manufacture of Accelerating Structures

Owing to the very large amount of structures, the implementation of tuning in the final design is not acceptable, hence the manufacturing tolerances are stringent. Micrometre tolerance level is required in cell disk fabrication and several micrometres in the structure assembly in order to satisfy stringent beam dynamics requirements without additional tuning and conditioning.

The rigorous manufacturing process is aimed at perfecting the copper surface and mitigating against any defects which could affect RF power transmission and create field emission sites. Despite this, the cavities will still not always perform to the desired specification hence cavities are often post-processed, this is known as tuning.

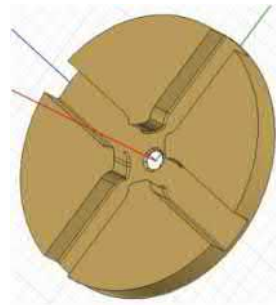


FIGURE 1.14: Internal Cell geometry for the CLIC Main Beam Accelerating Structures. All of the main features are limited to one side of the disk and the reverse is flat for ease of bonding

The cell geometry shown in Figure 1.14 is adapted to the manufacturing process based on the bonding of disks in which one side of the disks is flat and the other side carries all the cell features.

Sources of error due to manufacturing include:

- Inefficiency in acceleration due to RF de-phasing is mainly caused by systematic errors in the cell dimensions as it is a coherent effect.

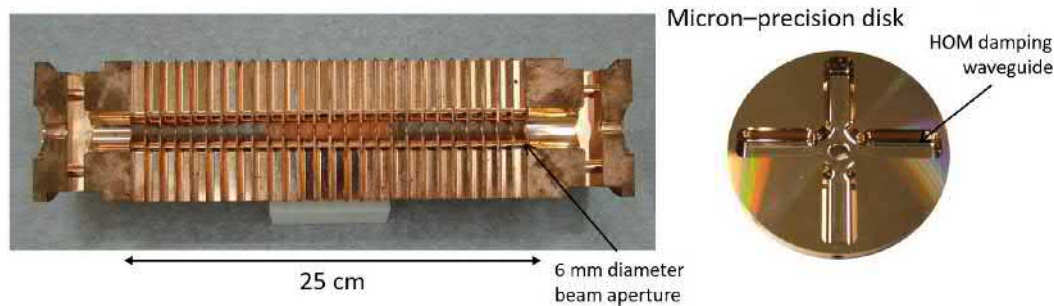


FIGURE 1.15: Cross Sectional view of a CLIC Main LINAC Accelerating Structure

- Cell-to-cell frequency error due to random errors in cell dimensions causes mismatch, reflections, and appearance of field enhancement due to standing waves.
- Tilt of the disks introduces a transverse kick which is proportional to the accelerating gradient.
- The positioning of the accelerating structures must be aligned with an accuracy below  $3.5\mu\text{m}$ .

## 1.4 High Gradient Testing and Conditioning

The objective of the X-band activity at CERN is to develop the high-gradient, high-power X-band RF system for the CLIC main LINACs. The current focus is on constructing and operating 100 MV/m prototype accelerating structures and establishing a significant high-power testing capability through klystron-based test stands.

### 1.4.1 Breakdown Studies

For many years, the accelerator community has been interested in understanding the high-breakdown limits of RF accelerator structures. In the absence of much experimental data, accelerator designers relied on the well-known Kilpatrick criterion which predicts that these limits are a function of the RF frequency and electrode geometries for the CW regime or very long pulses [32]. Recent experimental results show that the Kilpatrick criterion indeed could be exceeded considerably [33].

The evidence is that these limits do not appear to be sensitive to choice of metal as long as reasonable quality control and cleanliness precautions of cavity surfaces are observed. Careful and gradual RF processing enables one to bring these structure

up to a fairly well defined gradient limits above which breakdown invariably occurs [33].

The peak electromagnetic fields inside the accelerating structures create electromagnetic arcs stochastically, this occurs even under extremely low vacuum conditions. The electromagnetic arcs are referred to as breakdowns. When trying to increase the accelerating gradient of RF structures the breakdown rate, BDR, becomes a significant limiting factor. The target for CLIC is a breakdown rate of  $3 \cdot 10^{-7}$  breakdowns per pulse per metre [5].

The most recent understanding is that small deformities in the copper enhance the electric field close to the deformity. The deformities produced in the copper are referred to as field emission sites. The current produced by a field emission site is in the region of pico-amps to nano-amps. This produces fields of up to 10 GV/m across nano-metre distances [13] [27].

Breakdowns in the accelerating structure result in damage to the structure. if the breakdown process is allowed to continue uncontrolled then the damage is irreparable and 100 Mv/m will not be achieved. In an accelerator with beam, breakdowns will result in luminosity loss via transverse energy kicks. These are usually compensated by the alignment algorithms. However, during a breakdown, acceleration in the structure ceases while the beam still receives the kick provided by the alignment algorithm. The result is a net kick [5].

The quest to accumulate high gradient data in a coherent and quantitatively comparable way focused on two frequencies: 30 GHz and 12 GHz. According to the literature only at these two frequencies has a systematic study been done where the structure accelerating gradient was conditioned to the limit imposed by the RF breakdown and where relevant parameters were measured. In particular, all available data where the breakdown rate (BDR), the probability of a breakdown during an RF pulse, was measured at certain gradient and pulse length was collected. Data from structures where the performance was limited by an identified defect or by some other area of the structure, such as the power couplers, which are not directly related to the regular cell performance were not included [34].

The relationship between the unloaded accelerating gradient,  $E$ , breakdown rate and pulse length,  $\tau$ , is described by:

$$BDR \propto E^{30} \tau^5 \quad (1.2)$$

This is an empirical relationship resulting from a systematic study where accelerating structures were pushed up to their maximum achievable gradient where the limitation was due to RF breakdown, at this point the relevant parameters were measured [32].

It is most convenient to compare performance in terms of achieved gradient at a given value of the pulse length and BDR. To do this the measured data has had to be scaled. This involves two steps—first scaling the gradient versus BDR and then scaling the gradient versus pulse length. Both of these scaling behaviors have been measured in a number of structures, showing that all have remarkably similar dependencies. In the CLIC study, The BDR is often normalised to 100 MV/m and 250 ns pulse length to produce the following equation [35]

$$BDR^* = BDR \left( \frac{100}{E} \right)^{30} \left( \frac{25}{\tau} \right)^5 \quad (1.3)$$

#### 1.4.2 X-band Test Stands at CERN

CLIC requires 100 MV/m beam-loaded gradient for a pulse duration of 244 ns with 156 ns flat top. A high power X-band research and development program began at CERN in 2012. CERN has implemented and operated three standalone X-band test stands in order to research high gradient acceleration using high power RF pulsed power sources.

After the RF properties have been corrected and verified through the tuning process, a structure is ready for high power RF. Initially, the full design gradient and pulse lengths are not reachable. Although the fabrication steps are designed to clean and treat the copper surface, they are not fully adequate to remove all field emission sites and impurities. Typically structures will be able to obtain accelerating gradients up to 10- 20 MV/m for pulse lengths of 50-100 ns before outgassing events start to occur. From this point the power must be increased while trying to keep the vacuum level below an acceptable threshold (typically  $10^{-7}$  mbar) [27], [36]. structure start to become the limiting effect when trying to increase the power. The power is now increased while trying to keep the breakdown rate (BDR) at the order of 10 -5 breakdowns per pulse (or about 2 per hour at 50-60 Hz). Once the nominal gradient has been exceeded by a few percent, the pulse length is increased and the power level decreased. This process is repeated until the nominal parameters are achieved.

### 1.4.3 RF Conditioning

RF accelerating cavities cannot handle high gradients and long pulse lengths immediately after manufacture. Cavities must undergo a gradual conditioning process to be able to reach the design gradient. This process involves slowly increasing the power level, usually starting around from 5 MV/m and a 50 ns pulse length. Simultaneously the vacuum level inside the structure must be maintained below a level of around  $10^{-7}$  mbar to prevent outgassing. Once the structure surpasses 20 MV/m then the impact of breakdowns begin to supersede outgassing. At this point the conditioning scheme will usually swap from vacuum conditioning to breakdown conditioning. The break down rate, BDR, is maintained below a target value of  $10^{-5}$  breakdowns per pulse while the power level is ramped up to the design power and pulse length, nominally 100 MV/m and 200 ns. An example of the conditioning process of shown in Figure 1.16.

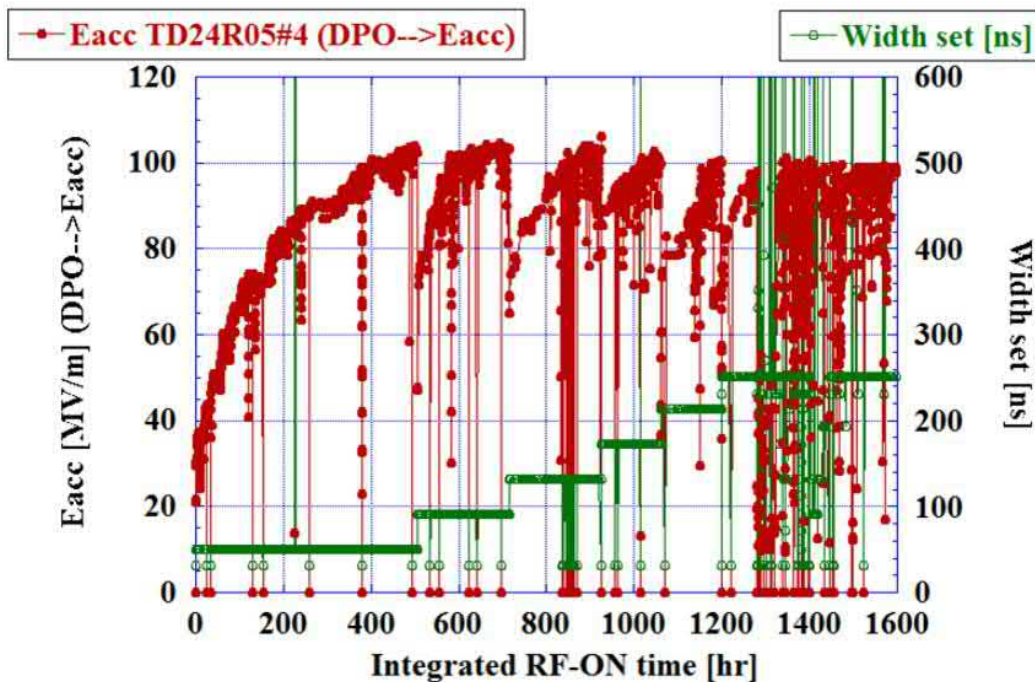


FIGURE 1.16: Data showing the processing history of a TD24R05 CLIC prototype structure tested at KEK [37]. The red and green points show the accelerating gradient and the pulse width respectively

Conditioning also allows for the BDR to reach a steady state. From experience this is usually 1-2 times lower than the initial breakdown rate of a newly manufactured structure. The conditioning process is time consuming and involves exposing the structure to around 350 million pulses. At 50Hz this is 1600 hours of pulsed RF

power. This process is greatly improved by the implementation of conditioning algorithms to safely increase the power whilst monitoring vacuum levels, BDR, and all other safety and system interlocks [7].

#### 1.4.4 Breakdown Localisation

Breakdown localisation is an important diagnostic tool of accelerating structure tests. Generally, localisation is an estimation problem where one has a finite set of indirect and noisy observations, into which a set of coordinates specifying a location are encoded. Conceptually, vacuum arcs are similar to gas discharges, of which lightning and static discharge are the most commonplace examples. Breakdown occurs when the potential difference between a charged object and a grounded object exceeds the dielectric resilience of the material in-between the two. Consequently, the insulator breaks down and electrical current starts flowing across the potential gap. Similarly, a vacuum arc is an electrical discharge between two or more electrodes under vacuum [38].

In most experiments, RF power and phase are monitored, since they are the main diagnostic tools of structure testing. RF pulses and breakdowns also pull off electrons from the surface of the bulk copper. These electrons are accelerated by the electromagnetic fields in the structure before being ejected through the beam pipe. Additionally, currents picked up by Faraday cups are regularly used to determine the absolute timing of breakdowns [27], [36]. In traveling-wave structures, three signals are typically recorded: RF power incident on the structure, INC, power reflected from the structure, REF, and power transmitted through the structure, TRA. If the accelerating structure is well matched to the rest of the RF network, reflections from the structure should be minimal, which means that during normal operation only the incident and transmitted RF power are nonzero. A breakdown acts as a short circuit, which causes reflection and loss of transmission. The transmitted and reflected signals are delayed and attenuated by the propagation in the structure and RF network. These signals can be used to determine the location of the breakdown. Since the precise reflection/absorption characteristics of the breakdown are unknown, a ‘time difference of arrival’, TDOA, approach is often the most robust. Therefore, the round-trip time of REF ( $\tau_{RT}$  in Figure 1.17) is estimated. In practice, the time taken by the incident signal to travel from the directional coupler to the breakdown cell and back is measured ( $\tau_d$  in Figure 1.17).



transport scheme was initiated [41] [42].

#### 1.4.6 RF Pulse Compression

Pulse compression is a general term used to describe the process of altering the shape of a propagating waveform using the properties of the transmission line network. In this instance pulse compression will be used to describe the process of amplifying the peak power of a transmitted impulse by shortening it in the time domain. The advantage of this is that the high resolution of a short pulse is combined with the high power from a longer pulse. In high power RF applications it is common to use the Stanford Linear Accelerator Pulse Compressor method of pulse compression, this method is referred to using the acronym SLED [41] [43].

In essence, the SLED method uses two resonant cavities to store energy from an RF source for a relatively long interval, in the range of a few microseconds. After this, a reversal in the RF phase releases the stored power over a much shorter time interval. This increases the peak power of the incident pulse at the structure. However the pulse shape is a decaying exponential. The pulse compressor requires a phase-modulated input pulse in order to produce a compressed pulse with a flat top. In addition, the storage. The cavities must be identical and tuned to resonance for the compression to be most effective [41].

## Chapter 2

# Low Level RF Systems

### 2.1 Introduction

RF wireless communication began at the turn of the 20th century, when Marconi established the first successful and practical radio system. Amplitude modulation, AM, and later frequency modulation, FM, was used in the first half of the 20th century for transmitting information via a radio carrier wave [44]. The Digital Revolution describes the shift from mechanical and analog electronic technology to digital electronics which began anywhere from the late 1950s to the late 1970s with the adoption and proliferation of digital computers [45].

RF engineering is a subset of electronic engineering involving the application of transmission lines, waveguide, antenna and electromagnetic field principles to the design to produce or utilize signals within the microwave and radio band, the frequency range of about 20 kHz up to 300 GHz. RF engineering is incorporated into almost all devices that transmit or receive radio waves, which includes, but is not limited to, mobile phones, radios, Wi-Fi, radios and particle accelerators [45].

RF engineering manipulates data signals using up- or down-conversion, modulation and demodulation, filtering and amplification at the transmitter and again at the receiver. In wireless communication systems the transmitted signal usually propagates through the air and is attenuated by several propagation mechanisms [46].

In particle accelerators, the RF systems covers the hardware dedicated to the generation and control of the electromagnetic fields which accelerate charged particle beams. They have been mainly developed in the microwave region of the electromagnetic spectrum, because of both physics (synchronization with the revolution frequencies of synchrotrons and cyclotrons) and technical (availability of power sources) motivations. In RF systems for particle accelerators, the signal propagates

along coaxial cables or waveguide [47].

Typically, operating a system in the range of radio frequencies impose special constraints on their design, these constraints increase in importance with higher frequencies. Hence operating test stands at 12 GHz requires well designed RF systems for both control of the cavity fields and diagnostics. This chapter will introduce the principles of RF frequency generation, measurements and sources of error.

## 2.2 RF Systems

RF transmitters are an essential part of modern communications. They have many different forms and applications; cellular phones, radar, military communications, avionics, wireless LAN, modems, and signal generators are just a few examples. To improve spectral efficiency and permit multiple users for a given spectrum, RF transmitters use a variety of modulation techniques to encode and send information.

A radio receiver uses an antenna to capture radio waves and processes those waves to extract only the signal at the desired frequency. The detector is responsible for separating the desired information from the carrier wave [48].

Receiver selectivity refers to the capability to detect and decode desired signal in the presence of other unwanted interfering signals. In the other way, selectivity of the receiver means how well a receiver performs in the presence of other unwanted co-channel and adjacent channel interfering signals [48]

## 2.3 Frequency Conversion Techniques

Heterodyning is a signal processing technique which creates new frequencies by combining or mixing frequencies. Heterodyning is used to shift one frequency range into another, and is also involved in the processes of modulation and demodulation. High frequency microwave signals can be reduced to a much lower frequency which can be sampled with less sophisticated equipment. The simplest frequency conversion device is a diode.

### 2.3.1 Frequency Mixers

In electronics, a mixer, or frequency mixer, is a nonlinear electrical circuit that creates new frequencies from two signals applied to it. The advantage of mixing for data sampling is that the converted signal preserves all of the characteristics, namely the phase and amplitude, of the original signal. An ideal mixer should convert only

in the frequency domain and should not alter the amplitude. A variety of mixing topologies can be created by combining diodes, the most common is the balanced mixer [49].

Mixers are usually three port devices, the ports are referred to as the local oscillator, LO, the RF port and the intermediate frequency port, IF. This is shown in the diagram in Figure 2.1.

In practice, if the RF is present at the RF port and a continuous sinusoidal signal is fed into the LO port then the LO signal acts like a gate for the mixer such that the mixer is 'ON' when the LO is large and the mixer is 'OFF' when the LO is low thus creating the sum and difference frequencies [49]. Usually the output of a mixer is low pass filtered in order to suppress the undesired harmonics.

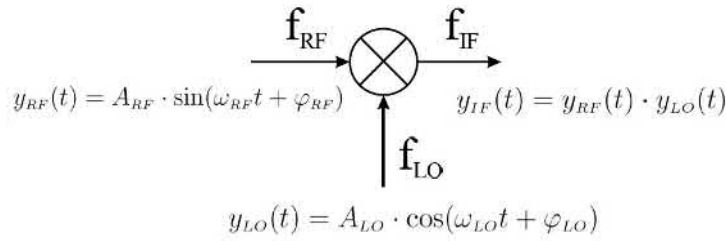


FIGURE 2.1: Diagram of Frequency Conversion using Mixing where the input and output signal frequencies are represented by 'F'. The central mixer effectively performs an arithmetic multiplication of the two input signals. Where  $\varphi_{RF}$  is the phase of the RF signal and  $\varphi_{LO}$  is the frequency of the LO signal

Mixing two frequencies creates new frequencies according to the mathematical properties of multiplying different sine functions. The new frequencies created from mixing are the sum and difference of the input frequencies as shown in Figure 2.1. In this way the behaviour of mixers is considered 'linear' even though the components are non-linear.

$$y_{IF}(t) = y_{RF}(t) \cdot y_{LO}(t) = \frac{1}{2} A_{LO} A_{RF}$$

$$\cdot (\sin[(\omega_{RF} - \omega_{LO})t + (\phi_{RF} - \phi_{LO})] + \sin[(\omega_{RF} + \omega_{LO})t + (\phi_{RF} + \phi_{LO})])$$

The mixing process also produces a range of other sum and difference frequencies at harmonic values which are also shown in the diagram in Figure 2.2. The output frequencies of the mixer will be produced according to Equation 2.1 where  $m$  and  $n$  are integers greater than zero.

$$f_{out} = |nf_1 + mf_2| \quad (2.1)$$

Non-linearities in the mixer and different input power levels mean the harmonics are produced in variable amounts.

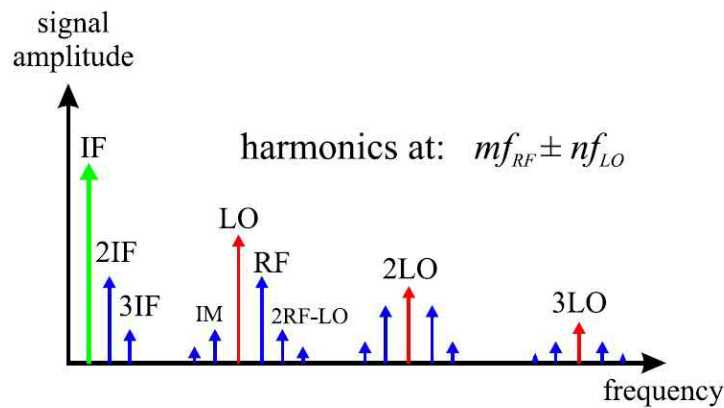


FIGURE 2.2: Example output frequency spectrum of a real, non-ideal mixer, this is showing the production of unwanted harmonics and sidebands at harmonic frequencies of the input signals. The amplitude of these unwanted signals (usually measured in dBm) is typically lower than the IF (which is the desired signal) [50]

### 2.3.2 Single Sideband Up-Conversion

In radio communications, single-sideband modulation, SSB, is a refinement of frequency conversion using mixers. The method uses transmitter power and bandwidth more efficiently.

SSB takes advantage of the fact that the entire original signal is encoded onto each of the two sidebands produced by a mixer. It is not necessary to transmit both sidebands plus the carrier, as a suitable receiver can extract the entire original signal from either the upper or lower sideband. Occasionally the unwanted sideband will fall well outside the required bandwidth and can often be removed very easily. However, in some applications this is not the case and the unwanted or image product can be close to the wanted signal and can require complicated filtering to remove it sufficiently [51].

Single-sideband modulation avoids this bandwidth increase, and the power wasted on the unwanted sideband, at the cost of increased device complexity [49].

Single sideband mixers (sometimes referred to as image reject or IQ mixers) utilise phasing of the RF signals to cancel out the unwanted mix products. To achieve this an image reject mixer utilises two balanced mixers and quadrature ( $90^\circ$ ) hybrids as shown in Figure 2.3.

It is not possible to achieve 'perfect' cancellation in a single sideband mixer, for perfect cancellation the mixers must be identical. The amplitude balance and phase

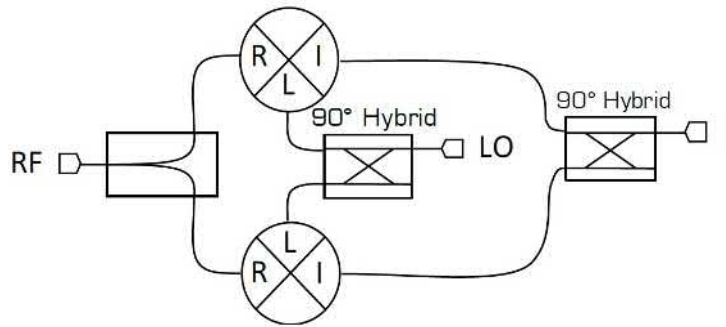


FIGURE 2.3: Single Sideband Mixer Configuration [51]. The introduction of the two hybrids enables the trigonometric cancellation of the unwanted sideband

shift of all the quadrature and in-phase power splitters. Hence the result of single sideband mixing is a reduction in the power of the carrier and the unwanted sideband rather than complete cancellation.

Although they are more complicated and more expensive than standard mixers, image reject mixers can be particularly useful in reducing the overall system cost by enabling the complexity of filters to be reduced in the successive signal chain.

### 2.3.3 Phase Locked Loops

Phase-locked loops are widely employed in radio, telecommunications, computers and other electronic applications. They have several useful applications: demodulating a signal, recovering a signal from a noisy communication channel, distributing precisely timed clock pulses in digital logic circuits and generating a stable frequency at multiples of an input frequency (frequency synthesis) [52].

A phase-locked loop is a system where an oscillator produces an output signal which maintains a constant phase angle relative to a reference signal. Phase-locked loops are commonly used to generate stable output frequency signals from a fixed reference signal. The basis of a PLL is a phase comparator, voltage controlled oscillator and feedback loop.

A portion of the output frequency is fed back into the error detector via the feedback loop, the other input to the error detector is the reference signal. The error detector compares the two signals and the output of the error detector is proportional to the relative phase error between the input and feedback signals. When the two signal inputs are equal in frequency, the error will be zero and the loop is said to be in a 'locked' condition [52].

The components of a PLL (shown below in the block diagram in Figure 2.4) which contribute to the loop gain include:

- The phase detector (PD) and charge pump (CP) which together make up the Error Detector
- The loop filter, with a transfer function described by  $Z(s)$
- The voltage-controlled oscillator (VCO)
- The feedback divider with a division ration of  $N$

The block diagram shown in the figure shows an input signal,  $F_{Ref}$ , with a phase of  $\theta_{Ref}$ , which is used to generate an output,  $F_O$  with a synchronised phase of  $\theta_O$ . The input signal is often called the reference signal.

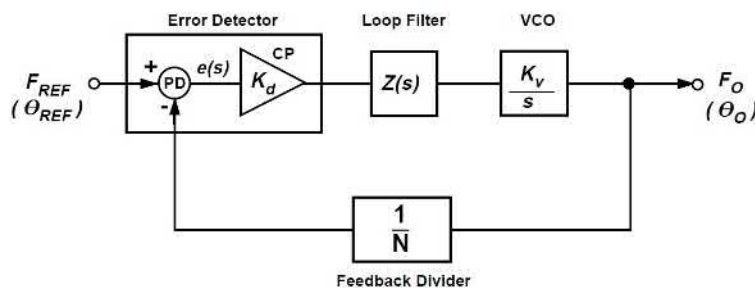


FIGURE 2.4: Simplified block diagram of a Phase-Locked-Loop [52]. The error signal from the phase detector is passed to the loop filter and then filtered signal is applied to the voltage controlled oscillator to produce the locked output signal

The output of the error detector is the error signal,  $e(s)$ , which is a changing voltage over time. Using a Laplace transform, the error signal is converted from a function of a real variable in the time domain to a function of the variable  $s$  (in the complex frequency domain, also known as  $s$ -domain, or  $s$ -plane) [53].

The charge pump is a variation on a DC-to-DC converter, it uses capacitors for energetic charge storage to raise or lower voltage depending on the magnitude of the error signal. This is a form of derivative control, represented by  $K_d$  in Figure 2.4. a derivative control term does not consider the magnitude of the error (meaning it cannot bring it to zero), but the rate of change of error, trying to bring this rate to zero.

The primary function of the loop filter (usually a low-pass filter) is to determine loop dynamics, also called stability. This is how the loop responds to disturbances, such as changes in the reference frequency, changes of the feedback divider, or at

startup. proportional to the current value of  $e(s)$ , if the error is large, the control output will be proportionately large by using the gain factor. The filter transfer function is simple low-pass arrangement [52].

All phase-locked loops employ an oscillator element with variable frequency capability, the VCO in Figure 2.4. This is an electronic oscillator whose oscillation frequency is controlled by a voltage input. The applied input voltage determines the oscillation frequency [52], [54]. Note that the VCO performs an integration of the control voltage and thus provides a factor of  $1/s$  in the loop transfer function. Because of this, a PLL is always at least a first order feedback system [52].

PLLs can be used to produce a higher frequency output with respect to the input frequency by using a frequency divider in the feedback loop, as shown in Figure 2.4, where the division ratio is  $N$ .

## 2.4 RF Measurements

A wide variety of methods and equipment are available for RF measurements ranging from signal sources, power meters, analog components and spectrum and network analyzers. These instruments are used to generate RF signals and measure a wide range of signal parameters. For the characterization of components, systems and signals in the microwave range several dedicated instruments are used.

RF signal strength can vary by many orders of magnitude, in particular, at the X-band test stands the power at the structure is in the range of mega-Watts while the power at the down-conversion mixer should be milli-Watts.

High resolution measurements are also important in high power RF conditioning where breakdown localisation is crucial to improving understanding of conditioning and breakdown phenomena. The RF measurements allow operators or control systems to set the accelerating voltage and phase for a given RF station in order to maintain the desired amplitude and phase at the required stability. LLRF systems for particle accelerators typically need to collect measurements of amplitude, phase, and frequency [55] In order to do this the operators need to be able to extract calibrated waveforms from the RF system, in this case the high power network and accelerating structures.

Directional couplers are used to extract a small portion of the energy from the high voltage network without interfering with the system operation. Their function is to sample RF signals at a predetermined degree of coupling, with high isolation

between the signal ports and the sampled ports [56]. Several techniques can be applied to detect amplitude and phase of RF signals which come from the directional couplers. The output is a continuous analog signal which is digitised by ADCs for further processing. [57].

Direct measurements of the circuit performance while the signal frequency is in the range of 12 GHz offers the ideal test quality but at the price of extremely high testing costs [47].

Prior to the advancement of converter technologies, direct sampling architectures were not practical because of the limitations in converter sample rates and resolution. Semiconductor companies have been able to expand resolution at higher sampling frequencies using new techniques to reduce noise within the converter. With the availability of much higher-speed converters featuring increased resolution, you can directly convert RF input signals up to several gigahertz [58].

This conversion rate enables digitization with very wide instantaneous bandwidth at the L and S-bands. As converters continue to evolve, direct RF sampling at other bands (such as C and X-bands) will likely become viable as well.

### 2.4.1 Phase and Amplitude Detection

Amplitude and phase properties of an RF system are important parameters of an accelerator system. Rich information is embedded in these two parameters. The standard method for measuring phase and amplitude is using two separate detectors, an amplitude detector and a phase detector. Recently, quadrature signal processing by using I/Q detection techniques has been widely used in sophisticated applications. This method can provide precision measurement, but with complicated circuitry and occupying much space. Most precision phase detectors are not designed to operate at the RF frequency and require down-conversion to an intermediate frequency before measuring [59]. The three methods for amplitude and phase detection are summarised in Figure 2.5.

The simplest method of amplitude detection is using a diode, traditionally a Schottky diode. The diode produces a continuous DC signal which is digitized using an ADC. The equivalent of this for measuring phase are phase detectors. One such example is an exclusive OR gate, this is the technique most commonly used in PLLs. These two methods sample the RF signal directly.

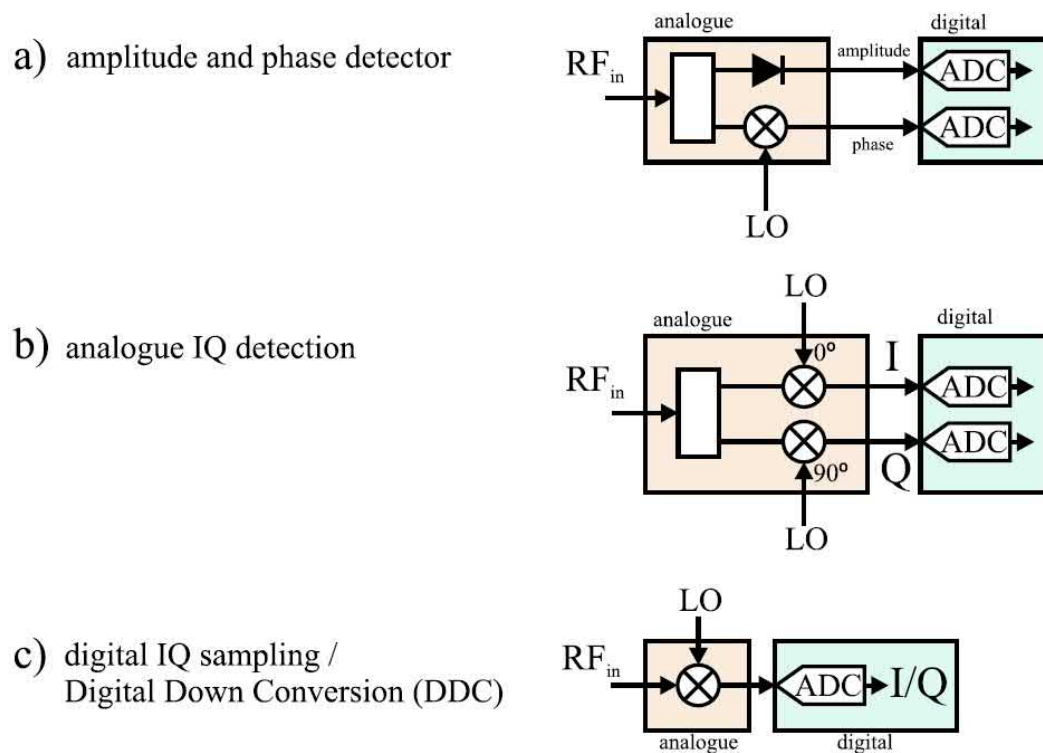


FIGURE 2.5: Three commonly used methods for Amplitude and Phase Detection [50]. All three methods use a combination of analog and digital components. In scheme *a*, the LO is the same frequency as the RF such that the output is a DC voltage which is proportional to the phase difference between the LO and RF. In schemes *b* and *c*, The LO frequency is usually at least an order of magnitude lower than the RF frequency in order to achieve down conversion to produce an AC signal containing both phase and amplitude information

The alternative is indirect detection where a parameter of the signal is measured, such as power, and the desired parameter is inferred from the known information, for example voltage.

### Analog IQ Demodulation

Using an analog demodulation IQ system, two matched copies of the RF signal are separately mixed with two LO signals with a  $90^\circ$  phase shift between the two signal chains. Both signals are subsequently digitized using separate channels of an ADC. In order to obtain accurate IQ measurements the two signal paths of the demodulator must be very closely matched. This makes the design susceptible to matching errors, leakage between lines, impedance mismatch and phase mismatch if the  $90^\circ$  line is not completely stable. This method will be referred to as analog IQ demodulation.

### Digital IQ Demodulation

The RF signal is transformed to an intermediate frequency and sampled to create the I and Q components digitally. Quadrature sampling of the IF obtains both components of a complex signal by taking subsequent samples from the two signals which are offset from each other by  $90^\circ$ , this is referred to as 'IQ' sampling. The trigonometry for converting the digital IQ samples to amplitude and phase is simple so the conversion is fast and the computing overheads are low.

The I and Q components are then extracted in a purely digital way by sampling the RF signals with a sampling period that corresponds to a phase shift of exactly  $90^\circ$  between samples at the IF. As the digital demodulation uses a single RF path this removes the error due to gain and impedance matching between the two paths. The precision of the quadrature phase shift is determined by the timing of the ADC clock. As well as improving the performance, this also saves on ADC channels compared with analog IQ demodulation which requires two ADC channels per RF signal [59].

A  $90^\circ$  phase shift between samples will only exist at the centre frequency of the IF so the IF must be very stable. Any frequency instability in the IF will introduce a quadrature phase error. If the ADC clock and the IF clock originate from the same source then any long term frequency drift will exist in both channels [50].

In polar coordinates the signal is represented as a rotating vector with amplitude,  $A$ , angular frequency,  $\omega$ , and initial phase of  $\phi_0$ . Positive frequencies rotate the phasor anticlockwise. The phasor is translated from the rectangular plane (I and Q values) onto the polar plane (phase and angles values) using the following:

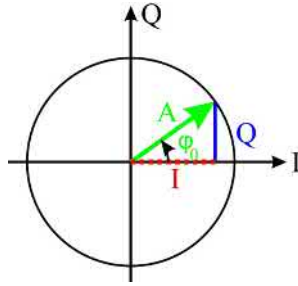


FIGURE 2.6: Phasor Representation of RF signal on a complex plane [50]. Using basic mathematical relations the I and Q values can be converted to phase and amplitude and vice versa

$$y(t) = A \cos(\phi_0) \sin(\omega t) = A \sin(\phi_0) \cos(\omega t) \quad (2.2)$$

$$y(t) = I \cdot \sin(\omega t) = Q \cdot \cos(\omega t) \quad (2.3)$$

The I and Q information is converted to amplitude and phase information using the following:

$$I = A \cos(\phi_0) \quad A = \sqrt{I^2 + Q^2}$$

$$Q = A \sin(\phi_0) \quad \phi_0 = \text{atan}\left(\frac{Q}{I}\right)$$

If the initial position of the rotating vector is known, then the new position is measured at a known time later, the algorithm rotates the phasor back to the initial position obtaining the change in amplitude and phase between the two vectors. The algorithm rotates the vector between the current position and the previous position and the change in phase and amplitude is extracted.

There are a number of potential problems associated with IQ sampling.

- The samples are usually taken at four points on the phasor circle and hence the systems only utilises four points of the ADC range for constant amplitude
- DC offsets at the input of the ADC or phase advances between samples (which differ from the expected 90°) systematically result in a ripple with frequency  $f_{IF}$ , this type of error is easily detectable.
- Non-linearities of mixers and differential non-linearities of ADCs generate higher harmonics of the input signal frequency  $f_{IF}$ .

Sampling this signal four times per period maps the second harmonic on the Nyquist frequency, while the third harmonic aliases directly on the IF frequency again. As a general rule, all odd harmonics alias to the carrier frequency while even harmonics alias to DC or to the Nyquist frequency. Any harmonics which map onto the IF frequency become indistinguishable from the carrier [50].

In the bottom diagram of Figure 2.7 the case for IQ sampling is visualised, in this case the harmonics (numbered from 2 to 8) align with the IF frequency, Nyquist frequency and zero.

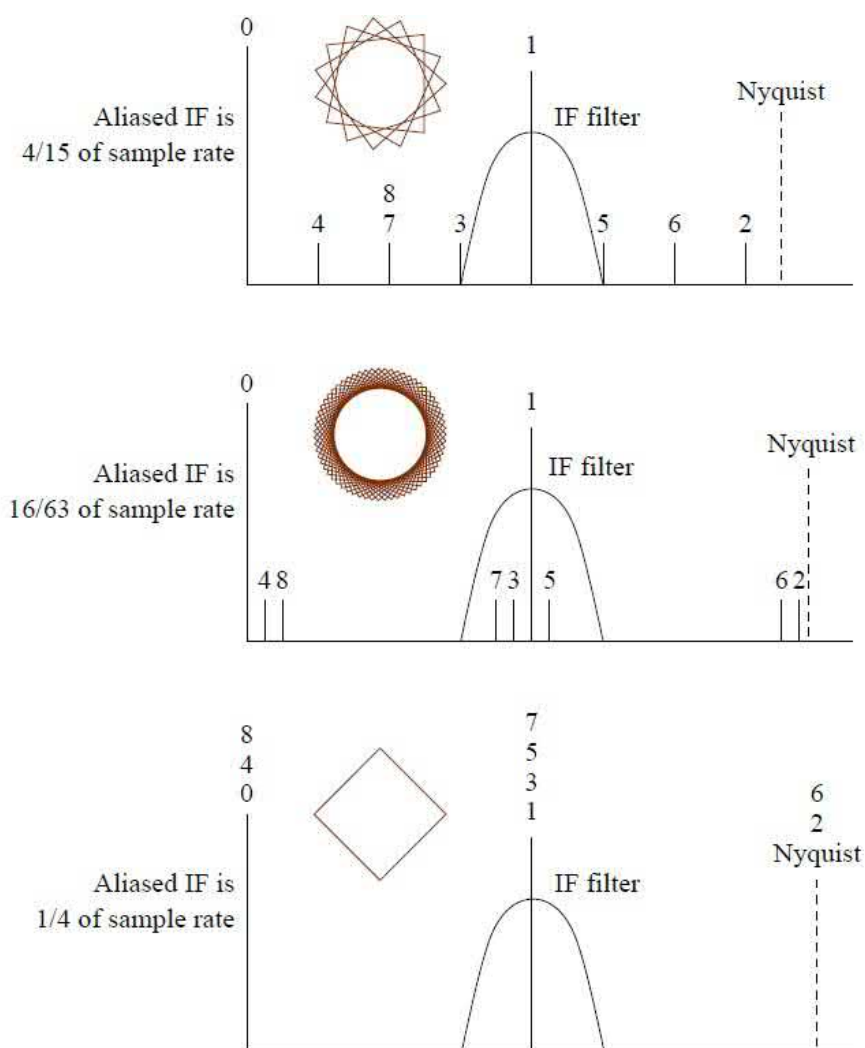


FIGURE 2.7: Aliased Harmonic Frequencies shown as a function of the chosen sample rate [60]

By comparison, the top two diagrams in Figure 2.7 show sampling at a non-IQ rate. The harmonic frequencies (numbered from 2 to 8) are spread throughout the samples spectrum and therefore could be easily filtered.

## 2.5 Sources of Errors and Instability in RF Systems

An ideal fixed-frequency oscillator without noise would produce a single frequency sine wave with no instability in its frequency or power level. In reality, any oscillator is affected by internal random noise processes, such as thermal and flicker noise, as well as aging and external influences, such as temperature and vibrations. In addition there will be parasitic frequencies produced by the RF components, in particular non-linear components.

The limiting noise source in a receiver depends on the frequency range in use, at very high frequency and ultra high frequency and above, these error sources are often lower, and thermal noise is usually the limiting factor [48].

Long-term and short-term stability are of critical importance. Long term frequency stability is concerned with how the output signal varies in timing periods on the order of hours, days or months. It is usually specified as the ratio,  $\frac{\Delta f}{f}$  for a given period of time, expressed as a percentage or in dB. Short-term stability refers to variations that occur in a period of seconds or less. These variations can be random or periodic.

Instabilities in an oscillator will perturb both the amplitude and phase. By design all practical oscillators are built with an amplitude-limiting mechanism. As a result amplitude fluctuations are usually greatly attenuated and phase noise generally dominates [61].

Unwanted signals that are integer multiples of the main carrier signal frequency are said to be harmonically related, the main source of these signals are amplifiers and mixers. These signals may be low enough in amplitude so they are insignificant, or they may be far enough away in frequency that they can be reduced with filtering. Harmonics are easy to detect because their frequency is predictable, for example, the harmonic content of a signal at 1 GHz, can be found at 2 GHz, 3 GHz, and so on [49].

Intermodulation distortion is the amplitude modulation of signals containing two or more different frequencies, caused by nonlinearities or time variance in a system. The intermodulation between frequency components will form additional components at frequencies that are not just at harmonic frequencies (integer multiples) of either, like harmonic distortion, but also at the sum and difference frequencies of the original frequencies and at sums and differences of multiples of those frequencies [62].

Intermodulation products are signals generated by nonlinear interactions in the

RF chain. Mixers are an example of a circuit component with nonlinear behavior. In RF transmitters, the output is filtered to isolate the higher frequency sum in a process known as up-conversion. In this way, through one or more up-conversion stages, the low-frequency baseband information can be translated to the final RF frequency for transmission. Unfortunately, mixers also provide a host of other signals including combinations of the input signals and their harmonics, as well as leakage of the input signals to the output. The frequency and amplitude of the intermodulation products change with changes in the input signals. With careful analysis, intermodulation products can be predicted, making it possible to minimize their impact [63] [62].

The term spurious or spur is often applied to any unwanted signal which are not harmonics or intermodulation products. Spurs can occur at any frequency and power level from sources such as leakage and electromagnetic interference. The unpredictable nature of spurious signals makes them more challenging to detect and remove. Empirical and analytical methods along with good design practices are the best tools to minimize their impact [64].

In wireless communications it is likely that an unwanted interfering signal is present in the same channel as the wanted signal and that the power of the unwanted signal could also be significantly larger than the desired signal. In an RF transmitter, unwanted signals represent wasted RF power which has a variety of consequences including lower efficiency, excessive heat production, reduced battery life or lower test yields [48]. The best plan of action is to perform proper analysis during the design phase to identify and mitigate unwanted signals from the transmitter. Operating parameters, cost, and design considerations impact RF system performance and, subsequently, the RF signal quality [49].

### 2.5.1 Thermal Noise

Thermal noise, also known as Johnson–Nyquist noise, is the electronic noise generated by the thermal agitation of the charge carriers inside an electrical conductor at equilibrium, which happens regardless of any applied voltage.

Thermal noise is present in all electrical circuits, in sensitive electronic equipment such as radio receivers thermal noise could drown out weak signals and can be the limiting factor on sensitivity of an electrical measuring instrument.

Thermal noise can be modeled by a voltage source representing the noise of the non-ideal resistor in series with an ideal noise free resistor. The one-sided power

spectral density, or voltage variance (mean square) per hertz of bandwidth, is given by [49]:

$$\overline{v_n^2} = 4k_B TR$$

For a given bandwidth, the root mean square (RMS) of the voltage,  $v_n$ , is given by:

$$v_n = \sqrt{4k_B TR \Delta f}$$

Where:

- $k$  is Boltzmann's constant in joules per Kelvin ( $1.380649 \cdot 10^{-23}$ )
- $\Delta f$  is the bandwidth in Hz
- $T$  is the resistor's absolute temperature in Kelvin
- $R$  is the resistance in  $\Omega$
- $f$  is the frequency in Hz

Thermal noise in an ideal resistor is approximately white, meaning that the power spectral density is nearly constant throughout the frequency spectrum (however see the section below on extremely high frequencies). When limited to a finite bandwidth, thermal noise has a nearly Gaussian amplitude distribution [65]. Thermal noise is distinct from shot noise, which consists of additional current fluctuations that occur when a voltage is applied and a macroscopic current starts to flow. Hence there is a theoretical limit to the noise floor of an oscillator determined by the thermal noise of a matched source, at 25°C the thermal noise contribution is  $-174\text{dBm/Hz}$  [66].

However, thermal noise is not the only noise contribution. Other sources of noise, such as flicker, as well as phase noise from components will add on to the noise floor.

## 2.5.2 Phase Noise in RF Systems

Phase noise is the most common expression of frequency instability. Phase noise, the random phase fluctuations of a periodic signal, is an important parameter to characterize high-frequency devices, in particular reference oscillators and microwave synthesizers.

The fundamental effect of phase noise is a random rotation of the received signal constellation that may result in detection errors. Furthermore, performance of systems with high carrier frequencies is more severely impacted by phase noise than low frequency systems, mainly due to the poor phase noise performance of high-frequency oscillators [67].

Phase noise is rapidly becoming the most critical factor in sophisticated radar and communication systems. This is because it is the key parameter defining target acquisition in radars and spectral integrity in communication systems. Phase noise is also key parameter in particle accelerator RF systems where it is commonly used as a measure of frequency stability within an oscillator [64].

Phase noise appears as power across a spectrum of frequencies very close to the desired output. The power level in the sidebands is dependent upon the quality of the oscillator and is measured in dBc/Hz at an offset frequency from the desired signal, typically the carrier [68].

Phase noise is a secondary effect directly related to the topology and construction of the oscillator and thermal noise within the active devices of the oscillator. Therefore phase noise is directly impacted by oscillator choice, this problem can be addressed by spending considerable time and money to design or procure a low noise oscillator. However, most oscillators do not generate sufficient output power on their own and amplification will be necessary which amplifies the phase noise contribution [46].

Any phase fluctuations will modulate the signal, the phase change of the signal will no longer be entirely linear. This modulation will manifest as sidebands offset from the carrier and increased noise floor. Finally, the frequency multiplication process also multiplies phase noise, which limits signal quality attainable from high frequency synthesis [69].

Furthermore, the Barkhausen conditions for steady oscillation, unity gain and zero phase, impose that the internal phase fluctuations of an oscillator are transformed into frequency fluctuations [69]. This results in enhanced phase fluctuations at the output of the oscillator and decreases the SNR.

The oscillator will convert phase noise from its internal components into frequency noise, which results into a reduction in the phase noise by a factor  $f^2$  in the phase-noise power spectral density. This phenomenon is known as the Leeson effect [70]. Leeson's equation is an empirical expression that describes an oscillator's phase noise spectrum.

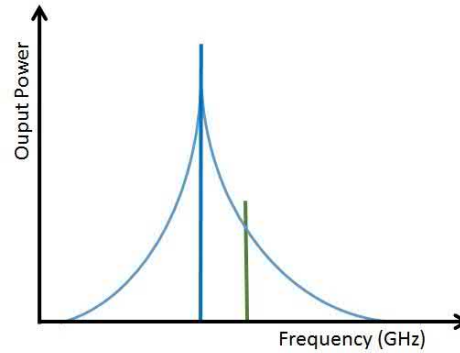


FIGURE 2.8: Pictorial representation of an LO signal with phase noise (Blue), and an RF signal close in frequency to the LO (Green).

The discrete spurious components could be caused by known clock frequencies in the signal source, power line interference, and mixer products. The broadening caused by random noise fluctuation is due to phase noise. It can be the result of thermal noise, shot noise and/or flicker noise in active and passive devices [54].

### 2.5.3 Phase Noise in Frequency conversion

During frequency heterodyning the input RF signal can be very close in frequency to the LO which makes the conversion process susceptible to phase noise, especially if the desired signal strength is low. If the power level of the RF signal falls below the phase noise spectrum of the LO signal (as demonstrated in Figure 2.8), we will be unable to recover any baseband information, as the signal will be lost in the noise. Therefore, reducing the phase noise will increase the receiver sensitivity [64], as shown visually in Figure 2.9.

Figure 2.10 shows a typical spectrum, with random and discrete frequency components causing a broad skirt and spurious peaks.

To be able to characterize the phase noise of a real oscillator, its output signal can be modelled by:

$$V(t) = V_0 + \epsilon(t)\sin(2\pi\omega_0t + \Phi(t))$$

Where  $\Phi(t)$  is the random phase fluctuations,  $V_0$  is the nominal amplitude,  $\omega_0$  is the nominal frequency.  $\epsilon(t)$  is the random amplitude fluctuations which are generally neglected in oscillators.

The frequency instability is expressed as the ratio of the power of the carrier signal to the noise power within a predefined bandwidth, usually 1Hz, at increasing

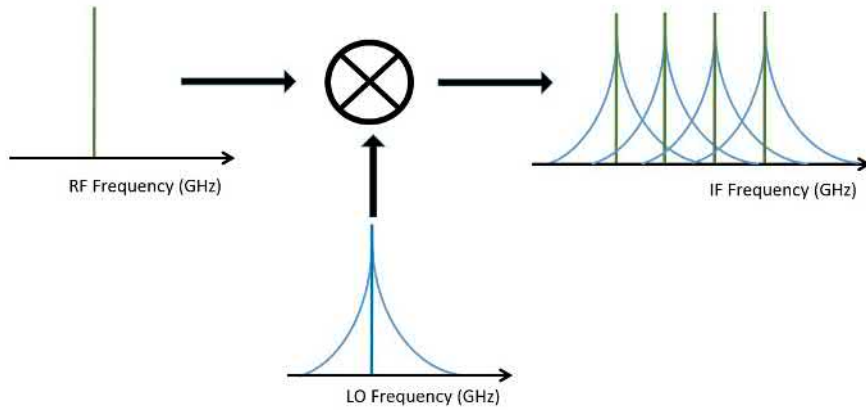


FIGURE 2.9: Pictorial representation of phase noise issues in communications systems. LO signal with phase noise (Blue), RF signal (Green). In this figure, we note that if the phase noise of the LO is too high, then the noise will be converted into adjacent channels of the baseband data, thereby ruining the integrity of the information.

offsets from the carrier. Phase noise is often quoted as being single side band, SSB. Although noise does add signals to both sides of the carrier the sides will usually be symmetrical [68].

The spectral density of phase noise  $S_{\Phi}(f)$  defined as:

$$S_{\Phi}(f) = \Phi^2(f) \frac{1}{BW} [\text{rad}^2 / \text{Hz}]$$

Where  $\Phi(f)$  is the rms phase fluctuations and BW is the bandwidth. The single sideband phase noise:

$$\Gamma(f) = \frac{1}{2} S_{\Phi}(f)$$

In theory, the power level of the carrier frequency is not relevant in this measurements as the performance should be consistent at all carrier power levels unless operating conditions are changed [68].

#### 2.5.4 Phase Noise in PLLs

The phase noise can be separated into the contributing portions of each component and includes the reference noise, the phase frequency detector noise, the VCO noise, and wideband noise due to amplifiers and other internal circuitry. The overall phase error is made up of the phase error due to the combination of all the individual sources as shown in Figure 2.11.

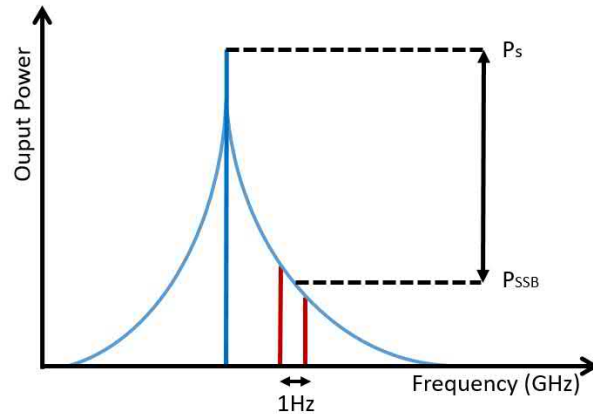


FIGURE 2.10: Example of Spreading of the Fundamental Frequency due to Phase Noise Sidebands and Spurious Signals. Ideally the difference between  $P_s$  and  $P_{SSB}$  should be maximised to ensure the cleanest signal [52]

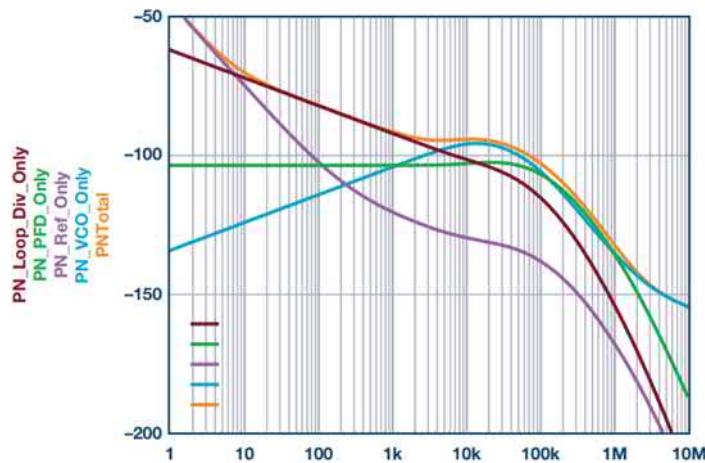


FIGURE 2.11: Diagram showing the individual phase noise contribution of each component in the PLL loop and how the sum of these sources creates the total PLL Phase Noise

2.11

### 2.5.5 Phase Noise to Jitter

Jitter is the deviation from true periodicity of a periodic signal, often in relation to a reference clock signal. In clock applications it is called timing jitter. Jitter is a significant, and usually undesired, factor in RF systems. Jitter may be caused by electromagnetic interference and cross-talk with carriers of other signals.

Jitter can be quantified in the same terms as all time-varying signals, root mean square, RMS, or peak-to-peak displacement. Also like other time-varying signals, jitter can be expressed in terms of spectral density. Jitter frequency, the more commonly quoted figure, is its inverse. Jitter can have a significant effect on SNR performance.

Low jitter clocks are used in digital sampling so that the ADC performance is not

degraded. However, oscillators used for sampling clock generation are more often specified in terms of phase noise rather than time jitter.

The first step in calculating the equivalent rms jitter using the phase noise plot is to obtain the integrated phase noise power over the frequency range of interest. This is usually done in segments as shown in Figure 2.12.

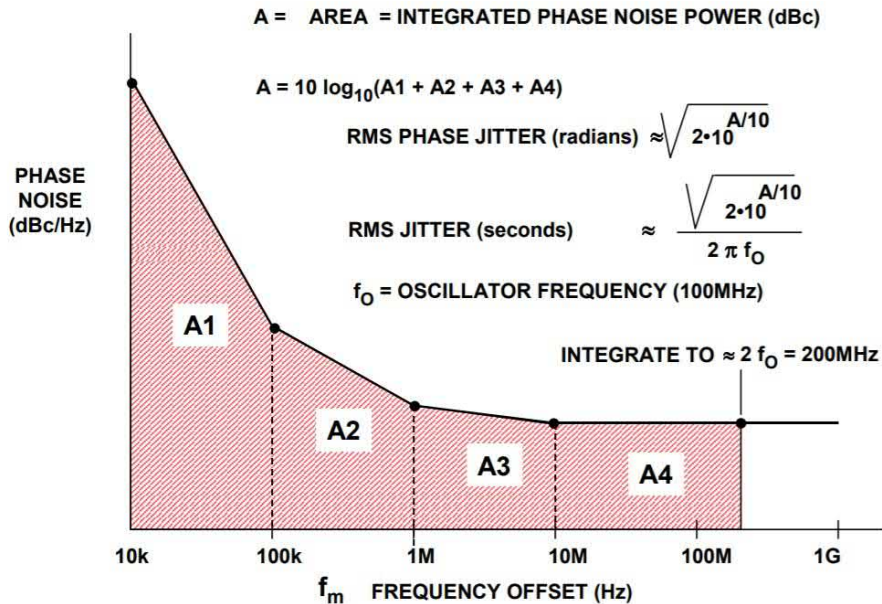


FIGURE 2.12: Calculating Jitter from Phase Noise by integrating the phase noise contribution from individual sections [66]. The phase noise profile is often separated into decades along the x-axis (Frequency offset)

The frequency is specified as an offset from the carrier frequency, usually phase noise is specified in the range of 1 kHz to 10 MHz away from the carrier. The lower frequency bound should be as low as possible to get the true rms jitter. The low frequency contributions may be negligible compared to the broadband contribution if a crystal oscillator is used. Other types of oscillators may have significant jitter contributions in the low frequency area, and a decision must be made regarding their importance to the overall system frequency resolution [66].

The integration of each individual area yields individual power ratios. The individual power ratios are then summed and converted back into dBc. Once the integrated phase noise power is known, the rms phase jitter in radians is given by Equation 2.4 and the conversion to seconds is shown in Equation 2.5, where A is the integrated phase noise.

$$\text{RMSPhaseJitter(radians)} = \sqrt{2 \cdot 10^{A/10}} \quad (2.4)$$

$$\text{RMSPhaseJitter(seconds)} = \frac{\sqrt{2 \cdot 10^{\frac{A}{10}}}}{2\pi f_0} \quad (2.5)$$

## 2.6 RF Reflections

Signal reflection occurs when a signal is transmitted along a transmission medium, such as a coaxial cable or waveguide, which contains an impedance mismatch along its length. The signal will be partly, or wholly, reflected back in the opposite direction when the travelling signal encounters a discontinuity in the characteristic impedance of the line, or if the far end of the line is not terminated in its characteristic impedance. This can happen, for instance, if two lengths of dissimilar transmission lines are joined together [46].

Due to reflections, an electromagnetic wave on a transmission line can be thought of as being composed of two traveling waves, one moving toward the load (the 'forward' wave) and one moving in the opposite direction (the 'reflected' wave). These waves, moving through the transmission line, interfere with one another to produce the standing wave. Each of these waves have a voltage amplitude, the forward voltage and the reflected voltage [55].

Reflections cause several undesirable effects, including modifying frequency responses, causing overload power in transmitters and over-voltages on power lines. However, the reflection phenomenon can also be made use of in such devices as stubs and impedance transformers [46].

### 2.6.1 Reflection Coefficient

The ratio of reflected energy depends on the impedance mismatch. Mathematically, it is defined using the reflection coefficient. It is equal to the ratio of the amplitude of the reflected wave to the incident wave, with each expressed as phasors.

In RF and transmission line theory, the reflection coefficient is the ratio of the complex amplitude of the reflected wave to that of the incident wave. The voltage and current at any point along a transmission line can always be resolved into forward and reflected traveling waves given a specified reference impedance  $Z_0$  [49]. The reference impedance used is typically the characteristic impedance of a transmission line.

The reflection coefficient is typically represented with a  $\Gamma$  and can be written as [47]:

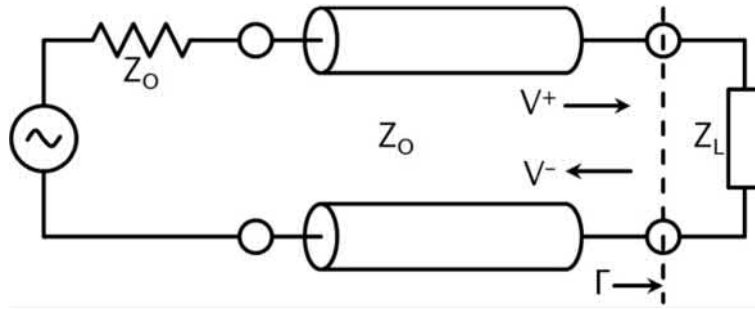


FIGURE 2.13: Reflections and VSWR on a Transmission Line

$$\Gamma = \frac{V^-}{V^+} = V_+ \frac{Z_L - Z_0}{Z_L + Z_0}$$

Where:

- $V^-$  is the reflected voltage wave
- $V^+$  is the forward voltage wave
- $Z_L$  is the terminating impedance in  $\Omega$
- $Z_0$  is the characteristic impedance of the transmission line in  $\Omega$

In RF systems the magnitude of the reflection can also be expressed by the dimensionless ratio known as voltage standing wave ratio (VSWR). VSWR is defined as the ratio of the maximum voltage to the minimum voltage in standing wave pattern along the length of a transmission line structure.

$$VSWR = \frac{1 + |\Gamma|}{1 - |\Gamma|}$$

VSWR is the conventional means of expressing the match of a radio transmitter to its antenna. It is an important parameter because power reflected back into a high power transmitter can damage its output circuitry [46].

### 2.6.2 Phase of Reflected Signal

Reflections of signals on conducting lines typically exhibit a phase change from the incident signal, the phase change is dependent on the impedance mismatch.

The voltage wave reflection on a line terminated with a short circuit is  $180^\circ$  phase shifted. Conversely the current wave, is not phase shifted. A transmission line terminated with an open circuit is the dual case; the voltage wave is shifted by  $0^\circ$  and the current wave is shifted by  $180^\circ$ .

## 2.7 Visual Programming Languages

In computing, a visual programming language (VPL) is any programming language where programs are created by manipulating elements graphically rather than by specifying them textually [71]. Examples of elements include graphics, drawings, animation, buttons or icons. A VPL allows programming with spatial arrangements of text and graphic symbols. In principle visual programming resembles flow diagrams, where boxes or other screen objects are treated as instructions, connected by arrows which represent relations and data flow [72].

These languages provide many built-in elements that can be implemented quickly, in addition, new objects can also be created. The elements are placed on the main interface component where they can be manipulated, resized and rearranged [73].

VPLs require computer with more memory, high storage capacity of hard disk, and faster processor. Furthermore, these languages can only be implemented on graphical operating systems like Linux and windows [72].

### 2.7.1 Labview

LabVIEW was first launched 1986 as a tool for scientists and engineers to facilitate automated measurements. The name LabVIEW is a shortened form of its description: Laboratory Virtual Instrument Engineering Workbench [71]. LabVIEW was developed by National Instruments as a workbench for controlling test instrumentation. However its applications have spread well beyond just test instrumentation to the whole field of system design and operation [73]. Easy to interface to many hardware items like data acquisition and test equipment.

LabVIEW an environment that enables programming in G, this is a graphical programming language created by National Instruments that was initially developed to communicate via GPIB, but since then it has been considerably updated. LabVIEW now provides other facilities including debugging, user interface, hardware management and interface for system design.

LabVIEW is from a closed sourced which makes it unsuitable for some applications where standardisation or specific customisation is required. Closed source also increases cost of owning and running a National Instruments system.

## Graphical Programming in Labview

Each VI has three components: a block diagram, a front panel, and a connector pane. LabVIEW integrates the creation of the user interface, called front panels, into the development cycle. Individual pieces of LabVIEW code are called virtual instruments, (VIs) [71].

The front panel is built using controls and indicators. Controls are inputs which allow a user to supply information to the VI. Indicators are outputs which indicate, or display, the results based on the inputs given to the VI. A front panel and corresponding block diagram are shown in 2.14.

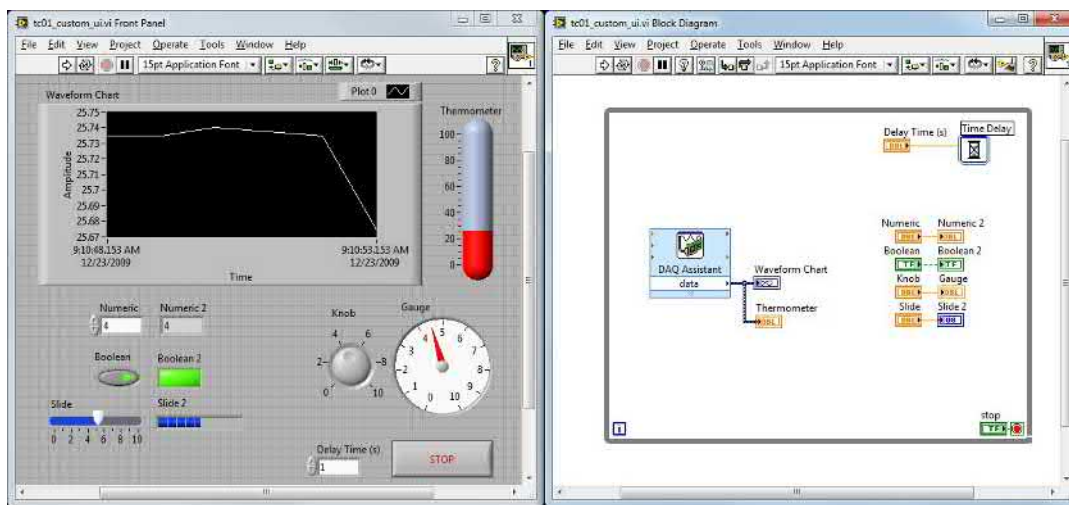


FIGURE 2.14: An example of a basic piece of code in LabVIEW. The block diagram (white background) is used to send instructions to the front panel (grey background). The instructions can be used for control, data collection, data viewing or indication of status

The back panel of the VI, which is a block diagram, contains the graphical source code. All of the objects placed on the front panel will appear on the back panel as terminals. The back panel also contains structures and functions which perform operations on controls and supply data to indicators [73].

Collectively controls, indicators, structures, and functions are nodes. Nodes are connected to one another using wires.

Thus a VI can be run as either a program, with the front panel serving as a user interface. Alternatively, the connector pane is used to integrate the VI into the block diagrams of other higher order VIs. When a VI is dropped as a node into a higher level block diagram, the front panel defines the inputs and outputs for the node through the connector pane. This implies each VI can be easily tested before being embedded as a subroutine into a larger program [71].

Programming in Labview is based on data availability. If there is enough data available to a VI or function then it will execute. Execution flow is determined by the structure of the graphical block diagram on which the programmer connects different function-nodes by drawing wires. These wires propagate variables and any node can execute as soon as all its input data becomes available. Since this could be the case for multiple nodes simultaneously, LabVIEW can execute inherently in parallel. [74].

The graphical approach allows non-programmers to build programs by dragging and dropping virtual representations of lab equipment with which they are already familiar. The LabVIEW programming environment, with the included examples and documentation, can be used to make user interfaces and simple routines very quickly.

However, there is also a risk of underestimating the level of complexity required for high-quality G programming. For complex systems or large pieces of code it is important that the programmer possess an extensive knowledge of the special LabVIEW syntax and the topology of its memory management [74].

### **PXI Chassis**

PCI eXtensions for Instrumentation (PXI) is the National Instruments hardware system which can be used as a basis for building electronic test equipment, automation systems, and modular laboratory instruments[75].

PXI is designed for measurement and automation applications that require high-performance and a rugged industrial form-factor [76]. With PXI, the user selects the modules from a number of vendors and integrate them into a single PXI system, over 1150 module types were available in 2006 [75]. A typical 8-slot PXI chassis is 4U high and half rack width, full width chassis contain up to 18 PXI slots which can each accept a module[75].

PXI modules can be customized through the choice of module for a vast range of measurement and automation applications. There are also companies specializing in writing software for PXI modules, as well as companies providing PXI hardware-software integration services.

Most PXI instrument modules are register-based products, which use software drivers hosted on a PC to configure the instruments, taking advantage of the increasing power of PCs to improve hardware access and simplify embedded software in

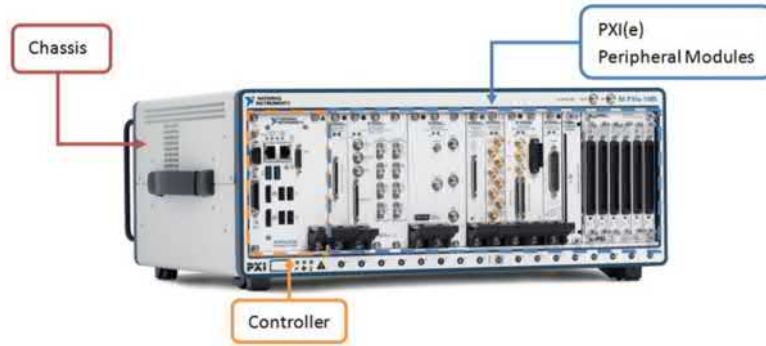


FIGURE 2.15: A PXI Chassis similar to those used at the X-band Test Stands. The controller is the left-most unit which controls the other modules. There are up to 18 slots in a PXI crate of this size, these can be filled by a variety of cards such as: ADC's, DAC's, voltage probes, digital multi meters, and timing cards

the modules. The open architecture allows hardware to be reconfigured to provide new facilities and features [76].

The modular PXI systems allows the user to incorporated only the required features without adding unnecessary cost. In addition it is not necessary to create custom software or drivers, this reduces the manpower and development facilities required to complete the system [56].

## 2.8 Diagnostics and RF Control in Particle Accelerators using Labview

The selection of a suitable technology is a key factor in the development of any project to achieve the requirements of the project [76].

Fifteen years ago, LabVIEW had not been widely accepted for control systems of accelerators and large experimental control systems due to limitations in performance, scalability, and maintainability of large LabVIEW designs [77].

The diagnostics and control of RF fields are essential aspects in every accelerator experiment. Diagnostics are key for the adjustment and normal operation of the machine. They provide useful information related to several processes and components of the machine, and they can be based on different physical phenomena depending on the variable to be measured and the accelerator type. The diagnostic tools need to perform high accuracy measurements in order to generate valuable information.

Particle accelerator experiments are complex systems that require a large number of devices and tools for development and operation. Therefore, the research and

innovation in technologies applied to particle accelerators is very dynamic, resulting in new tools, applications and improvements from year to year. Among these technologies, those focused on the RF control and diagnostics are specially relevant, as they play a key role in the acceleration and the correct operation of the whole machine.

The usage of X-band frequencies leads to very high sampling rates which directly translates in the need for expensive equipment.

Digital LLRF feedback loops typically implement the phase and amplitude controls in a single loop, taking advantage of the parallel execution possibility offered in digital signal processing architectures [78].

The main requirements for a control system for the X-band test stands is a flexible, modular and re-configurable system. The hardware required requirements are:

- Digital: the solution architecture must be mainly based on digital hardware, microprocessors and FPGAs, minimizing the usage of analog components.
- Modular: the platform selected must have a modular nature, giving the opportunity to easily exchange independent modules without being the rest of the system being affected.
- Reconfigurable: the solution must allow for quick changes or the addition of new functionalities and adapt to future changes in requirements.

Considering this, the PXI platform of National Instruments has been selected as the main architecture for the development of the proposed applications. PXI provides a large variety of modules of very different types, like data acquisition, signal generation, FPGA technology, timing, to name a few. Another big advantage of working with this architecture is that all the system is integrated under a common environment operated in LabVIEW. This eases the task of integrating a wide amount of hardware devices, thus reducing the effort employed in complex tasks such as driver development, use of peer-to-peer streaming or DMA transfers among others. It is also worth pointing out that LabVIEW allows to program FPGA based cards in standard LabVIEW language, not requiring the development of low level VHD code, a fact that eases the development of programs in terms of effort and time [76].

### Timing And Synchronisation using PXI Chassis

Control and data acquisition systems for particle accelerators often need to ensure time-coherent behavior in a distributed environment. This is usually achieved by a dedicated timing network whose purpose is to distribute a common notion of time from one master to many receiving nodes [77].

Real-life accelerator timing systems often combine two approaches. Detecting event-type behavior is required for safety systems and highlighting a specific system behaviour such as breakdown detection, For event-type control the master control system needs to react to external conditions with low latency. On the other hand, having a solid time base everywhere is practical for general operation and for time-tagging acquired data [77].

Typically a time dependent application consists of a network containing multiple clocks that each require synchronisation within set tolerances. In particle accelerator applications the quality of timing and synchronisation is of critical importance. Poor timing and synchronisation will directly impact the performance of the application or the usefulness of the data generated by it [77].

No oscillator perfectly generates the specified frequency, the major clock error components being accuracy, stability, and jitter. when using distributed timing systems, cable distances begin to dictate performance due to clock skew and clock drift [77].

NI provides timing and synchronization control via the PXI chassis which maintains the 10 MHz back plane clock and length-matched PXI star trigger signals. With the PXI chassis you can distribute a 10 MHz reference clock on the back plane to achieve synchronization across modules within a PXI chassis. The 10 MHz reference clock can be synchronised between multiple chassis'. For an NI PXI Express chassis, this oscillator is accurate to 25 parts per million (ppm) [79].

With the NI PXI chassis clocks and triggers are physically connected between subsystems, this typically generates the highest precision of synchronization [79].

## Chapter 3

# Xbox1 LLRF: Design and Commissioning

### 3.1 Introduction

Xbox1 is the first standalone test stand to be operated at CERN. As discussed in the previous chapters, the primary objective of the test stands is to support the development of high-gradient, accelerating structures and high-power, 50-100 MW range, RF components for the CLIC project [5]. Before Xbox1 started operations the only place where X-band power was available at the pulse lengths and power required to test CLIC accelerating structures was CTF3 at CERN. The CTF3 facility was described in Section 1.2.5.

Xbox1 has the same modulator, klystron, pulse-compressor, waveguide distribution system and accelerating structure configuration as previous test stands at KEK and SLAC [80], [81]. Due to the shift in frequency from the 11.4 GHz used at SLAC and KEK to the 12 GHz used in Europe, many new waveguide components had to be designed. This included the pulse compressor, directional couplers, mode converters, vacuum ports, hybrid splitters and waveguide loads.

The X-box test stands require advanced instrumentation and control for proper operation and to avoid damaging the structure. An important part of the RF instrumentation is the low level radio frequency (LLRF) system which drives the high power RF system. The LLRF regulates the RF field in the accelerating structures by measuring the magnitude and phase of cavity fields. Regulation of the field phase in accelerating structures is an important parameter that controls performance, especially in machines like FELs. A phase error induced by the LLRF that controls the X-band structure directly affects beam quality.

The LLRF system is responsible for generation, modulation and reception of the

X-band pulses and can be generally split into two sections; a transmitter and a receiver. The transmitter must produce an 11.9942 GHz RF pulse with phase and amplitude modulation and sub-microsecond pulse lengths. At Xbox1 the X-band pulses must use the 2.9985 GHz master oscillator from the CLEAR accelerator as a source so beam and RF timing can be synchronised. A master oscillator is a single RF source used to generate a constant frequency from which is derived any other frequencies required in an RF system. The 2.9985 GHz CLEAR master oscillator is generated using a Rhode and Schwarz SMC100A signal generator.

The X-band receiver must produce a modulated pulse which is amplified using a 50 MW klystron, compressed in the time domain and passed to the accelerating structure.

The receiver must perform down-conversion of the returning RF signals so they are suitable for digitisation. The receiver will use frequency mixing to translate the X-band signals down to the MHz region where they can be sampled using the existing acquisition cards at Xbox1. A crucial aspect of the LLRF receiver is the local oscillator (LO). The phase noise performance is a parameter of interest which is used to quantify the quality of the LO as direct measurements are not readily available for X-band frequencies. Errors from the LO will be directly mixed with the RF signals, as such they appear as errors in the cavity field detection which influences the regulation of the acceleration field. A phase-locked loop (PLL) and an alternative single side-band mixing technique are both tested for the LO generation at Xbox1.

The requirements for the LLRF will be determined from the timing and phase resolution required to perform breakdown localisation and from the current ADC hardware. The design and commissioning of the LLRF system will be described in this chapter.

In some cases, the requirement on phase stability differs by time scale, short term (during the pulse), medium term (pulse-to-pulse), long term (minutes to hours).

Facility	Frequency Band (GHz)	Amplitude Stability Target (%)	Phase Stability Target (°)
XFEL	X	0.01	0.01
ILC	L	0.1	0.1
SNS	X	0.5	0.5
JPARK	L	1	1

TABLE 3.1: Stability in Different Accelerators [13], [33], [82]. The stability is specified in peak to peak rather than in rms in proton machine due to beam velocity is dependent on energy gain.

At this junction the phase and amplitude stability tolerances of the CLIC main beam have not been very strictly defined and as such there are no strict tolerances to be reached by the LLRF at this junction. Hence it would be prudent to consider some other X-band RF sources to help quantify the achievable stability. This was particularly the case prior to serious consideration of a klystron based first CLIC stage, as in the initial CLIC design the RF for the main beam was provided by the drive beam rather than a traditional LLRF system.

Several particle accelerator facilities utilise X-band RF systems and their target performances will be summarised here. The most prudent comparison is perhaps the other X-band test stands at CERN as they have the most overlap in similarities.

Facility	Frequency Band (GHz)	Amplitude Stability Target (%)	Phase Stability Target ( ° )
Xbox2 LLRF	X	0.4	0.9
ELETTRA FEL	X	0.5	0.5
Swiss XFEL	X	0.018	0.027
CLIC Drive Beam	X	0.1	0.05
Libera Digital LLRF	S	0.027	0.033
LCLS Klystron Output	L	0.1	0.5

TABLE 3.2: Comparison of phase and amplitude stability targets at the output of the LLRF system from a variety of particle accelerator facilities operative at or below X-band frequencies [5], [14], [37], [58], [83], [84]. X-band is in the range of 12 GHz (in these specific cases, in actuality X-band can extend down to 9 GHz) , S-Band is 3 GHz and L-band is 1.5 GHz

A summary of the literature described here suggests that a reasonable long-term phase and amplitude stability of the RF arriving at the structure (after the klystron) is  $0.5^\circ$  and 0.5% respectively from Tables 3.2 and 3.1.

## 3.2 Design of the X-Band Pulse Forming Network

Previously, the pulse forming network (PFN) at Xbox1 was a complex chain of analog amplifiers, phase shifters, pulse amplifiers and voltage controllers. These were controlled using individual timing signals, individual control systems and a PLC that communicated with the PXI crate.

The intention for the new PFN is to reduce the complexity of this system and increase the resemblance with the system used at Xbox2 and Xbox3. The reduction in complexity will increase stability by reducing the number of error sources in the RF chain. The pulse control will also be integrated directly into the PXI system.

### 3.2.1 Requirements

- The pulse forming network must use the 2.9985 GHz CLEAR master oscillator as an RF source and must have the ability to be synchronized with the CLEAR accelerator timing signals.
- The system must generate a signal at 11.9942 GHz with pulse, phase and amplitude modulation
- RF pulse stability of  $0.5^\circ$  and 0.5% respectively at the output of the LLRF.

Formerly, the 11.9942 GHz was produced in a mixing crate belonging to CLEAR, and the RF was transferred to Xbox1 using a coaxial cable, which was approximately 30 M. The new LLRF system will generate the 11.9942 GHz at Xbox1. This will reduce thermal drifts and will allow for easier local diagnostics.

The X-Band RF requires pulse, amplitude and phase modulation. This can be achieved in analog, digitally or using a combination of both. In this case, one digital modulation card is used to replace a number of modulation components that were used in the original PFN. Modulation becomes more expensive and difficult as frequency increases. It is impractical to modulate the 11.9942 GHz signal directly, so the system will modulate the S-band master oscillator signal. The modulated master oscillator can then be multiplied up to the X-band frequency; the X-band signal will retain the modulation after mixing. This method has been demonstrated at Xbox2 and Xbox3 with success.

The NI5793 RF modulation card generates a modulated 2.9985 GHz signal which is synchronised to the CLEAR master oscillator of the same frequency. The RF modulation card has an amplitude resolution of 0.23 dB and frequency tuning resolution of 25 kHz. The previous system for phase modulation used 10-bit phase shifters (1024 voltage levels) but the NI5793 uses 16bit DACs (65,536 voltage levels).

The modulated 2.9985 GHz input is up-converted to 11.9942 GHz output using mixing. Thus, an oscillator is required at either 8.995 GHz or 14.9925 GHz. Two schemes have been proposed that use frequency multiplication and mixing. The phase noise performance of the two schemes will be considered to determine which will be optimal.

- Scheme 1 (Shown in Figure 3.1): Multiply the master oscillator by 4 to produce 11.9942 GHz. Mix this again with the master oscillator to produce 8.995 GHz and 14.9925 GHz. Low pass filter to obtain 8.995 GHz and mix with the modulated 2.9985 GHz.

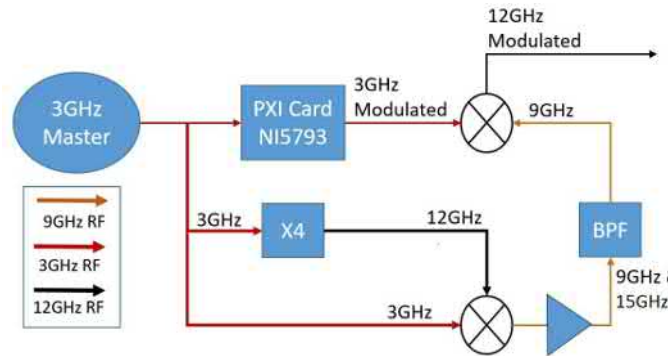


FIGURE 3.1: Scheme 1: Proposed LLRF layout for the generation of a modulated 11.9942 GHz signal using a the CLEAR local oscillator source. This generation scheme uses a x4 Multiplier to produce sidebands close to 15 GHz and 9 GHz, of which the 9 GHz will be used

- Scheme 2 (Shown in Figure 3.2): Double the master oscillator to produce 5.9975 GHz. Mix this with the master oscillator to produce 8.995 GHz and 2.9986 GHz. High pass filter and mix with the modulated 2.9985 GHz.

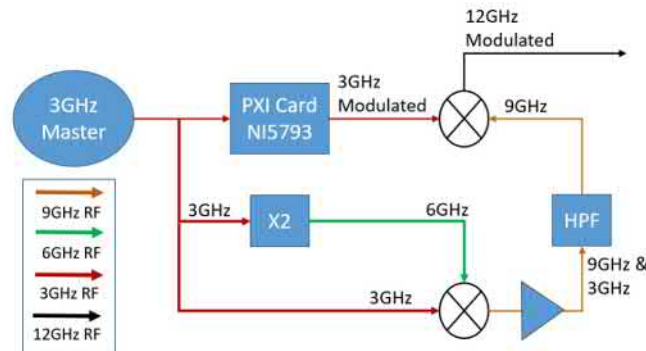


FIGURE 3.2: Scheme 2: Proposed LLRF layout for the generation of a modulated 11.9942 GHz signal using a the CLEAR local oscillator source. This scheme differs from the previous (Scheme 1) only in the use of a x2 multiplier (instead of a x4 multiplier)

### 3.2.2 Managing Phase Noise in Chains of RF Components

Phase noise and timing jitter are both measures of uncertainty in the output of an oscillator in the frequency and time domain respectively. Phase noise is a measure of the short-term phase/frequency instability of an oscillator. Phase noise adjacent to the desired frequency will spread the fundamental signal over a range of frequency

bins and broadband noise degrades the signal-to-noise ratio. The signal-to-noise ratio is given by:

$$SNR_{dB} = 10 \log_{10} \left( \frac{P_{signal}}{P_{Noise}} \right)$$

Because phase modulation is symmetrical around the centre frequency, the phase noise is measured in a single side-band. The frequency axis is plotted on a log scale as shown in Figure 3.3. The curve can be segmented into a number of regions which each have a slope of  $\frac{1}{f^x}$ . Moving from the furthest offset towards the carrier, the white noise region is where  $x = 0$ . The 'flicker' phase noise region is where  $x = 1$  and past this point the phase noise increases at approximately 20 dBm per decade. The transition from flicker noise to white noise is referred to as the corner frequency,  $f_c$ , low values of corner frequency are desirable as this increases signal-to-noise ratio.

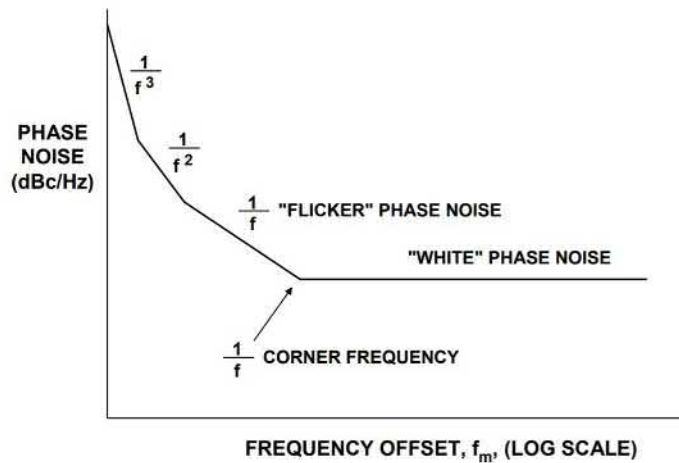


FIGURE 3.3: Example of Single Sideband Oscillator Phase Noise measured in dBc/Hz vs Offset Frequency. The spectral purity of the carrier is affected by the device generated flicker noise at frequencies close to the carrier and shows a  $1/f$  component with a corner frequency known as  $f_c$

A sinusoidal signal with phase error can be defined as:

$$V(t) = V_0 \cos[\omega_0 t + \theta(t) + \Phi(t)]$$

Where  $\theta(t)$  is a constant phase (offset) and  $\Phi(t)$  is the random phase error. The phase noise modulates the desired tone to produce sum and difference sidebands at either side of the carrier which can be seen on the spectral output. For noise sources in a narrow bandwidth, (a reasonable approximation), the noise is considered to modulate the oscillator output.

$$V(t) = V_0 \cos[\omega_0 t + \Phi(t)] = V_0 [\cos(\omega_0 t) \cos(\Phi(t)) - \sin(\omega_0 t) \sin(\Phi(t))]$$

$$V(t) \approx V_0 [\cos(\omega_0 t) - \sin(\Phi(t))]$$

Phase noise is plotted as the ratio of the phase noise power in a 1 Hz bandwidth at an offset frequency from the carrier, relative to the power of the carrier. The unit is decibels below the carrier per Hz bandwidth, dBc/Hz. A diagram of a phase noise plot is shown in Figure 3.3,

### 3.2.3 Models for Predicting Phase Noise in RF Components

An analytical method is used to predict the phase noise in RF chains in order to attempt to predict the levels of phase noise in each design before commissioning. For each type of component in the chain an individual model is devised by taking into account gain, loss and frequency conversion. Finally, the whole chain is summed to predict the final phase noise at the output. Table 3.3 summarises all of the parameters used in the following analysis.

#### Amplifier

Although amplifiers increase the signal power level, the carrier-to-noise ratio of the signal is degraded by the added noise of the amplifier. An ideal amplifier would not contribute any additional noise so the amplifier noise figure,  $F$ , would be zero. This is not the case practically. The noise figure is a measure of the degradation of the signal-to-noise ratio. The noise figure has an intrinsic flicker noise corner frequency, which will cause the noise figure to increase at 10db per decade below the corner frequency [85]. The corner frequency is represented by  $f_c$  and was shown in the diagram in Figure 3.3. The flicker noise component is mathematically represented as:

$$F = F_0 \left( 1 + \frac{f_c}{f_m} \right) \quad (3.1)$$

The single sideband, carrier-to-noise ratio is defined as  $\Gamma(f_m) = \frac{N_o}{C_o}$ . The output carrier power of the amplifier is simply the product of the input power and gain. The total output noise of an amplifier has two components. The first component is

G	Gain (dB)
F	Noise Figure (dB)
L	Conversion Loss (dB)
$C_i$	Carrier Input Power (dB)
$C_O$	Carrier Output Power (dB)
$N_i$	Input Noise Power (dB)
$N_O$	Output Noise Power (dB)
kT	Boltzmann's constant multiplied by the absolute temperature (kT = -174 dBm/Hz)
$\Gamma_i(f_m)_{dB}$	Input carrier-to-noise ratio in dBc/Hz at a carrier offset of $f_m$
$\Gamma_0(f_m)_{dB}$	Output carrier-to-noise ratio in dBc/Hz at a carrier offset of $f_m$

TABLE 3.3: Definition and Units of the parameters used in Phase Noise Estimation calculations in Section 3.2.3

the value of the noise floor. The second component represents the product of the noise and the gain.

$$C_O = GC_i \quad N_O = fkTG + GN_i$$

The noise contribution of the amplifier is a combination of the thermal noise floor and amplifier noise figure divided by the amplifier gain.

$$\Gamma_0(f_m) = \frac{N_O}{C_O} = \frac{fkTG + GN_i}{GC_i} = \frac{fkT}{C_i} + \frac{N_i}{C_i} = \Gamma_0(f_m) + \frac{FkT}{C_i}$$

Including the flicker noise component (from Equation 3.1) and expressing the result in a logarithmic form leaves the single sideband, carrier-to-noise ratio for an amplifier.

$$\Gamma_0(f_m)_{dB} = 10 \cdot \log \left( 10^{\left(\frac{\Gamma_i(f_m)_{dB}}{10}\right)} + \left(1 + \frac{f_c}{f_m}\right) \cdot 10^{\left(\frac{F_0 + kT + C_i}{10}\right)} \right)$$

### Passive Components

The model for an amplifier will be adapted for a passive component. Passive components, in this case a filter, will be modelled as an amplifier with gain of 0dB and noise figure equal to the insertion loss. In this case the signal-to-noise ratio is degraded only due to the losses in the passive component. The phase noise contribution of the filter is expressed as:

$$\Gamma_0(f_m)_{dB} = 10 \cdot \log \left( 10^{\left(\frac{\Gamma_i(f_m)_{dB}}{10}\right)} + 10^{\left(\frac{kT-LC_i}{10}\right)} \right) \quad (3.2)$$

### Frequency Multiplier

During frequency multiplication the carrier-to-noise ratio increases according to the following approximate relationship [86]:

$$\frac{N_O}{C} \propto \frac{f_0^2}{Q^2}$$

As frequency increases the performance of an oscillator will be degraded by both increased frequency and lower quality factor. Where the quality factor is a dimensionless parameter that describes how under-damped an oscillator or resonator is. It is defined as the ratio of the initial energy stored in the resonator to the energy lost in one radian of the cycle of oscillation. Quality factor is alternatively defined as the ratio of a resonator's centre frequency to its bandwidth when subject to an oscillating driving force [47].

### The Effect of Frequency Multiplication on Phase Noise

Let  $\frac{N_{OP}}{C}_1$  and  $\frac{N_{OP}}{C}_2$  be the phase noise density-to-carrier ratios before and after frequency multiplication. Similarly,  $\overline{\Phi}_1^2$  and  $\overline{\Phi}_2^2$  are the rms phase jitter densities before and after frequency multiplication. After frequency multiplication  $\Phi_2 = n\Phi_1$ , where  $n$  is the multiplication ratio. After frequency multiplication [86]:

$$\left(\frac{N_{OP}}{C}\right)_1 = \frac{\overline{\Phi}_1^2}{2} \quad \therefore \left(\frac{N_{OP}}{C}\right)_2 = \frac{n\overline{\Phi}_1^2}{2} = n^2 \left(\frac{N_{OP}}{C}\right)_1$$

The effect of frequency multiplication by a factor  $n$  on the carrier-to-noise ratio is to multiply by  $n^2$ . This is demonstrated in Figure 3.6 where the master oscillator is multiplied by four. The phase noise profile is almost identical but the phase noise increased by approximately 12 dBm which is  $20\log(4)$ .

So frequency multiplication by a factor  $n$  will multiply phase noise by  $n^2$  and total noise by  $\frac{n^2}{2}$ . The phase noise model of the frequency multiplier will include degradation of the signal due to conversion loss. As the frequency multiplier is an active device there will also be a noise figure and gain. The full model for the frequency multiplier is:

$$\frac{N_O}{C_O} = n^2 \Gamma_i(f_m) + \frac{n^2 + FkT}{C_i G} + \frac{kT}{LC_i}$$

Including the flicker noise component (from Equation 3.1) and expressing the result in a logarithmic form leaves the single sideband, carrier-to-noise ratio for a frequency multiplier.

$$\Gamma_O(f_m)_{dB} = 10 \cdot \log \left( 10^{\left(\frac{\Gamma_i(f_m)_{dB} + 20 \log(n)}{10}\right)} + \left(1 + \frac{f_c}{f_m}\right) \cdot 10^{\left(\frac{F_0 + kT + 20 \log(n) - C_i G}{10}\right)} + 10^{\left(\frac{kT - LC_i}{10}\right)} \right)$$

The additive noise attributable to a frequency multiplier is strongly dependent on the active element in the multiplier and the input drive level and hence an amplifier may be required before the input to the multiplier. However, whenever an amplification is added it is clear that the noise from the input amplifier will also be multiplied by  $n^2$ , so from this perspective it would be desirable to multiply before amplifying. Thus, there is a design trade-off between power level and phase noise.

### Mixer

Phase noise analysis of a mixer is complicated by the presence of at least two input frequencies. An ideal mixer would have a noise figure of zero, whereby the only signal degradation would be due to conversion loss. This is not the case in practice. The cumulative effect of the mixer is the rms sum of the carrier-to-noise ratios of the input signals. The phase noise model for a mixer will include a conversion loss, noise figure, and the carrier-to-noise ratios of both input ports.

$$\frac{N_O}{C_O} = \Gamma_{i1}(f_m) + \Gamma_{i2}(f_m) + \frac{FkT}{C_i} + \frac{kT}{LC_i}$$

$$\Gamma_O(f_m)_{dB} = 10 \cdot \log \left( 10^{\left(\frac{\Gamma_1(f_m)}{10}\right)} + 10^{\left(\frac{\Gamma_2(f_m)}{10}\right)} + \left(1 + \frac{f_c}{f_m}\right) \cdot 10^{\left(\frac{F_0 + kT - C_i G}{10}\right)} + 10^{\left(\frac{kT - LC_i}{10}\right)} \right)$$

Where the mixing process uses an RF frequency much higher than the LO frequency it is clear that the higher frequency input will dominate the phase noise.

### 3.2.4 Predicting Phase Noise of RF Generation Schemes

Now that each component type has been approximated the cascade of components can be modelled as a whole. This phase noise analysis will account for only the RF components and ignore other sources of noise such as cables, auxiliary circuits and power supplies. There will be a small variation of the performance of the amplifier due to varying input frequency and driving voltage, which is accounted for.

For both schemes the amplifier, filter, mixer, and modulation card are identical models. The difference between the two schemes is the frequency multiplication factor, (both of the annotated schemes are shown in Figure 3.4 and Figures 3.5). The drive power for the AQA1933K active frequency quadrupler is +2 to +5dBm. The drive power for the ADA0416 active frequency doubler is 0 to +6dBm. Hence an input power of +3dBm will be assumed for both schemes. No amplification is required after the frequency multipliers as they are active components.

The amplifiers are the ZVA-183-s+ wideband amplifier operating from 700 MHz to 18 GHz with a gain of 24dBm. The mixers are M1-0616 double balanced passive mixers. The LO and RF ports accept 6 GHz to 16 GHz and the IF port accepts DC to 4 GHz. The conversion loss is typically 10 dBm from the datasheet. The same filter can be used for both schemes to isolate the 9GHz, the filter will be the FB0955 band-pass filter with insertion loss of -3dBm. The schemes are shown with the relevant parameters in the following figures:

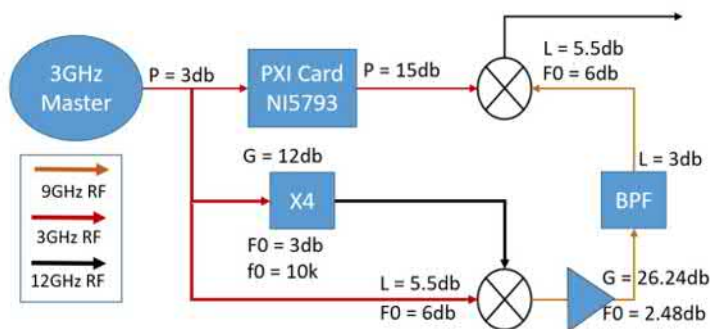


FIGURE 3.4: Scheme 1 Annotated: This is the same scheme as was shown previously in Figure 3.1 for 12 GHz Generation using x4 Multiplier. This diagram contains all of the available gains, corner frequencies, noise figures and input powers which can be collected from the component data-sheets

The 2.9985 GHz CLEAR master oscillator is generated using a Rhode and Schwarz SMC100A signal generator. The measured phase noise spectrum is plotted in orange

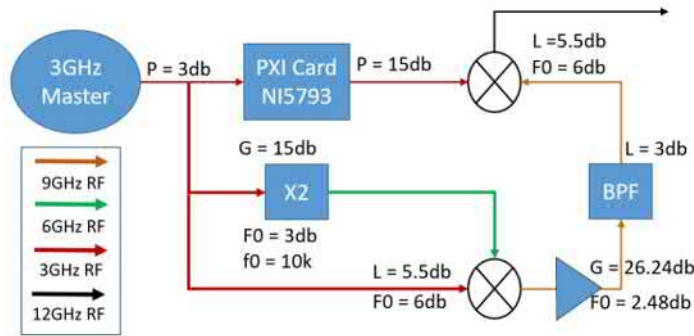


FIGURE 3.5: Scheme 2 Annotated: similarly, This is the same scheme as was shown previously in Figure 3.2 for 12 GHz Generation using x2 Multiplier plus additional annotations

in Figure 3.6. This source will be used to generate all of the other LLRF frequencies; therefore, the master oscillator provides the baseline for signal quality. The measured data shown in blue in Figure 3.6 is generated by using an AQA1933 frequency multiplier to multiply the master oscillator by four, this generates a signal at 11.9942GHz. This signal acts as a benchmark for the quality of the X-band source.

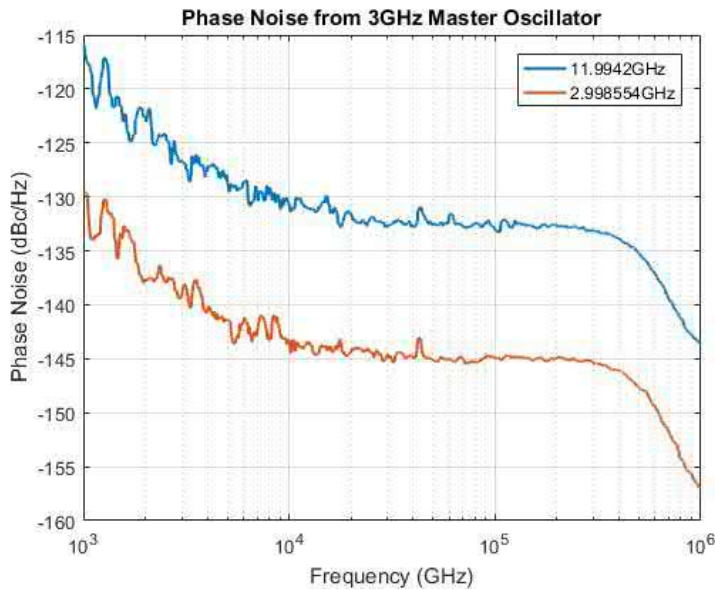


FIGURE 3.6: Measured Phase noise of 2.998 554 GHz Master Oscillator and 11.9942 GHz produced by frequency multiplication by a factor 4 (followed by amplification and filtering)

The phase noise analysis prediction for the two schemes is almost identical, and is shown in Figure 3.7. The doubler shows 4.2dBm improvement at small offset frequencies. This is due to the two schemes being essentially identical; the difference in dBm between  $20\log(2)$  and  $20\log(4)$  is 6dBm, which is the primary source of the variation. The phase noise performance is degraded by around 15dBm with respect to the 2.9985 GHz source oscillator.

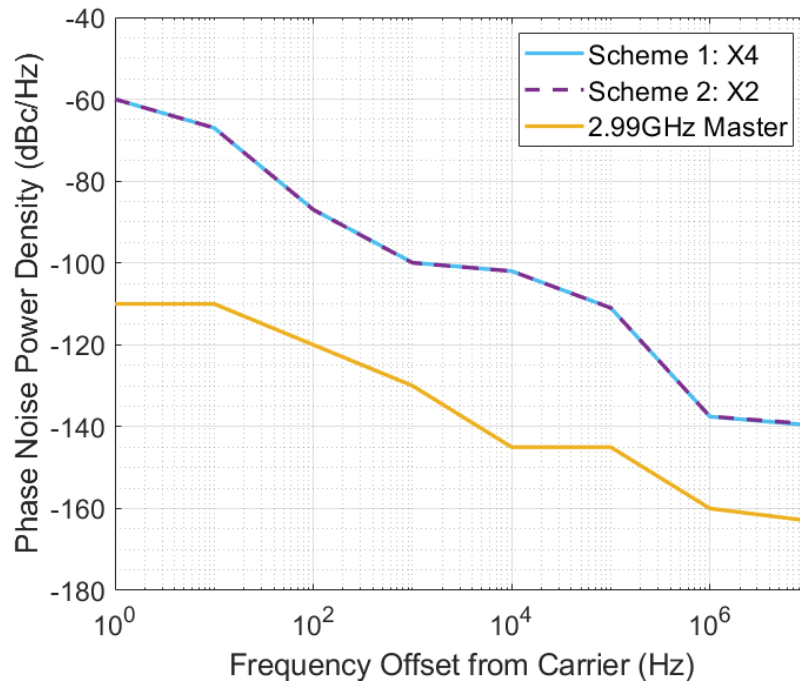


FIGURE 3.7: Predicted Single Sideband Phase Noise for the Quadrupler (blue) and Doubler (purple) Schemes (from Figures 3.4 and 3.5) with respect to the 3GHz Master Oscillator (yellow) which is the source for both schemes. So the additional phase noise above the level of the master oscillator is added by the components in the chain

The phase noise for the modulated 12GHz with respect to the phase noise performance of the PXI modulation card is much more illuminating, this is shown in Figure 3.9. The output phase noise for both schemes is highly correlated to the phase noise of the PXI card which is shown in Figure 3.8. As the final stage is mixing with the modulated 2.9985 GHz the phase noise performance of both schemes is limited by the phase noise performance of the NI5793 PXI card.

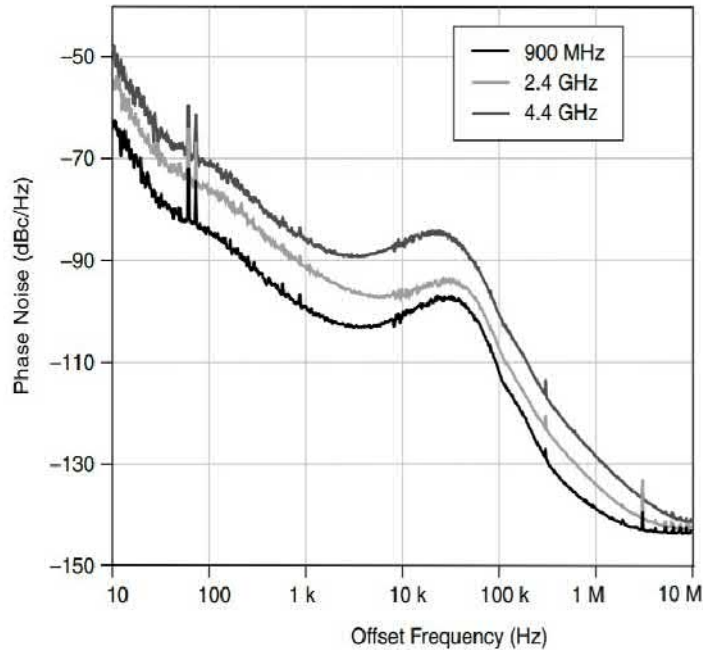


FIGURE 3.8: Phase Noise of the NI5793 PXI RF Generation Card taken from the component datasheet. The phase noise profile is dependent on the programmed output frequency of the card, in this case the frequency will be 2.998 554 GHz

This can also be highlighted by plotting the phase noise performance of the 8.995 GHz post filtering. Prior to mixing with the modulated 2.9985 GHz the phase noise of the 8.995 GHz signal is on average 13.58dBm better for the quadrupler and an average of 15.3 dBm better for the doubler.

### 3.2.5 Converting Phase Noise to Jitter

Oscillator specifications often use timing jitter rather than phase noise so the method for converting phase noise to timing jitter is described.

The integrated phase noise power is the integral of the phase noise spectrum over the offset frequency range. The lower bound for the integration should be as low as possible to obtain true rms jitter. In practice oscillator specifications may not be specified below 1 kHz. Jitter can be calculated from the following [87]:

$$RMSPhaseJitter(seconds) = \frac{\sqrt{2 \cdot 10^{A/10}}}{2\pi f_0}$$

Where  $A$  is the integrated phase noise power in dBc and  $f_0$  is the centre frequency. It is common to simplify the computation by considering each decade individually to examine the respective contributions to the jitter. The individual power ratios for each section can then be summed.

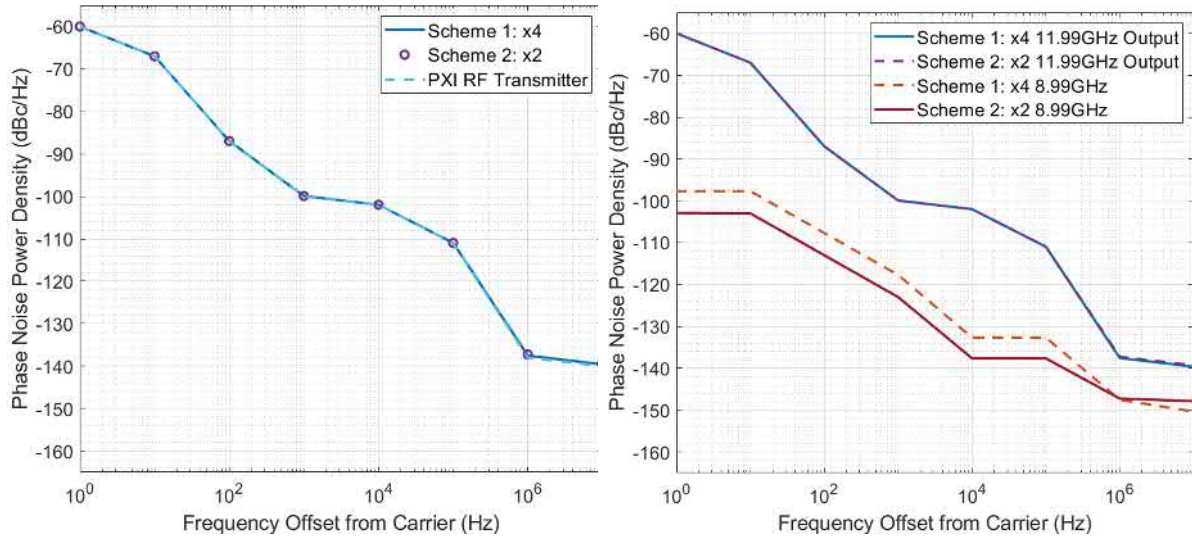


FIGURE 3.9: Single Sideband Phase Noise at 11.9942 GHz for the Quadrupler and Doubler Schemes with respect to the NI5793 PXI Card (left) and at 8.995 GHz before being mixed with the modulated pulse from the NI5793 (right)

$$A = \int_0^{10} A_1 dx + \int_{10}^{100} A_2 dx + \int_{100}^{1k} A_3 dx + \int_{1k}^{10k} A_3 dx + \int_{10k}^{100k} A_1 dx + \int_{100k}^{1M} A_2 dx$$

Where  $A$  is the integrated phase noise power in dBc. The rms phase jitter and timing jitter at various points along the signal chain are tabulated:

Signal	RMS Phase Jitter (°)	RMS Timing Jitter (ps)
2.9985GHz Master Oscillator	0.0012	0.0034
2.9985GHz PXI Card	0.0559	0.0518
8.995GHz Quadrupler	0.0015	0.0050
8.995GHz Doubler	0.0032	0.0056
11.9942GHz Quadrupler	0.0529	0.0123
11.9942GHz Doubler	0.0488	0.0113

TABLE 3.4: Predicted RMS Phase Jitter and RMS Timing Jitter

Table 3.4 shows that the limitation on jitter performance of the up-conversion scheme is the jitter of the NI5793 PXI card, which is an order of magnitude larger than the other jitter contributions below X-band frequencies.

As mentioned, the quality of the pulse generation scheme is limited by the PXI modulation card so this is not a useful metric to decide whether to use the doubler or quadrupler. A consideration in the decision could then be the possible introduction of unwanted harmonic.

The potential disadvantage of using a doubler is the introduction of an additional frequency into the system at 5.995 GHz, this frequency is not used anywhere else in the LLRF. Although this would be attenuated significantly by the band-pass filter, there is still a risk that the extra frequency will cause unwanted modulation of the 11.9942 GHz RF pulses. The internal circuitry of both the doubler and quadrupler will both produce frequencies at 5.995 GHz, 11.9942 GHz and other harmonics such as 9 GHz and 15 GHz which are filtered inside the component. Hence this is also not a suitable metric for deciding between the two schemes.

The design for the LLRF receiver uses a down-conversion scheme that utilises a cw signal at 11.9942 GHz, thus for practical reasons the quadrupler scheme is selected, as the output at 11.9942 GHz can be split into two and used in both the transmitter and receiver.

### 3.2.6 Commissioning the X-Band Pulse Generation System

The master oscillator power arriving at the LLRF crate is 0 dBm. This signal is required for four different functions inside the crate hence the master oscillator is split into four channels. After splitting the power in each channel is reduced by approximately 6 dBm. Three of the channels are used in the RF generation and the fourth is used to produce the local oscillator. Ideally the RF design would minimize the total number of components, in particular amplification stages, in order to minimize the phase noise and error sources. In actuality this is not possible as the power budget determines the required stages.

Figure 3.10 shows the proposed diagram of the up-conversion systems after commissioning, it is based on the schematic shown in Figure 3.4. The up-conversion system is shown with the PLL in Figure 3.11 during commissioning.

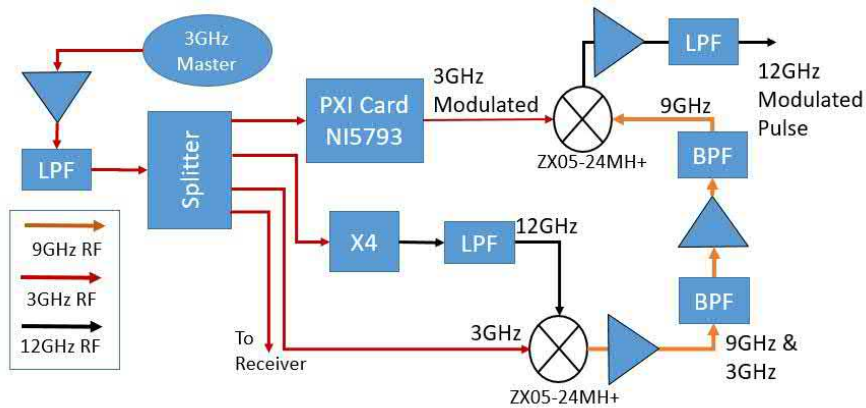


FIGURE 3.10: X-Band Pulse Generation Schematic. The S-Band master oscillator is shown in the top left and is the source for all the signals in the LLRF crate. This is used to create the 11.9942 GHz modulated pulse and is sent to the receiver (bottom left) to produce the local oscillator for down-conversion

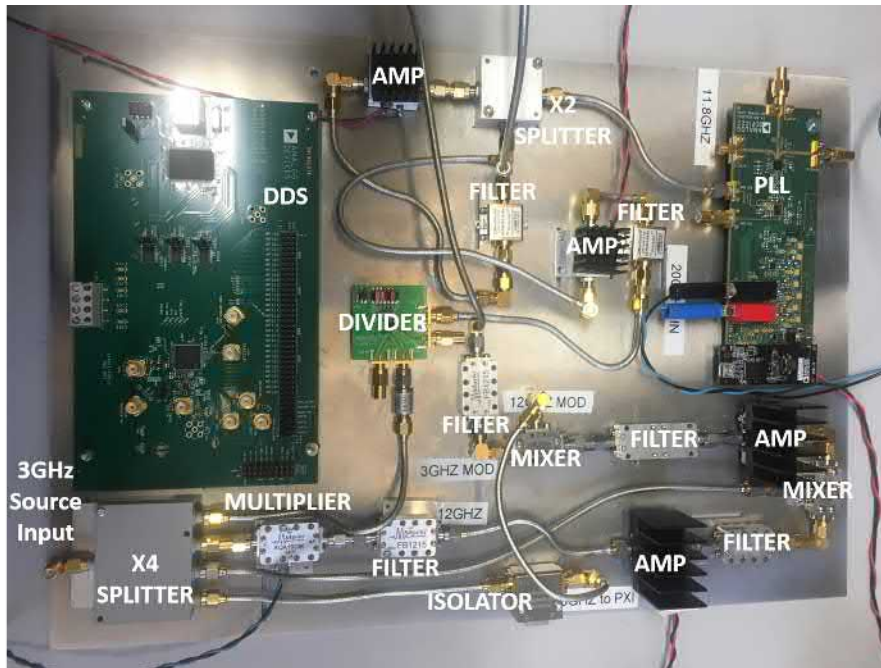


FIGURE 3.11: Proposed X-Band Pulse Generation during Commissioning. During commissioning additional components (amplifiers and filters) were added in order to ensure all components are operating within their desired range

The final implementation of the LLRF will be described here and can be seen in the schematic in Figure 3.12. The purpose of the four channels which will be derived from the master oscillator are as follows:

- One channel of the master oscillator will be sent to the PXI RF generation card (NI5793) as a reference input for synchronisation.

- The second 2.998 554 GHz channel will be used to produce 11.9942 GHz using a x4 frequency multiplier.
- The third channel will be used as the IF for mixing 11.9942 GHz and 2.9985 GHz to produce 8.995 GHz using the ZX05-24MH+.
- The fourth channel is used in the local oscillator generation; this channel is divided by 16 to produce 186 MHz.

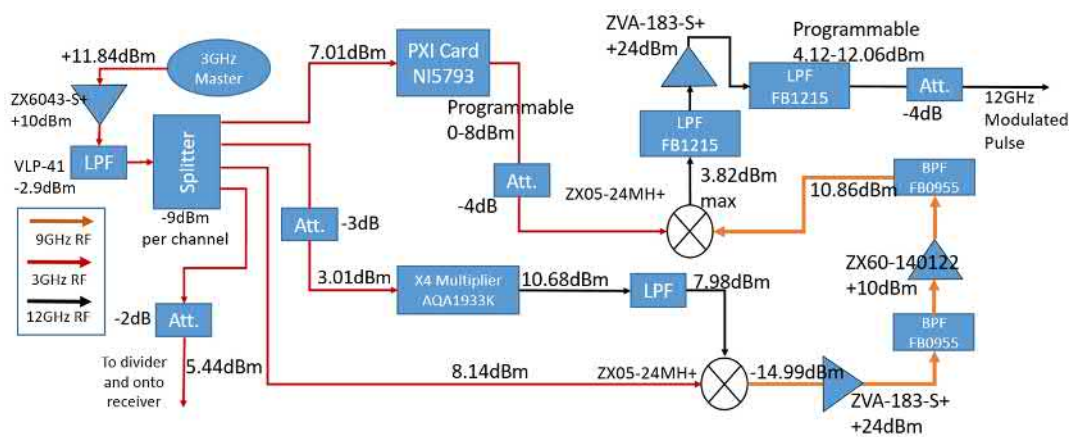


FIGURE 3.12: Final implementation of the X-band LLRF Transmitter system. This schematic contains the power levels measured throughout the system. The output power from the master oscillator (SMC100A) is +15dBm which is then transported over to the LLRF at Xbox1.

The output power from the master oscillator (SMC100A) is +15dBm. This signal is then transported over to the LLRF at Xbox1, the power arriving at the LLRF crate from the master oscillator is +11.84dBm.

Without amplification, after filtering and splitting, the master oscillator the power would be in the region of 0 dBm due to the losses in the filter and the splitter. Measured losses in the splitter are on the order of  $-9$  dBm per channel. Such low power levels at the output of the splitter (around 0 dBm) are unsuitable for the AQA1933K multiplier, the NI5793 card and as an LO input to the ZX05-24MH+ mixer. The acceptable input power ranges for these three components are shown in Table 3.5.

Hence the master oscillator was amplified before splitting, it would have been possible to amplify all three channels after splitting but this would add more amplifiers and filters into the system than was necessary. The ZX6043-S+ was used to add 10 dB followed by the VLP-41 low pass filter (with a measured attenuation of  $-2.9$  dB). The power level entering the splitter is approximately 18 dBm. After splitting the output power in each channel is around 7/8 dBm (with some variation due

to imperfect splitting and differences in cable lengths and adapters). In addition, 3 dB of attenuation was added before the multiplier and 2 dB before the divider. The power levels in all four channels are summarised in Table 3.5.

Channel	Required Power Level (dBm)	Power Level (dBm)
PXI NI 5793	$3 \pm 3$	7.01
AQA1933K Multiplier	2 to 5	3.01
ZX05-24MH+ Mixer IF	-10 to 15	8.14
HMC705 Divider	-15 to 10	5.44

TABLE 3.5: Required and Measured Power levels for each of the four 2.99855GHz Channels from the Master Oscillator

The AQA1933K is an active multiplier so the output power at 11.9942 GHz is 10.86 dBm. The output power of the multiplier is very sensitive to both the component temperature and fluctuations of the input 5 V power supply. As a result, a heat sink is added on the exposed surface of the multiplier and a smoothing capacitor is used on the input power supply. The approximate capacitance is calculated from:

$$c > \frac{1}{fR_{Load}}$$

Where  $f$  is the approximate frequency of the voltage fluctuations and  $R_{Load}$  is the impedance of the load, a  $100\mu F$  capacitor was found to be suitable.

The first mixing stage is used to produce a constant 8.995 GHz using the ZX05-24MH+ mixer.

The mixer was followed by a FB0955 9.55GHz band-pass filter which has a pass-band ranging from 8.9 GHz to 10.2 GHz. With a constant LO power of 7.98 dBm and IF input power of 8.14 dBm the output power of the mixer is  $-14.99$  dBm. The mixer exhibits significant conversion loss, this is shown in Figure 3.13. The data sheet for the ZX05-24MH+ (shown in Figure 3.14) states that the conversion loss is between 7 dbm and 10.2 dbm for a 30 MHz IF. The data sheet also states that the conversion loss increases with increasing IF. As the IF in this setup is 2.9985 GHz the conversion loss is much greater.

The output of the first mixing stage at 8.995 GHz will be fed as the local oscillator into the second mixing stage with the modulated 2.998 554 GHz signal as the RF input to generate the final 11.9942 GHz modulated RF pulse. The power level after the first mixing stage was measured at  $-14.99$  dBm, hence it must be amplified in order

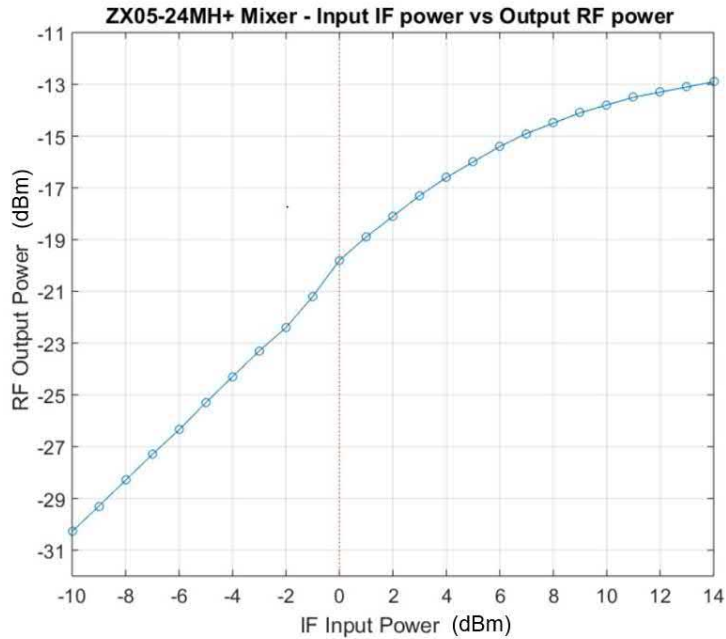


FIGURE 3.13: ZX05-24MH Mixer Measured Conversion Loss - IF Input Power (dBm) vs RF Output Power (dBm) with 11.9942 GHz LO at 10.78dBm

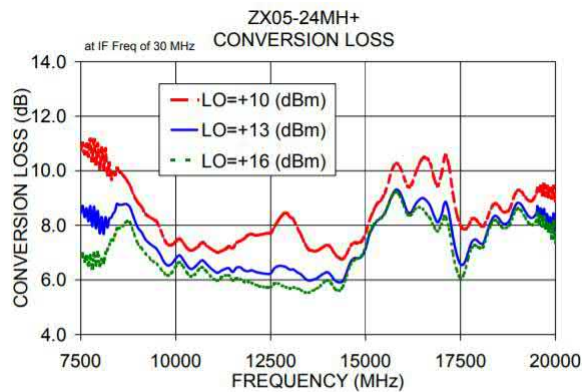


FIGURE 3.14: Expected Mixer Conversion Loss as a function of both Input RF Frequency and LO Power Level as taken from the ZX05-24MH+ Datasheet

to be used as a LO for the second mixing stage. As the signal needs to be amplified by at least 25 dBm, two stages of amplification were required, each followed by a FB0955 band-pass filter. The ZVA-183-S+ amplifier has a gain of 24 dBm, but can only accept input powers up to 4 dBm. The ZX60-140122 amplifier produces an extra 10 dBm of gain, this amplifier must be placed second as it can accept an input power up to 10 dBm. The output power of the 8.995 LO after amplification and filtering is 10.86 dBm.

The IF for the second mixing stage is the 2.9985 GHz modulated pulse. The output power from the NI5793 ranges from 0 dBm to 8 dBm, this power level must be

adjusted so that this range lies within the linear region of the ZX05-24MH+ mixer. Figure 3.15 shows that the linear region of the mixer is approximately between  $-4$  dBm and  $5$  dBm, hence the output from the NI5793 is attenuated by  $4$  dBm to align with this region.

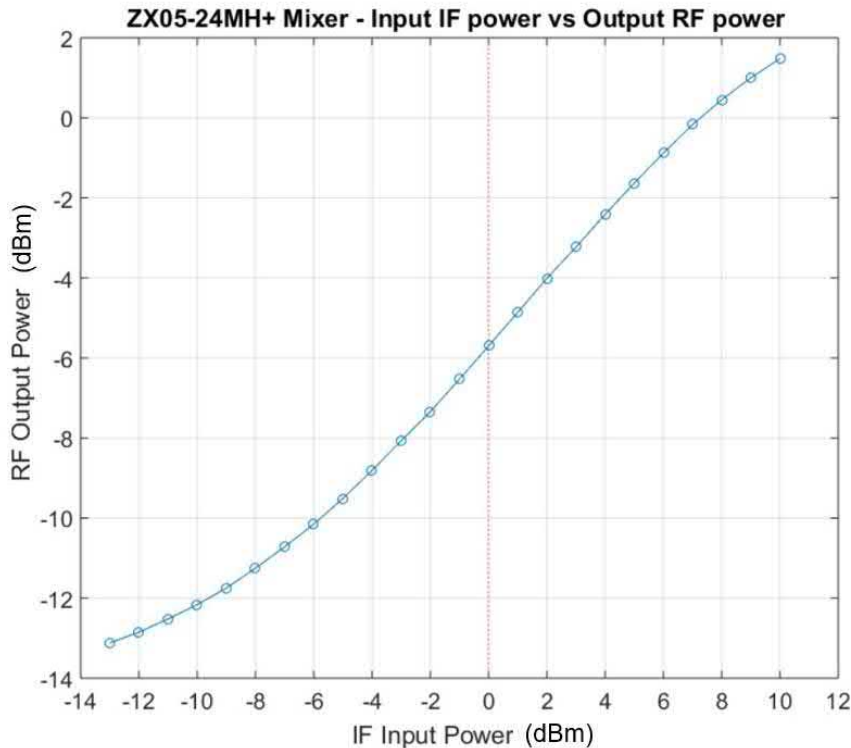


FIGURE 3.15: ZX05-24MH Measured Power Scan - 2.9985 GHz Pulse Input Power provided by the NI5793 (dBm) vs 11.9942 GHz Output Power (dBm) with constant LO power of 10.86 dBm at 8.995 GHz

The output of the 2nd mixing stage is an 11.9942 GHz pulse with a maximum power of 3.82 dBm. This signal is filtered using the FB1215 low pass filter and amplified using the ZVA-183-S+ amplifier then filtered again. The output power range of the 11.9942 GHz pulse is 4.12 dBm to 12.06 dBm.

An attenuation of 4 dBm was applied to the output power to bring it within the range of 0 dBm to 8 dBm. This was done for two reasons. Firstly, it allows room to either attenuate or increase the output power range of the LLRF to suit the requirements of the TWT and klystron. Secondly, it is to ensure the optimal performance of the NI5793 card. The output is produced using a 16 bit TI3482 DAC. Not fully utilising the full dynamic range of the DAC in the RF generation card will reduce its resolution. For example, at Xbox2 the RF transmitter will saturate the klystron at 15% of its full power range thereby only utilizing a small range of the DAC.

### 3.3 Design of the LLRF Receiving End

At Xbox1 the high power RF can be used to power X-band structures in the CLEAR LINAC to drive the acceleration of an electron beam. Alternatively, it is possible for the RF pulses from Xbox1 to be used to condition a CLIC prototype structure. Either of these applications will greatly benefit from localisation of arcs inside the structure, this is known as breakdown localisation and was described in Section 1.4.4, as well as being able to accurately measure the fields in the structure. Breakdown localisation requires accurate phase and amplitude information. The RF design of the receiver will be determined by the required timing and phase resolution for breakdown localisation.

Furthermore, at Xbox1 there is a requirement to synchronise the RF pulses with a beam in accelerating structures which are more than 30 m away. Hence the requirements for the phase and amplitude detection are more stringent than required for breakdown localisation. Successful acceleration requires that the phase of the electromagnetic wave in each cavity be synchronized to the moment the particles enter. Phase noise added during down-conversion directly will appear as jitter on the RF pulses, resulting in an incorrect instantaneous measurement of the RF phase at the accelerating structure. From Section 3.2.5, for a timing jitter of 10 fs, an rms phase jitter below  $0.75^\circ$  is required at 11.9942 GHz.

There are three ways in which the X-band signals can be measured. They can be measured directly through a diode, this translates the signals to DC which discards much of the information encoded in the signal, only amplitude information is retained. Alternatively the X-band signal could be directly digitized. However, this would require sampling rates above 24 GHz which is not feasible and is certainly not possible with existing National Instruments hardware. The high data rates would also place too much stress onto the PXI processors and Labview real-time software. The fastest oscilloscope offered by NI can sample at 12.5GSPs however the resolution is reduced to 8bits and the module would cost approximately \$30,000 for only 2 channels. The final method is down-conversion. In order to retain more than the amplitude information the signals will have to be converted down to a lower frequency where they can be processed. The most common method for obtaining all of the phase and amplitude information with minimal processing overhead is to convert the IF signal into polar components which are converted to Cartesian IQ coordinates.

In the Xbox1 PXI crate there are four acquisition cards each with four channels,

therefore there are 16 acquisition channels meaning only eight of the channels can be processed using sampling rates in the GSPS range as the Xbox1 PXI has only two processors. Eight of the channels can still be used to process DC amplitude signals at a sampling rate of 250 MHz and the other eight channels can be used for more detailed measurements using GSPS sampling speeds.

Quadrature sampling obtains both components of a complex signal by taking subsequent samples from the two signals which are each offset 90°. This is referred to as IQ sampling.

A conventional analog IQ demodulator uses analog components to translate an RF signal to two baseband I and Q channels before converting to digital data samples. Low-quality analog RF components can cause numerous errors that degrade IQ demodulator performance, including DC offset, gain imbalance, and phase imbalance. High-quality analog components in an IQ demodulator reduce these errors but increase the cost of RF system. High-speed ADCs and digital demodulation are now widely used as an alternative approach in order to reduce errors caused by analog RF components.

When using digital IQ demodulation the single signal path ensures perfect gain-matching between the two I and Q signals. The concerns of gain balancing and impedance matching for all the RF and analog components is eliminated. Consequently, analog DC offsets and drifts do not affect the digital IQ demodulator.

The quadrature phase shift is dependent upon the precise timing of the sampling. The ADC clock period provides an exact phase shift at the center frequency only. Signal frequencies not equal to the centre frequency contain a quadrature phase error when measured. For a limited signal bandwidth, this quadrature phase error is maintained at insignificant levels.

The LLRF at Xbox1 can use IQ demodulation provided the RF signals are mixed down to a sufficiently low IF. For digital IQ demodulation, the sampling frequency is four times the signal frequency. This creates a special case where the samples will measure I, -Q, -I, Q. This has the benefit of reducing the required trigonometry and hence reduce the computing power required to reconstruct the I and Q components from the instantaneous voltages [88]. The analog signal is described by:

$$V_t = A \cos(\omega t + \phi) = \text{Re}[(I + jQ)e^{j\omega t}]$$

The signal can be modelled in polar coordinates as a rotating vector with amplitude,  $A$ , angular frequency,  $\omega$  and initial phase of  $\phi_0$ . Positive frequencies rotate the phasor anticlockwise. The phasor is translated into cartesian coordinates using the following:

$$y(t) = A \cos(\omega t + \phi) = A[\cos(\phi_0) \sin(\omega t) - \sin(\phi_0) \cos(\omega t)]$$

The I and Q information is converted to amplitude and phase information using the following [88]:

$$I = A \cos(\phi_0) \quad Q = A \sin(\phi_0)$$

$$A = \sqrt{I^2 + Q^2}$$

If the initial position of the rotating vector is known, then the new position is measured at a known time later, and the algorithm rotates the phasor back to the initial position obtaining the change in amplitude and phase between the two vectors. The easy translation between Cartesian and polar coordinates makes signal processing less computationally intensive. The latency of IQ sampling is two samples. For IQ sampling the IF will be sampled four times every cycle to  $F_{\text{Sampling}} = 4 \cdot F_{\text{IF}}$ . The use of IQ sampling forms part of the specification for the IF and lock frequency.

### 3.3.1 PXI Acquisition Cards

The LLRF system at Xbox1 will reuse the acquisition cards which are already in place. These are two fast oscilloscope cards (NI5162) and two slow ADCs (NI5762). Each card has four channels.

The NI5762 can sample each channel at 250 MSPs, these cards will be used to sample pulsed DC signals provided by log detectors. In general, log detectors are used to measure signal strength, as opposed to detecting signal content.

The edge method of breakdown localisation uses the timing difference between the falling edge of the transmitted signal and the rising edge of reference signal. Assuming that the vacuum arc starts absorbing and reflecting RF power instantaneously as the breakdown is ignited, the delay between the two edges should correspond to a unique longitudinal position. Identifying where the breakdown begins relies on the accuracy of resolving the rising and falling edge. Ability to detect the

rising edge depends on the sampling rate, signal-to-noise ratio and allowable rise time in the ADC.

Rise time is measured with respect to time, while bandwidth is measured with respect to electrical frequency. In this case the rise time is the time taken for the rising edge to increase from 10% to 90% of the desired output value in response to an input step function [43]. The bandwidth is found by referencing the system's frequency response. The inversely proportional relationship between rise time and bandwidth can be derived by considering the time and frequency response of an ideal RC low-pass filter, which consists of a resistor and capacitor in series. The resolvable rise time is related to the bandwidth by the following equation when the system's response resembles that of an RC low-pass filter [89]:

$$RiseTime = \frac{Bandwidth}{0.35}$$

There is a bandwidth limiting filter on the input to the NI5162 oscilloscope which limits the rise time to 320 ps, this is ample for this application. The RF pulses have a rise time of approximately 7 ns. This can be resolved using a bandwidth of 50 MHz. However, for 50 MHz IF the rising edge would only be represented in one sampling bin so detection of the rising edge is limited to one bin. An IF of 300 MHz would spread the rising edge over 6 sampling bins. Therefore, a suitable IF will be in the range of 150 MHz to 300 MHz to be able to digitize the rising edge with reasonable resolution whilst satisfying IQ sampling requirements using existing PXI Cards.

Within this range there are advantages to using a smaller IF frequency. A larger IF will have a larger bandwidth that results in a larger thermal noise floor, this reduces the dynamic range of the measurement. For an ambient temperature of 290 K the noise floor of a 300 MHz IF is 1.76 dBm larger than that of a 200 MHz signal. A lower IF frequency will also be less sensitive to phase and frequency instabilities. A 10 ps jitter at 300 MHz corresponds to 1.08° phase error while the same jitter results in only 0.72° phase error at 200 MHz and 0.54° phase error at 150 MHz [89].

The NI5162 accepts an external sampling clock up to 1.5 GHz, however there is a sample clock time base divisor in the card with a minimum value of 2, and therefore the actual sample will be half the input rate.

Thus the IF needs to be an 1/8th of the clock frequency. Both the IF and the sampling rate must be generated from the 2.9985 GHz source. An IF of 187.4 MHz was

chosen as this can be produced by dividing by 16, the clock frequency at 1.499 GHz can be easily generated from the master oscillator.

The requirements for the down-conversion system can be summarised as:

- Mixing the 11.9942 GHz signals down to 187.409 MHz ensuring the RF to IF conversion process is linear
- Minimising the error contribution from the down-conversion process by generating a low phase noise oscillator at 11.8068 GHz using the master oscillator as a source
- Generating a stable, low noise sampling clock at 1.499 GHz

### 3.3.2 Generating the Local Oscillator Frequency

Now the IF frequency has been determined the local oscillator frequency is also known. The 11.9942 GHz RF will be mixed down to 187.4 MHz using a local oscillator at 11.80688 GHz. This frequency must be generated using the 2.998554 GHz. The process has two stages, firstly, the master oscillator is divided to produce an intermediate frequency which is then used as the input for up-conversion to X-band.

The quality of the local oscillator directly affects the quality of the measurements. A superheterodyne receiver, is a type of radio receiver that uses frequency mixing to convert a received signal to a fixed intermediate frequency which can be more conveniently processed than the original carrier frequency [55]. All superheterodyne receivers use one or more local oscillators to convert an input frequency to an intermediate frequency before the signal is demodulated. In the ideal receiver, these frequency conversions would not distort the input signal, and all information on the signal could be recovered. In a real receiver, both the mixer used for conversion and the local oscillator will distort the signal and limit the receiver's ability to recover the modulation on a signal. Mixer degradation, such as from undesired mixing products, can be minimized by proper design in the rest of the receiver. The local oscillator degradation, which is principally random phase variations (phase noise), cannot be decreased except by improving the performance of the oscillator. The local oscillator phase noise will limit the ultimate signal-to-noise ratio which can be achieved when receiving a modulated signal [90].

Phase noise can also limit the angular resolution which can be achieved by an interferometric receiver. Reciprocal mixing may cause the receiver noise floor to increase when strong signals are near the receiver's tuned frequency; this limits the

ability to recover weak signals. All of these effects are due to local oscillator phase noise [90].

Local oscillator phase noise will effect the bit error rate performance of a transmission system. A transmission error will occur any time the local oscillator phase, due to its noise, becomes sufficiently large that the digital phase detection makes an incorrect decision as to the transmission phase [90]. In this case, as the phase of the field needs to be measured as accurately as possible, any phase errors could cause an incorrect reading and hence contribute to the bit error rate.

The division ratio is 16 which converts the master oscillator from 2.998 554 GHz down to 187.4MHz. Frequency dividers are widely used in many communication systems such as frequency synthesizer and clock generation circuits. Two methods will be considered and compared; a programmable divider and a direct digital synthesiser.

An arrangement of flip-flops is a classic method for integer  $n$  division, programmable frequency dividers are a chain of flip-flops. The easiest configuration is a series where each flip-flop is a divide-by-2. Such division methods are frequency and phase coherent to the source over environmental variations including temperature [91].

As mentioned in Section 3.2.3, multiplying the frequency of a signal by a factor  $n$  increases its theoretical phase noise by  $20\log(n)$ , in addition to the component self-noise. Conversely, dividing the frequency of a signal by  $n$  will lower its theoretical phase noise by  $20\log(n)$ . For a division ratio of 16 the phase noise should be reduced by 24 dBm with respect to the reference.

The programmable divider for this application is the HMC705. The divider can be programmed to divide by any number from  $n = 1$  to 17. The datasheet phase noise specifications of the HMC705 from the are shown in figure 3.16.

A direct digital synthesiser, DDS, is a modern method of producing a tuneable output signal referenced to a high frequency fixed input signal. However, this technology is currently limited to relatively low frequency regions, generally less than 5 GHz. The DDS for this application is the AD9914.

The high frequency reference signal will be divided by a scaling factor determined by a programmable binary tuning word. The output frequency can be programmed with hertz resolution and sub degree phase tuning. In addition the DDS can eliminate the need for manual tuning due to long term temperature drifts or

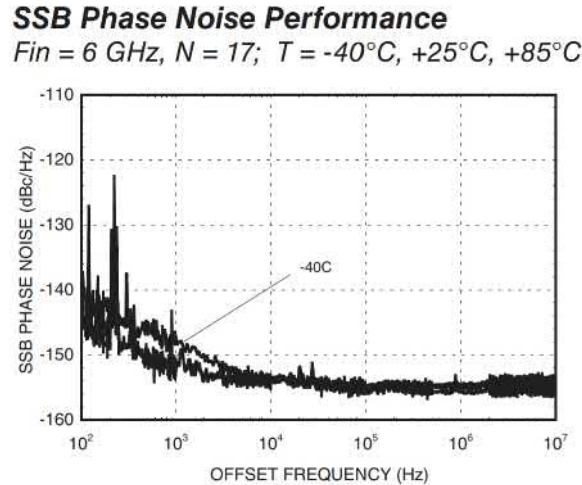


FIGURE 3.16: Expected Phase Noise vs Temperature Performance of the HMC705 Programmable Divider as taken from the datasheet

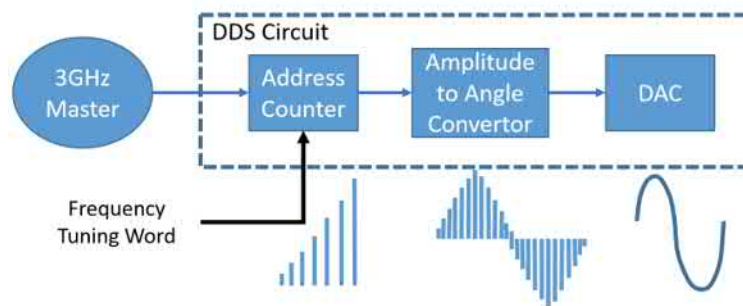


FIGURE 3.17: Simplified Diagram of the operation of a DDS showing the main blocks and a visual representation of the conversion from digital values to analog sine wave

component aging. The tuning can simply be done using the digital control interface of the DDS.

The internal blocks of a simple DDS are the address counter, programmable read only memory (PROM), and digital to analog convertor (DAC). A simplified scheme is shown in Figure 3.17. The PROM functions as a sine lookup table containing the digital amplitude information corresponding to a complete cycle of a sine wave at the desired output frequency. The address counter increments with each clock cycle to access each memory location in the PROM. For each location the digital amplitude is passed to the DAC which produces the output sine wave. The output frequency is determined by the reference frequency and the sine wave step-size. The magnitude of the step-size is determined by the programmable binary tuning word.

The output frequency of the DDS is defined by:

$$f_o = f_s \frac{FTW}{2^N} \quad (3.3)$$

Where  $f_O$  is the desired output frequency,  $f_s$  is the frequency of the source, FTW is the frequency tuning word and N is the number of bits in the address counter.

Due to the Nyquist theorem, the maximum output frequency of the DDS is half of the reference frequency. The output frequency spectrum will contain the desired output frequency plus harmonics at sum and difference frequencies of the output and reference frequency. A low pass filter can be used to suppress the unwanted harmonics and is usually included in the output circuitry of the DDS.

The general noise floor of a DDS device is determined by the cumulative combination of substrate noise, thermal noise effects, ground coupling, and a variety of other sources of low-level signal corruption. The noise floor, spur performance, and jitter performance of a DDS device is greatly influenced by circuit board layout, the quality of its power supplies, and the quality of the input reference clock.

It is logical to assume that the DDS quantization noise is white, as it is with most data acquisition systems. However, the DDS is more complex because the truncation of the address counter introduces a deterministic error. To ideally reconstruct a signal each value in the address counter would correspond to a value in the lookup table [92]. However, the DAC often has less bits than the address counter which leaves a disparity between the resolution of the two components. This is the source of phase truncation spurs which can be seen in the phase noise spectrum in Figure 3.18.

The measured phase noise results from both division techniques are shown in Figure 3.18. All of the following phase noise measurements are collected by connecting the signal chains to a Rhode Schwarz FSWP50 phase noise analyser.

The phase noise is approximately 10 dBm lower than the 2.998 554 GHz reference due to the reduction in frequency. At this stage it is difficult to determine which system is optimal. Although the divider has a slightly higher close-in phase noise it does not exhibit the spurious performance of the DDS.

### 3.3.3 Generating the Sampling Clock

The sampling clock at 1.499 GHz could be generated by dividing the master oscillator by 2. However it isn't practical as the master oscillator is already being split into at least four channels, splitting this signal again would have a significant effect on the power budget and result in the need for extra amplification throughout the entire LLRF system. The alternative is to split the output of the 187.4 MHz into two and multiply one channel by 8 to produce the clock.

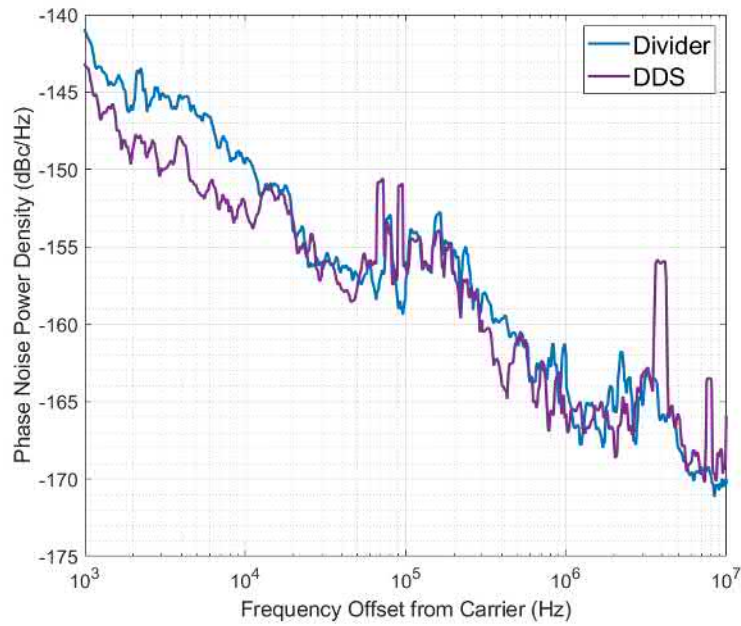


FIGURE 3.18: Measured Phase Noise of each of the 187.409 MHz signals which were generated by dividing the 2.998 554 GHz by 16 using the divider (Blue) and DDS (Purple)

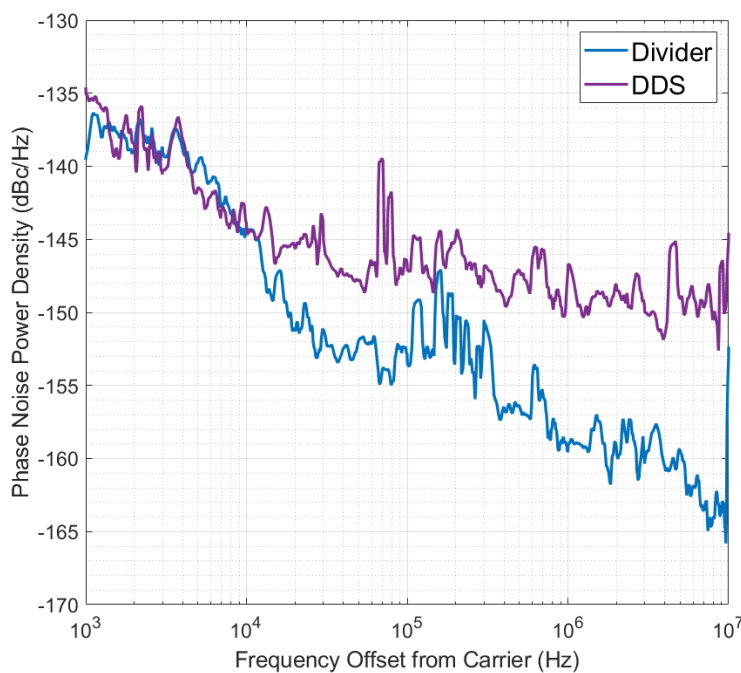


FIGURE 3.19: Measured Phase Noise profile of two versions of the 1.499 GHz Sampling Clock which were generated by multiplication of the output signal from the divider (Blue) and DDS (Purple)

Figure 3.19 shows the phase noise performance of the clock when produced from the divider and the DDS. The phase noise from the DDS hits an apparent higher noise floor around  $-147$  dBm at 100 kHz offset. In a DDS circuit a significant portion of the phase noise can be attributed to the internal reference clock, which in this case

appears to exhibit worse phase noise than the master oscillator. This is logical as the DDS is a commercial product designed for a wide variety of applications where perhaps in this case the phase noise performance has been sacrificed for flexibility or price. Hence the divider will be the optimal solution carried forward.

### 3.3.4 Frequency Up-Conversion to produce the Local Oscillator

The receiver must produce an X-band local oscillator at 11.8068 GHz using an 187.4 MHz input. It is not possible to use frequency multiplication as a multiplication factor of 64 is required. Direct frequency multipliers are built from a nonlinear electronic components which generate a series of harmonics followed by a band-pass filter which passes one of the harmonics to the output and blocks the others. Since the power in the harmonics declines rapidly, usually a frequency multiplier is tuned to only a small multiple (twice, three times, or five times) of the input frequency [93].

A commonly used method of up-conversion is a phased locked loop. This has been implemented before in the X-band test stands. Keeping the input and output phase locked keeps the input and output frequencies constant. Consequently, in addition to synchronizing signals, a phase-locked loop can track an input frequency, or it can generate a frequency that is a multiple of the input frequency. The disadvantages are that PLL's do not have good phase noise profiles and introduce a secondary oscillator into the RF chain so the noise from the PLL is not correlated [94].

An alternative for up-conversion is frequency mixing. The single side-band (or image reject) mixer is used in specialist applications where only one mixing product is needed. Image rejection mixers remove one of the two output signals from the mix process by trigonometric phase cancelling techniques. Although they are more complicated and more expensive than standard mixers, single side-band mixers can be particularly useful in reducing the overall system cost by enabling the complexity of filters to be reduced.

The phase locked loop is a negative feedback loop which uses a phase detector and a voltage controlled oscillator to produce an output frequency with constant phase angle relative to the input signal. They are commonly used to generate a stable high frequency signal from a low frequency input. The negative feedback loop tries to force the difference, the error signal, between the input signal and the output frequency to zero at which point the two signals will be in phase and the signals are in a 'locked' state. A frequency divider in the feedback loop is used to set the output frequency, the input frequency will be multiplied by the division ratio

to produce a higher frequency output signal [95] [96]. A simplified PLL circuit was shown earlier in Figure 2.4.

The PLL is the AFD5355 which is a wideband PLL which can produce output frequencies from 5 GHz to 13 GHz. The AFD5355 has both integer and fractional dividers allowing for very precise adjustment of the output frequency. The integer divider can produce output frequencies at integer multiples of the input frequency whereas the fractional divider can produce output frequencies at fractional multiples of the input frequency. The difference between a PLL and frequency multipliers is that when using a PLL the input signal is not used as an output. The output signal is created using a separate VCO and synchronised to the input signal using the phase comparator. The output frequency is selected by programming the division ratios into the registers [95] [96].

The phase noise results from the PLL are shown in Figure 3.20 using a PFD of 62.47 kHz. For lowest jitter applications, it is optimal to use the highest possible PFD frequency to minimize the contribution of in-band noise from the PLL. The spur on the PLL phase noise shown in Figure 3.20 is present when using both the DDS and divider, hence it is a product of the PLL. The phase noise results are comparable with the phase noise from the PLL data sheet, which is shown in Figure 3.21.

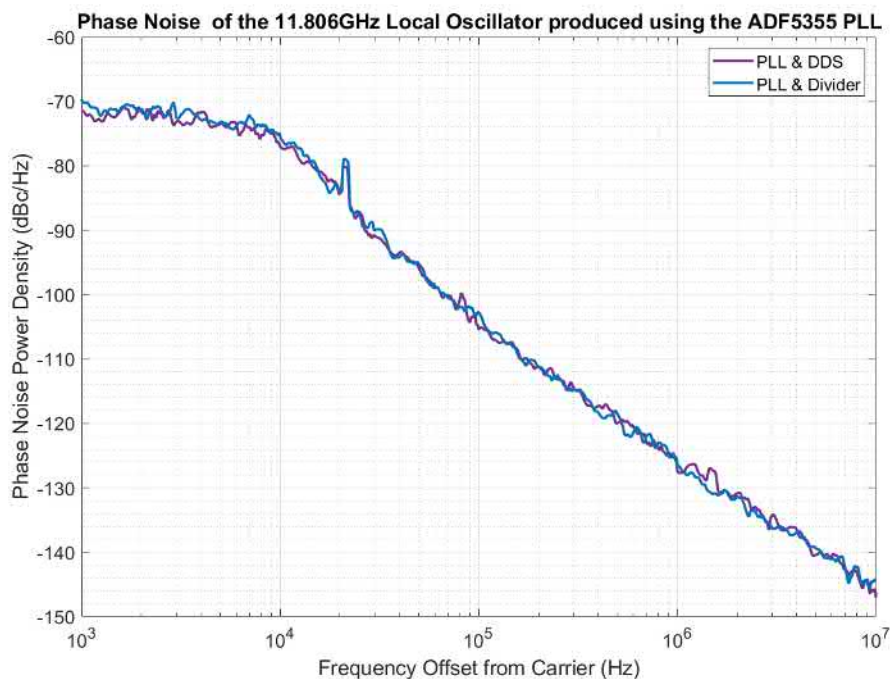


FIGURE 3.20: Measured Phase Noise at 11.8068 GHz generated by using the AD5355 PLL. Two versions of the signal are shown which compare the output of the PLL when using the Divider (Blue) and DDS (Purple) as the input

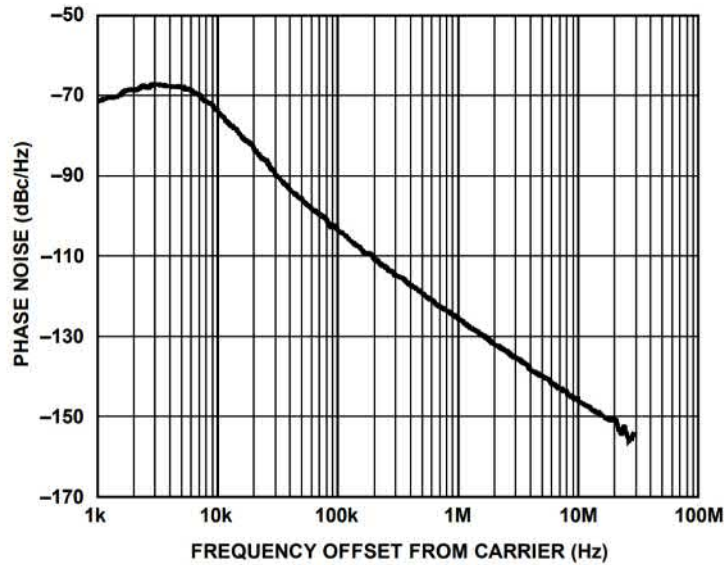


FIGURE 3.21: Expected Closed Loop Phase Noise of the PLL for an output frequency of  $RF_{Out} = 13.6\text{GHz}$  taken from the ADF5355 datasheet

Further analysis of the phase noise is possible using the ADISim PLL software produced by analog devices [97]. The ADF5355 PLL is simulated using the input phase noise profile from Figure 3.18. The loop filter is not changed and the phase detector frequency, PFD, is set to 62.47 kHz. Using the ADISim software it is possible to isolate the phase noise contribution of the individual PLL components. The result is shown in Figure 3.22. The quality of the reference, the loop filter and the PFD frequency are not important in this case as the PLL phase noise is dominated by the quality of the internal VCO.

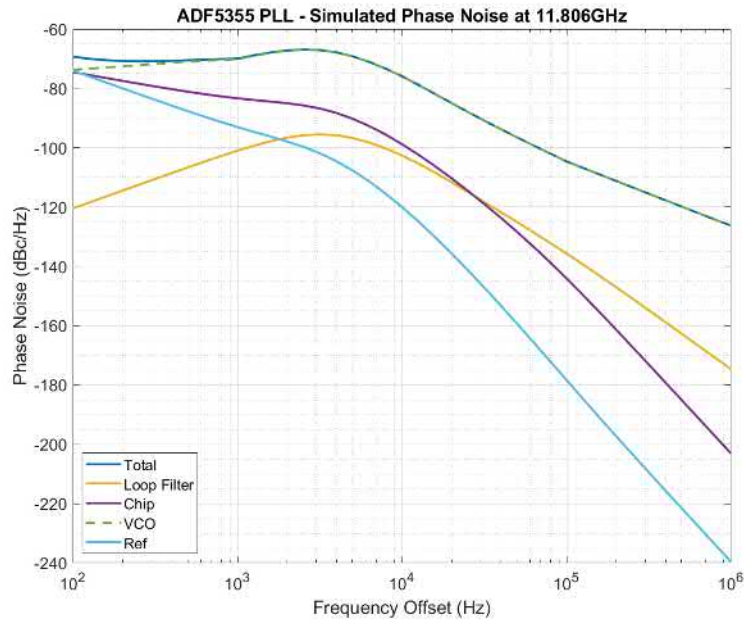


FIGURE 3.22: ADI SimPLL Simulation of the Phase Noise of the PLL output at 11.8068 GHz and the individual contributions to the total Phase Noise of the major components inside the PLL. It can be seen that the phase noise is dominated by the quality of the VCO

Single side-band mixing schemes utilise phasing techniques to cancel out the unwanted mix products. To achieve this the single side-band mixer utilises two balanced mixers and the quadrature ( $90^\circ$ ) hybrids as shown in Figure 3.23. The two balanced mixers within the single side-band mixer are driven in quadrature by the IF signals. The LO drive to each mixer is in-phase and the output is combined in quadrature [98].

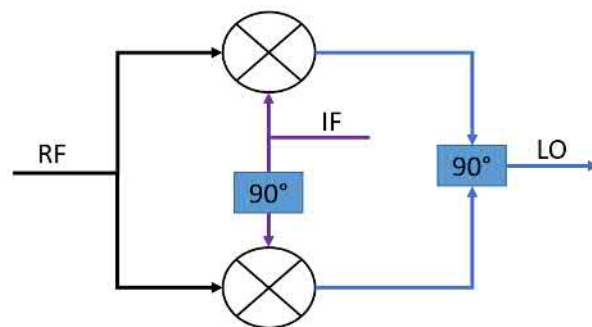


FIGURE 3.23: Schematic of Single Side-band Up-Conversion

Using the analysis methods described in Section 3.2.2 the phase noise of the up-converter can be predicted. As the up-converter is a mixer-based process the primary source of phase noise comes from the input signals, any noise on the LO or RF will be transmitted to the output. In this case the 11.9942 GHz RF input will be the main source of phase noise, this is shown in Figure 3.24.

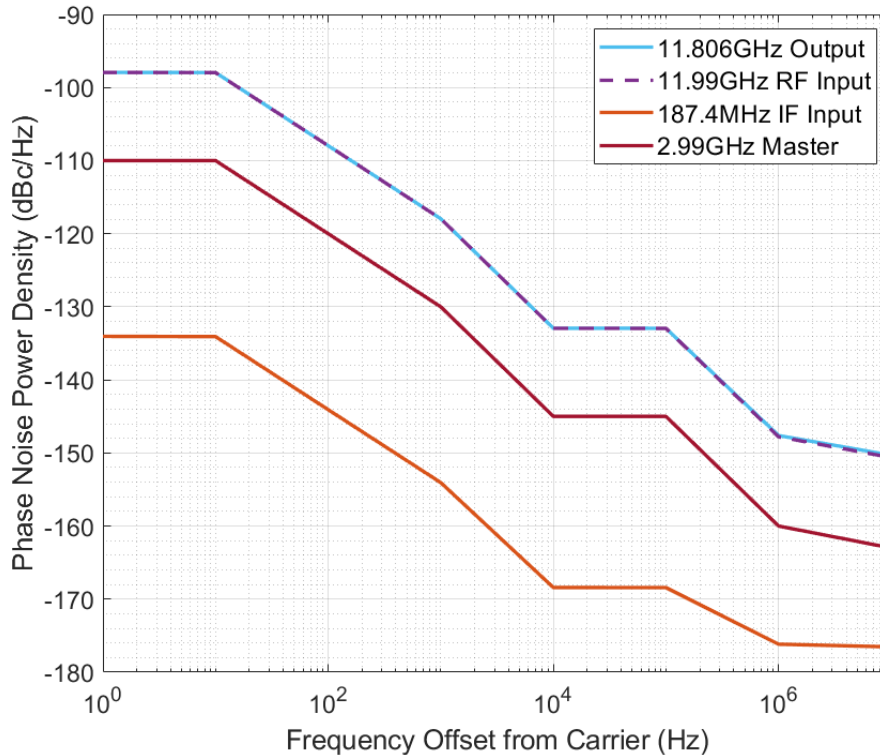


FIGURE 3.24: Predicted Phase Noise of the Up-Converter

It is not possible to achieve complete cancellation in a real single side-band mixer. For perfect cancellation the mixers must be identical and the amplitude balance and phase shift of all the inputs must be exact. Levels of image rejection of around  $-20$  dB should be obtainable using this approach. The up-converter used will be the ADRF6780. The achievable side-band suppression is in the region of 25 dBm from the datasheet information, as shown in Figure 3.25. The plot on the left shows side-band suppression as a function of input RF frequency, temperature and VATT voltage for a baseband input of 100 MHz. The VATT voltage controls the output attenuator and will be left at 2.6 V. For 12 GHz the sideband suppression at 25° is approximately 25 dBm. The datasheet plot on the right shows the output spectrum for a baseband input of 100 MHz, the suppression is the difference between peak 1 (the desired output) and peak 3 (the unwanted sideband) with peak 2 being the RF frequency, the suppression is  $-37.02$  dBm.

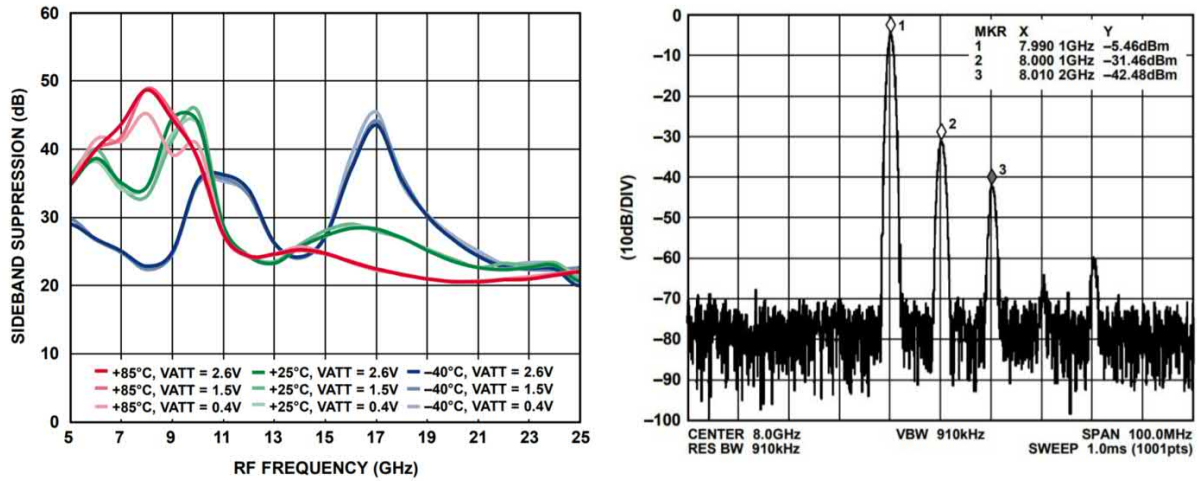


FIGURE 3.25: ADRF6780 Side-band Suppression at Three Gain Settings and Temperatures (Left) and spectral output (right)

Figure 3.26 shows initial phase noise results which are testing the up-converter board in isolation, this measurement is only the ADRF6780 output with cw inputs at 187.409 MHz and 11.9942 GHz .The set-up does not include signal conditioning on the inputs to improve the phase and amplitude balance to improve the suppression (which is not measured here). The up-converter phase noise is dominated by the 11.9942 GHz reference input as predicted.

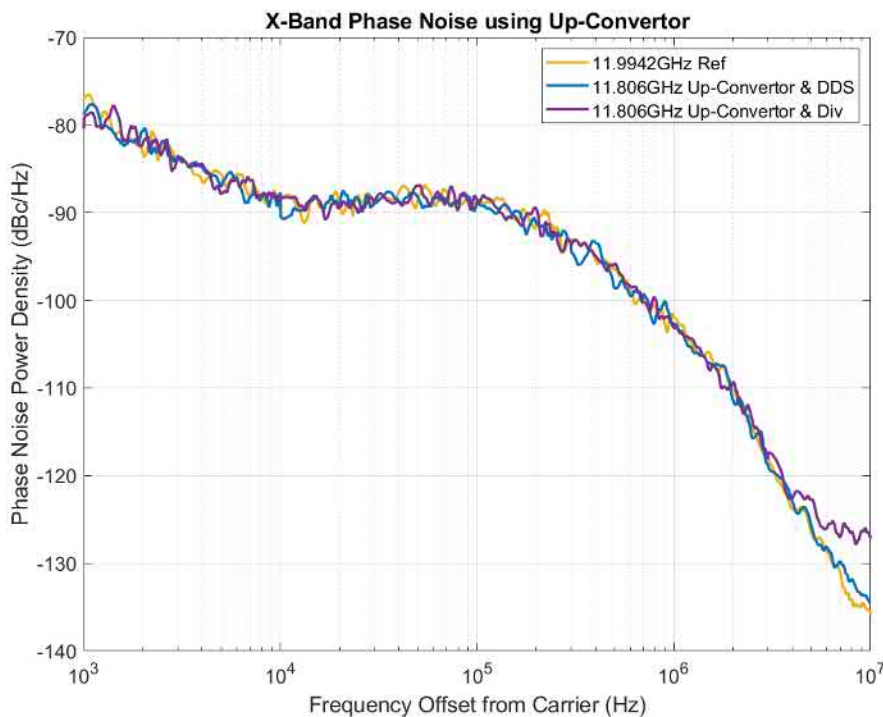


FIGURE 3.26: Initial Phase Noise results at 11.8068 GHz from the ADRF6780 Up-Converter

Signal conditioning is required in order to improve the sideband suppression and reduce the phase noise of the up-converter. The up-converter requires four base-band input signals at 187.409 MHz which must be amplitude matched and correctly phased, (I, -I, Q and -Q). The ADRF6780 can up-convert to signals from 5.9 GHz to 23.6 GHz. The full schematic of the up-converter including the signal conditioning is shown in Figure 3.27.

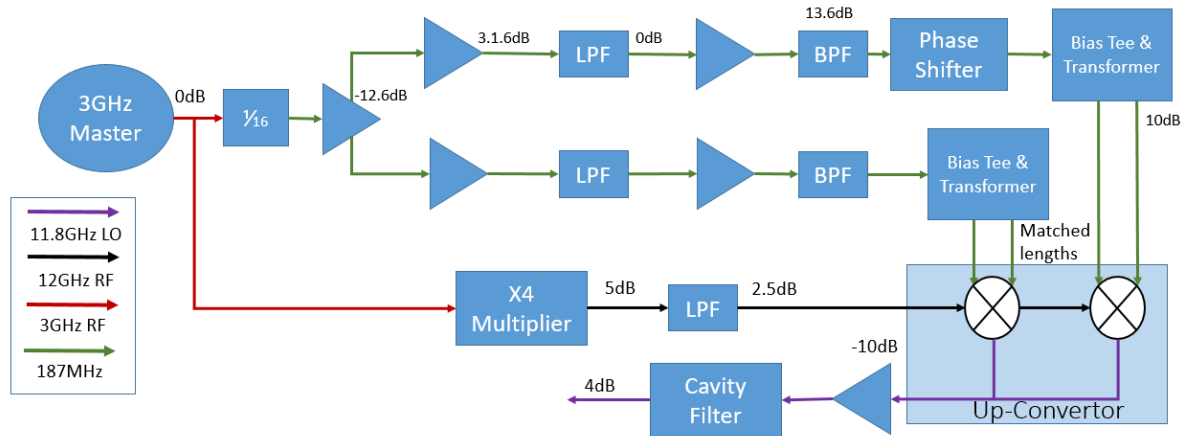


FIGURE 3.27: Up-Converter Schematic

The input 187.409 MHz signal will be the same as the source for the PLL, the input power is 0 dBm. The signal is split into two using a differential amplifier, this will produce a positive and a negative output thereby introducing a 180° phase shift between the two channels. The amplifier model is the LTC6402. The LTC6402 bandwidth extends from DC to 600 MHz and the input to the LTC6404 accepts 0 to 18 dBm. The transformer and the series resistors at the amplifier differential outputs create -12.6 dBm of attenuation for a 50 Ω load. The amplifier has significant loss as the board is designed so that the amplifier sees a higher 400 Ω load impedance as it is designed as a high impedance ADC input. After the differential amplifier the power in the two channels are -11.97 dBm and -12.01 dBm.

After the differential amplifier two amplification stages were required. Both channels are amplified using the ZLJ-4HG+, filtered using the ZX75LP-216 low pass filter, amplified again and finally filtered again using the ZAPB-184-S+ band pass filter. The output power in each channel is now 13.6 dBm and 13.4 dBm.

A 90° phase shift will be induced between the two channels using a delay line and a phase shifter. After this point all of the cable lengths and components must be identical in order to retain the 90° phase shift. The exact phase shift induced by the delay line is 89.766°. Finer adjustment of the phase was not possible as the

phase shifter is tuned manually. The cables each have a different attenuation induced by the difference in length of the delay lines, the difference is 0.08 dBm at 187.409 625 MHz.

Each 187 MHz signal must be split again while maintaining their phase. In addition, the ADRF6780 baseband inputs must be biased to 500 mV. Two boards were produced which split and bias the 187 MHz signals. The signals are split using the ADT2-1T-1P+ surface mount RF transformer. At 187 MHz the insertion loss the phase and amplitude balance are 0.11 and 0.13 dBm respectively. The signals are biased using the TCBT-123+ surface mount bias tee. A board was designed for these components using PCB Eagle, the board outline and assembled boards are shown in Figures 3.28 and 3.29.

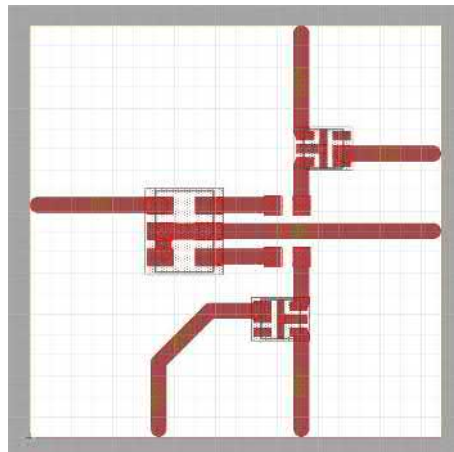


FIGURE 3.28: Board Outline for Balancing IQ Inputs

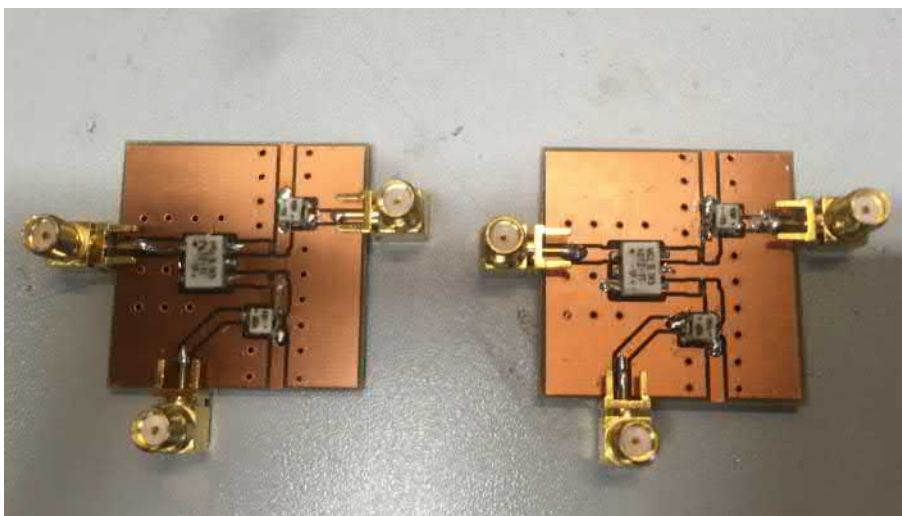


FIGURE 3.29: Prototype Boards for Balancing IQ Inputs

After the IQ balancing boards the four phased output signals are connected to the input ports of the up-converter using identical RF cables to maintain the phase

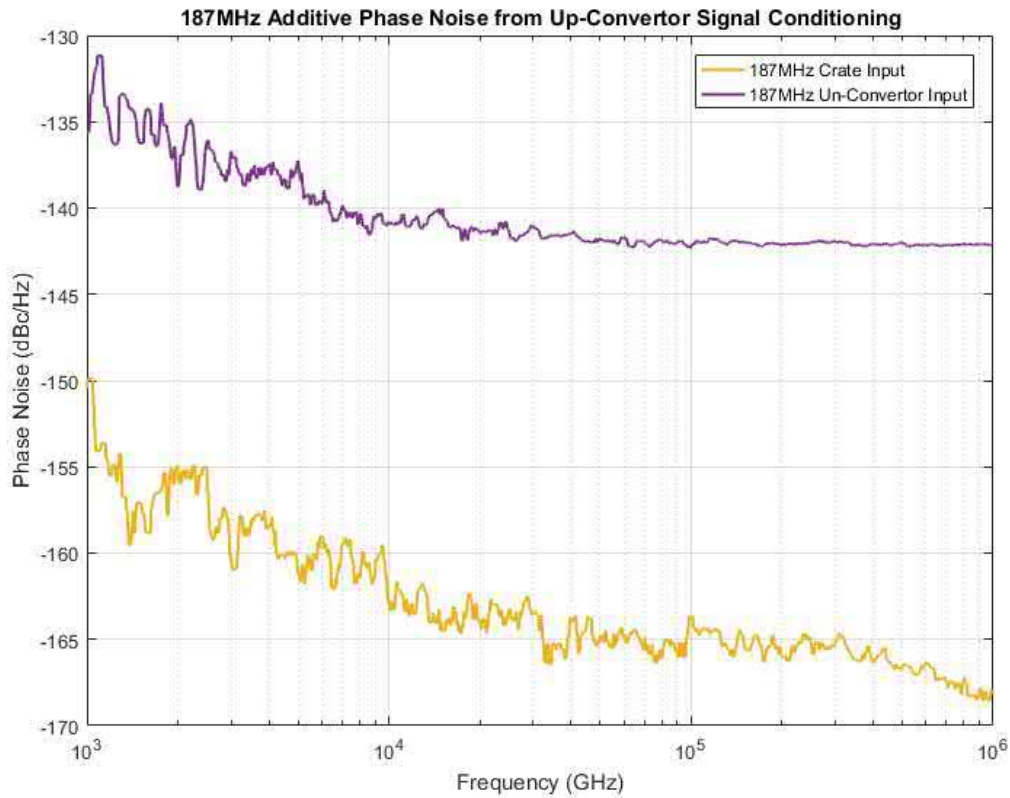


FIGURE 3.30: Added phase noise due to signal conditioning of the 187.4 MHz inputs. The input to the up-converter crate is shown in yellow, this is produced by dividing the master oscillator by 16. The input to the up-converter is shown in purple, this is after all the stages of splitting, amplifying, filtering and biasing

and amplitude balance. Figure 3.30 shows the added phase noise due to signal conditioning between the crate input and the up-converter input.

The RF input to the up-converter at 11.9942 GHz will be generated from the 2.9985 GHz master oscillator. In the original LLRF crate, a cw signal at 11.9942 GHz was produced in the transmitter chain. However, this will not be re-used as splitting this signal will reduce its power by approximately  $-3$  dBm and this will affect all of the power budgets in the RF generation scheme. Instead, the 2.998 55 GHz reference used by the NI5793 RF Pulse Generation card will be split into two. Splitting this signal generates a spare 2.998 55 GHz signal which is used for the up-converter. The power of this signal was 7.01 dBm but it will be reduced to around 4 dBm, this has no impact on the operation of the NI7593 card. The 2.998 554 GHz input is multiplied using the AQA1933K active multiplier and filtered using the FB1215 low pass filter, the output signal at 11.9942 GHz is 2.54 dBm. This is acceptable for the ADRF6780 which accepts  $-6$  dBm to 6 dBm. The output power of the up-converter is 4.169 dBm. The commissioned up-convertors is shown in Figure 3.31.

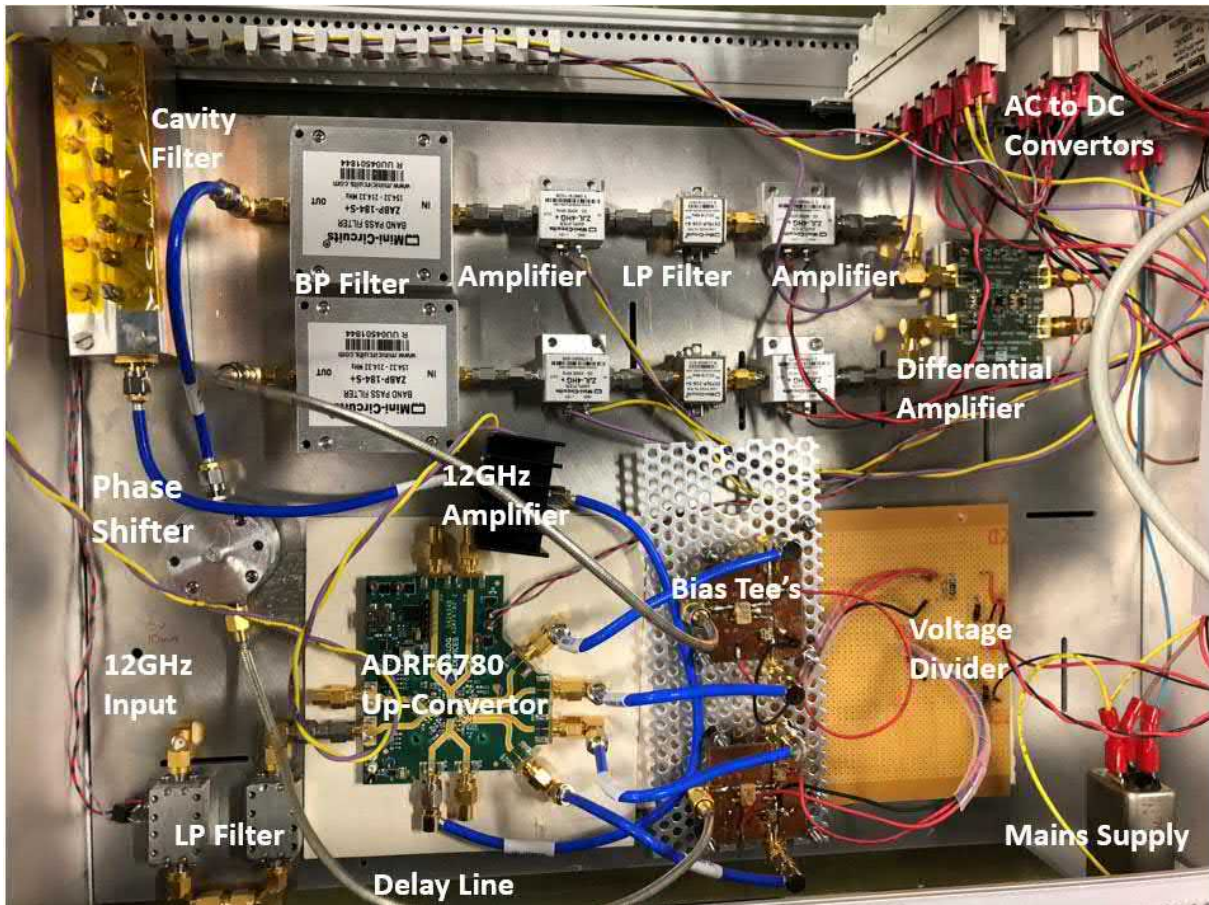


FIGURE 3.31: Up-Converter after Commissioning

The phase noise profile of the 11.9942 GHz closely resembles that of the 2 998554GHz input, this was shown in figure 3.6. The additive phase noise at 11.9942 GHz is due to the increase in frequency as described in section 3.2.3. The noise to carrier ratio increases by  $n^2$  where  $n$  is the multiplication factor, in this case  $n=4$  so the phase noise should increase by 16 dBm, the average increase in phase noise is 14.536 dBm.

With the signal conditioning and cavity filter from chapter 3 the performance of the up-converter is significantly improved with respect to both the rejection of unwanted mixing products and phase noise. This is compared with the initial phase noise results shown in Figure 3.26.

The spectral output is shown in Figure 3.32. The power in the spectrum at 11.9942 GHz is  $-64.179$  dBm so the rejection is 68.348 dBm. Similarly, the power at 12.1816 GHz is  $-63.375$  so the rejection at this frequency is 67.543 dB.

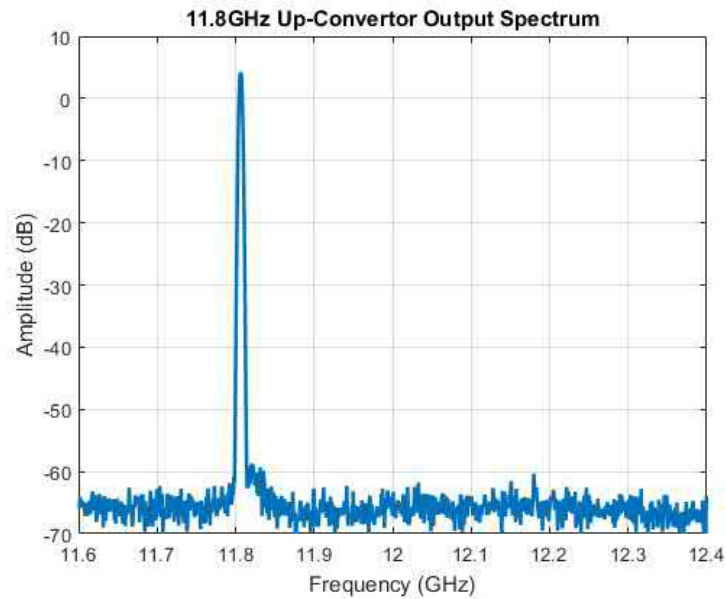


FIGURE 3.32: Measured Frequency Spectrum at the output of Up-Converter. The rejection of the carrier and upper side-band is below the noise floor of the measurement

The final phase noise results of the 11.8068 GHz local oscillator are shown in Figure 3.33. The single-sideband up-converter and cavity filter combination produce significantly lower phase noise results than the X-Band PLL. The average reduction in phase noise close to the carrier (up to 10 kHz) is 40.64 dBm. Also the phase noise floor is reduced by 6.38 dB (at offset frequencies above 100 kHz). Figure 3.34 shows the phase noise results at the output of the receiver. The 11.9942 GHz cw reference is down-converted using both of the local oscillator production methods. The improvement in phase noise from the single side-band up-converter is maintained through the down-conversion.

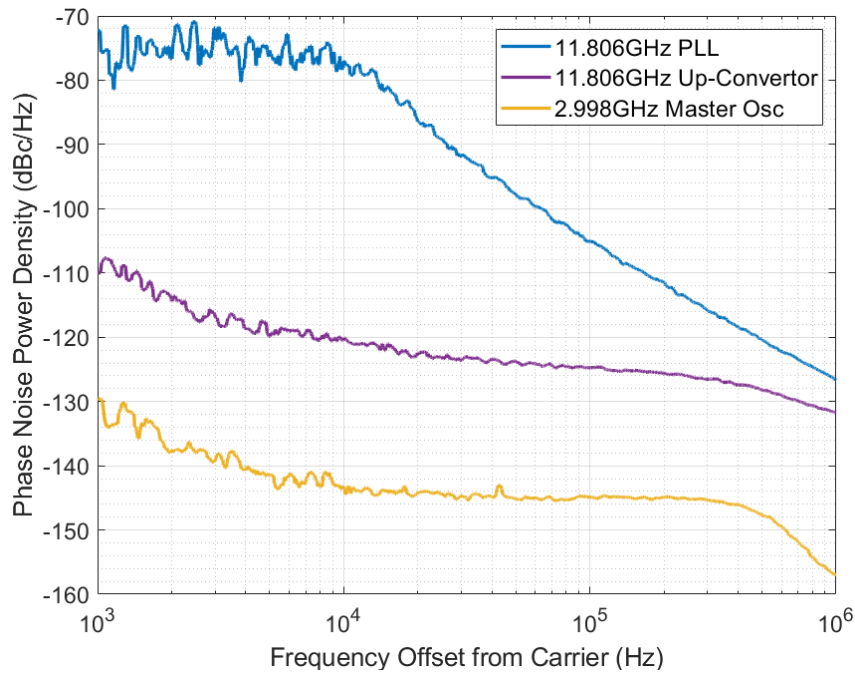


FIGURE 3.33: Measured phase noise spectrum after Commissioning: comparison of the phase noise of the LO when produced with the PLL and the Up-Converter. The master oscillator is included for reference

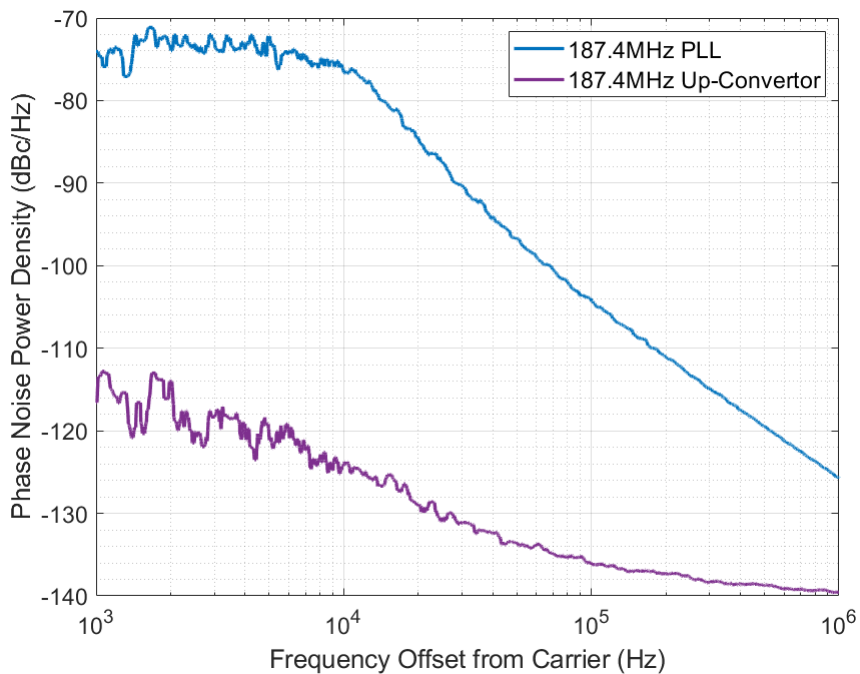


FIGURE 3.34: Measured phase noise spectrum after down-mixing the PLL and the Up-converter with an X-Band signal at 11.9942 GHz to produce two versions of the IF at 187.4 MHz

### 3.3.5 Commissioning the Receiver/Down-Conversion

The full schematic of the receiving end using the PLL is shown in figure 3.35. The LLRF crate is built in two layers, the eight down-conversion channels are built onto the top layer. The down-conversion channels are shown during commissioning in Figure 3.36.

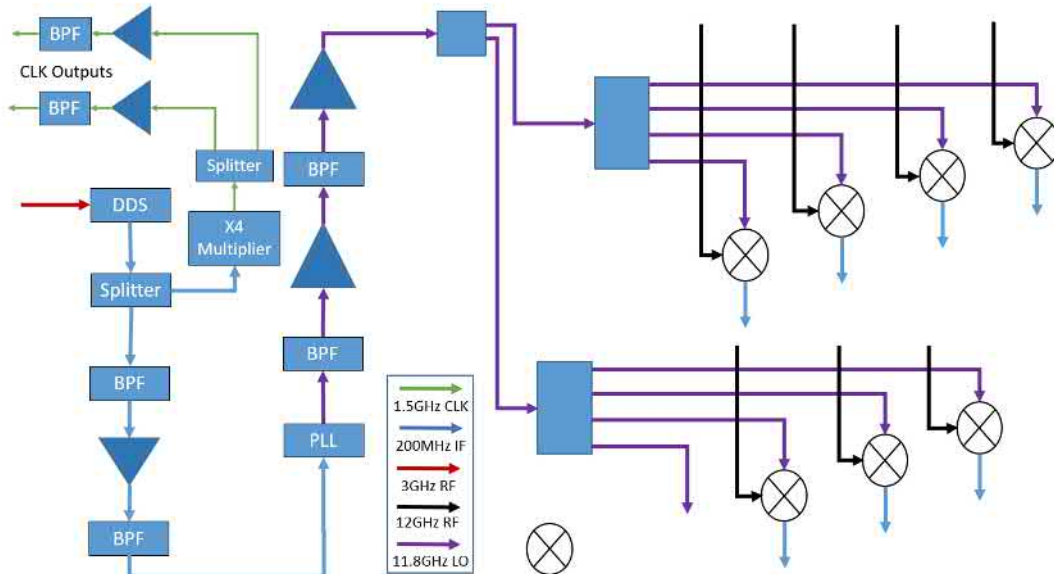


FIGURE 3.35: Schematic for the LLRF Down-Conversion with the PLL. The PLL can be replaced by the single side-band up-converter

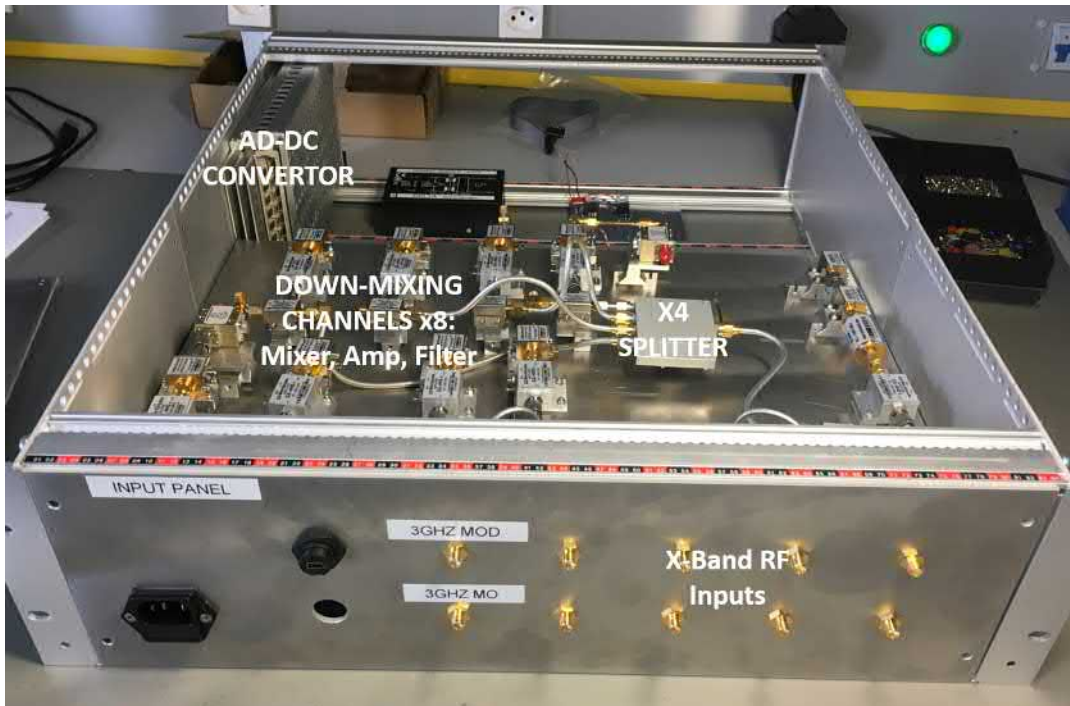


FIGURE 3.36: Down-Conversion section of the LLRF Crate during Commissioning

The fourth channel from the master oscillator is divided by 16 to produce 187 MHz using either the programmable divider or the DDS. The output power of the division stage is 7.05 dBm. This is followed by a ZX75LP-216 low pass filter, a ZJL-3G amplifier and another low pass filter. The ADF5355 PLL accepts 0 dBm as an input power so 9 dBm of attenuation is required before the PLL.

The output power of the PLL is 1.89 dBm. The PLL output signal must be split into 8 in order to feed all of the down-mixing channels, this will reduce the power by around 12 dBm. Between the PLL output and the signal splitting there are two amplification stages which amplifies the power to 23.45 dBm.

Each of the eight ZX05-24MH+ mixers has an LO power of approximately 11.36 dBm  $\pm$  0.1 dBm depending on cable lengths. The RF signals return from the system and are attenuated before the crate so that the power is in the range of  $-10$  dBm to 0 dBm.

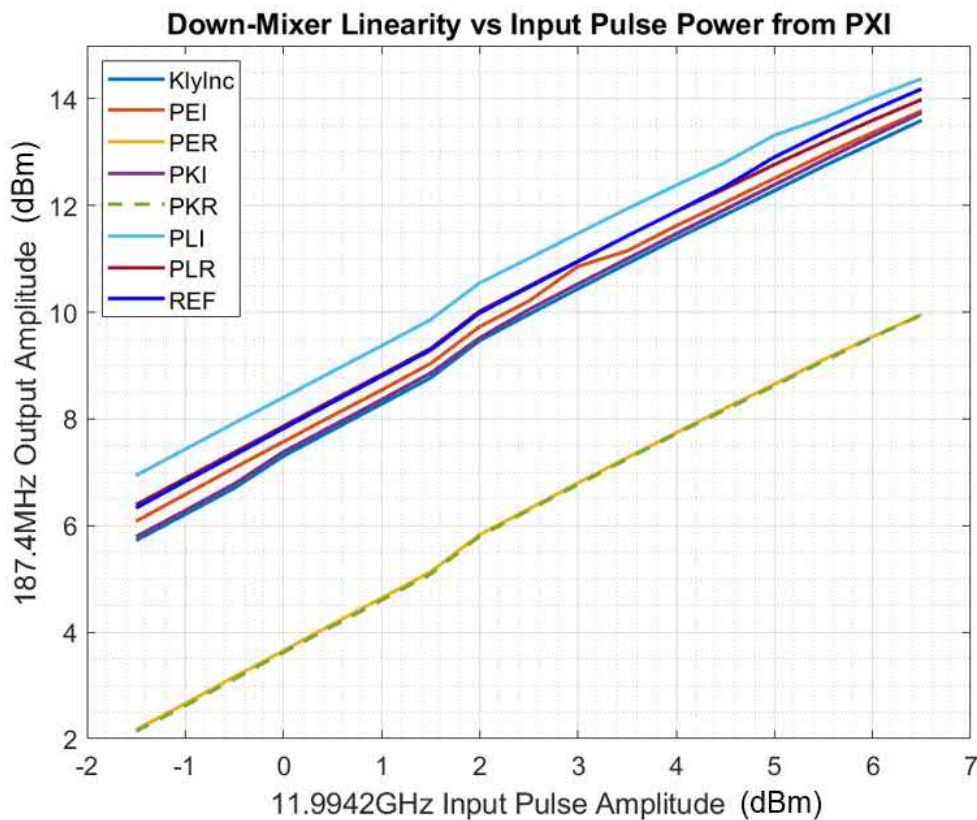


FIGURE 3.37: Measured Power at the Output of the Mixer at 187.4 MHz vs Input 2.998554 GHz Pulse Power provided by the NI5793 RF Generation card

After each mixer there is a ZX75 amplifier and a ZJL-3G amplifier. Two of the channels also have an isolator, these channels will be used for reflected power signals, PKR and PLR.

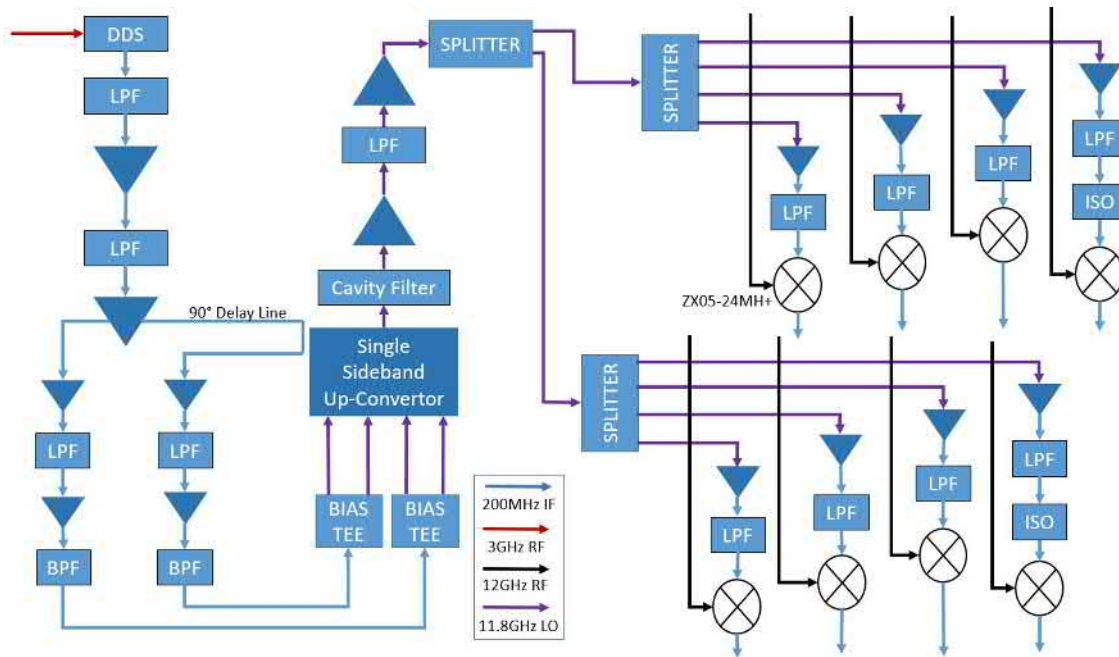


FIGURE 3.38: Schematic for the LLRF Down-Conversion using Up-Converter in place of the PLL

### 3.4 DC Power Supply Stability

The LLRF crate uses power supplies which derive from the mains power supply. The stability of the LLRF components will depend on the stability of the power supplies. The output power of the AQA1933K frequency multiplier is particularly sensitive to fluctuations of the input 5 V power supply. A voltage fluctuation of  $\pm 0.5V$  results in an output power deviation of  $\pm 0.1\text{dBm}$  at the output of the LLRF crate, this is only a 0.001% fluctuation in the input power to the TWT which is negligible.

The AC voltage is passed through two AC-DC convertors which produce 5 V and 12 V DC respectively in order to power the active components in the LLRF system. Without additional filtering, mains power supplies can be less stable than bench-top DC power supplies which have additional circuitry to smooth and control the output DC voltage. The DC voltages from the LLRF crate are sampled every 60 s using the NI5162 and compared with a NGE103B bench-top power supply during the same 50 hours period to validate if the stability is within an acceptable range and free from spurs from spikes in the mains supply. The data is shown below in Figure 3.39.

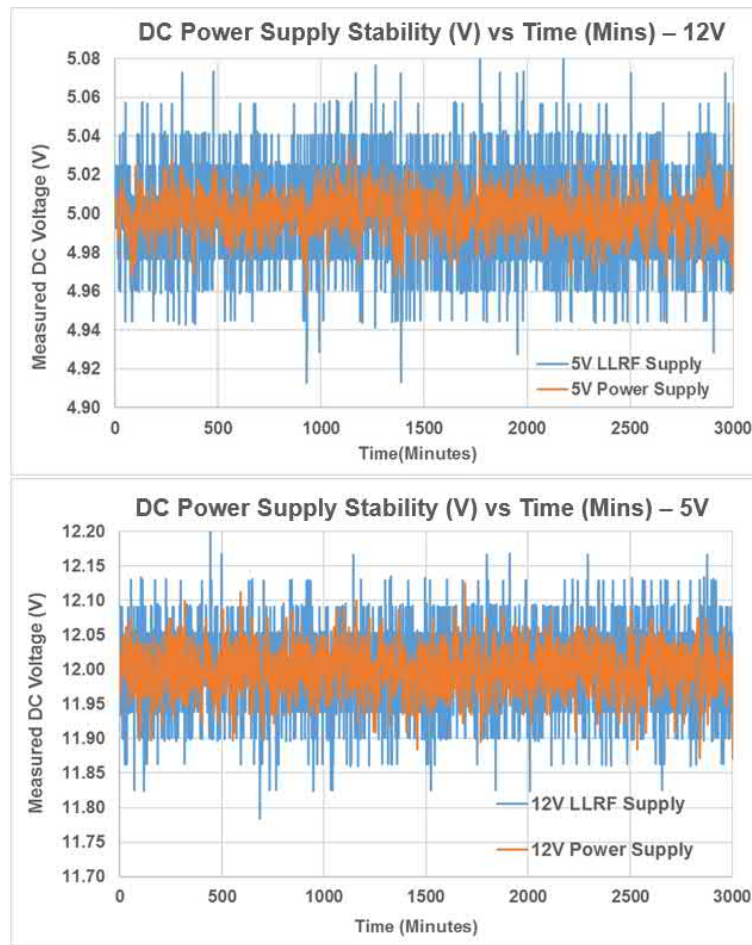


FIGURE 3.39: Measured Stability of the 5 V (Top) and 12 V (Bottom) DC Power Supplies to the LLRF Crate vs a NGE103B DC Power Supply over 50 Hours during February 2021

The mean and standard deviation of the measured voltages are shown below in Table 3.6. The stability of the bench-top power supply surpasses that of the LLRF AC-DC convertors, this is likely to additional circuitry in the bench power supply. However, both the NGE103B and the LLRF power supplies have a standard deviation of less than 0.06 V and an average value within 0.05 V of the voltage setpoint. Additionally, there are no spurs so the LLRF power supply. Hence the stability of the LLRF power supply is deemed acceptable.

	5 V Supply		12 V Supply	
	LLRF	NGE103B DC	LLRF	NGE103B DC
Mean (V)	4.998	4.999	11.994	12.005
$\sigma$ (V)	0.049	0.029	0.051	0.032

TABLE 3.6: Mean and Standard Deviation of the Stability of the 5V and 12V DC Power Supplies

### 3.5 Conclusion

The LLRF can be considered in two parts, a transmitter and a receiver. Two schemes were considered and the phase noise of both designed was predicted. It was determined that the difference in phase noise between the two schemes was not significant because the largest contributor to the phase noise is the NI5793 RF Modulation. The scheme selected used a frequency quadrupler and this transmitter was commissioned.

The receiver uses a local oscillator to convert the input X-band signals to an intermediate frequency before the signal is digitally demodulated in the PXI. The 11.9942 GHz RF will be mixed down to 187.4 MHz using a local oscillator at 11.8068 GHz. This frequency must be generated using the S-band master oscillator.

A commonly used method of generating a local oscillator is a PLL, this has been implemented before in the X-band test stands. The PLL phase noise is dominated by the quality of the internal VCO of the PLL and hence cannot be improved any further. An alternative for up-conversion is frequency mixing. The single side-band (or image reject) up-converter is used in specialist applications where only one mixing product is needed. The up-converter is the ADRF6780 and the achievable side-band suppression is in the region of 25 dBm from the datasheet. Signal conditioning was used to improve the sideband suppression and reduce the phase noise of the up-converter. With the signal conditioning and cavity filter from Chapter 4 the performance of the up-converter is significantly improved with respect to both the rejection of unwanted mixing products and phase noise.

The single-sideband up-converter and cavity filter combination produced significantly lower phase noise results than the X-Band PLL. The average reduction in phase noise close to the carrier (up to 10 kHz) is 40.64 dBm. The 11.9942 GHz cw reference is down-converted using both of the local oscillator production methods. The improvement in phase noise from the single side-band up-converter is maintained through the down-conversion.

## Chapter 4

# Design of a Narrow-band Cavity

## Filter at 11.806GHz

### 4.1 Introduction

The up-converter mixes two frequencies at 11.9942 GHz and 187.4 MHz which will produce first sidebands at 11.806 GHz, 12.182 GHz. The lower side-band is required, while the upper side-band and carrier are contamination. The upper side-band, carrier, and any spurious frequencies falling close to the desired bandwidth must be sufficiently attenuated while the 11.806 GHz is transmitted. Phase and amplitude balancing at the inputs to the up-converter will increase suppression of unwanted mixing products but will not remove them entirely. Additional suppression can be achieved using filtering. A filter fulfilling the requirements does not exist commercially as the bandwidth must be less than 187 MHz and centred at 11.806 GHz, hence a custom filter was designed by the author.

The filter can be considered as a loss free, ideal two-port network located between a source and the load. The network will transmit power from the source to the load with frequency dependent attenuation. Depending on the configuration of pass and stop bands a filter can be classified as: low-pass, high-pass, band-pass or band-stop.

### 4.2 Design Specification

The most important properties of the filter will be rejection outside the pass-band and sharp transition between pass-band and stop-band. This is due to the relatively small bandwidth with respect to the centre frequency, this ratio is called the fractional bandwidth. The filter design is heavily influenced by the fractional bandwidth, which in this case is 0.85%. This parameter also determines the physical

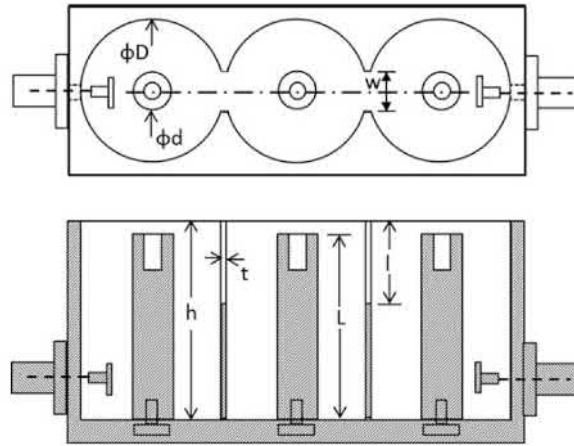


FIGURE 4.1: Iris Coupled Cavity Filter

realization of the filter. For fractional bandwidths below 1% an iris coupled cavity filter is most suitable [99], this type of filter is shown in Figure 4.1. This filter type is physical cavity, where the capacitance and inductance are formed by the geometry and volume of the structure.

Reducing the fractional bandwidth further will significantly complicate the filter design. In addition, using a bandwidth of 100 MHz allows flexibility of the local oscillator so that the LLRF system can be used to produce different intermediate frequencies if required (such as for non-IQ sampling).

Cavity filters are characterised by low insertion loss in the pass-band and high rejection in the stop-band. In particular, iris-coupled filters have the advantage of achieving narrow bandwidth, although their design is mechanically more complex and thus milling operations can be more expensive.

Other design considerations are related to the mechanical manufacture, these are: connector type, filling material, construction method and material. The filling material will be air at ambient temperature and humidity. A summary of the design specification is shown in Table 4.2.

Centre Frequency	11.806	GHz
Bandwidth (3dB)	100	MHz
Pass-band Edge	$\pm 200$	MHz
Rejection at Pass-band Edge	-70	dB
Input & Output Connector	SMA	
Input & Output Impedance	50	$\Omega$
Dielectric Filling Material	Air	

TABLE 4.1: Specification for 11.806 GHz Band Pass Filter

### 4.3 Equivalent Lumped Circuit Model

The class of a filter refers to the class of polynomials from which the filter is mathematically derived and the type of polynomial used to characterise their transfer function [53]. For this specification the Chebyshev type 1 filter type was chosen due to high selectivity and high stop-band attenuation. The compromise for Chebyshev type 1 filters is unavoidable ripple in the pass-band. The maximum allowable pass-band ripple therefore becomes part of the specification. This determines the filter order which is the first stage in the design process.

The dominant method for filter design is network synthesis. This approach requires approximating the response of an ideal filter using a transfer function which describes the filter's output for each possible frequency input.

A polynomial is fitted to the transfer function. Using fraction or partial fraction expansions of the polynomial, enables the element values for a lumped element model to be found. Lumped inductances and capacitances are combined to form a cascade of resonant circuits, which each represent one of the physical cavities of the cavity filter.

Each pass-band can be produced using passive lumped elements. Inductors pass low frequencies while capacitors pass high frequencies. Combining these two components and altering their values can create a circuit that can transmit any required frequency band. At a given frequency, the series sections will be at their minimum impedance and the shunt sections at their maximum impedance; for a band-pass filter this will occur at the centre frequency [99].

This filter design process begins with a lumped circuit model which demonstrates the desired behaviour of the filter, this is called the low pass prototype filter. The values of the elements in the prototype design are called 'g-values'. The g-values have been tabulated for common filter topologies. The tabulated values are normalised to a source impedance of  $50\Omega$  and a centre frequency of 1 rad/second.

The g-values will be transformed to the design frequency and source and load impedance [53]. The prototype is an example of a normalized design from which the desired filter can be scaled or transformed. The actual filter is obtained by transforming the prototype filter [53] to generate the low-pass lumped element filter.

A second transformation is used to transform the low-pass lumped element filter into a band-pass filter. The transformation requires that the low-pass filter be considered with both its positive and negative frequency responses mapped to the upper

and low halves of the pass-band. The frequency response of the lumped element filters will be simulated and verified in Microwave office. When the component values of the band-pass lumped element model are known they can be converted into the physical dimensions of the cavity filter.

To summarise, the stages in the design of a lumped element model of the desired cavity filter are as follows:

- The number of elements in the cavity filter is determined using the stop-band attenuation and pass-band ripple for a Chebyshev type 1
- The g-values of the low-pass prototype filter are determined using look-up tables or calculated from design equations
- The element values of the scaled low-pass filter are obtained when the g-values of the prototype are transformed to the desired corner frequency and impedances
- The low-pass filter is converted to a lumped element band-pass filter

The power transfer ratio of a Chebyshev type filter is expressed as:

$$|S_{21\text{Chebyshev}}(\omega')|^2 = \frac{1}{1 + \varepsilon^2 T_n^2(\omega')}$$

Where N is the filter order,  $\omega'$  is the normalised angular frequency,  $\varepsilon$  is related to the maximum pass-band ripple and  $T_n$  is the Chebyshev polynomial of the nth order. The pass-band ripple of the Chebyshev filter response is:

$$RP = 10 \log_{10}(1 + \varepsilon^2)$$

The pass-band ripple will oscillate between 1 and  $(1 + \varepsilon^2)^{-1}$ , for this reason Chebyshev filters are said to be equiripple. The parameter  $\varepsilon$  is referred to as the 'ripple factor.' Keeping the order constant, the higher the value of  $\varepsilon$ , the higher the pass-band ripple and the stop-band attenuation. If a better stop-band attenuation is required without compromising the pass-band ripple, then the filter order must be increased. Filters with lower pass-band ripple have reduced selectivity. Insertion loss inside the pass band is determined by the quality factor of the filter elements. Adding more reactive elements increases the rejection capability of a filter [100].

### 4.3.1 Determining Filter Order

In order to use the design tables for the prototype filter the filter type and required number of elements must be determined. The filter order will be determined from the stop-band attenuation, bandwidth and the type of filter, in this case Chebyshev type 1 [99]. The Chebyshev filters are typically normalised so that the edge of the ripple band is at  $\omega_0 = 1$

The number of filter sections is determined by selecting an acceptable level of pass-band ripple and solving the following equations for the number of sections,  $n$ . The pass-band ripple is the amount of variation in amplitude within the pass-band of the filter.  $L(\omega)$  is the rejection as a function of the angular frequency.

$$L(\omega) = 10 \log_{10} [1 + \epsilon \cosh^2 [n \cosh^{-1} \frac{\omega'}{\omega_1}]]$$

The pass-band exhibits equiripple behavior described by the ripple factor  $\epsilon$ . The ripple factor is related to the pass-band ripple,  $L_{ar}$ .

$$\epsilon = [e^{\frac{L_{ar}}{10}} - 1]$$

The ratio of the upper rejection frequency to the upper pass-band edge frequency in radians is also required in order to determine the number of sections. At the pass band edge the rejection is specified as  $-70$  dB.

$$\frac{\omega'}{\omega_1} = \frac{2}{\omega} \cdot \frac{f + f_U}{f} = 1.0009$$

Where  $f_U$  is the upper rejection frequency (centre frequency  $\pm 200$  MHz) and  $f$  is the centre frequency. The ratio of the bandwidth to the centre frequency is  $\omega$ :

$$\omega = \frac{100 \text{ MHz}}{11.806 \text{ GHz}} = 0.00847$$

Selecting an odd number of elements will result in a filter which is symmetric about the centre cavity. This will make the design and optimisation easier as the filter elements can be optimised as pairs of identical cavities placed symmetrically around the central cavity. Increasing the filter order will result in a steeper roll-off into the stop-band until the filter order is approximately 10. Thereafter, the improvement in performance with added elements is almost negligible with respect to the

additional time and complexity in the design [53]. The optimal value to satisfy the filter specification is 7 cavities for a maximum pass-band ripple of 0.1dB.

### 4.3.2 Low-Pass Prototype Element Values

There are two methods for obtaining the g-values. Firstly, g-values for common filter configurations are tabulated, for Chebyshev the order and ripple must be known. Secondly the values can be computed from design equations. Both the tables and design equations are found in [53] The prototype element values for the normalised low-pass function assume a cut-off frequency of 1 rad/sec and source and load impedances of  $1\Omega$ . Either an input capacitor or an input inductor can be used interchangeably. The design equations for calculating g-values are based on an odd number of filter elements and Chebyshev filter type. The number of the g-values that need to be computed is related to the number of resonators. Values are computed for  $n$  resonators,  $g_0$  to  $g_{n+1}$ . For a cavity with an odd number of sections, the two end resonators always have a g-value of 1. For the g-values of the internal sections, the intermediate values,  $\beta$ ,  $\gamma$ ,  $a_k$  and  $b_k$  must also be calculated.

$$g_1 = \frac{2a_1}{y} \quad (4.1)$$

$$g_n = \frac{4a_n a_{n-1}}{b_{n-1} g_{n-1}} \quad (4.2)$$

$$g_0, g_{n+1} = 1 \quad (4.3)$$

Where:

$$\beta = \ln(\coth \frac{L_a}{17.37}) \quad \gamma = \sinh(\frac{\beta}{2n})$$

$$a_k = \sin(\frac{(2k-1)\pi}{2n}) \quad b_k = \gamma^2 + \sin^2(\frac{k\pi}{n})$$

Where:  $k = 1, 2, 3, \dots, n$ .

The g-values will be converted to inductances and capacitances by normalising with respect to the design frequency and impedance [53], [99]: Impedance scaling is invariably a scaling to a fixed resistance. This is because the terminations of the filter, at least nominally, are taken to be a fixed impedance. The frequency and impedance

scaling are combined into a single step:

$$L_n = \frac{g_n R_s}{\omega_c} \quad (4.4)$$

$$C_n = \frac{g_n}{\omega_c R_s} \quad (4.5)$$

Where  $\omega_c$  is the upper cut-off angular frequency and R is the source or load impedance, in this case  $\omega = 2\pi \cdot 11.856\text{GHz}$  and  $R_s = R_L = 50\Omega$  respectively. The source and load impedances are both  $50\Omega$  as SMA connectors lines will be used to couple in and out of the filter.

### 4.3.3 Low-Pass to Band-Pass Transformation

The following equations are used to transform the low-pass prototype into a band-pass filter prototype, this involves shifting the centre frequency of the filter. The centre frequency of the low-pass prototype is at  $\omega = 0$ , this is transformed to  $\omega_0$  which is the centre frequency of the band-pass filter.

The upper and lower pass-band limits are  $\omega_1$  and  $\omega_2$  respectively and  $\Delta$  is the normalized bandwidth [53]. The band-pass mappings (equations 4.6, 4.7 and 4.8) are applied to the reactance of the components from the low pass filter, these were shown in Equations 4.4 and 4.5:

$$\omega_0 = \sqrt{\omega_2 \omega_1} \quad (4.6)$$

$$\Delta = \frac{\omega_2 - \omega_1}{\omega_0} \quad (4.7)$$

$$\frac{\omega}{\omega_c} = \frac{1}{\Delta} \left( \frac{\omega}{\omega_0} - \frac{\omega_0}{\omega} \right) \quad (4.8)$$

The transfer function of the band-pass filter is derived from the transfer function of the low-pass filter with  $\omega$  replaced by  $(\frac{\omega}{\omega_0} - \frac{\omega_0}{\omega})$ . This separately maps the band-edge frequency of the low-pass response to the band-pass frequencies  $\omega_1$  and  $\omega_2$ .

$$\omega \rightarrow \frac{\omega}{\omega_0} - \frac{\omega_0}{\omega}$$

$Z_L$	Impedance of band-pass series element
$Z_C$	Impedance of band-pass shunt element
$L_{LP}$	Inductance of low-pass series element
$L_{BP}$	Inductance of band-pass series element
$C_{LP}$	Capacitance of low-pass series element
$C_{BP}$	Capacitance of band-pass series element

TABLE 4.2: Specification for 11.806 GHz Band Pass Filter

The series inductor transforms to a combination of an inductor and capacitor in series, as shown in Equation 4.9. Similarly, the shunt capacitors are transformed into a parallel combination of inductor and capacitor which is shown in Equation 4.10.

$$Z_L = L_{LP} \frac{1}{\Delta} \left( \frac{\omega}{\omega_0} - \frac{\omega_0}{\omega} \right) = L_{BP} \frac{\omega}{\omega_0} - \frac{1}{\omega_0 C_{BP}} \left( \frac{\omega_0}{\omega} \right) \quad (4.9)$$

$$Z_C = -\frac{1}{\omega_0 C_{LP}} \frac{\omega_0}{\omega} = \frac{1}{C_{BP} \left( \frac{\omega}{\omega_0} \right)} - \frac{1}{\omega_0 L_{BP} \left( \frac{\omega_0}{\omega} \right)} \quad (4.10)$$

The values of the series elements can be found from Equations 4.11 and 4.12 [99]:

$$L_{BP}^n = g_n \frac{R_S}{\omega_0 \Delta} \quad (4.11)$$

$$C_{BP}^n = \frac{1}{g_n} \frac{\Delta}{\omega_0 R_S} \quad (4.12)$$

The values for the shunt parallel inductors and capacitors can be found from Equations 4.13 and 4.14:

$$L_{BP}^n = \frac{1}{g_n} \frac{\Delta R_S}{\omega_0} \quad (4.13)$$

$$C_{BP}^n = g_n \frac{1}{\Delta \omega_0 R_S} \quad (4.14)$$

#### 4.3.4 Verifying Prototype Circuits

Design equations were used to verify the tabulated values for a seven element Chebyshev filter where the first element is a series inductance. The tabulated 'g-values' are compared with the calculated results in Table 4.3.

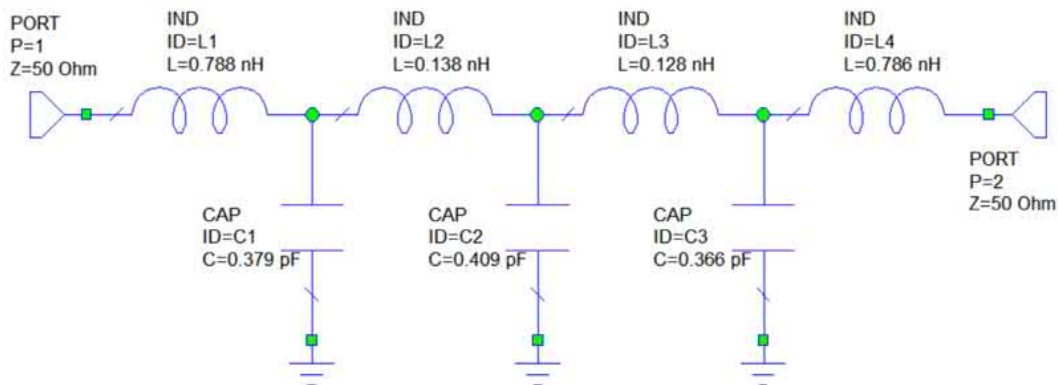
G	Computed ( $\Omega$ )	Tabulated ( $\Omega$ )	Difference (%)
0	1	-	-
1	1.168	1.181	1.11
2	1.404	1.423	1.35
3	2.056	2.097	1.99
4	1.517	1.573	3.69
5	1.982	2.097	5.48
6	1.355	1.429	5.64
7	1.165	1.181	1.37
8	1	-	-

TABLE 4.3: Comparison of Tabulated and Computed 'g-values'

The low-pass prototype values are shown in Table 4.4. The results were simulated in Microwave Office to verify the behaviour by observing the scattering parameters, the results are shown in Figure 4.3.4 and Figure 4.2.

G	$L_n$ (nH)	$C_n$ (pF)
1.168	0.788	
1.404		0.379
2.056	0.138	
1.517		0.409
1.982	0.128	
1.355		0.366
1.165	0.786	

TABLE 4.4: Element Values for the 7 Element Chebyshev Low-Pass Prototype Filter



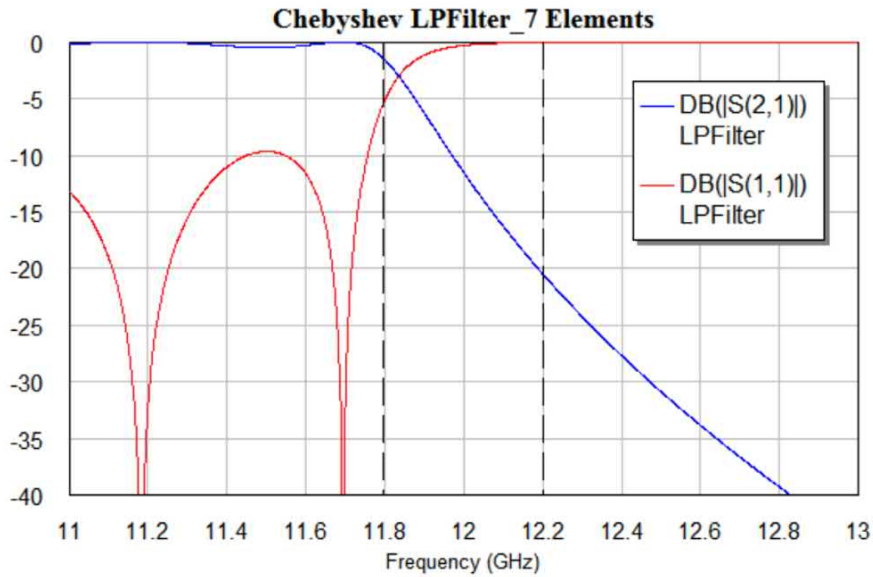


FIGURE 4.2: Simulated Scattering Parameters of Low-Pass Lumped Element Prototype Filter

Simulation in Microwave Office was repeated to verify the behaviour of the band-pass prototype. The inductance and capacitances are no longer ideal, they must be modelled with a frequency dependent quality factor. The element values are shown in Table 4.5. The quality factor was evaluated at the centre frequency of the filter and the quality factor was set at 100. This is reasonable when considering that the Q-factor can be expressed as the reciprocal of the fractional bandwidth, which was 0.85%.

It was found that the series capacitances were extremely small and thus were considered to be negligible and therefore discarded. This is consistent with an iris-coupled cavity filter design, where the cavities are inductively coupled and the capacitive coupling is negligible. Though both inductive and capacitance couplings exist between resonator sections, only an inductance is shown between the shunt

$L_n$	(nH)	$C_n$	(pF)
L1	0.00361	C1	50.735
L2	0.533	C2	142.156
L3	0.00129	C3	205.422
L4	0.392	C4	228.001
L5	0.000891		
L6	0.335		
L7	0.00802		

TABLE 4.5: Calculated Element Values for Lumped Element Band-pass Prototype

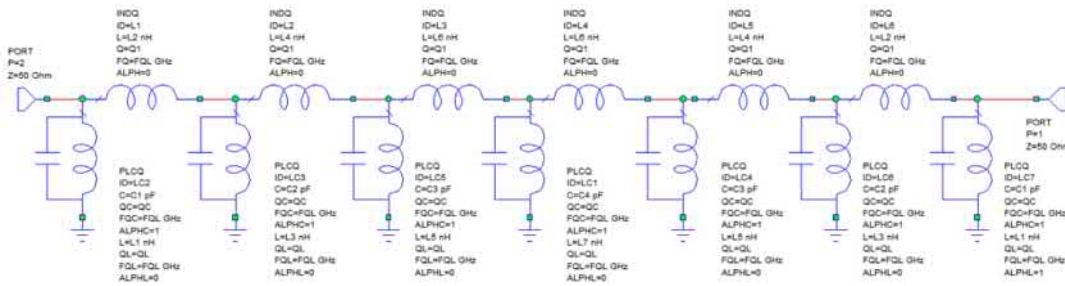


FIGURE 4.3: Band Pass Lumped Element Prototype Filter

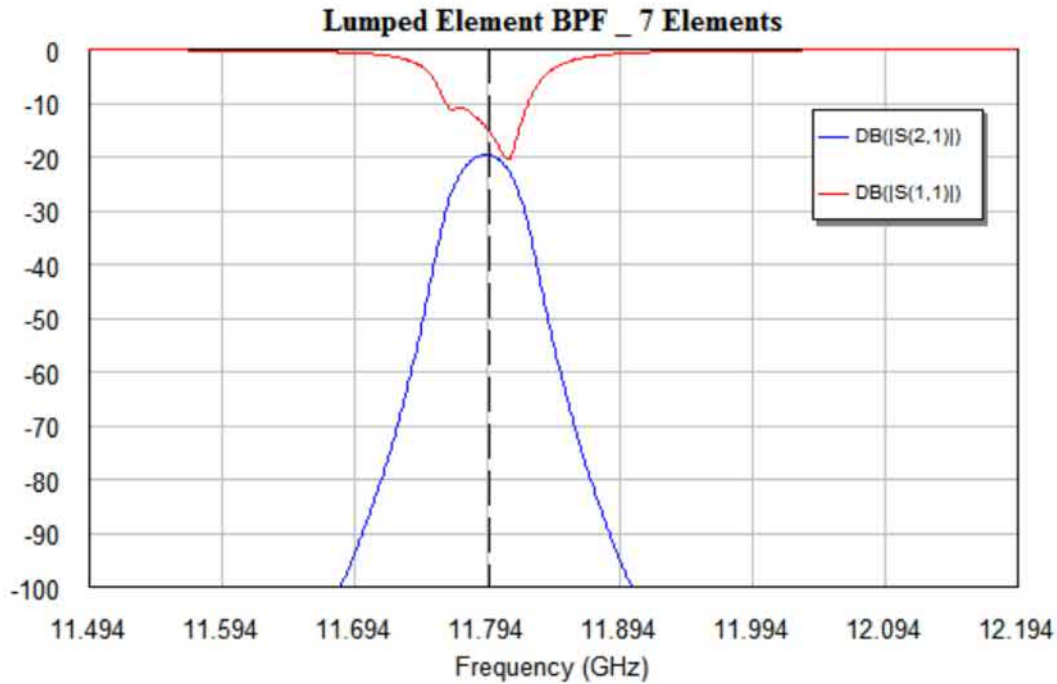


FIGURE 4.4: Scattering Parameters of Band Pass Lumped Element Prototype Filter

sections as the predominant coupling between resonator sections is inductive [53].

The low-pass element filter is shown in Figure 4.3 and the frequency response is shown in Figure 4.4. The simulated performance of the band-pass filter shows that the filter operates correctly in the desired pass and stop-bands. However, the simulated results show a large insertion loss in the pass-band. This is due to the low value of the Q-factor in the simulations. In reality, the Q-factor of the distributed elements will be higher than micro-strip technology, which will reduce the insertion loss by increasing the stored energy in the cavities.

## 4.4 Conversion to Physical Dimensions

Most filters can be placed into one of three different categories which describes their physical realisation. These categories are lumped, semi-lumped and distributed. A lumped circuit is constructed from discrete inductors and capacitors, these are appropriate for frequencies up to 100 MHz. Semi-lumped filters use discrete inductors and distributed capacitances. For frequencies in the range of GHz, entirely distributed elements are common because lumped elements are difficult to construct at microwave frequencies [99].

In a cavity filter, both the inductance and capacitance are distributed through the filling medium inside a closed metallic container. Inside the metallic container there is a small metallic cylinder that is secured to the base at the bottom and free at the other end, this is an inductive resonator. The resonator itself has distributed inductance, while the distributed capacitance is formed in the gap between the free end of the resonator and the upper wall of the enclosure. The inductance of the resonator and the distributed capacitance resonate at a frequency determined by the mechanical dimensions of the cavity and the resonator [99].

When designing a cavity filter, the lumped circuit model must be transformed into the physical dimensions of the cavities. The cavity filter in this design will be an iris-coupled cavity filter, a diagram of this filter type was introduced in Figure 4.1. This design has the advantage of achieving narrow bandwidth, although their design is more mechanically more complex than other common filter type (such as waveguide or comb-line), and milling operations can therefore be more expensive than some other cavity filter designs.

In an iris-coupled cavity filter, each cavity is coupled to the adjacent cavities through a coupling slot. The coupling will alter the dimensions of the cavity from the nominal dimensions.

The electrical specifications of iris-coupled filters are converted into the mechanical dimensions of the parts of the filter. The mechanical dimensions which must be computed are:

- Diameter of cavity
- Height of the cavity block
- Length of resonator
- Diameter of resonator

- Dimensions of irises

The process for converting the band-pass lumped filter into a physical cavity is summarised below. There are several intermediate computations which are required in order to characterise the coupling and determine the dimensions of the irises.

1. Determining the number of filter sections - completed in section 4.3.1
2. Computing the initial cavity dimensions - these include the diameter, height, resonator height and resonator diameter
3. Computing the height, width and thickness of irises
  - Calculate g-values - previously calculated in Section 4.3.4
  - Calculate coupling reactance and magnetic polarizability of the irises
  - Find initial width and length of irises from empirical measurements
  - Calculate compensated magnetic polarizability of the irises
  - Final width and length of irises from empirical measurements
4. Deciding the diameter and the length of tuning screws

#### 4.4.1 Determining Diameter of Cavity and Resonators

The characteristic impedance of the cavities will be used to determine the diameter of the cavity and the inner resonator. The characteristic impedance is a function of the various dimensions of the transmission line and the dielectric constant of the non-conducting material in the transmission line. For most RF systems, the characteristic impedance is normalised to either 50  $\Omega$  or 75  $\Omega$ . For low-power applications, transmission lines are optimized for low loss, which occurs when the characteristic impedance is approximately 75  $\Omega$  for transmission lines with air dielectric [101]. The cavity and resonator form a coaxial transmission line [53], [99] and their characteristic impedance is defined by:

$$Z_0 = \frac{60}{\sqrt{\epsilon}} \ln \left( \frac{D}{r} \right) \quad (4.15)$$

Where  $D$  is the diameter of the outer cavity,  $r$  is the diameter of the inner resonator and  $\epsilon = 1$  as the filling material will be air. The losses are minimised for a

given diameter ratio which corresponds to a characteristic impedance ( $Z_0$ ) of  $75 \Omega$  [53].

The diameter of the coaxial cavity has its implications on the insertion loss and the size of the filter. Higher diameter results in a larger sized filter with lower insertion loss [99]. However, it is important to select a diameter such that the cavity is not over-moded. As the diameter is increased, an unwanted TE or TM mode can appear. This restricts the diameter of the cavity.

The cavities are half-wavelength transmission line resonators; the outer diameter of the cavity will be half the guide wavelength at the centre frequency. The guide wavelength is the distance between two equal phase planes along the waveguide as a function of the frequency and material. The guide wavelength will always be longer than the wavelength in free space. The guide wavelength for a centre frequency of 11.806 GHz in air is 25.4 mm.

Considering size and design data on similar cavity filters [53], [99], a cavity diameter of 12 mm for the iris-coupled filter is suitable. From Equation 4.15 the diameter of the inner resonator is 3.4 mm. The resonators are quarter wavelength resonators, this property determines their height. The resonators height will be 6 mm.

Cavity height is determined by assuming a clearance of several millimetres at the free end of resonators for tuning. In this case the cavity height will be set to 9.50 mm, which leaves a tolerance of 3.50 mm. These will be the initial values for cavity and resonator dimensions, the actual values will be refined during simulation.

#### 4.4.2 Calculating Iris Parameters

In an iris coupled filter, a cascade of resonant cavities are coupled through irises, this coupling between cavities can be either capacitive or inductive. The coupling is determined by altering either the height, width or thickness of the iris [99].

Thinner irises produce higher coupling, hence the prototype design (shown in Figure 4.1) will be amended to minimise the thickness of the iris by directly overlapping the cavities rather than building an iris of finite thickness. The iris coupling will therefore be determined using only one parameter. The length of the iris is adjusted by changing the distance between the centres of the adjacent cavities. This iris design simplifies the cavity design and eases manufacture.

The length of the iris will be determined physically by overlap between adjacent cavities. The correct overlap, and therefore the correct iris width, will be achieved by adjusting the distance between the centre of two adjacent cavities. The iris width

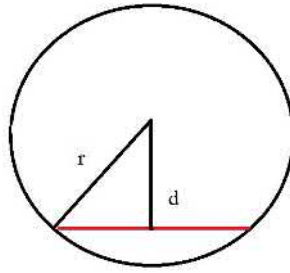


FIGURE 4.5: Chord Length of a Circle

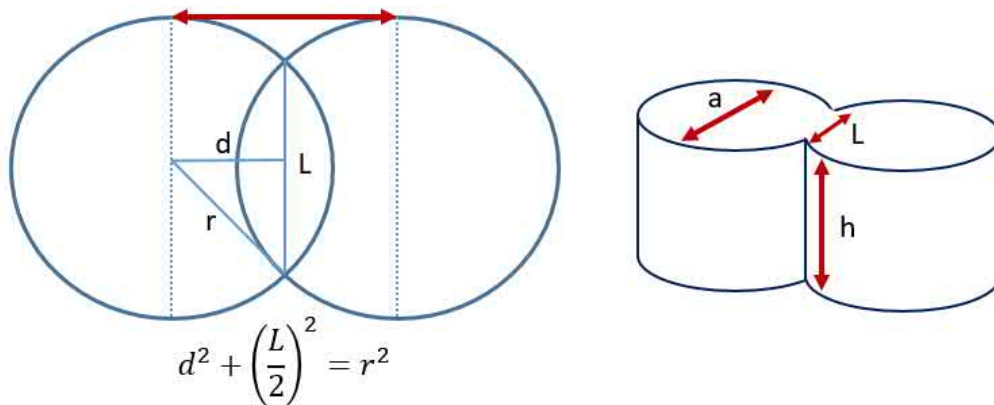


FIGURE 4.6: The iris length ( $L$ ) is a chord of the cavity and can be calculated from the expression (shown in the bottom left corner) using the cavity radius ( $r$ ) and the distance between the centres of the two cavities ( $2 \cdot d$ ). In the successive calculations the diameter of the cavity is referred to as  $a$  as shown on the right

will be a chord of the cavity circumference. This is shown in Figure 4.5 where the iris length is shown in red and will be referred to as the iris length,  $l$ . The equation to find this length is:

$$\text{ChordLength} = 2 \cdot \sqrt{r^2 - d^2} \quad (4.16)$$

The relevant dimensions and the description of the irises is shown in Figure 4.6. The irises are rectangular and are fully characterised by their height and length. The iris height is already known, this is the height of the cavity (12 mm). Thus, only the length will determine the coupling between adjacent cavities. The iris length is computed from empirical relationships between iris shape, dimensions and magnetic polarizability, these relationships are collated in the literature and the relevant graph is shown in Figure 4.7 [53]. In order to use the graph, the magnetic polarizability of the irises is required. This can be calculated by starting from the coupling

between cavities.

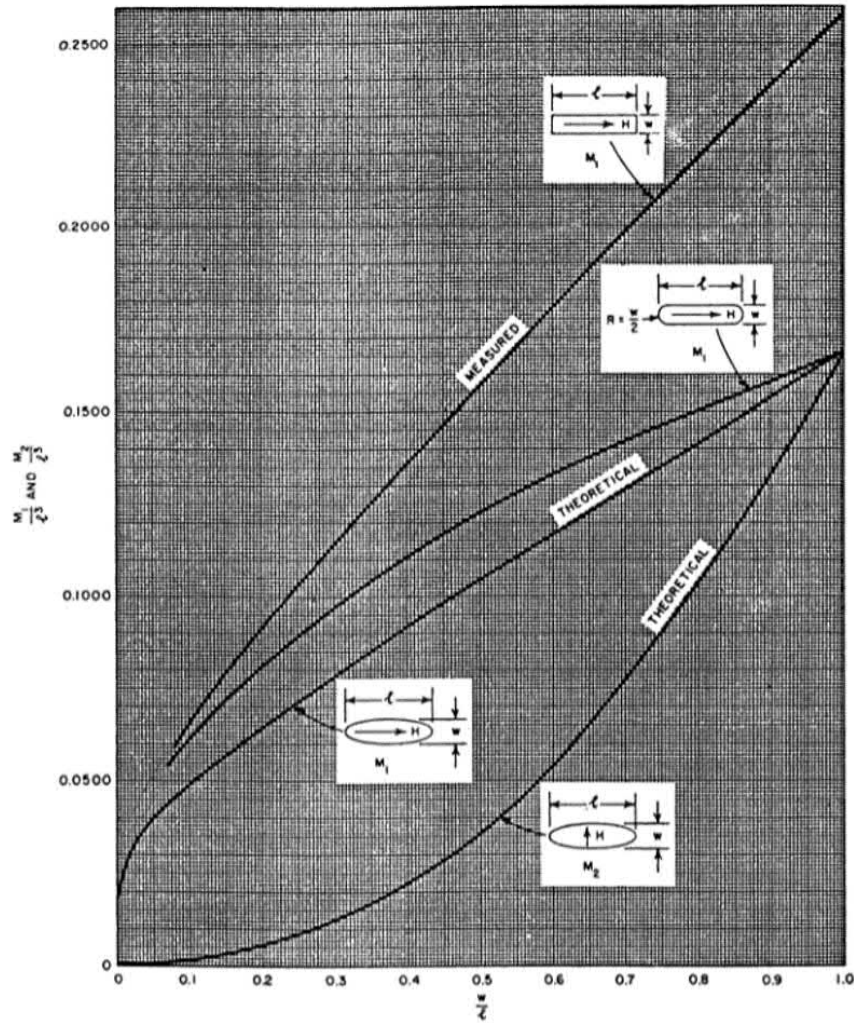


FIGURE 4.7: Empirical measurements which describe the relationships between Iris shape, Dimensions and Magnetic Polarizability [53]. These relationships are used to calculate dimensions for a given iris shape

The coupling coefficient is a dimensionless value that describes the interaction between two resonators. This concept is used widely in filter theory. Approximation formulas give the values for coupling for this filter topology [53]. The following equation can be used to approximate the coupling between cavities:

$$k_{n,n+1} \approx \frac{w}{\omega_1 \sqrt{g_n g_{n+1}}}$$

Where  $k$  is the coupling between cavity  $n$  and  $n+1$ ,  $w$  is the fractional bandwidth,

$\omega'_1$  is the low-pass cut-off frequency and  $g_1$  to  $g_n$  are the previously calculated  $g$ -values. The accuracy of the approximation increases inversely to the fractional bandwidth. The exact values of the coupling coefficients at the centre frequency depend on the specifications for the pass-band and the derivatives  $\frac{dk_{i,(i+1)}}{df_0}$ , this means that the exact values cannot be calculated [53]. The exact values can only be obtained after optimisation. The approximate values are shown in Table 4.6.

Coupling Coefficients			
k12	0.00661	k45	0.00499
k23	0.00499	k56	0.00527
k34	0.00480	k67	0.00674

TABLE 4.6: Calculated Coupling Coefficient between Adjacent Resonators, the values calculates can only ever be approximate

The magnetic polarizability of each iris is required in order to calculate the physical dimensions of the coupling irises using the coupling coefficients. When an iris is present in a transmission line the electric and magnetic fields become distorted. The distortion of the magnetic field arises from two magnetic dipole moments induced in the iris by an exciting tangential magnetic field. The magnetic dipole moment is the strength and orientation of an object producing a magnetic field. The strength of the magnetic dipole moment is proportional to the product of the magnetic polarizability of the iris and the magnitude of the exciting tangential field. The magnetic dipole moment in the iris will radiate power into the mode in the second transmission line, when the magnetic field of the mode being excited has a component parallel to the magnetic dipole moment. This also holds true for the electric dipole moment.

When two resonant cavities are coupled via a small iris they will have two natural resonant frequencies, these will be  $\omega_r$  and  $\omega_r - \Delta\omega$ . When the tangential magnetic fields are pointing in the same direction on either side of the iris, the cavities will oscillate at frequency  $\omega_r$ . This is the same as the resonant frequency of the cavities without the iris. When the tangential magnetic fields are pointing in opposite directions on either side of the window, the natural resonant frequency is  $\omega_r - \Delta\omega$ . Provided the perturbation ( $\Delta\omega$ ) is small relative to the centre frequency, then the coupling coefficient is defined by substituting the equation for stored energy inside the cavity into this, which produces the coupling between cavities in terms of their dimensions. From [53], the coupling factor in terms of the physical cavity dimensions is:

$$k = \frac{M\lambda_g^2 s^2}{l_1^3 a^2}$$

Where:

- $M$  is the magnetic polarizability ( $mm^3$ )
- $\lambda_g$  is the guide wavelength, this was calculated in section 4.4.1 (mm)
- $s$  is the number of field variations in the diameter of the cavity, in this case  $s = 1$
- $l$  is the iris length (mm)
- $a$  is the cavity diameter (mm)

The magnetic polarizability of the irises will be calculated from the coupling between cavities. The coupling between cavities is rearranged to find the following expression [53]:

$$M = \frac{kl_1^3 a^2}{\lambda^2}$$

The relationship for a rectangular iris from Figure 4.7 has been repeated in Figure 4.8 for clarity. For a rectangular iris,  $W$  is the height of the cavity which has been set at 9.5 mm. This will be constant for all the cavities. For a rectangular iris the plot is approximately linear when the width to height ratio is between 0.09 and 0.2575. The ratio of height to width of the iris must be selected, in this case 0.5 was chosen as it lies comfortably within the linear region for rectangular irises and is suitable for circular cavities. The linear region can be approximated as an expression which is shown in Equation 4.4.2. This expression was solved for  $l$ , iris width, and the results are shown in Table 4.7.

$$\frac{w}{l_{n,n+1}} = 4.57 \cdot \frac{M_{n,n+1}}{l_{n,n+1}^3} - 0.2454 \quad (4.17)$$

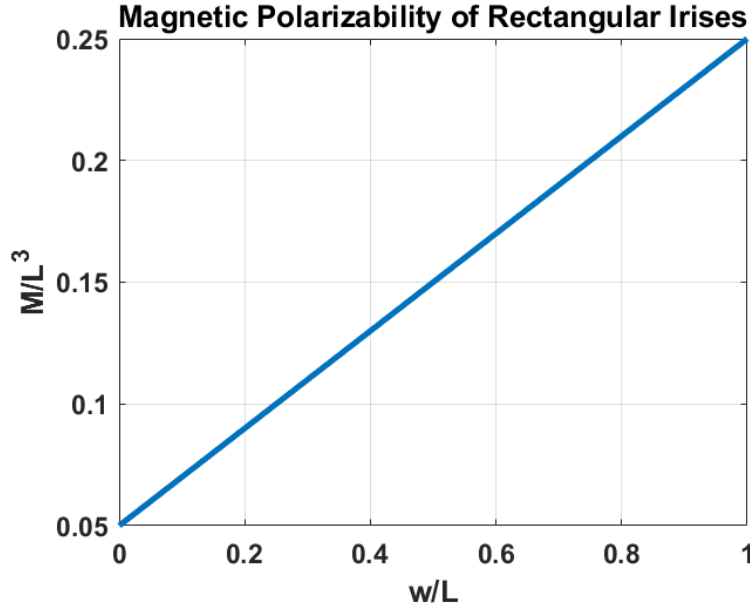


FIGURE 4.8: The Empirical Relationship between Iris Dimensions and Magnetic Polarizability for a Rectangular Iris which was shown in Figure [53] has been converted to a linear equation for the region where  $w/L$  is between 0 and 1.

#### 4.4.3 Adjusting Resonant Frequencies due to Irises

The addition of the irises will reduce the resonant frequency of the cavities; hence, their dimensions should be adjusted to account for this. This accounts for a small adjustment to the diameter of the cavity. Although each cavity will have its own resonant frequency, and therefore optimum radius, in the final design all of the cavities will have a diameter of 12 mm for simplicity of manufacture.

The lengths of the irises determined above are approximate, and their accuracy is improved by computing compensated magnetic polarizabilities of the irises and then recalculating the lengths of the irises.

$$(M_{n,n+1})_{Comp} = M_{n,n+1} \left[ 1 - \left( \frac{2 \cdot l_{n,n+1}}{\lambda_c} \right)^2 \right] \quad (4.18)$$

Final values for the lengths of the irises are calculated using Equation 4.4.2 with the compensated values for the magnetic polarizability. The original and adjusted iris lengths are shown in Table 4.7. There should also be a small adjustment in the cavity radii due to the irises. However, these adjustments are in the range of 0.25 mm, which is close to the manufacturing tolerances. Consequently, in the final design all cavities will be 9.5 mm radius for simplicity.

Cavities	Coupling Coefficients	M ( $l^3$ )	Iris Length (mm)	
			Original	Adjusted
12	0.00661	123.857	6.643	5.286
23	0.00499	301.714	10.110	8.140
34	0.00480	311.150	10.256	8.261
45	0.00499	310.483	10.823	8.140
56	0.00527	301.714	10.110	8.140
67	0.00674	123.857	6.643	5.286

TABLE 4.7: Coupling between Cavities, the resulting Magnetic Polarizability of Irises and Iris Length before and after adjustment



FIGURE 4.9: SMA Probe which will be used to couple into the Input and Output Cavities. The radius and length of the coax probe is fixed

#### 4.4.4 Final Design Dimensions

An SMA probe (shown in Figure 4.9) will be used to air-couple into the end resonators near to their base, at the short-circuited end of the resonator. The probe radius and diameter are the dimensions of the SMA connector, which will be used to couple to the external cavities and hence these dimensions are fixed. Probe height is the distance from the bottom of the cavity. This can be optimised during simulation to improve external coupling but must be at least 2.05 mm from the bottom of the cavity due to the external dimensions of the SMA connector.

The design dimensions are summarised in Table 4.8, these are initial parameters and will be optimised during simulation. Using the adjusted iris lengths from Table 4.7 the overlap required to achieve this cavity length is calculated using the method described in Section 4.4.2.

Dimension (mm)		Cavities	Overlap between adjacent cavities (mm)
Cavity Height	12.00	12	0.613
Cavity Diameter	9.50	23	1.591
Resonator Height	6.35	34	1.648
Resonator Diameter	3.38	45	1.632
Probe Outer Radius	2.05	56	1.591
Probe Conductor Radius	0.65	67	0.613

TABLE 4.8: Final Calculated Design Dimensions for the Seven Cavity filter with SMA connections

## 4.5 Simulations in CST

The calculated dimensions were used to build the cavity structure in CST where the design can be verified and dimensions optimised. As the filter is symmetric about the central cavity, the cavities will be modelled and optimised in pairs. The filter can be tuned to the centre frequency and the scattering parameters improved by optimisation. The features which will be used for optimisation are the distances between adjacent cavity centres, the heights of the central resonators and the height of the SMA coupling into the end cavities.

The mesh is a tetrahedral mesh with 4,641 cells. Symmetry planes are used along the centre (the long edge). Cells per wavelength in the structure are 8 in the filter and 2 in the background.

### 4.5.1 Initial Optimisation

Initially the filter can be modelled as just two cavities and the probe couplings, as shown in Figure 4.11. The background is modelled as a perfect electrical conductor and the filling material is air. At the upper side-band frequency, 12.182 GHz, the magnitude is  $-35.881$  dB for two cavities where the background material is a perfect electrical conductor. It was found that 4mm was the optimal height for the central resonator.

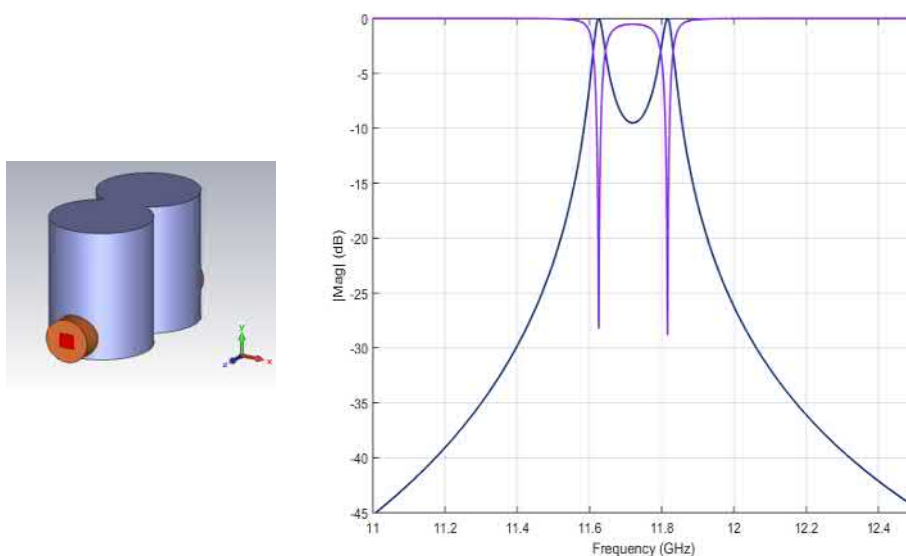


FIGURE 4.10: CST Model of Two Cavity Filter (Left) and Scattering Parameters of Two Cavity Iris Coupled Filter (Right). The resonant frequencies of the two cavities can be seen clearly from the S21

The optimisation was repeated for three and five cavities. The CST model of the three cavity filter is shown in Figure 4.11 and the five cavity filter in Figure 4.12. At 12.182 GHz the magnitude is  $-42.972$  dB for three cavities where the background material is perfect electrical conductor. The reflection at the centre frequency is  $-8.19$  dB.

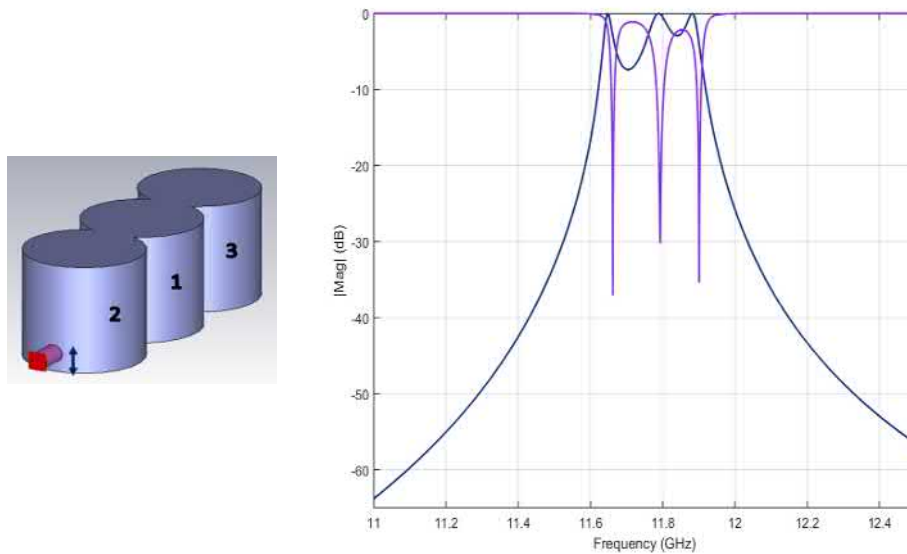


FIGURE 4.11: CST Model of Three Cavity Filter (Left) and Scattering Parameters of Three Cavity Iris Coupled Filter (Right)

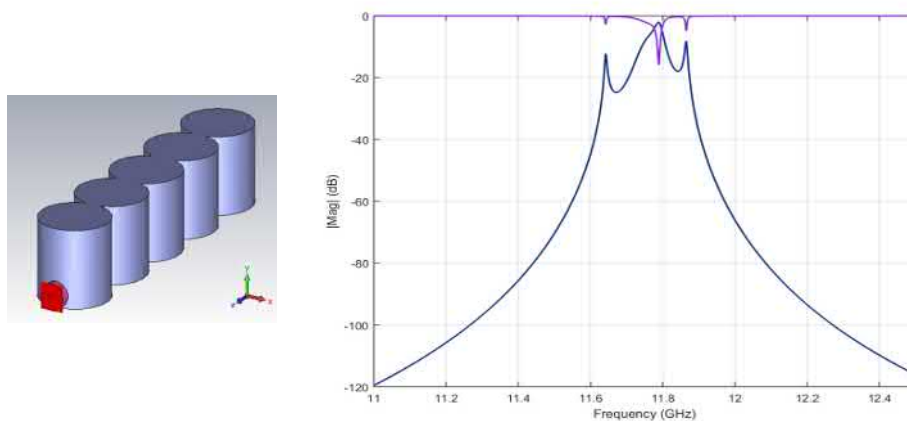


FIGURE 4.12: CST Model of Five Cavity Filter (Left) and Scattering Parameters of Five Cavity Iris Coupled Filter (Right). The resonant frequencies of the individual cavities are no longer clearly defined but the rejection outside the pass band is significantly improved

Finally, the full seven cavity model is shown in Figure 4.13. At 12.182 GHz the magnitude is  $-95.682$  dB for seven cavities where the background material is a perfect electrical conductor. The transmission at the centre frequency is  $-11.2$  dB. A

seven cavity design satisfies the specification for rejection in the stop-band, with excellent transmission and minimal reflection in the pass-band. As more cavities are added into the simulation the rejection in the stop-band increases.

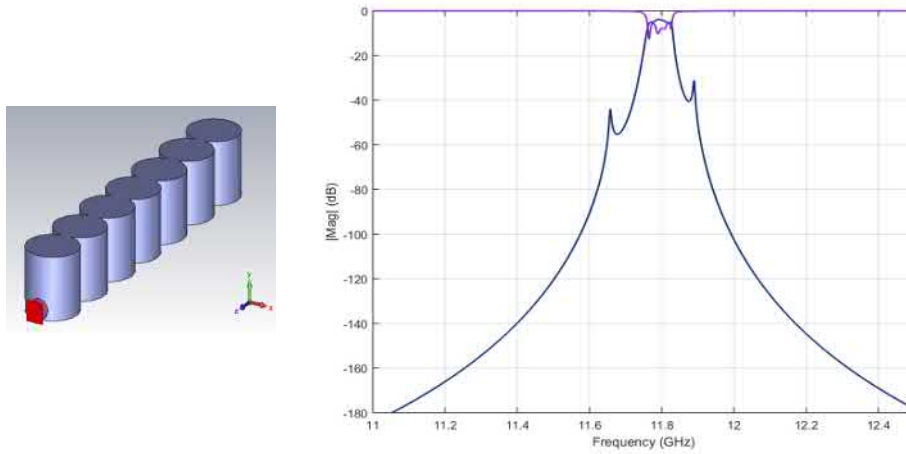


FIGURE 4.13: CST Model of Seven Cavity Filter (Left) and Scattering Parameters of Seven Cavity Iris Coupled Filter (Right). The rejection outside the pass-band far surpasses the specification

### 4.5.2 Manufacturing Material

Two materials were considered, copper and aluminium. Copper exhibits the best electrical properties due to its high electrical conductivity. Pure copper is very soft and therefore difficult to machine; hence, a suitable alloy was found that balanced machinability, cost and electrical conductivity. These alloys are known as 'free machining copper.' Two of the most common are C109, Copper Tellurium alloy, and C111, Copper Sulphur alloy. C109 was chosen due to its availability with a local supplier. The electrical conductivity of C109 copper alloy is 5.35 MS/m.

Manufacturing in aluminium will reduce the material cost. Aluminium has lower electrical conductivity which will result in more power losses in the filter. However, this could be beneficial as the additional attenuation will reduce the reflected power rejected by the filter, thereby reducing the standing wave ratio. The aluminium alloy AL6082 was selected due to its high machinability and electrical conductivity of 2.63 MS/m. As shown in Figure 4.14, there is only a reduction in transmission for aluminium with respect to copper. Thus the filter will be manufactured in AL6082.

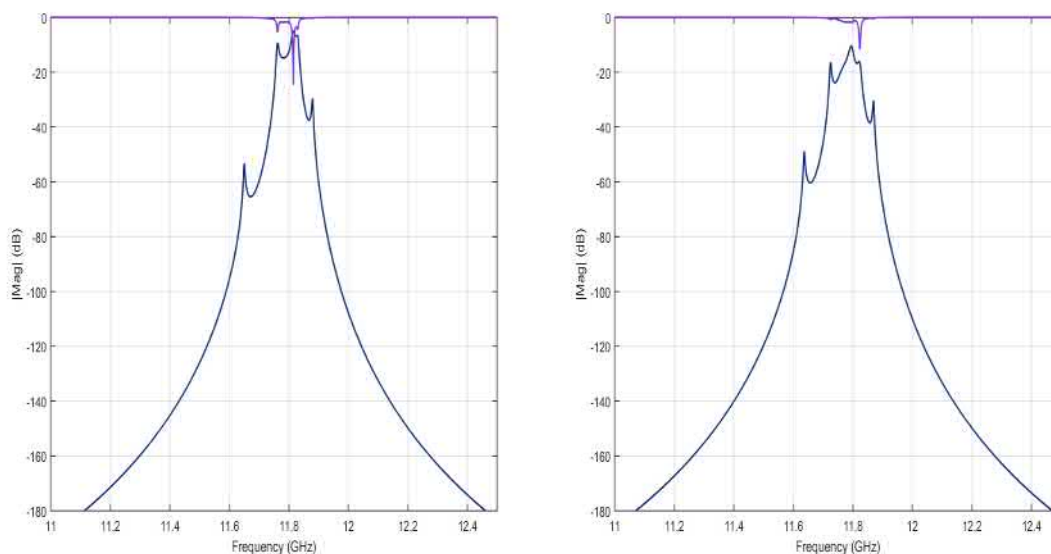


FIGURE 4.14: Comparison of S<sub>21</sub> for the Seven Cavity Filter when the background material is changed from PEC to Cooper C109 (left) and Aluminium AL6082 (right)

### 4.5.3 Manufacturing Tolerances, Bend Radii and Mechanical Design

The dimensions must be adjusted for manufacturing tolerances. The most precise tolerance of 20 $\mu$ m will be slow and expensive to machine and hence it was only

Parameter	Final Value (dB)
Transmission at 11.806GHz	-10.67
Reflection at 11.806GHz	-20.02
Transmission at 11.9942GHz	-98.82
Transmission at 12.189GHz	-128.47

TABLE 4.9: Simulated Performance of Seven Cavity Filter Manufactured in AL6082 with Tolerances

used for the most sensitive dimensions, the resonator heights and distance between cavity centres. Additionally, a radii of 0.5 mm was added to all internal corners.

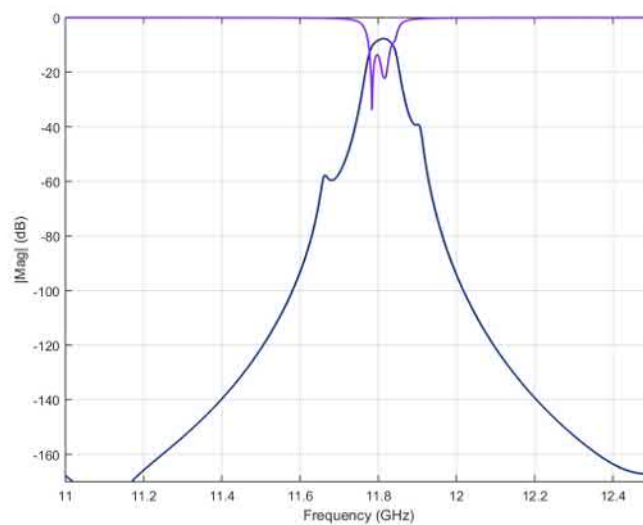


FIGURE 4.15: Final Results from CST Frequency Domain Simulations. The Seven Cavity Filter will be Manufactured in AL6082 and the simulated results include all Tolerances and Radii on internal corners

The filter was simulated again to account for tolerances. The optimised result is shown in Figure 4.15 and the final dimensions are in Table 4.10. The final mechanical design is shown in Figure 4.16, the design also includes a lid piece the ability to add a tuning screw into each cavity.

Parameter	Final Value (mm)	Parameter	Final Value (mm)
Outer Cavity Diameter	12.00	Resonator 1 Height	4.46
Cavity Height	9.50	Resonator 2 and 3 Height	4.59
Probe Radius	0.65	Resonator 4 and 5 Height	4.49
Probe Length	2.00	Resonator 6 and 7 Height	4.49
Probe Height	2.05	Overlap 12 and 67	1.60
Coax Substrate Radius	2.05	Overlap 23 and 56	1.26
Resonator Diameter	1.00	Overlap 45 and 34	0.93

TABLE 4.10: Final Dimensions of Seven Cavity Filter Manufactured in AL6082 with Tolerances

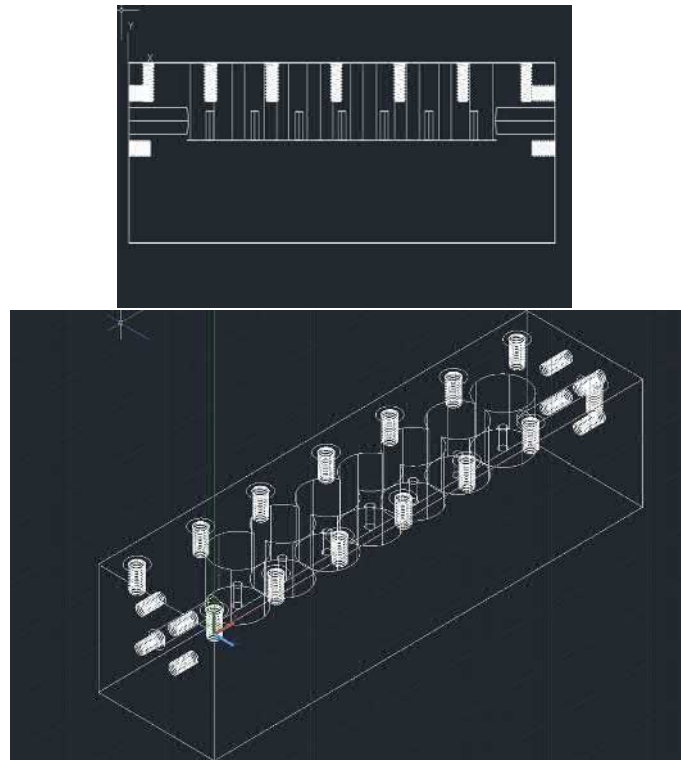


FIGURE 4.16: 3D Model of Seven Cavity Band Pass Filter without the lid. The internal structure of the cavities with central resonators is shown as well as tapped holes for attaching the lid and SMA connectors

#### 4.5.4 Tuning Pins

In mathematics and electronics, Cavity perturbation theory describes methods for derivation of perturbation formulae for performance changes of a cavity resonator. These performance changes are assumed to be caused by either introduction of a small foreign object into the cavity, or a small deformation of its boundary.

Inserting a metallic structure into the cavities will perturb the electromagnetic field, thereby changing the resonant mode inside the cavity and altering the parameters of the filter. As the capacitance is distributed in the cavity and determined by the dimensions, inserting tuning screws is equivalent to changing the capacitance of the cavity.

Tuning pins are used to alter the behaviour of a resonant cavity after manufacturing. Tuning of the filter is required in order to compensate for non-ideal factors that will cause the manufactured cavity to deviate from the ideal CST model. Such parameters can include surface roughness, material imperfections, manufacturing imperfections and imperfect contact between surfaces, for example between the lid and base or the input and output connectors.

The tuning pins will be standard sized screws as these are easily accessible and therefore reduce the cost and complexity of the filter. Three different widths of tuning screw were simulated in order to see which would be most effective. Each simulated cavity was probed individually with a 3 mm radius self-tapping screw. The maximum possible insertion depth is 5 mm as this would touch the top of the central resonator.

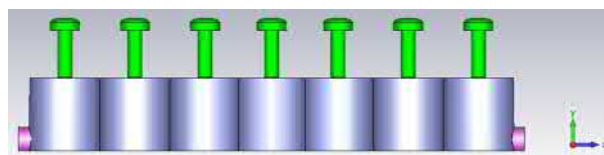


FIGURE 4.17: CST Simulation of Filter with Tuning Screws, a single pin is entered into the centre of each cavity, it would also be possible to add tuning pins into the irises to alter the coupling between cavities but the space is limited and the tuning would become overly complicated

The filter will be tuned in order to optimise several parameters of significance, the most important being the transmission coefficient in the pass-band and the rejection in the stop-band.

The transmission co-efficient at the unwanted frequencies should be very low to indicate that the power at these frequencies is being significantly reduced. In the

original filter design the goal for suppression at 11.9942 GHz and 12.182 GHz was  $-40$  dB. The final CST design showed attenuation of  $-98$  dB and  $-128$  dB respectively, this already surpasses the design specification without additional tuning.

In a perfect filter the transmission coefficient at the centre frequency will be close to 0 dB, this indicates almost no additional power is lost in the filter other than resistive losses. Realistically, it is normal for filters to have around  $-3$  dB to  $-5$  dB of loss. The insertion loss in the pass-band from the CST simulation is  $-10.67$  dB.

The stability of the transmission in the pass-band is the most important parameter as the output of the filter is amplified and used during the RF down-conversion. If the output power of the filter varies, from fluctuations in the pass-band transmission, then these power level changes will be directly converted down to the intermediate frequency. These power changes will then be falsely interpreted as originating from the RF signals.

For seven tuning pins simulated with several possible positions, the number of permutations becomes unfeasible to optimise in a timely manner. In addition, s-parameters do not respond linearly when inserting individual tuning screws. For these reasons, a full simulation of the tuning would not be possible without a complex and time-consuming optimisation. Therefore, a simulation of the full tuning with seven pins will not be covered in this work. It will be deemed sufficient to determine if the size and number of tuning pins are able to perturb the fields significantly enough to provide an adequate tuning range.

The filter will be tuned in order to optimise several parameters which must all be balanced; this creates a goal function. In CST, a probe will be placed at 11.806 GHz, 11.9942 GHz, and 12.182 GHz on both the S11 and S12. A 3rd order polynomial was fitted using a 'least squares' approximation to the extracted s-parameters from CST. This simulation was used to identify the individual effects of tuning each cavity.

A goal function optimisation is used to find solutions that satisfy the design requirements. This method finds the minimum of a problem specified by a set of goal functions, a weighting for each goal and any bounds or relationships between the goal functions [102]. The lower and upper bounds are 0 mm and 4 mm and the initial value for each tuning pin position is 0. The full optimisation goals are shown in Table 4.11.

Min S11(x)	< -30dB
Frequency Min S11(x)	11.806GHz
Max S21(x)	> -10dB
Frequency Max S21(x)	11.806GHz
S21 @ 11.9942GHz	> -90dB
S21 @ 12.182GHz	> -100dB

TABLE 4.11: Tuning Optimisation Goals for the filter, these will be monitored by observing the S11 and S21 while the tuning pin positions is changed

The insertion depth of the tuning screw was simulated between 0 mm and 4 mm using 8 iterations. In practice the tuning screw will be tuned manually by turning a screw; thus it is not unreasonable to assume that the screws can be adjusted to much less than 0.5 mm by hand without devising a mechanical solution. From the s-parameters the tuning parameters were extracted with respect to insertion depth; namely the frequency when the S11 is minimised, the frequency when the transmission is maximised and the rejection at 11.9942 GHz and 12.182 GHz. The optimisation procedure is carried out for each cavity in turn. The single cavity tuning results are summarised in Table 4.12:

All of the parameters cannot be tuned to their ideal values with single cavity tuning. Although some of the parameters can be satisfied, they cannot all be satisfied simultaneously to within an acceptable tolerance. However, the single cell tuning does validate the effectiveness of the tuning pins.

The results show that most of the optimal tuning positions are in the region of 1 mm, these would be the starting positions for further optimization. The rejection in the pass-band always meets the set goals so this information will not be considered in further optimisation. In addition, the insertion loss in the pass-band is always improved with respect to the original simulated results. As these are considered the two most important parameters, the tuning pins can be considered acceptable. The

Parameter	Cavity						
	1	2	3	4	5	6	7
x	1.742	2.034	1.468	3.1749	1.729	0.9156	1.00
S11 Minimum	-21.465	-17.09	-15.95	-32.49	-15.50	-30.01	-17.58
S21 Maximum	-11.93	-9.18	-12.04	-10.35	-8.24	-9.03	-13.59
S21 at 11.9942GHz	-123.66	-120.19	-103.57	-115.66	-107.39	-102.48	-120.36
S21 at 12.1824GHz	-141.16	-121.19	-133.59	-128.96	-131.69	-129.36	-132.35
All Goals Achieved?	No						

TABLE 4.12: Tuning Results from Individual Cavity Tuning

process was repeated with two cavities being tuned simultaneously. The full results for each screw combination are included in Appendix A. The best combination is when pin 7 is at 1.40 mm and pin 4 is at 2.30 mm and the s-parameters are shown in Figure 4.13.

S11 Minimum (dB)	S11 Minimum Frequency (GHz)	S21 Maximum (dB)	S21 Minimum Frequency (GHz)
-31.23	11.834	-9.86	11.797

TABLE 4.13: Tuning Results from Two Cavity Tuning

With two tuning pins the design specifications can be met with an acceptable error whilst at the design frequencies.

Beyond this point the tuning will not be simulated as the number of combinations begins to become unfeasible, and it has been shown that the tuning screws can achieve the desired tuning ability. The screws can perturb the cavity field sufficiently to induce significant changes in the resonant mode. Furthermore, the tuning becomes increasingly effective when two screws are tuned instead of one. It can be extrapolated that tuning even more cavities simultaneously, up to seven, will be able to yield ideal tuning.

## 4.6 Manufacture and Test

Three prototypes of the filter design were manufactured by CNC Proto using CNC milling with a surface finish of 0.1 mm tolerance [103]. One of the manufactured filters is shown in Figure 4.18.

Figures 4.19 and 4.20 show the S-parameters of two of the filters after assembly and tuning. The s-parameters were measured on an X-band VNA with a range of 4 GHz to 20 GHz. The measurements were taken with 10,001 points, 600 MHz range and a bandwidth of 500 Hz. The filter response varies slightly between the two. Prior to assembly, the second filter was cleaned using ultrasonic cleaning, however this did not improve the filter response with respect to the first filter. The final s-parameters for both filters are collated in Table 4.14.



FIGURE 4.18: Interior and Lid of one of the Manufactured Cavity Filters, the SMA connector can be seen on the left.

Parameter	Filter 1		Filter 2	
	Initial Value (dB)	After Tuning (dB)	Initial Value (dB)	After Tuning (dB)
S11 at 11.806GHz	-2.54	-39.54	-0.79	-37.30
S21 at 11.806GHz	-12.21	-8.66	-13.79	-8.59
Transmission at 11.9942GHz	-43.02	-69.40	-12.18	-69.55
Total Rejection at 11.9942GHz	-30.81	-60.74	-1.61	-60.36
Transmission at 12.1894GHz	-56.37	-78.19	-52.32	-78.53
Total Rejection at 12.1894GHz	-44.16	-69.53	-54.63	-69.87

TABLE 4.14: Final S-Parameters of Two Manufactured Filters Before and After Tuning

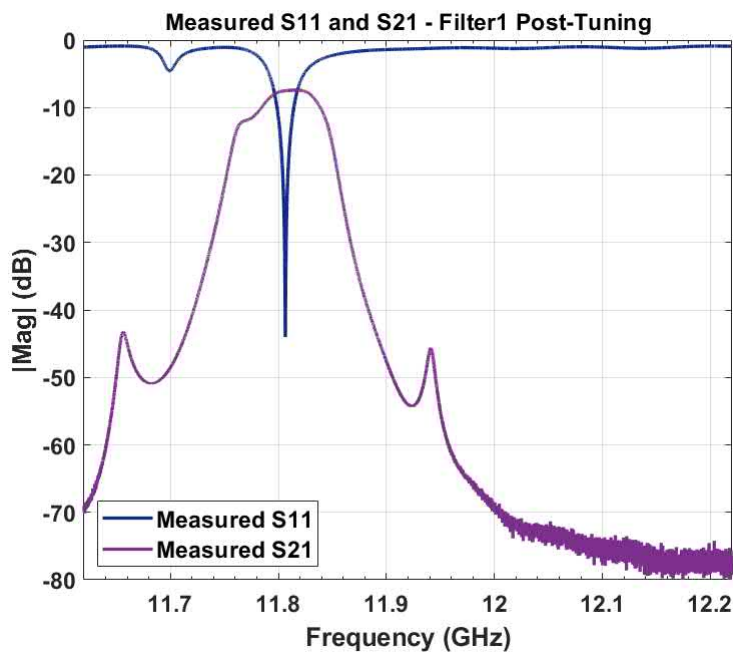


FIGURE 4.19: Measured transmission (S21) and reflection (S11) of the 1st filter after tuning

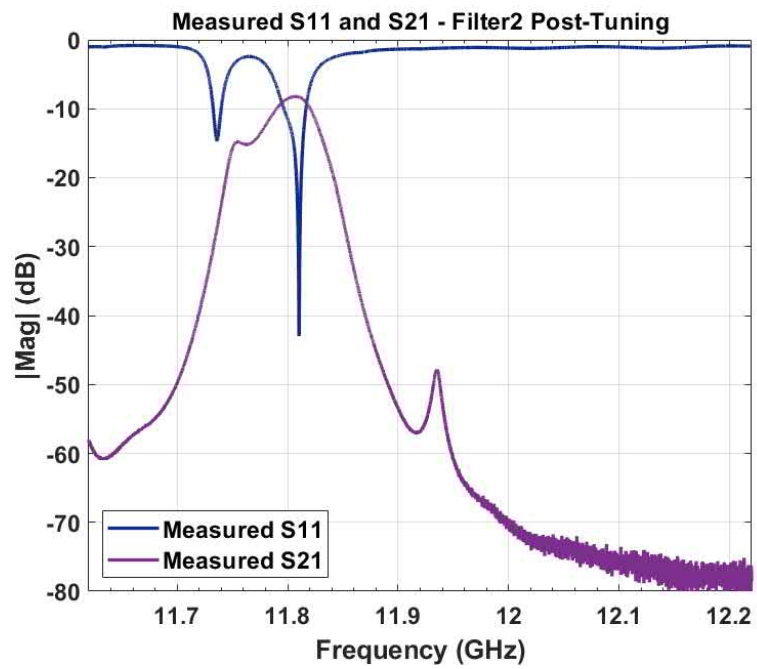


FIGURE 4.20: S11 and S21 of the 2nd Filter after Tuning

Both filters are very close to the design specification for rejection at 11.9942 GHz; the specification was  $-70$  dB and the final results are  $-69.40$  dB and  $-69.55$  dB. The transmission in the pass-band for both filters are  $-8.66$  dB and  $-8.59$  dB, which is lower than for an ideal filter but is comparable to the simulation which suggested  $-10$  dB.

#### 4.6.1 Thermal Dependence

Figure 4.21 shows the variation in the pass-band behaviour as the temperature is varied. It is likely that the temperature of the filter will vary seasonally or when the system is switched 'on' due to a 'heating-up' period. The reflection at 11.806 GHz varies  $0.0103$  dB per $^{\circ}$  C and the transmission varies by  $0.0161$  dB per $^{\circ}$  C. The LLRF crate is well contained and hence the internal temperature is likely to change by no more than  $10^{\circ}$  during operation. As such, the total transmission and reflection will change by less than  $0.2$  dB due to temperature, and this fluctuation can be compensated by the amplifier which follows the filter.

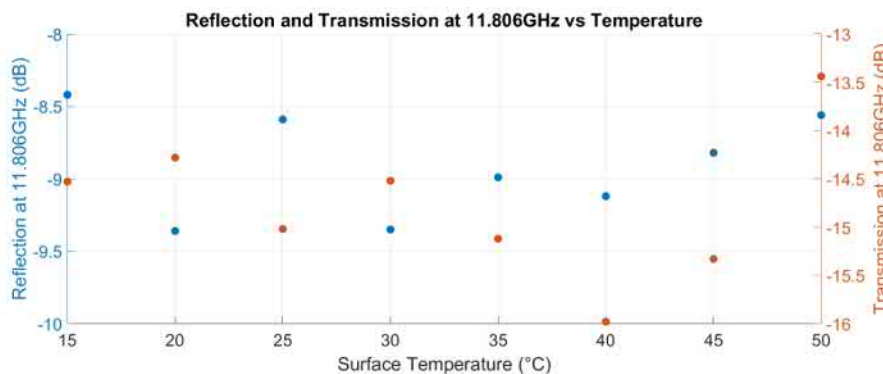


FIGURE 4.21: Variation of the reflection and transmission at 11.806 GHz with temperature measured with an RTD probe placed onto the cavity surface and external air heating

## 4.7 Conclusion

The up-converter mixes two frequencies at 11.9942 GHz and 187.4 MHz which will produce first sidebands at 11.806 GHz, 12.182 GHz. Additional suppression of unwanted sidebands can be achieved using filtering hence a custom filter was designed.

The most important properties of the filter will be  $-70$  dB of rejection at 12.182 GHz and sharp transition between pass-band and stop-band. The filter design is dictated

by the fractional bandwidth, which in this case is 0.85%. This parameter determines the physical realization of the filter. An lumped circuit model is developed which demonstrates the desired behaviour of the band-pass filter. Simulation in Microwave Office verified the behaviour of the band-pass prototype.

The simulated results show a large insertion loss in the pass-band. This is due to the low Q-factor of the filter. The lumped circuit model was transformed into the physical dimensions of the cavities. The calculated dimensions were used to construct the cavity structure in CST where the design was verified and dimensions optimised.

The filter will be tuned into order to optimize several parameters of significance, the most important being the transmission coefficient in the pass-band and the rejection in the stop-band. The results of simulating the tuning pins validated the effectiveness of tuning pins.

Three prototypes of the filter design were manufactured by CNC Proto using CNC milling, two filters were constructed and the performance of both filters was improved by tuning.

The s-parameters of both filters meet the design specification for rejection at 11.9942 GHz, the specification was  $-70$  dB and the final results is  $-69.19$  dB. The transmission in the pass-band is lower than for an ideal filter but is comparable to the simulation which suggested  $-10$  dB. The conversion loss is not significant as the power can be easily recovered this with an amplifier.

## Chapter 5

# High Power X-Band Measurements at Xbox1

### 5.1 Introduction

Firstly, this chapter will describe the network at Xbox1 in detail, covering the high power, low power, and PXI control systems. This is the system into which the new LLRF from Chapter 3 has been integrated. The system at Xbox1 will be used to quantify whether a reduction in the phase noise of the local oscillator translates to improved RF measurements.

Secondly, this work will aim to characterise the phase and amplitude stability of the klystron output. This will be measured initially under one set of conditions (10 MW, 150 ns, 80% of full RF power for a Modulator Voltage setting of 330 kV). However, this measurement is not a complete characterisation of the klystron. The full system at Xbox1 will be expected to operate under a variety of conditions, which will be dictated by either the needs of a conditioning algorithm or by the requirements from the CLEAR LINAC. Hence, a sensitivity analysis of the klystron is undertaken to broadly examine the effects of changing various input parameters on the phase stability of the klystron. The parameters of interest are pulse length, RF power level and modulator voltage properties.

### 5.2 Xbox1

The primary objective of the X-band test stands is to support the development of high-gradient, accelerating structures and high-power RF components for the CLIC project. Recent studies have explored the possibility of a klystron-based initial energy version of CLIC for which the test stands are an important research tool. Before Xbox1 was commissioned. The only availability of 12 GHz power (at the pulse

lengths and required power level) was CTF3 at CERN. CTF3 has now become the CLEAR experiment which was described in Chapter 2. After a significant upgrade, Xbox1 now has a similar blueprint to the other two X-band test stands, Xbox2 and Xbox3. However, some of the specific features remain the same as they are related to the beam facility and the initial design requirements. The Xbox1 system post-commissioning is described in [36] and the new system after upgrade is described here. The main changes are related to the LLRF and control systems.

### 5.2.1 High Power Network

The Xbox1 klystron is an XL5 designed by SLAC. It is able to produce 50 MW of 12 GHz pulsed power with a pulse width and repetition rate of 1.5  $\mu$ s and 50 Hz respectively. A ScandiNova solid state modulator is used as the power source. The klystron is followed by a 'SLED-I' type RF pulse compressor, designed and built by IAP and GYCOM [104]. The pulse compressor was not used in the following experiments, therefore the operation will not be described in detail, (a detailed description of the pulse compressor operation is contained in [36]). The pre-amplifier for the klystron is an X-band 1 kW TWT from Power Amplifiers. The TWT provides an additional 30 dB of gain after the LLRF system.

Copper WR90 waveguide under high vacuum is used to extract the RF power from the klystron and transport it from the klystron gallery down into the CTF2 bunker, after which the WR90 is converted to circular over-moded waveguide. Mode converters transform the fundamental TE<sub>10</sub> mode in the WR90 waveguide into the low-loss TE<sub>01</sub> mode. The over-moded waveguide section runs between CTF2 and the test station in the CLEAR beam-line in CTF3, approximately 30 m. The test station contains two CLIC structures in series. The waveguide from Xbox1 is currently terminated with two high power loads next to the CLEAR beam-line; there is no connection to an accelerating structure.

High power directional couplers (each with 50 dB of attenuation) followed by low power directional couplers (between 20 dB and 40 dB attenuation) are used to send RF signals to the LLRF system for acquisition and control. There are seven high-power X-band signals which transfer RF power back to the LLRF crate at Xbox1 using semi-rigid coaxial cables. A functional diagram of the high power network is shown in Figure 5.1.

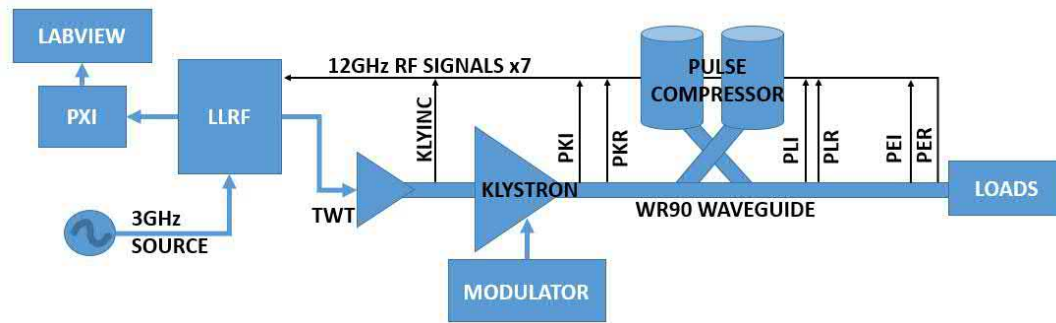


FIGURE 5.1: Xbox1 functional diagram of the high power network. The position of seven high power RF signals are shown. The low power section has been simplified and ancillary systems are not included

## 5.2.2 Klystron

The current klystron arrived at CERN in 2020 from CPI after a repair and installed at Xbox1 in the same year. The conditioning commenced in early 2021 and the klystron successfully reaching 46 MW for a 50 ns RF pulse. As mentioned in the previous section, the klystrons used at CERN are derived from an R&D effort to produce power sources for the klystron based, Next Linear Collider project (NLC). The most reliable klystron to emerge from that effort was the XL-4, which has been re-scaled in frequency from 11.4 GHz to 12 GHz by SLAC and re-named the XL-5 [105]. The commercialised version produced by CPI (the VKX-8311A) is currently in Xbox1.

Klystrons are vacuum tube amplifiers that use an electron beam to amplify RF signals. An electron beam is produced by a thermionic gun and accelerated by a high voltage DC electric field, (typically, the gun is pulsed at a large negative voltage and the body is at ground potential). The electron beam is focused by a solenoid or permanent magnet that envelops much of the device. Velocity modulations are excited in the beam as it passes through one or several RF cavities which are excited by a low-level input signal. The electrons are then passed through a drift tube, inside of which the velocity modulations transform into spatial variations as the faster electrons outpace the slower electrons [106], [107]. The resulting beam is highly bunched, with a longitudinal space charge pattern which matches that of the input signal. Higher order and correction cavities can be added to improve the efficiency of this bunching process [108]. The highly bunched beam is then passed through one or several output RF cavities where the beam induces electromagnetic fields. Typically, 30-65% of the beam power is transmitted into the RF. In this way, multiple MW's of peak power can be extracted from the beam. The power is coupled out of

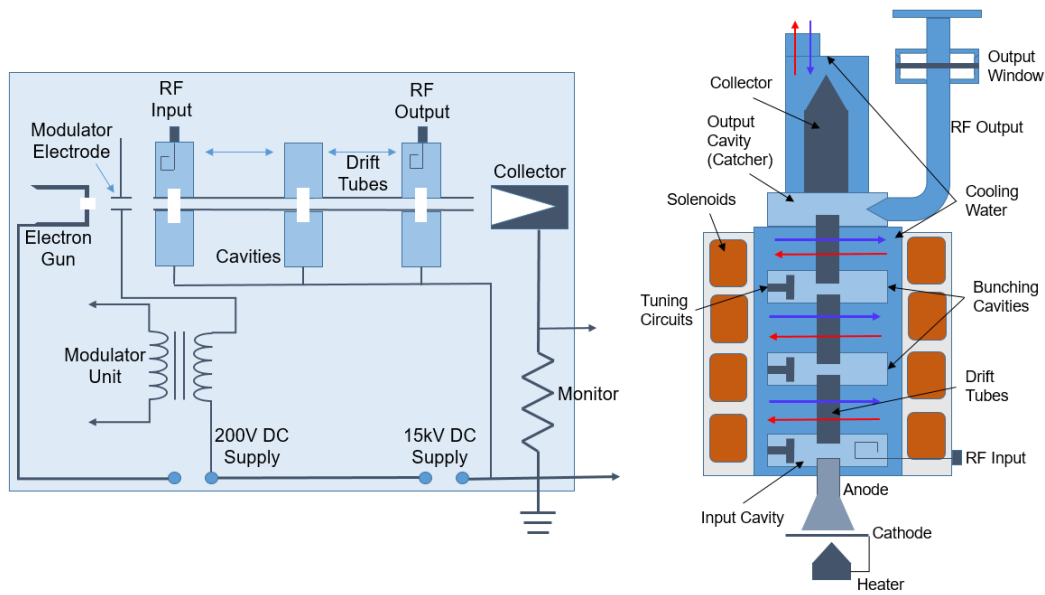


FIGURE 5.2: Two functional representations of a multiple cavity klystron. Modern klystrons usually have additional bunching cavities but only three are shown. On the left is a circuit diagram and the physical model is shown on the right

the cavities via waveguides and passed through an RF window towards the desired load. Two diagrams of a multi-cavity klystron are shown in Figure 5.2; three cavities are shown for simplicity but in reality modern klystrons are likely to have many more bunching cavities. The diagrams in Figure 5.2 are based on the VKX-8311A [104].

The pulse-to-pulse stability of the RF system is usually dominated by the stability of the klystron amplifier and the high-voltage klystron modulator [107], [109]. The phase stability of the output from a klystron depends on the stability of the RF input, plus external factors such as: modulator voltage stability, cooling water flow and temperature fluctuation, induced vibration as well as internal factors such as noise, multi-pacting, vacuum quality, erosion, and cathode deterioration [18], [110]

It can limit their working and high power handling capability, besides causing irreversible surface damage. RF breakdown in a structure can be defined as a phenomenon that suddenly and significantly changes the transmitted RF power towards a structure. During a breakdown event, the stored energy in the electromagnetic field suddenly pierces through the walls, usually in localized places, causing local melting and contamination of the surrounding surface. This results in a very fast and localized dissipation of stored energy [110]. Evaluation of used klystrons indicates that significant beam erosion from RF breakdown often occurs in the output cavity as this is a high field region [111].

Multipacting is an electron resonance effect that occurs when RF fields accelerate electrons in a vacuum causing them to impact with surfaces, which depending on the energy, release one or more electrons into the vacuum. These electrons can then be accelerated by the RF fields and impact with the same or another surface. When the impact energies, number of electrons released and timing of the impacts are such that a sustained multiplication of the number of electrons occurs, the phenomenon will grow exponentially and may lead to operational problems [33], [111].

Multipacting is a low power, electron multiplication based resonance breakdown phenomenon in vacuum and is often observed in RF structures. A multipactor discharge is undesirable, as it can create a reactive component that detunes the resonant cavities and components, generates noise and induces gas release from the conductor surfaces.

### 5.2.3 Modulator

Most high-power Klystrons need a pulsed high voltage power supply called a modulator. The modulator must deliver pulses which are typically in excess of 100 kV at current levels well above 100 A [112]. The klystron receives a high voltage modulator pulse starting a little before the RF pulse and continuing a little after the RF pulse.

The CPI VKX-8311A klystron can produce up to 50 MW of peak RF power with a perveance of 1.18  $\mu\text{P}$ . The perveance is one of the most important parameters for the characterization of klystron operation. The electrical characteristics are completely determined by the geometric structure of electron gun and the electron emission characteristics of cathode materials. When the electron gun operates in space charge limited mode, the current emission will be the function of high voltage during operation while the perveance will be the function of anode and cathode structures.

For an electron gun, the gun perveance  $P$  is determined as a coefficient of proportionality between a space-charge limited current,  $I$ , and the gun anode voltage,  $U_a$ .

The unit micro-perveance,  $\mu\text{P}$  is defined as  $\mu\text{P} = 10^6 IV^{-1.5}$ , where  $I$  and  $V$  are the klystron current and voltage respectively. However, the klystron efficiency is around 40%, which means the power source has to be able to provide a peak pulsed power of 125 MW. This power level and perveance demands a voltage of 410 kV and a current of 310 A from the modulator [36], [104].

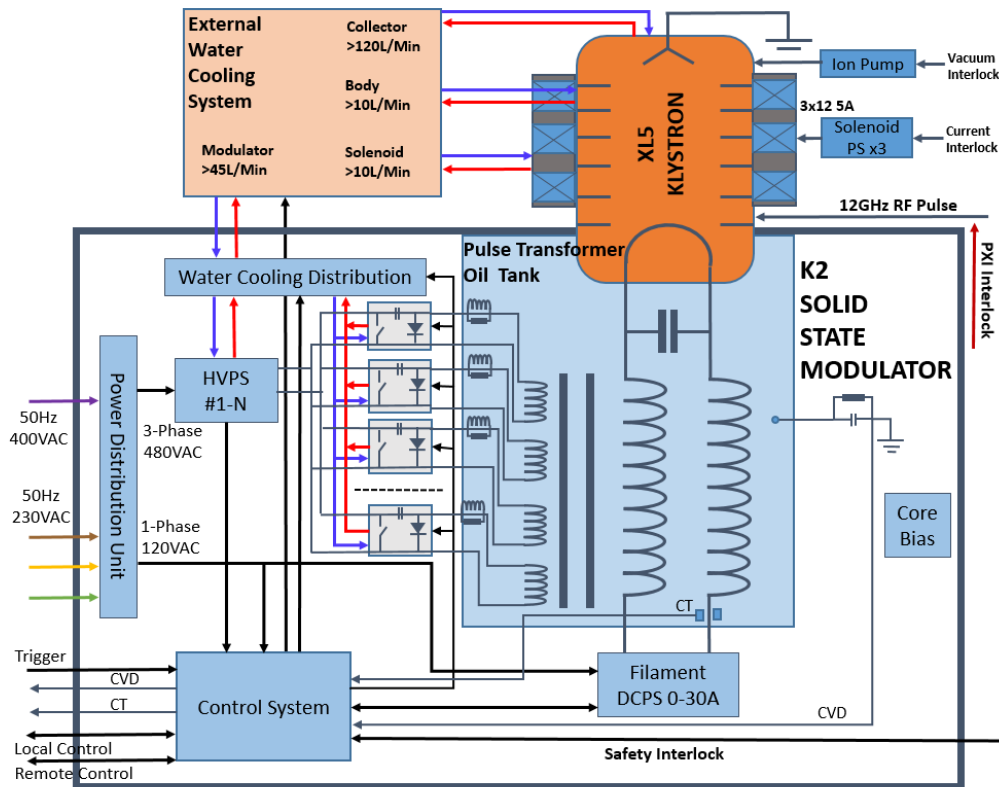


FIGURE 5.3: Xbox1 ScandiNova K-3 Modulator with the XL5 Klystron Functional Diagram, the model is extracted from the klystron datasheet [37]

At the time of construction of Xbox1, few vendors are capable of producing such a device. Furthermore, the first test stand at CERN was designed with high flexibility in mind, consequently, a solid state modulator was chosen to power the XL-5 [36]. The only company capable of manufacturing such a device was ScandiNova.

The klystron is powered by a ScandiNova solid state modulator specified to deliver pulses up to 400 kV, 300 A and 3.25  $\mu$ s high voltage pulse at 50 Hz repetition rate [36]. The stability is specified as 0.25% HV ripple and 0.1% HV repeatability. The compact design ( $3 \times 2m^2$ ) integrates the HV oil tank and klystron, as well as an integrated control and interlock system with integrated vacuum and solenoid power supplies for klystron [104]. The ScandiNova K-3 modulator is shown as a functional diagram in Figure 5.3 [104].

The charging power supplies convert the 3-phase, 415 V mains voltage into a DC voltage of up to 1400 V, which is stored in a capacitor bank. The charge stored in the capacitor bank is then switched through a bank of solid state switches; although only four are shown in Figure 5.3, there are actually 60 in the real system. The switched pulse is transferred through a tuning circuit into a pulse transformer with a transformer ratio of 1:360, thus enabling the system to step up the 1400 V to 500 kV [36].

Using this transformer ratio and the 310 A that the klystron requires, it is easy to calculate that nearly 112 kA of current needs to be switched on the timescales of microseconds. It is at this juncture that the greatest technological challenge is presented. To reduce the current load on the switches, the current is split evenly between 60 solid state switches, each conducting 1.9 kA of current [113]. The flexibility of a solid state modulator is now made apparent; the pulse length is controlled directly by the length of time that the switches remain closed [108].

Due to the high voltages involved, the pulse transformer and klystron gun are submerged in a bath of insulating oil. The oil quality is checked periodically for signs of breakdown. For instance, the oil was cleaned and filtered before installation of the repaired klystron into Xbox1 in 2020. The modulator contains a control system which can monitor the klystron's vacuum, temperature and power dissipation, and subsequently interlock the system if there are any issues [107], [108]. The water cooling is integrated into the CTF3 main water cooling system.

The high voltage should be regulated, filtered, and have some feedback on both the voltage and current. It must be protected against over-voltage and over-current conditions, and be capable of withstanding high stress during normal operation or failure. The modern method uses high frequency switching supplies. Regulation of the high voltage is important, as changes in high voltage result in changes in RF output and ultimately causes changes in the output of the LINAC [106].

The gain of the klystron is a function of the modulator voltage and RF input power. Fluctuations of the modulator voltages lead to phase variations of the amplified RF signals, and these variations can disturb the bunch compression process, leading to arrival-time and energy variations of the electron bunches [107], [108].

The maximum output of the klystron is determined by the modulator voltage set-point. The gain curve of the Xbox1 klystron were measured in 2021 and are shown in Figure 5.4.

To meet the specified RF power quality for a LINAC, the modulator voltage absolute precision and pulse-to-pulse repeatability is of critical importance. Ripple and pulse-to-pulse repeatability on the high voltage should be compensated or controlled, either from low level RF control or from the modulator control. This will require high voltage precision measurement [106], [109].

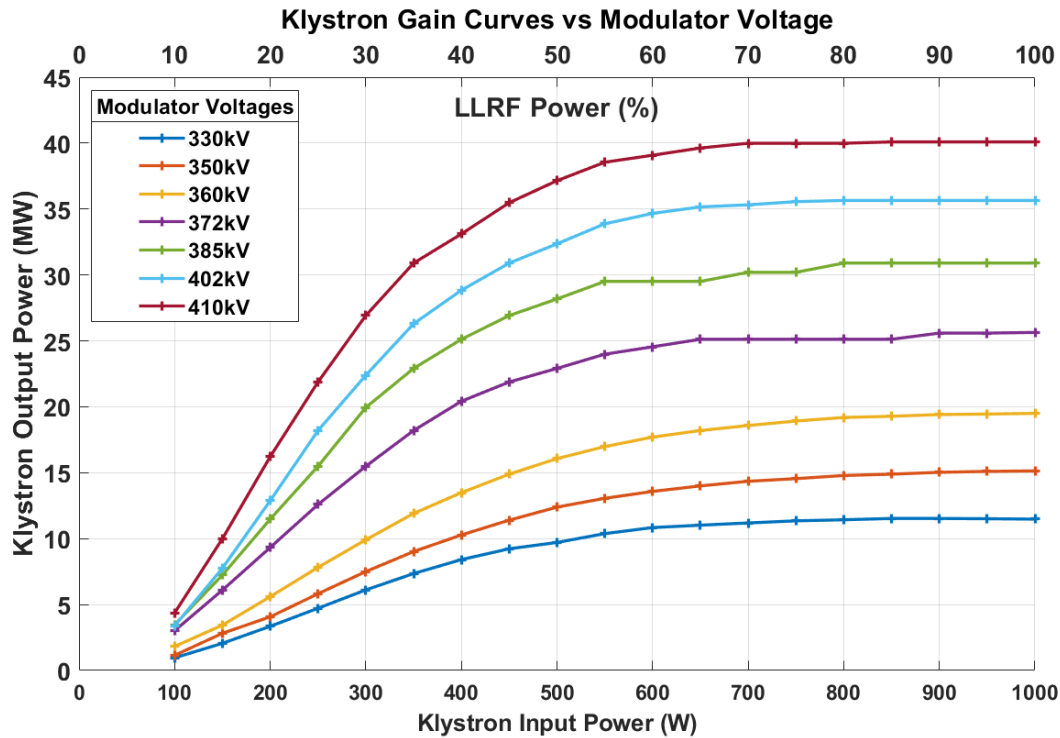


FIGURE 5.4: Measured klystron output power vs LLRF output power (%) vs modulator voltage setting (kV). The klystron output power is monitored directly using a power meter

### 5.2.4 Low Power Network

The new LLRF (described in Chapter 3) was commissioned and installed in order to introduce IQ modulation for phase and amplitude information on the X-band RF signals. The low power network produces the modulated RF pulse and acquires the RF signals in the system. A functional diagram of the low power network and a broad overview of the PXI control are shown in Figure 5.5

The modulated 12 GHz output from the LLRF is split equally using a 3 dB splitter. Half of the power is sent to the reference channel of the LLRF crate and the other half to the TWT pre-amplifier.

All of the RF cables returning from the high-power waveguide terminate at the LLRF and control rack, positioned near the operator's desk. Each high-power RF channel (seven in total) arriving at the electronics rack is split so that each signal can be directed to different LLRF systems, such as the log detectors, LLRF crate for down-mixing and a patch panel for calibration. Any unused outputs of the splitter are terminated with  $50\Omega$ . Where necessary the channels are attenuated as not to saturate any of the RF detectors. Inside the LLRF crate, the signals are passed through 12 GHz band-pass filters in order to filter out higher order harmonics generated in

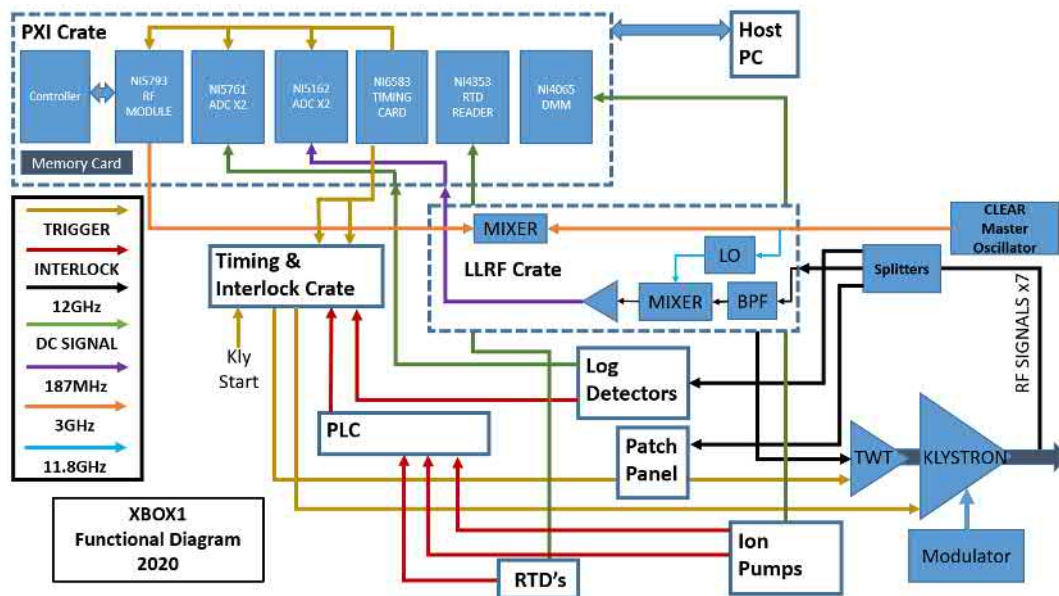


FIGURE 5.5: Xbox1 low power functional diagram showing the LLRF, timing and control. The PXI is also included with the internal cards shown [73]

the TWT or klystron. The reference channel comes directly from the X-band source back into the LLRF down-mixers, bypassing the high power network. The reference channel is used to allow for an absolute phase measurement of the other RF channels.

Logarithmic Detectors are particularly suited to perform high dynamic range power measurements and are used in a wide range of pulse detection applications. These devices produce a low frequency (DC) output that is logarithmically ('linear in dB') related to the input signal level. The log detectors at Xbox1 have already successfully been used to detect high reflections and successfully interlock the system before the upgrade.

There is an interlocking and timing crate which is used for interfacing between the PXI control system and other components, such as the klystron, log detectors or ion pumps. The log detector crate has an internal interlock for each channel which can be adjusted with a potentiometer. The output is a boolean, which is fed into the interlock crate and then into the PXI for interlocking. The output waveform of the log detectors is a DC signal which is acquired by the NI5761 cards in the PXI crate.

There are external safety systems from CLEAR that connect to SIEMENS PLC's. These are crucially integrated into the safety systems for the beam facility and thus cannot be changed. The relevant interlocks are transmitted to the PXI via the interlocking crate so that the PXI can interlock the X-band system. The interlock crate receives interlocks from the PLC for water, vacuum, and 'RF on' from CTF3. The

'RF on' interlock is a boolean which includes many features across the CTF3 facility. This will interlock if there is any issue in the facility, for example: high radiation levels, one of the bunkers being accessed, water stoppage, or any issues with the LINAC. The 'RF on' is also connected to the Xbox1 klystron and will interlock if the modulator is still heating-up or if there is an interlock in the klystron modulator.

The timing and interlock crate also transmits the triggers from the PXI, namely the triggers for the TWT, klystron, acquisition.

The vacuum system uses a combination of Nextorr Ion pumps (which are used are Xbox2 and Xbox3) and CERN vacuum gauges. The vacuum levels are read by the PXI, which incorporates a software interlock, and connected to the Siemens PLC for a hard interlock.

The reflected power from the structure and reflected power towards the klystron require a robust interlock system, because excessively high reflection over many pulses can result in damage to waveguide components and the klystron's output window. For this reason, there are several interlocking systems. Firstly, the log detector crate has a hardware interlock as mentioned. Secondly, there are two software interlocks which come from the log detector signals and the down-mixed RF amplitudes.

### 5.2.5 Control and Acquisition

The control system is a network which interfaces the electronics crates, modulator control system, the operator PC and the PXI crate. The PXI crate and LabVIEW based control system is used for control and acquisition of the test stand, the software is LabVIEW 2018. All of the RF control, acquisition, timing, data logging, and interlocking software is implemented on the PXI itself using LabVIEW real-time systems. The PXI crate communicates via the CERN technical network with several other devices, including the PLC and the main operator PC. The PXI system at Xbox1 contains the following PXI cards with the FPGA based cards highlighted:

- PXIe-8108 Dual Core Controller
- 2x NI5162 1.5GSPS ADC
- 2x NI5761 250MSPS ADC (FPGA)
- 1x NI5793 4.4GHz RF Modulation Card (FPGA)
- 1x NI6583 Timing Card (FPGA)

- 1x NI4353 Terminal Block for RTDs
- 1x NI4065 DMM and NI2053 Multiplexer for vacuum

The DC channels from the log detectors are acquired by two NI5761 ADC's. These cards contain 8 channels of each with a sample rate of 250MSPS, and a resolution of 14-bits. These ADCs are attached to programmable FPGAs which perform threshold detection on the reflected RF signals.

The NI5162 cards are used for IQ sampling of the down-converted RF channels, (these cards were described in detail in Chapter 3, including all the relevant frequencies and parameters of the ADC).

The IQ values are passed through an finite impulse response, FIR, filter and then converted to phase and amplitude values using the formulas detailed in Chapter 2. In digital signal processing, an FIR is a filter whose impulse response is of finite period, as a result of it settles to zero in finite time. The finite impulse response (FIR) filter is a non-recursive filter in that the output from the filter is computed by using the current and previous inputs. It does not use previous values of the output, so there is no feedback in the filter structure. FIR filters are most popular kind of filters executed in software and these filters can be continuous time, analog or digital and discrete time [114].

Each single RF channel outputs two waveforms, a phase and an amplitude waveform, hence there are 16 RF output waveforms in total. A sample of the demodulated phase and amplitude output from the NI5162 cards using IQ sampling is shown in Figure 5.6. This data was collected using CH0 of the two NI5162 cards; these will be referred to as NI5162A and NI5162B. Calibration of the two IQ demodulation cards is detailed in Appendix B. The IQ demodulation occurs within the acquisition loop in the main real-time code.

For the RF signal generation, the only card available on the market at the time of planning was the NI5793. It is an RF vector signal generator that can generate carrier frequencies up to 4.4 GHz. The NI5793 card performs all the modulation of the S-band waveform from the CLEAR master oscillator. For Xbox1, the modulated output is synchronised to the CLEAR master oscillator. At Xbox1 the PXI is also programmed to use the 10 MHz timing clock from CLEAR, as opposed to the 10 MHz internal PXI clock.

The PXI controls the triggering and interlocking for the entire system using the NI6583 Timing Card. Five of the interlocks originate in a Siemens PLC, these are

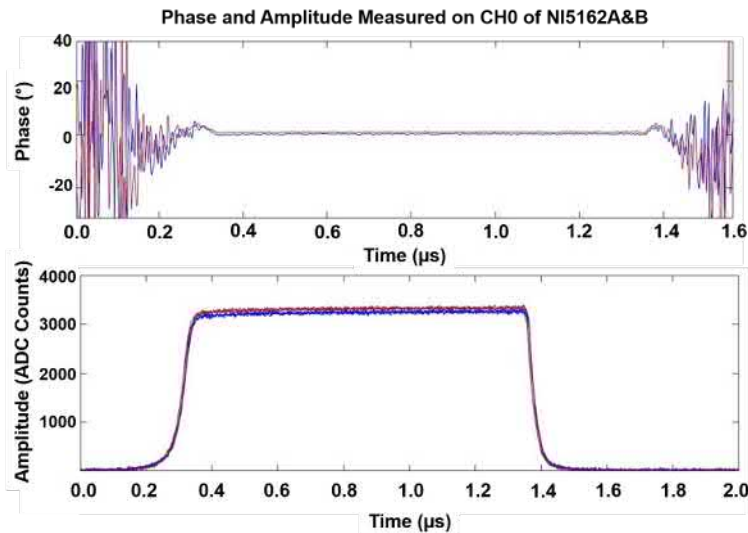


FIGURE 5.6: A sample Phase and Amplitude Profile collected using IQ sampling on CH0 OF the NI5162A and NI5162B. The source is produced using a Signal Generator at 187.46 MHz

boolean values for safety, vacuum and water. There are also four interlocks which are collected through the NI5761 ADC cards, with two FPGA based ADCs that are able to send an interlock along the back-plane of the PXI using one of the eight internal trigger lines.

The PXI controller regularly sends packets of information to the GUI on the host computer (such as un-calibrated waveforms, temperatures, vacuum levels and RF settings). This is data that can be viewed by the operator in real time. The host computer also transmits messages and commands from the operator onto the PXI where they can take effect in the real time code.

There are two types of data files created each day. Firstly, a 'Trend data' file saves data collected every minute, this data contains vacuum, water, temperatures and small amounts of RF data such as the maximum and average values for each channel. Secondly, an 'Event Data' file collects the RF waveforms in full. The waveforms are collected once every minute and also every time a 'breakdown' interlock is registered. The 'breakdown' interlock responds to large reflected power signals (and dark current signals in the case where an accelerating structure is present).

The main code is processed on the PXI using the controller. There are several crucial loops in the real-time which are 'strictly timed'. The strictly timed loops maintain their implementation frequency and are prioritized by the PXI processor. These loops are the control loop, acquisition loop, timing and interlocking loop and 'tag bridge'. The tag bridge transfers messages between different loops within the

main code and transmits packages of data to the main GUI which is on the host computer. The other loops are ‘not-strictly timed,’ these loops are: vacuum acquisition, temperature acquisition, and logging. The ‘logging’ loop is responsible for saving the data into trend files. These loops operate at a frequency of 1 Hz.

A 24 channel digital multi-meter (DMM) is used to read the vacuum signals from the ion pump controllers. The temperatures are measured using surface mounted PT100 thermocouple probes which are read into the PXI using the NI4353 PXI Temperature Input Module.

### 5.3 High Power Testing

The pulse-to-pulse stability is an important metric in LLRF, particularly for LINAC applications. Phase and amplitude errors from the RF will result in energy errors, causing emittance blow-up and luminosity reduction of the accelerated beam in a LINAC. The stability of the RF power source is therefore of critical importance.

For example, for the Swiss XFEL the stability goals for the RF system must satisfy tight requirements on amplitude and phase stability down to 0.018% RMS in amplitude stability and  $0.072^\circ$  RMS in phase stability X-band stations [115]. In this work the requirements for pulse-to-pulse rms phase and amplitude stability will be set at  $1^\circ$  and 0.1% from the high power source as this is achievable and reasonable according to the literature [108] [106].

The stability of the RF systems will be quantified using two parameters, which will be referred to as the intra-pulse and pulse-to-pulse stability. Their definitions will be described prior to the analysis; the definition remains the same for both phase and amplitude, with the exception that the phase is measured with respect to the reference channel to achieve an absolute phase measurement.

In the following analysis, the klystron and the ‘nominal’ parameters are summarised in Table 5.1:

RF pulse length	150 ns
RF Power Level	80%
Modulator Voltage	330 kV
Repetition Rate	50 Hz

TABLE 5.1: Nominal Parameters Used for the Klystron Phase Stability Study

The LLRF design in Chapter 3 presented two different methods for producing the X-band local oscillator from a low frequency input. The 11.806 GHz local oscillator

is used in the down-conversion and mixed with the incoming RF signals. The two methods are a PLL and single-sideband up-converter. Both up-conversion methods were tested successively in the LLRF system at Xbox1. This testing took place in May 2021 with a 150 ns RF pulse length and a klystron power output of 10.82 MW (330 kV modulator voltage setting). An IQ pulse measurement is saved every 5 seconds using the NI5162 ADC.

### 5.3.1 Intra-Pulse Stability

The intra-pulse stability will be calculated by taking the rms value across an individual flat top. This indicates how much each flat top is expected to deviate from perfect flatness, a diagram of this metric is shown in the top of Figure 5.7.

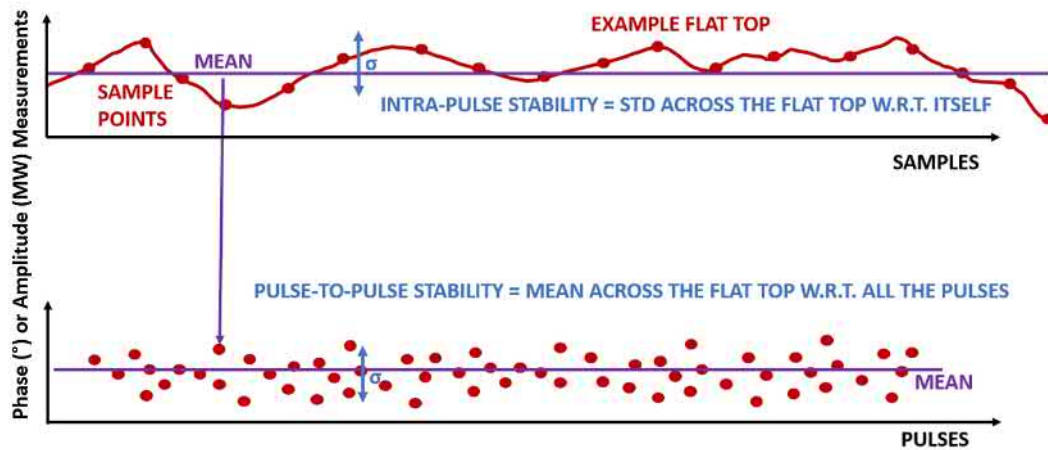


FIGURE 5.7: Diagram of the method which will be used for calculating the intra-pulse and pulse-to-pulse stability. The same method applies for both the amplitude and phase measurements hence the y-axis can either be the phase ( $^{\circ}$ ) or the amplitude (MW) across the flat top of a pulse. Gradient of the flat top is not considered here

### Amplitude Stability

The intra-pulse amplitude stability can be observed from the examples of pulse data in Figure 5.8. An example of an amplitude pulse from the reference, TWT and klystron channels are shown. The vertical axis is measured in ADC counts. From visual inspection it is clear that the intra-pulse amplitude stability increases after the TWT and again after the klystron.

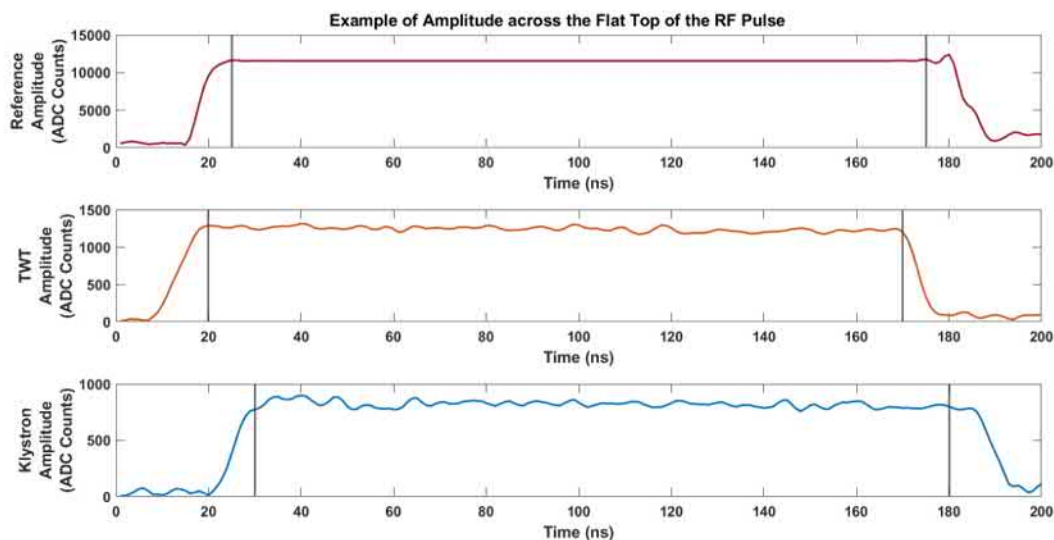


FIGURE 5.8: Example of a measured data which shows the amplitude of the Reference, TWT and Klystron channels for the same pulse. This is a 150 ns RF Pulse collected on 30.07.2021

The signals from the reference, TWT and klystron are on vastly different power scales so the amplitude stability measurements are characterised as a percentage

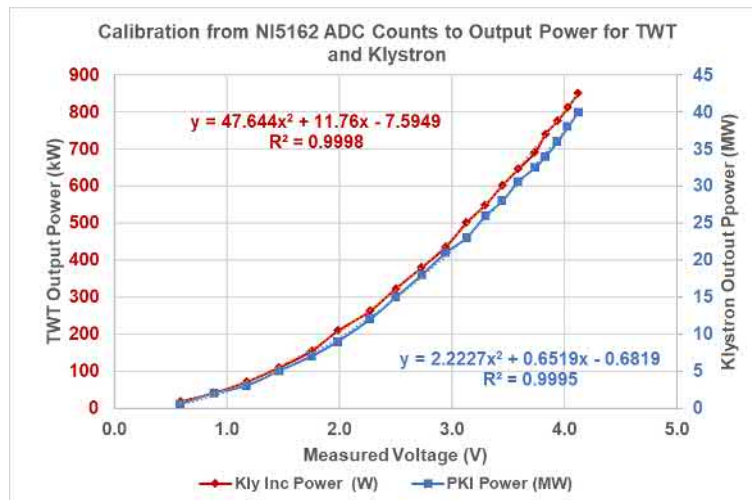


FIGURE 5.9: Calibration of the PXI NI5162 ADC cards which will measure the RF channels. The raw ADC Counts are converted to Output Power for TWT and Klystron respectively

change. The calibration curves from ADC counts to power for the TWT and klystron are shown in Figure 5.9. The calibration curves are only valid for the specific ADC channel on which the measurements were taken. The attenuation of the signals between the high power network and the input to the LLRF down-mixing crate are 59.6 dB for the TWT output and 87.10 dB for the klystron output. This includes high power directional couplers, low power directional couplers, co-axial cables, splitter and connectors.

The normalized intra-pulse amplitude stability is shown in a histogram in Figure 5.10. For the normalized stability the offset has been subtracted so that the values are centred around zero.

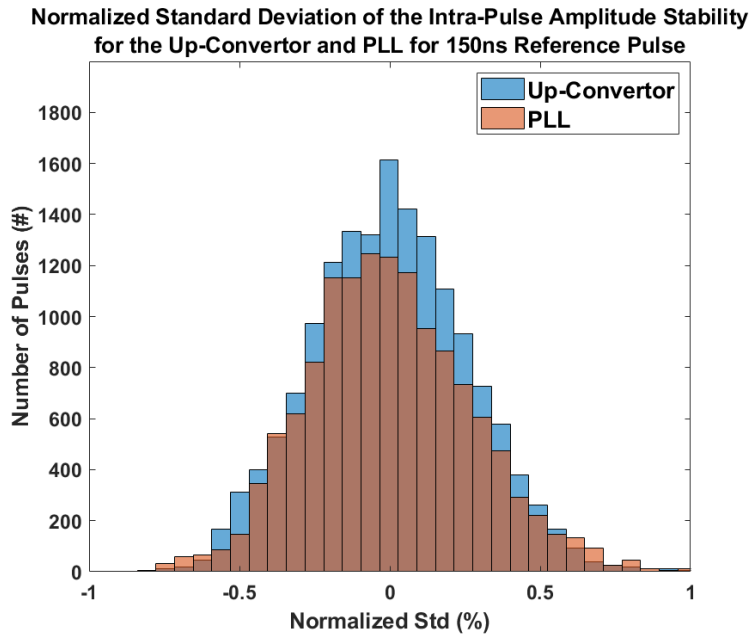


FIGURE 5.10: Normalized standard deviation of the intra-pulse amplitude stability at the output of the LLRF crate. The data shown here compares the LLRF output when the LO is produced by the up-Converter (blue) and PLL (orange) for a 150 ns RF Pulse

The histogram clearly highlights that the spread is almost identical for the PLL and the up-converter, with no noticeable difference in the intra-pulse amplitude stability between the PLL and the up-converter. The intra-pulse amplitude stability for the up-converter is  $0.1316\% \pm 0.036\%$  and for the PLL is  $0.1684\% \pm 0.033\%$ .

Regardless of the method for producing the LO, (using the PLL or up-converter), the amplitude stability becomes successively worse after the TWT and again after the klystron. The intra-pulse amplitude stability for reference, TWT and klystron outputs are shown as normalised histograms in Figure 11, the up-converter was used to produce the LO. The intra-pulse amplitude stability results are summarised in Table 5.2.

Reference	TWT (%)	Klystron (%)
$0.107\% \pm 0.144\%$	$0.192\% \pm 0.260\%$	$0.532\% \pm 0.717\%$

TABLE 5.2: Intra-Pulse Amplitude Stability for the Reference, TWT and Klystron Output for a 150 ns RF Pulse using the Up-Converter as the LO

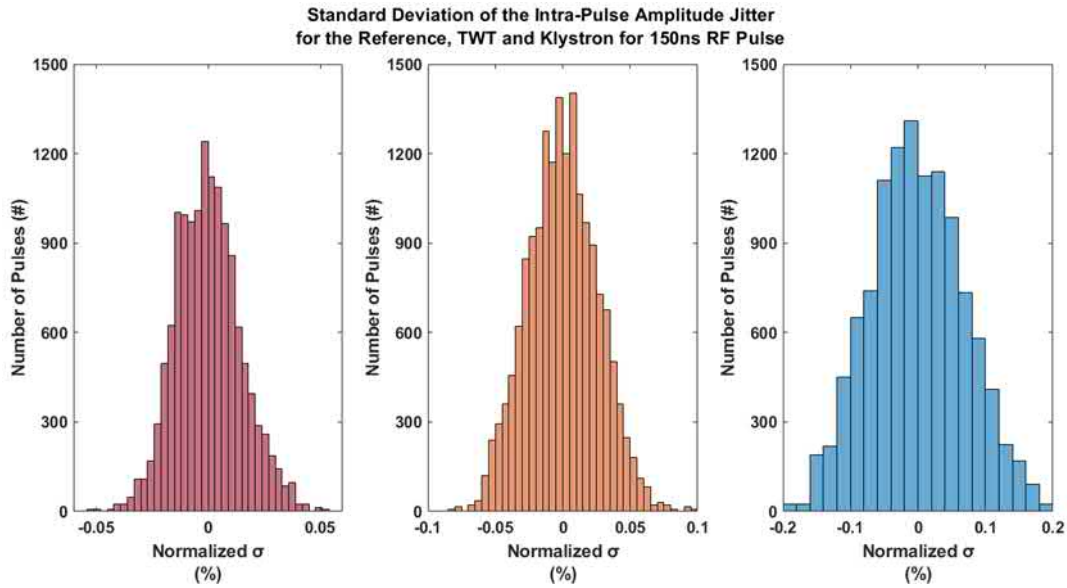


FIGURE 5.11: Normalized intra-pulse stability of the reference, TWT and klystron output amplitude for 150 ns RF pulse

### Phase Stability

The LLRF output is a modulated X-band pulse which is sent to the TWT and then onto the klystron. An example of the phase profiles from the reference, TWT output and Klystron output are shown in Figure 5.12.

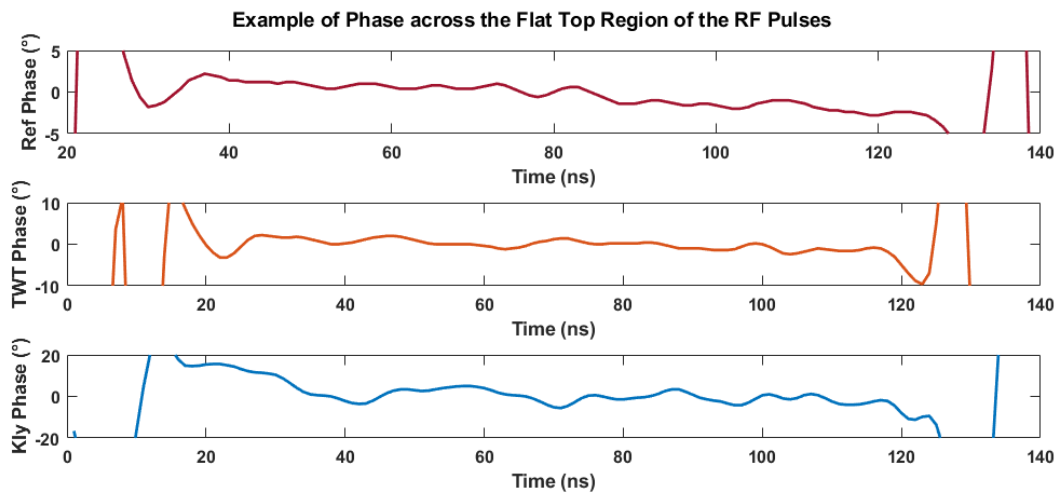


FIGURE 5.12: Measured data showing an example of the flat-top region of the phase of the RF pulses from the reference channel, TWT Output and klystron output. The data is measured on the same pulse for all three channels

From the same pulse (as in Figure 5.12) the average phase value across the flat top region (20 ns to 120 ns) was computed for each pulse and the deviation from the average computed. The resulting deviations are shown in Figure 5.13. It is clear that

the klystron phase (yellow) has the largest excursions and that the phase deviations increase as the signal travels from the LLRF reference through to the TWT and finally the klystron.

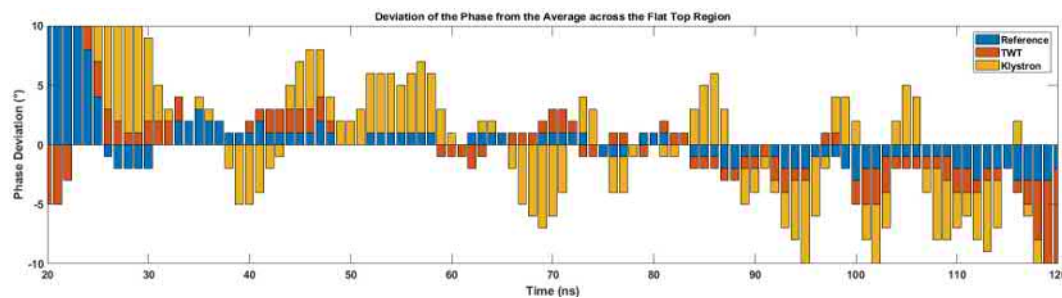


FIGURE 5.13: Deviation of the phase from the average across the flat top region (20 ns to 120 ns) for three channels, reference (blue), TWT output (orange) and klystron output (yellow), for the same pulse (pulses are the same as were shown in Figure 5.12)

Figure 5.14 shows the intra-pulse phase stability of the reference pulses using both methods for producing the LO. The intra-pulse phase stability across the flat-top region is  $2.184^\circ \pm 0.3159^\circ$  for the PLL and  $1.799^\circ \pm 0.2892^\circ$  for the up-converter. The reduction on phase noise of the up-converter with respect to the PLL, which was detailed in Chapter 3, has translated to improved intra-pulse stability. From visual inspection of Figure 5.14 the up-converter appears to increase measurement accuracy by approximately half a degree.

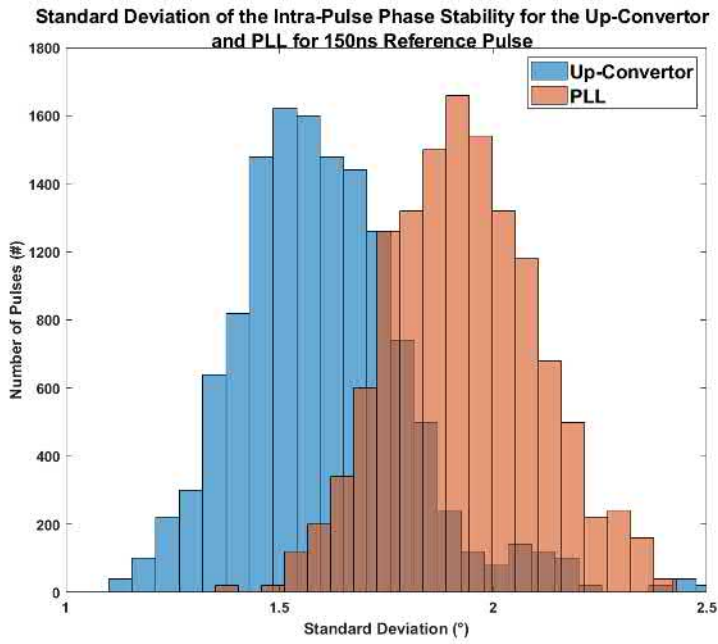


FIGURE 5.14: The intra-pulse phase stability for both the PLL and the Up-converter LLRF systems. This is the standard deviation across the flat top region taken from 7000 pulses.

The normalised intra-pulse phase stability of the reference, TWT output and klystron output are shown in Figure 5.15. The results are also summarised in Table 5.3. The improvement in the intra-pulse phase stability from the up-converter, compared to the PLL, is translated through to a small improvement in the intra-pulse stability of the TWT and the Klystron. However, this improvement is not as significant as with the improvement in the phase stability.

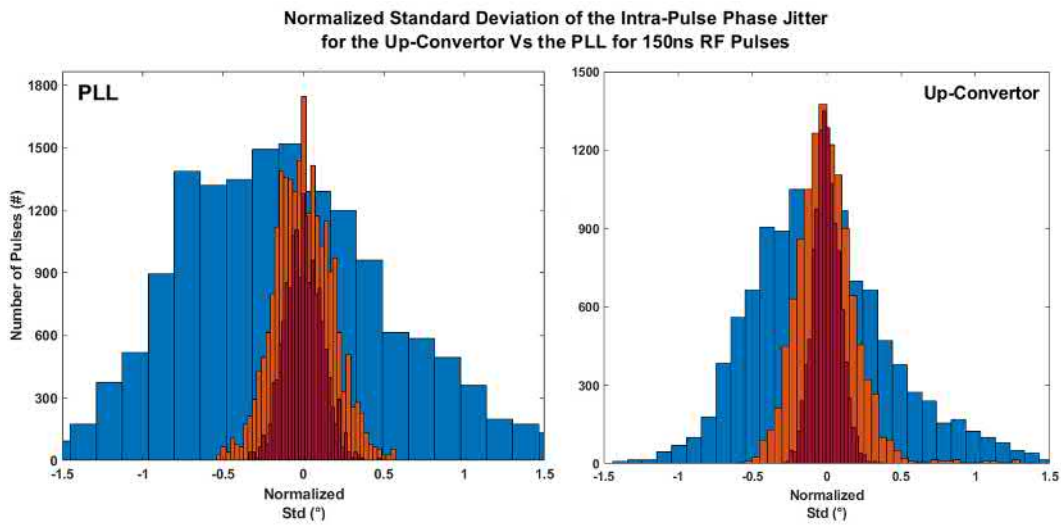


FIGURE 5.15: Normalized standard deviation of intra-pulse stability for the reference, TWT output and klystron output channels. In the plot on the left the PLL is used as the LO source. On the right the up-converter is used as the LO and the measurement is repeated

	Reference	TWT	Klystron
Up-Convertor	$1.798^\circ \pm 0.216^\circ$	$2.850^\circ \pm 0.356^\circ$	$4.736^\circ \pm 0.853^\circ$
PLL	$2.153^\circ \pm 0.178^\circ$	$2.587^\circ \pm 0.321^\circ$	$4.586^\circ \pm 0.784^\circ$

TABLE 5.3: Intra-Pulse Phase stability of the Reference, TWT output and Klystron Output for a 150 ns RF Pulse

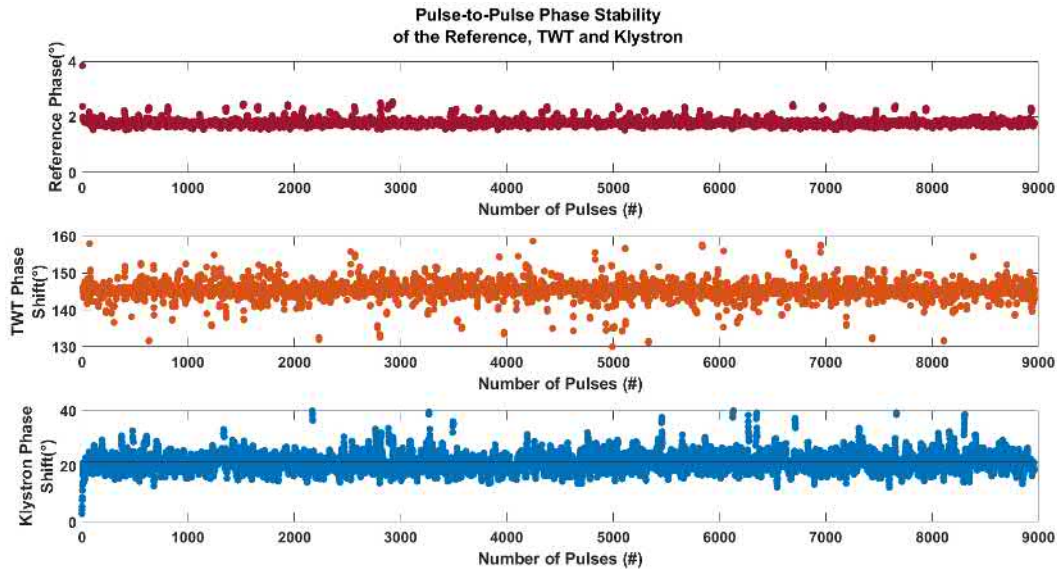


FIGURE 5.16: Measured Pulse-to-Pulse Phase stability on the Reference, TWT and Klystron channels. The data is taken from 7000 RF pulses with an RF pulse length of 250ns RF Pulses collected on 10.09.2021

### 5.3.2 Pulse-to-Pulse Stability

Pulse-to-pulse stability is usually characterized as phase and amplitude variation between successive pulses of a microwave signal [116]. The pulse-to-pulse stability will be measured by taking the average value of each flat top and comparing this with the average with respect to a number of other pulses, this metric is shown in the bottom of Figure 5.7. The pulse-to-pulse stability can be understood visually by observing the data in Figure 5.16

#### Amplitude Stability

The pulse-to-pulse amplitude stability is shown as the normalized standard deviations in Figure 5.17.

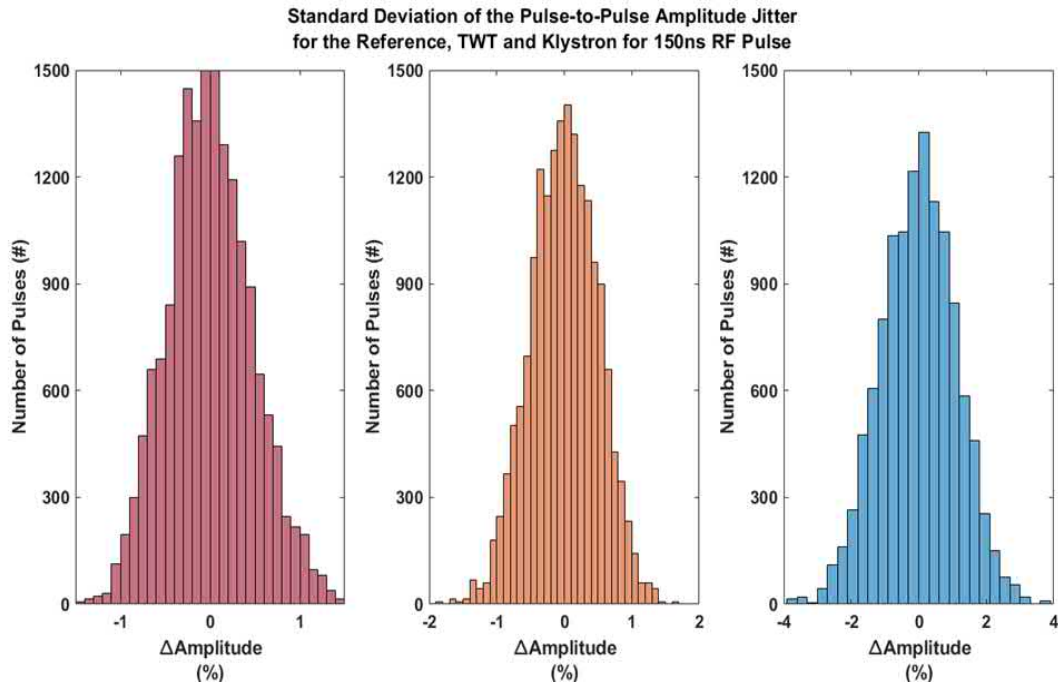


FIGURE 5.17: Normalized standard deviation of the pulse-to-pulse amplitude stability for the reference, TWT and klystron output pulses for a 150 ns RF Pulse

The desired amplitude stability leaving the klystron is 0.1%. This is not achieved on a pulse-to-pulse basis, as is shown in the first row of Table 5, which summarises the pulse-to-pulse amplitude stability results. Amplitude stability on the order of 0.1% at the klystron output could only be achieved after averaging over 500 pulses in post-processing, this is 8.33 minutes at a 50 Hz repetition rate.

Time (Minutes)	N	Pulse-to-Pulse Stability (%)		
		Reference	TWT	Klystron
0.02	1	0.3637	0.3976	1.0105
0.08	5	0.1761	0.2339	0.4669
0.17	10	0.1362	0.2083	0.3505
0.83	50	0.0962	0.1778	0.2391
1.67	100	0.0885	0.1652	0.2082
8.33	500	0.0399	0.0536	0.1063

TABLE 5.4: Pulse-to-Pulse Amplitude Stability of the Reference, TWT and Klystron Pulses using different lengths of Averaging Filter

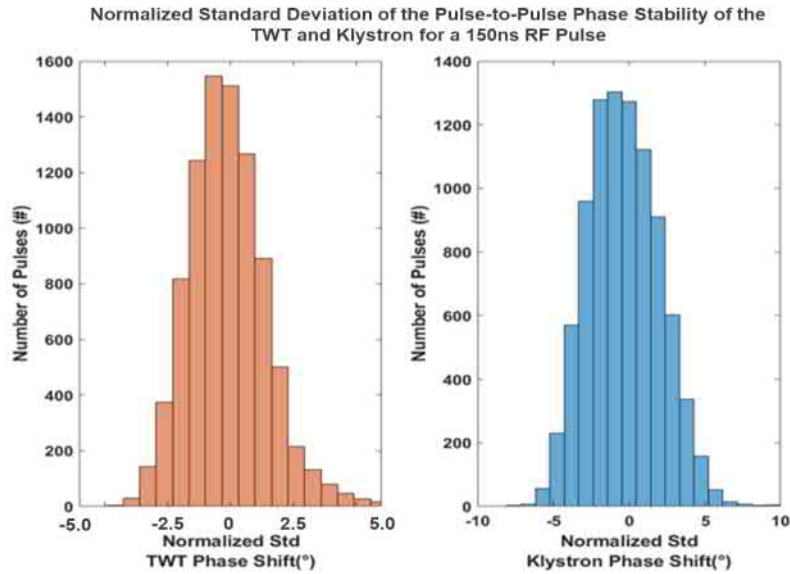


FIGURE 5.18: Measured pulse-to-pulse phase stability of the TWT (left) and klystron (right) output signals. The data has been normalised in order to be centred around zero

### Phase Stability

The reference pulse-to-pulse stability cannot be defined because the reference phase is not an absolute phase measurement. Absolute phase refers to the phase of a waveform relative to some standard, which in this case is the reference phase. The normalised pulse-to-pulse phase stability of the TWT and klystron output signals are shown in Figure 5.18.

The klystron and TWT phase stability do not achieve the  $1^\circ$  phase stability benchmark. The results of averaging over increasing time periods is shown in Table 5.5. A pulse-to-pulse stability on the order of  $1^\circ$  leaving the klystron was only found after averaging over 500 RF pulses in post-processing, which is equivalent to 8.33 minutes for a 50 Hz repetition rate. It is evident that this high power system does not meet the quality requirements to be used in an X-band LINAC facility. It would be necessary to develop and implement a feedback system on the klystron to regulate both the amplitude and the phase output.

Pulses	Time (Mins)	TWT ( $^{\circ}$ )	Klystron ( $^{\circ}$ )
1	0.02	7.7649	8.2275
10	0.17	3.2663	4.8888
100	1.67	0.6955	1.1539
500	8.33	0.3058	0.5765

TABLE 5.5: Pulse-to-Pulse Phase Stability of the Reference, TWT and Klystron Pulses using different lengths of Averaging Filter

## 5.4 Klystron Phase Stability Study

The klystron phase stability was analysed in the previous section under one set of conditions which can be found in Table 5.1.

In the following analysis three klystron input parameters will be varied, these are; RF pulse length, RF power level and modulator voltage set-point. This study will only examine the effect on the phase stability; (amplitude stability will not be covered in this work). The outputs of interest are the klystron output pulse-to-pulse phase stability and the phase shift across the klystron. Both of these parameters must be as stable as possible in order to meet the stringent phase stability requirements of a LINAC or FEL.

Sensitivity analysis is the study of how the uncertainty in the output of a system can be divided and allocated to different sources of uncertainty in the inputs variables [117]. The klystron is considered to be a 'black box' where the output is a function of its inputs. Decision making can be improved by identifying how and when optimal solutions change, or producing flexible recommendations that take account of changing circumstances [117].

### 5.4.1 RF Power Scan

The relationship between the PXI power set-point and the klystron output power is shown in Figure 5.19. The RF pulse length is 150 ns and each data set is averaged over 7000 pulses. The data points were collected over the same period each day, more tests over different periods of the day were not possible due to the HV safety limitations which dictated that the 50 MW klystron could not be operated overnight at this time.

Figure 5.20 shows the pulse-to-pulse phase stability at the klystron output. The phase stability improves as the LLRF output power increases. The study was repeated for modulator voltages of 330 kV and 360 kV. As the RF power increases, the

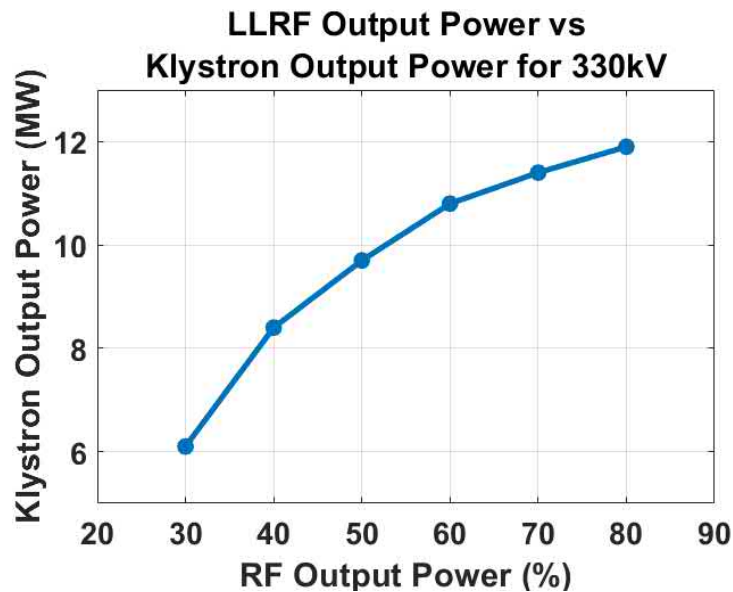


FIGURE 5.19: Measured LLRF output power vs klystron output power. The output power is varied by the user via a LabVIEW GUI and the klystron power is measured using a power meter.

pulse-to-pulse phase stability improves, the phase becomes more stable.

This is a result of the operation point being in the saturation region of the gain profile of the klystron, which was shown in Figure 5.4. Given that the demodulation is done digitally and the temperature drift of analog components between samples can be considered negligible, it is sensible to assume that the phase measurement is not sensitive to increases in the measured signal power level. Hence, it is sensible to surmise that the improved phase stability is due to approaching saturation rather than signal power

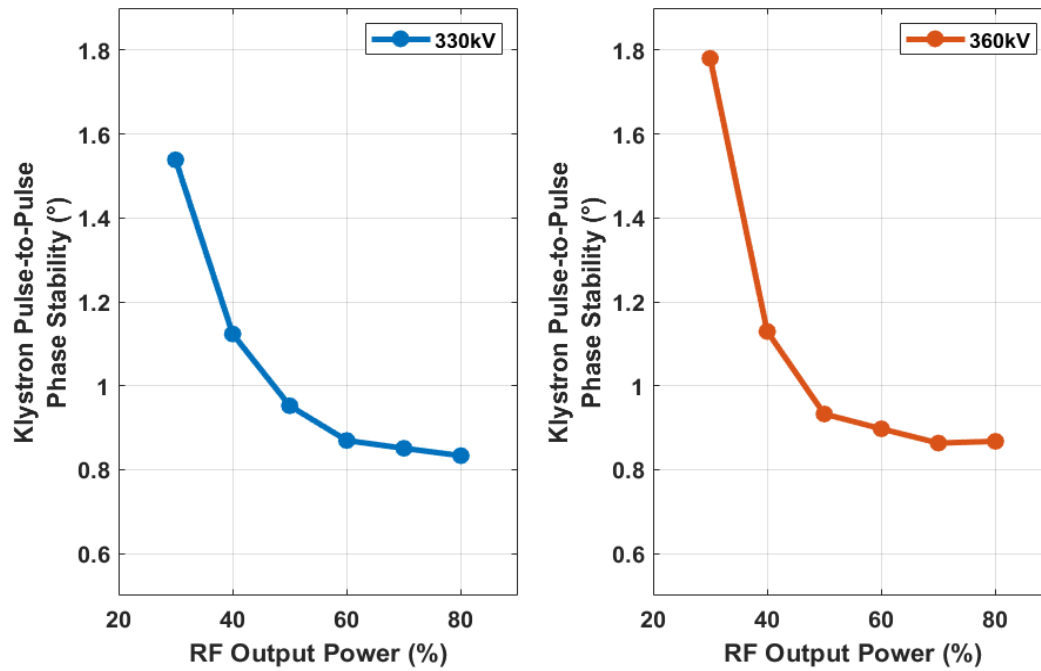


FIGURE 5.20: Klystron Pulse-to-Pulse Phase stability vs LLRF Power for 150 ns RF Pulse Length for 330 kV and 360 kV Modulator Voltages

Figure 5.21 shows the klystron phase shift with respect to the RF power. The phase shift increases as the RF input power increases, this is true for both modulator voltages. However, the change in phase shift is more significant as the modulator voltage increases. This is logical, as larger modulator voltages result in larger ranges of the klystron output power so the same amount of phase stability will create a larger output variation.

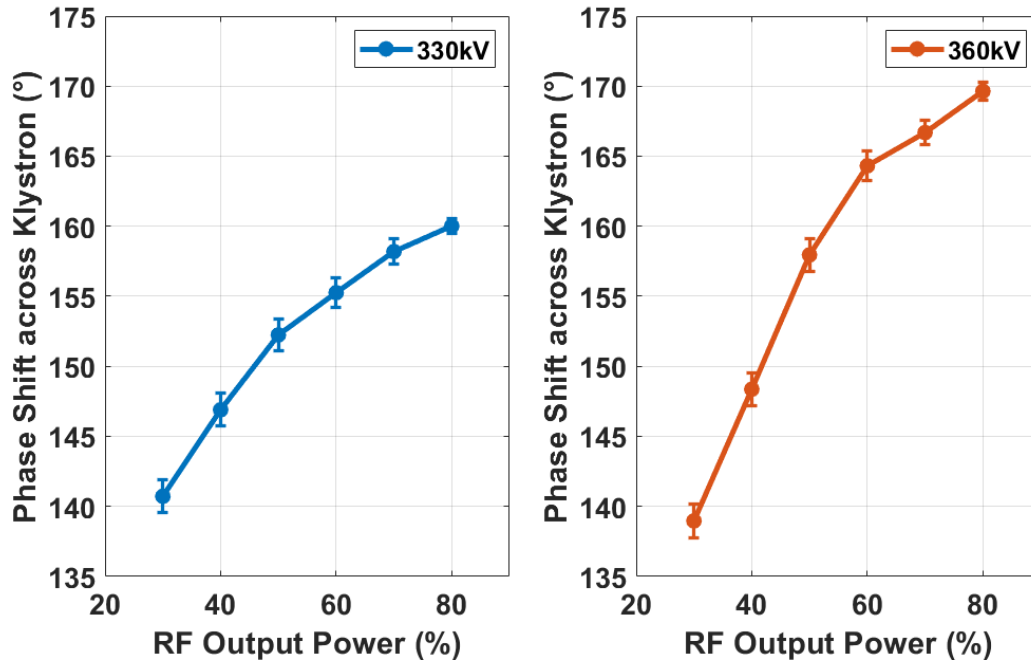


FIGURE 5.21: Measured phase shift across the klystron vs klystron output power for 150ns RF Pulse. The modulator voltage was manually set to 330kV (left) and 360kV (right)

Changing either the RF power level or the modulator voltage changes the efficiency of the klystron. A larger RF power changes the velocity of the electrons in the drift tube of the klystron, this changes the time the electrons spend in the drift tube and hence alters their depth of modulation. A change in the velocity of the electrons will result from this change in the modulation to produce a change in the phase shift across the klystron.

#### 5.4.2 Pulse Length Scan

The RF pulse length is adjusted using the NI5793 RF modulation card in the PXI. The flat-top region of the phase profiles is defined as the sample point at which the sum of the change in gradient between five adjacent samples is less than 5. The RF pulse is varied from 50 ns to 250 ns in steps of 50 ns.

Figure 5.22 shows the standard deviation of the pulse-to-pulse phase stability, which is calculated by averaging the phase across the flat-top of each pulse and taking the standard deviation of the average phase from each of the 7000 pulses.

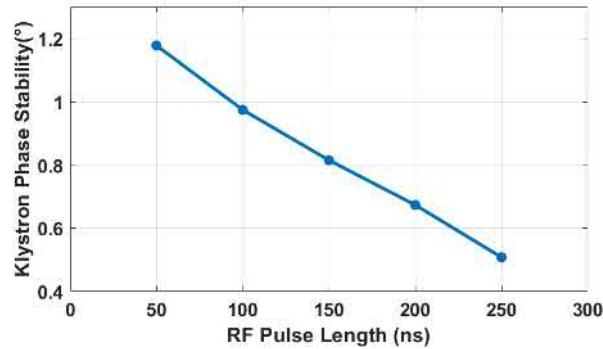


FIGURE 5.22: Standard Deviation of the Klystron Pulse-to-Pulse Phase stability vs RF Pulse Length for 8.7 MW Klystron Output Power and 330 kV Modulator Voltage

The pulse-to-pulse phase stability on the klystron output is inversely proportional to the RF pulse length. This is expected as the phase is the average over the pulse, for a longer pulse length the average will be taken over a longer time period.

The more measurements are averaged, the smaller the error in the mean. The error in the mean decreases as the square root of one over the number of measurements where in this case the samples are collected in time. For a longer pulse length the random phase deviations are reduced by  $\frac{1}{\sqrt{(N)}}$  where  $N$  is linear in time.

The average phase shift across the klystron for each pulse length is shown in Figure 5.23.

The phase shift is not correlated with the change in pulse length as the velocity of the electrons in the klystron is not altered by the pulse length.

The error in pulse length is not a significant issue as the beam passes through the cavity during a small period in the centre of the RF pulse flat top. In this case the method of measuring the pulse-to-pulse stability must be considered. This measurement of pulse-to-pulse stability is calculated by averaging over the whole flat-top region and comparing successive pulses. An alternative method could take a single

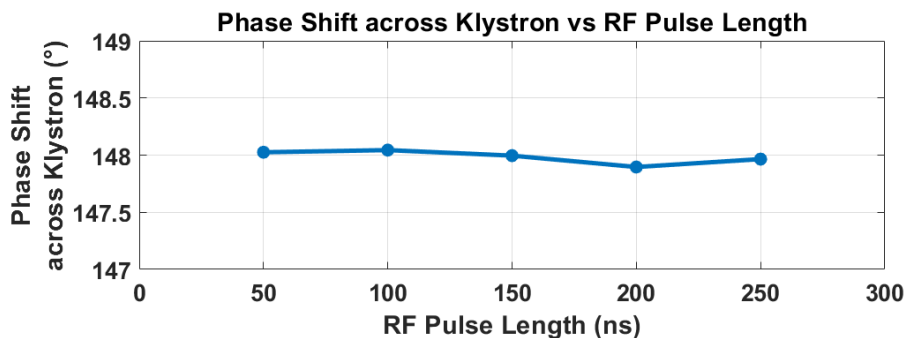


FIGURE 5.23: Phase Shift across the Klystron vs RF Pulse Length for 8.7 MW Klystron Output Power and 300 kV Modulator Voltage.

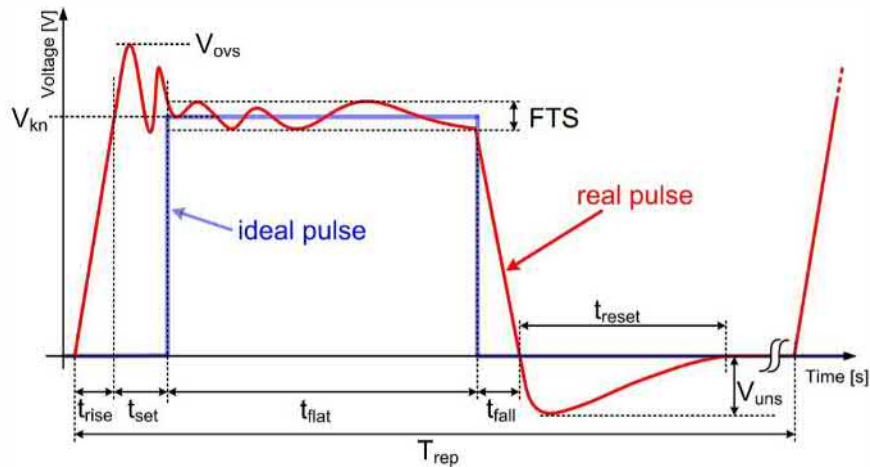


FIGURE 5.24: Diagram of an ideal voltage pulse (purple) and a real voltage pulse (red) [36]. After the initial ripple has decayed the stability across the flat top can be measured (FTS). The ripple can be reduced by increasing the rise time.

point in the flat top (for example 50% along) and comparing successive measurements of this point, at which point it is equally likely that random fluctuations will occur at that point regardless of the pulse length.

### 5.4.3 Modulator Voltage Scan

The most critical parameters of the solid state modulators, which may have a strong impact on the technology selection, are the modulator voltage ripple and the pulse-to-pulse reproducibility. The specifications for the ScandiNova modulator at Xbox1 state 0.25% ripple and 0.1% repeatability of the modulator voltage pulses [104]. An example of a modulator voltage pulse is shown in Figure 5.24.

To be able to characterise a pulse with 0.1% reproducibility it is necessary to measure more precisely than that. Therefore, a target of 0.05% reproducibility for the measuring system will be required [112]. The modulator voltage will be measured using the NI5761 cards; the FPGA program for these cards is already programmed to measure a DC voltage pulse. These cards have a higher resolution than the NI5162 cards. The NI5761 is a 14 bit card with a 250 MSPS sampling rate. The input range for a DC measurement is  $\pm 1.23V_{pk} - pk$ . The modulator voltage will be converted down to this range using a voltage divider. The modulator already has an internal system which divides the modulator voltage pulse down to a voltage which is suitable for an oscilloscope. The conversion ratio is 1:18500, so for the maximum modulator voltage of 420 kV, the output voltage will be 22.7 V. An additional voltage divider circuit with a division ratio of 40 was used. Resistor values of 1 k $\Omega$  and

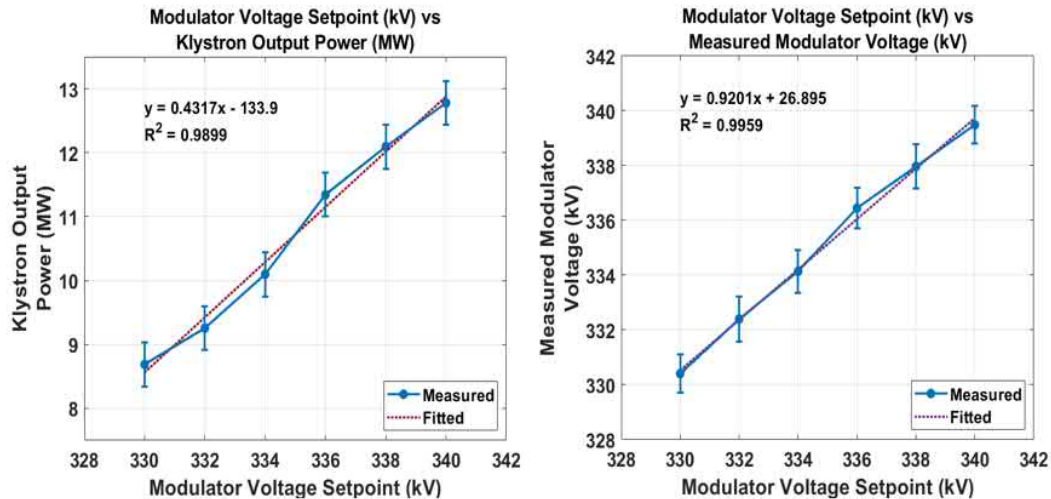


FIGURE 5.25: Relationship between Modulator Voltage and Klystron Output Power (Left) and measured modulator voltage at the PXI (Right) for a Klystron Input Power of 748.2kW (80% of the full TWT Output Power).

41.7  $\Omega$  were used. The resolution of the measurement will be 61.03  $\mu\text{V}$  and will be sampled every 4 ns, there will be 1500 samples per acquisition resulting in a window of 6  $\mu\text{s}$ . The acquisition will be triggered using the same PXI triggers.

The pulse-to-pulse modulator voltage stability is measured over a 1  $\mu\text{s}$  section of the flat-top which starts after the initial oscillations have stabilised. The variation over each pulse with respect to the average is measured. The stability is converted from ADC counts to kV and normalised around zero. During both modulator voltage scans the RF power level is 80%, this is an input power at the klystron of 750 W and is within the saturation region. The modulator voltage set-point is varied through two ranges: 330-340 kV and 360-370 kV. The relationship between the modulator voltage set-point, the klystron output power and measured modulator voltage at the PXI is shown in Figure 5.25. Changing the Modulator Voltage by 1 kV corresponds to a change in the klystron output power of 0.37 MW.

The standard deviation of the pulse-to-pulse stability on the modulator voltage at 330 kV is shown below in Figure 5.26. The standard deviation is  $\pm 0.404\text{kV}$  which would correspond to a change in the output power of 0.304 MW using the linear relationship shown in Figure 5.25. The standard deviation is calculated using the same method for each modulator voltage set-point and the results are shown in Table 5.6.

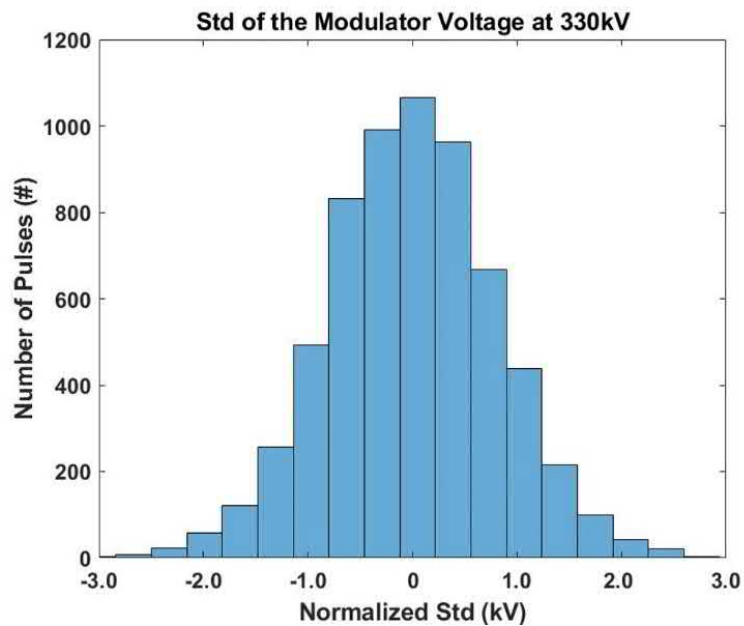


FIGURE 5.26: Normalized Standard Deviation of the Pulse-to-Pulse Modulator Voltage stability at 330 kV. The stability is taken by averaging across 1  $\mu$ s region of the flat-top of each pulse and comparing between pulses

The standard deviation is comparable for each modulator voltage set-point suggesting the modulator voltage stability is constant across the measured voltage ranges.

The phase shift across the klystron responds linearly to increasing modulator voltage as shown in Figure 5.27. The error bars are one standard deviation of the modulator voltage measurement and phase shift measurement from each data set.

Modulator Voltage Setpoint (kV)	Average (kV)	Standard Deviation ( $\pm kV$ )
330	330.015	0.404
332	332.103	0.408
334	333.938	0.398
336	336.075	0.410
338	338.107	0.397
340	340.057	0.399
360	359.982	0.423
362	362.374	0.412
364	364.585	0.412
366	367.482	0.514
368	368.194	0.476
370	370.493	0.487

TABLE 5.6: Pulse-to-Pulse Mean and Standard Deviation of the Measured Modulator Voltage vs Modulator Voltage Setpoint

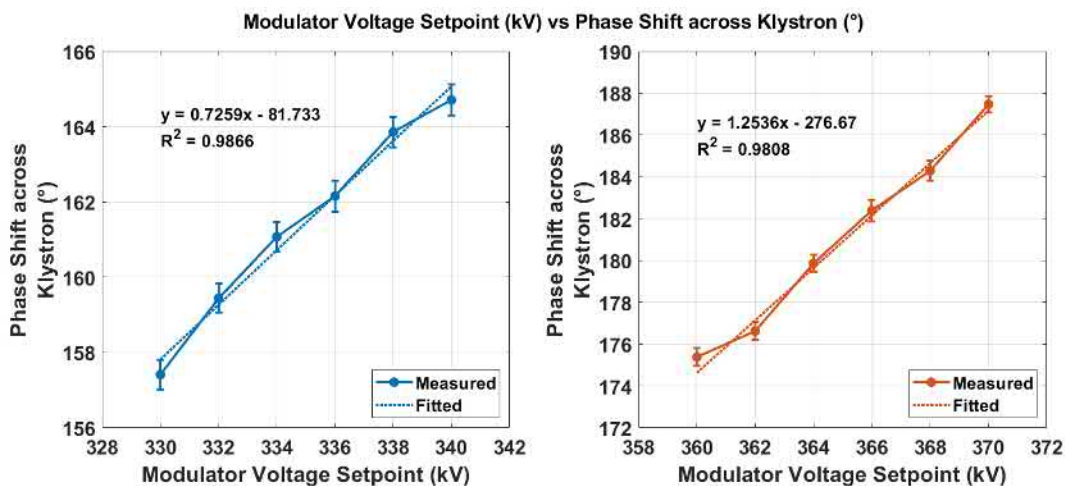


FIGURE 5.27: Klystron Output Phase vs Modulator Voltage Setpoint for 250 ns RF pulse at 80% of the Full TWT Output Power, the vertical and horizontal error bars are calculated as one standard deviation of the phase and modulator voltage stability respectively. The modulator voltage was swept twice starting at 330 kV (Left) and 360 kV (Right)

The increased pulse-to-pulse phase stability at the klystron is due to the phase shift in the klystron changing in between pulses. The change in phase is highly correlated with a change in the modulator voltage (stability) between pulses. An example of this is shown in Figure 5.28 for modulator voltages at 338 kV.

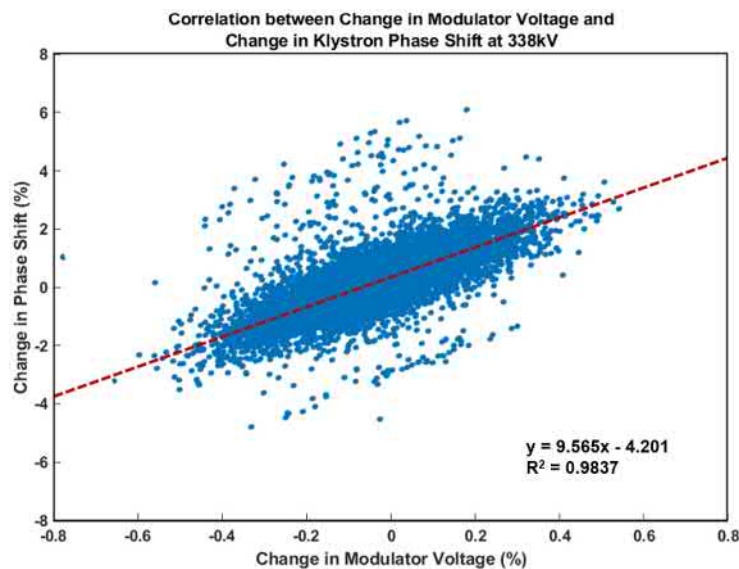


FIGURE 5.28: Relationship between the measured change in modulator voltage (jitter) and the klystron phase shift for a modulator voltage setting of 338 kV

This relationship is calculated using the average value of the modulator voltage across the flat top and is synonymous with the repeatability.

The klystron pulse-to-pulse phase stability responds linearly with increasing modulator voltage as shown in Figure 5.29. For higher modulator voltage settings the PFN must charge the resonant circuits up to a higher voltage. The charging diode keeps the PFN voltage at full until the discharge cycle, this is inherently more unstable for higher modulator voltages.

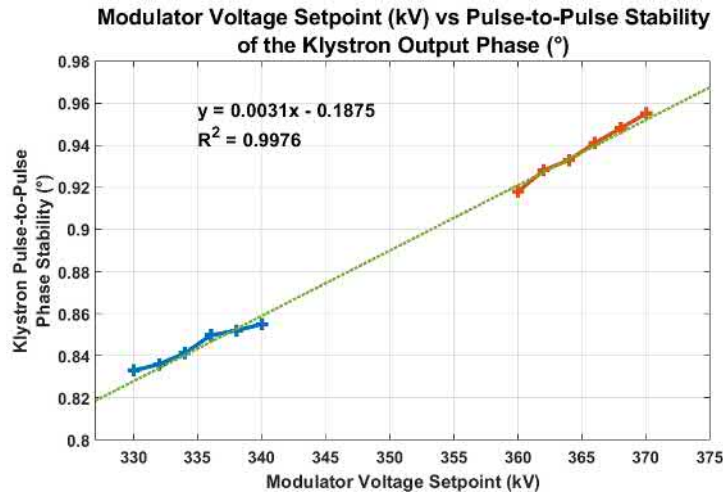


FIGURE 5.29: Measured modulator voltage (kV) vs pulse-to-pulse stability of the measured klystron phase ( $^{\circ}$ ). The modulator voltage was swept twice starting at 330 kV (Left) and 360 kV (Right)

#### 5.4.4 Sensitivity Analysis - Summary

The sensitivity of the phase at the klystron output to several input parameters was measured using one-at-a-time sensitivity analysis. The parameters are RF power level, RF pulse length and modulator voltage. Interactions between the input variables was not measured. The stability of the output of the klystron was characterised using two parameters, the phase shift across the klystron and the output phase stability.

##### Klystron Phase Shift

The phase shift changes in response to changes in the input RF power level and the modulator voltage. Both input changes will alter the velocity of the beam in the drift tube, which results in a change of velocity of the beam and therefore a change in the phase across the klystron. The phase shift is unresponsive with respect to the RF pulse length.

It is possible to infer from the plotted gain curves (shown in Figure 6.11) how the modulator voltage setting alters the phase shift across the klystron. This is based on the assumption that the phase shift generally exhibits the same response as for the amplitude with respect to modulator voltage. This is a sensible assumption given the results from the RF power level scan from Figure 6.11.

From Figure 5.21, the phase shift response is logarithmic with input RF power level. Therefore, a linear change in the modulator voltage changes the gradient and the offset in a predictable way.

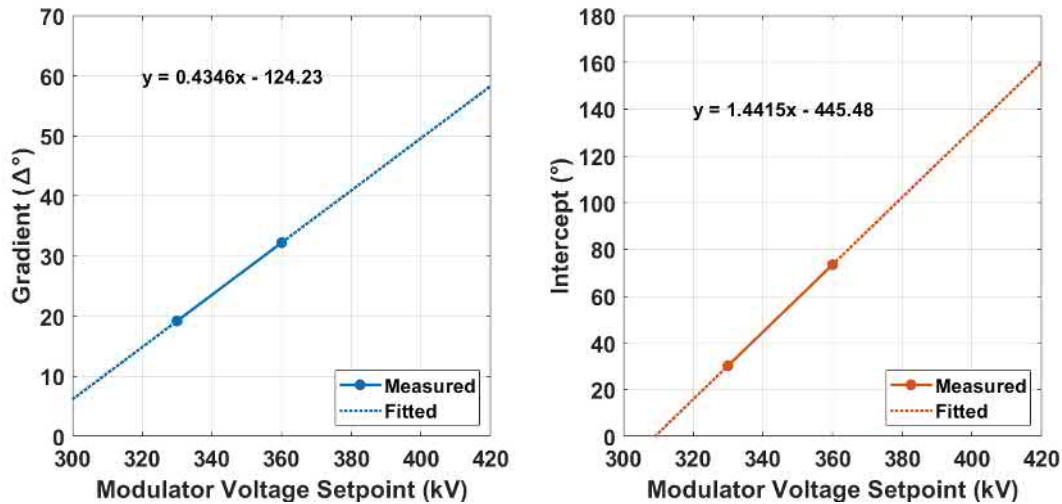


FIGURE 5.30: Calculation of the gain,  $a$  (Left), and the intercept,  $b$  (Right), with respect to each range of modulator voltage (330 kV and 360 kV). The gains and intercept are used to define how the phase shifts with RF power level using a logarithmic fit of the form:  $y = a \cdot \ln(x) + b$

It can be observed from the gain curves that changing the modulator voltage with a constant RF power is equivalent to moving vertically upwards at any point along the curve. Plotting this would result in a linear response which can be characterised with a gain and intercept value.

Under the same assumption that the phase shift responds akin to the gain curves, logarithmically, then the change in phase can be characterised by a logarithmic function of the form  $y = a \cdot \ln(x) + b$ . The gain and intercept ( $a$  and  $b$ ) of the logarithmic fit change linearly with modulator voltage. Hence, it is possible to take the two measurements of phase shift and calculate how the gain and intercept will change with modulator voltage. The klystron phase shift was measured twice, starting at 330 kV and 360 kV, the results are shown in Figure 5.27.

From this point, the equations for all of the modulator values can be calculated by extrapolation. For example, when the modulator voltage is 370 kV, the phase will change according to  $y = a \cdot \ln(x) + b$ , where  $a$  and  $b$  are extrapolated from the known values and the relationships. The results are shown in Figure 5.30.

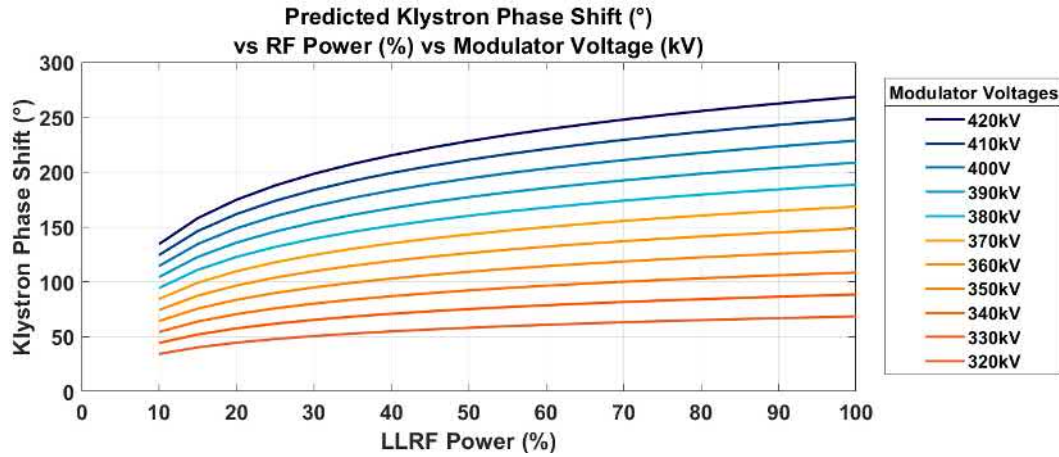


FIGURE 5.31: Predicted Klystron Phase Shift (°) with respect to changing RF power Levels (%) and Modulator Voltages (kV)

The phase shift across the klystron as a function of RF power level (%) and modulator voltage (kV) can be predicted by fitting a mathematical function to the data collected during the parameter scans (Figures 5.21 and 5.27), the resulting fittings are combined to produce the following (Equation 5.1) for phase shift with respect to RF power and modulator voltage.

$$\delta\theta = [a \cot \ln(x_{RF})] + b + [c \cdot x_{mv}] + d = [a \cot \ln(x_{RF})] + [c \cdot x_{mv}] + e \quad (5.1)$$

Equation 5.2 is found by inserting the calculated constants from the RF power and modulator voltage scan. The gradient and the intercept are calculated from the measurements in Figure 5.27.

$$\delta\theta = [(0.43x_{mv} - 124) \cot \ln(x_{RF})] + [1.4 \cdot x_{mv}] + 445 \quad (5.2)$$

The result is a surface plot (shown in Figure 5.30) showing the change in phase shift for all RF power and modulator voltage ranges. In this calculation the effect of the pulse length is ignored because it does not have a strong influence on the phase shift.

Partial differentiation can be used to predict how much the phase across the klystron will change due to changes in either the RF power or modulator voltage. The results are shown in Figure 5.32. The greatest change in the phase shift occurs when operating at high modulator voltage levels and low RF power levels, which can be seen in the top corner of the left hand plot (this is the steepest gradient)

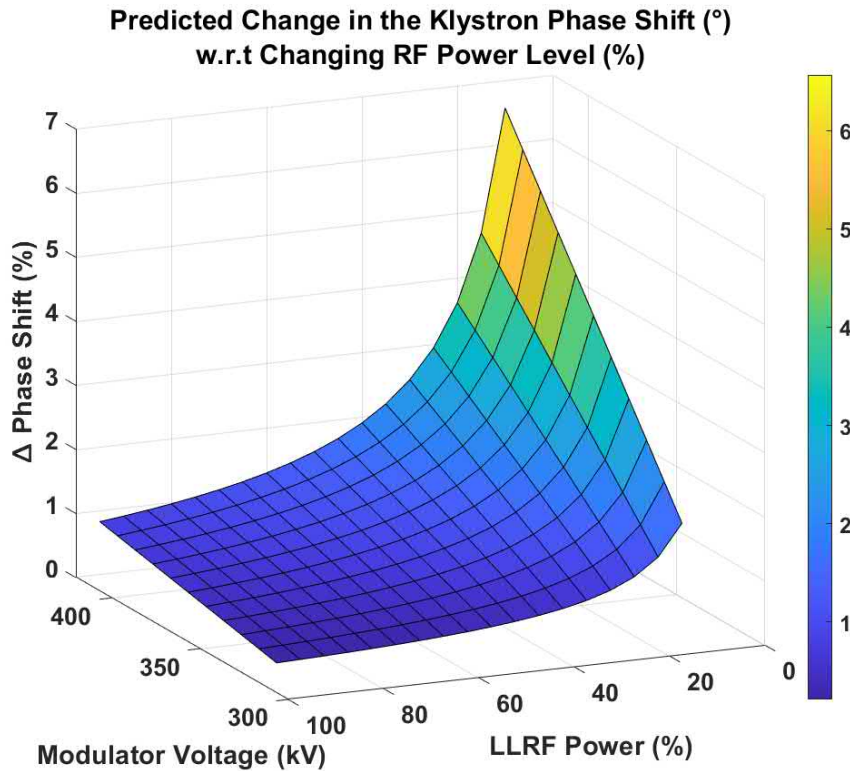


FIGURE 5.32: Predicted change in the phase shift across the klystron (°) when changing the RF power level (%)

### Klystron Phase Stability

The pulse-to-pulse phase stability at the output of the klystron responds to all three input variables. Using the relationships between input and output variables and the klystron gain curves, it is possible to create a 'mapping' which will describe how the phase shift and stability are likely to change in response to changes in the operating points. A percentage change in the modulator voltage behaves linearly, whereas a change in the RF power level changes according to the changing gradient of the gain curve. This is due to the fact that the RF power level determines the proximity to saturation on the gain curve. This process can be repeated when considering the phase stability, however the complexity is increased as the phase stability responds to all three input variables. The results were shown in Figure 5.20, Figure 5.22 and Figure 5.29. The phase stability responds linearly with modulator voltage and inversely to the RF pulse length. The phase stability is inversely proportional to the RF power level and the relationship can be described in the form:

$$y = a \cdot x^b$$

where both  $a$  and  $b$  are functions of the modulator voltage level.

The same mathematical fitting process has been repeated from Equation 5.1 whereby a function has been matched to the measured phase stability results from the parameter sweeps, the results were displayed in Figures 5.20, 5.22 and 5.29. The predicted pulse-to-pulse phase stability as a function of RF power level, modulator voltage and pulse length is described by Equation 5.4.4:

$$P2P_{Total} = [0.0031 \cdot x_{mv}] + [-0.0033 \cdot x_{PL}] + [(x_{mv} \cdot 0.1206) - 26.413 \cdot x_{RF}^{[(-0.0012 \cdot x_{mv}) - 0.289]}] + 1.1345$$

The change in phase stability with respect to the modulator voltage alone is  $0.0032^\circ$  per kV and for the RF pulse length is  $-0.0033^\circ$  per ns. These two parameters have similar but opposing effects on the phase stability. The RF power level has a more significant effect on the phase stability but the gradient is not constant. Differentiating with respect to the RF power level shows that the gradient is determined by the position along the gain curve as shown in Figure 5.33.

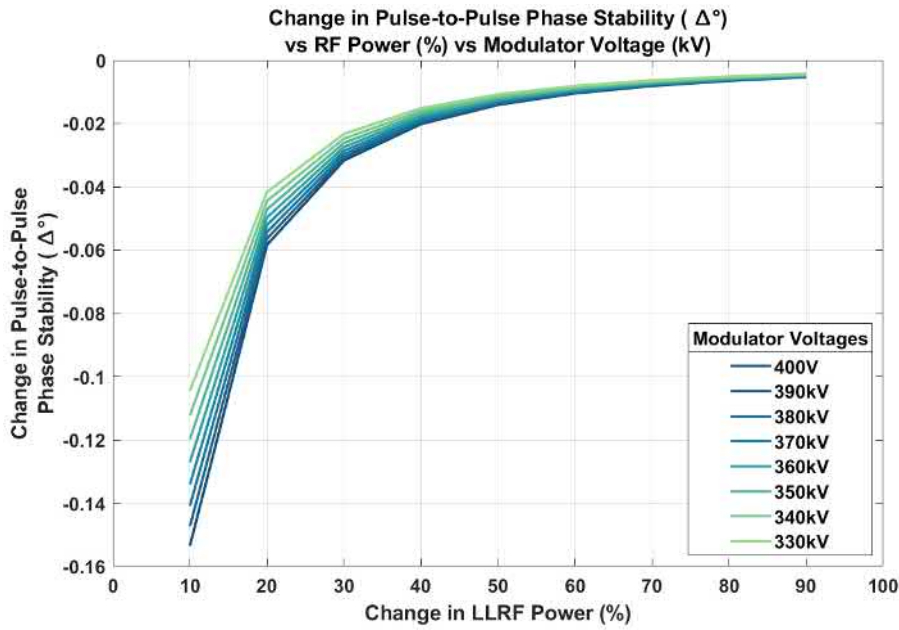


FIGURE 5.33: First Derivative of the Pulse-to-Pulse Phase Stability with respect to RF Power Level (%) and Modulator Voltage (kV)

#### 5.4.5 Modulator Voltage Ripple

A common feature of modulator high voltage pulses is ripple which was briefly mentioned in section 5.2.3. An example of the measured modulator voltage ripple is shown in Figure 5.34 for a 300 kV modulator pulse, (only the flat-top region is shown).

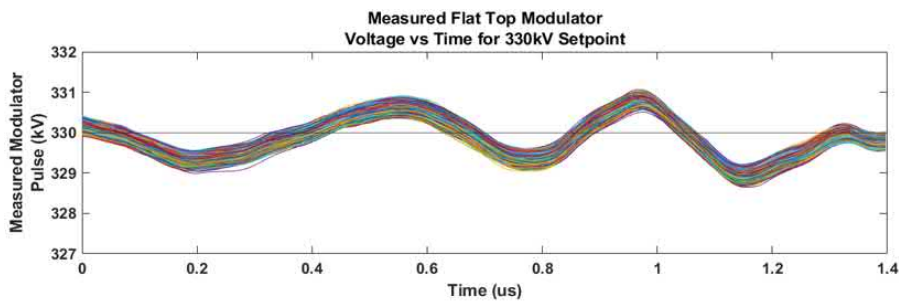


FIGURE 5.34: Measured modulator voltage ripple across the flat top region at for a modulator voltage setting of 330 kV

In this work the ripple will be defined as the maximum deviation between the minimum and maximum values along the flat top. The average measured ripple over 7000 pulses at 330 kV is 2.301 kV. The normalised standard deviation of the ripple at 33 kV is shown in Figure 5.35, the mean is 2.66 kV and standard deviation is 0.745 kV.

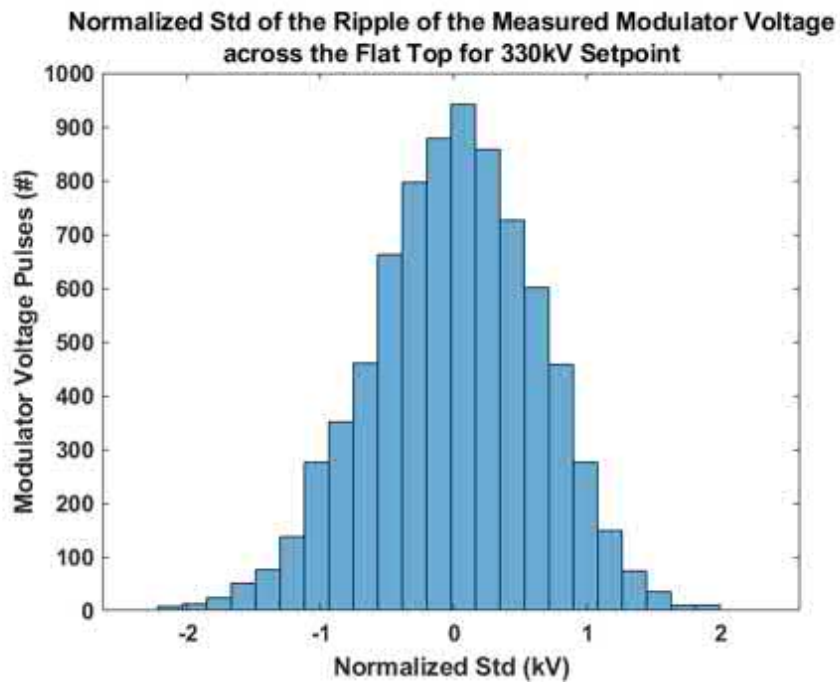


FIGURE 5.35: Normalized Standard Deviation of the Ripple across the Flat Top of the Modulator Voltage Pulse measuring the difference between the maximum and minimum across each flat top

The effect of the voltage ripple could be a contributor to the instability of the phase leaving the klystron. The ripple on the klystron phase affects the average phase value for each pulse which could be resulting in the large pulse-to-pulse stability. The correlation between the modulator voltage ripple and the total variation in the phase leaving the klystron is shown below in Figure 5.36. The phase variation is calculated as the maximum phase minus the minimum phase across each pulse flat top. The correlation is strong which suggests there is link between the two variables.

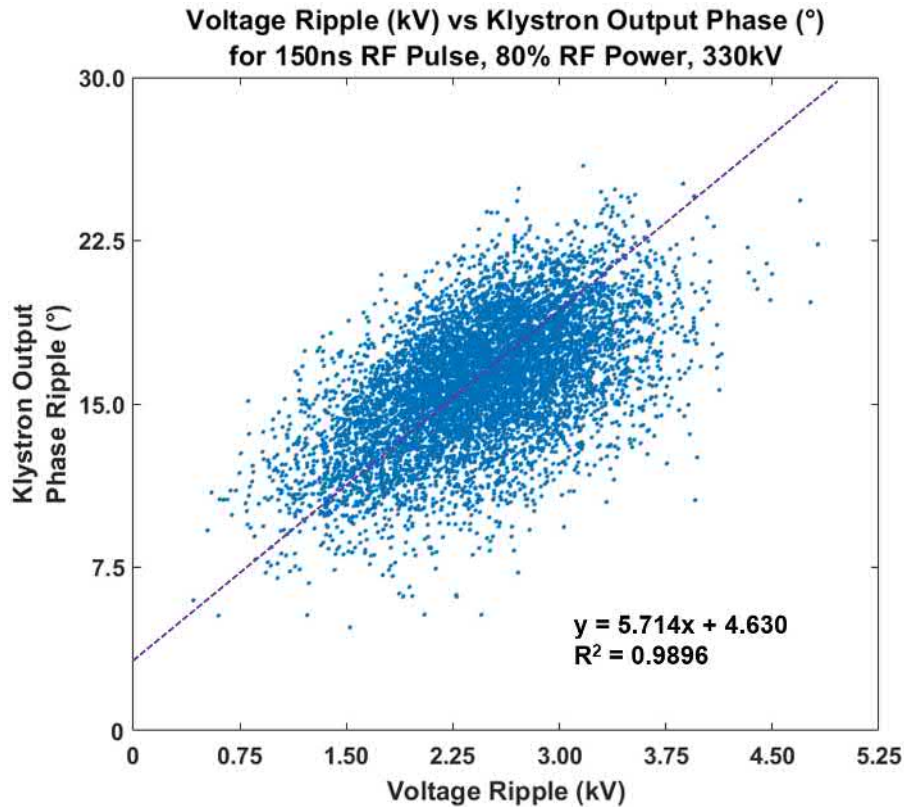


FIGURE 5.36: Correlation between the Modulator Voltage Ripple and the Deviation in Phase of Pulses exiting the Klystron, 250ns RF Pulse Length and 330kV Modulator Voltage Set-point

The PXI collects the traces for both the modulator voltage and klystron phase on each pulse: therefore, it is possible to apply a correction to account for the modulator voltage ripple to each individual pulse. The correction finds the point in time of highest correlation between the modulator voltage flat top and the klystron flat top. The deviation of the ripple from its mean is calculated and a corresponding phase is added or subtracted, the phase correction is calculated relative to the mean phase of the pulse. This correction method was applied in post-processing for a sample of 7000 pulses collected at 300 kV, 150 ns RF pulse length and 80% RF power. The correction theoretically reduces the phase stability at the output of the klystron as shown in Figure 5.37. Previously the standard deviation of the phase, without averaging, was  $\pm 3.157^\circ$ , after applying the ripple correction in post-processing the standard deviation is  $\pm 1.863^\circ$ .

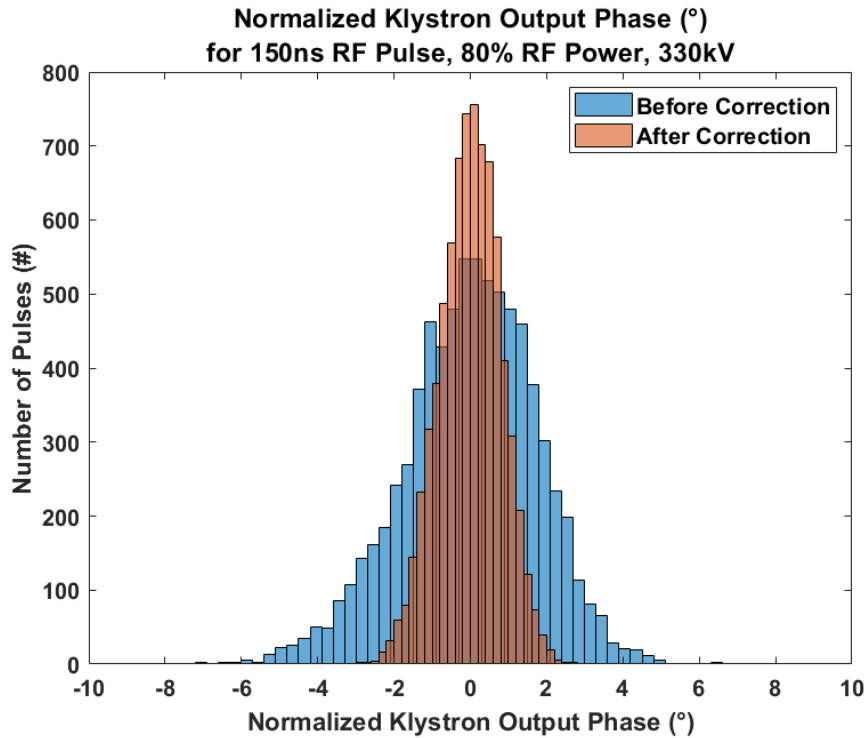


FIGURE 5.37: Klystron Output Pulse-to-Pulse Phase Stability Normalized around zero, before (Blue) and after (Orange) the ripple correction was applied in post-processing

## 5.5 Conclusion

The new LLRF system which was described in Chapter 3 has been installed at Xbox1 and integrated into the high power system and software. Each channel of the NI5162 oscilloscope cards is calibrated to correct for the DC offset and AC gain errors.

The up-converter and the PLL were both used successively as the 11.806 GHz local oscillator source. Data was collected over 7000 pulses in order to compare the phase and amplitude stability of the low power and high power components at Xbox1. The improvement in the phase noise of the up-converter translates to a reduction in the intra-pulse phase stability of the reference channel. The average intra-pulse phase stability of the reference channel is reduced by  $0.385^\circ \pm 0.027^\circ$ . The improvement in the intra-pulse stability of the reference translates to a small improvement in the intra-pulse stability of the TWT output and the klystron output;  $0.263 \pm 0.031^\circ$  for the TWT and for the klystron  $0.150 \pm 0.132^\circ$ . However, the intra-pulse stability is degraded by the TWT and klystron.

The pulse-to-pulse phase stability of the TWT and klystron do not achieve the  $1^\circ$  phase stability goal. There is not a significant difference in the intra-pulse amplitude stability between the PLL and the up-converter. The intra-pulse amplitude stability

for the up-converter is  $0.1316\% \pm 0.036\%$  and for the PLL is  $0.1684\% \pm 0.033\%$ . As with the phase stability, the amplitude stability becomes successively worse after the TWT and again after the klystron, the amplitude stability leaving the klystron is  $0.532\% \pm 0.717\%$ . The desired amplitude stability leaving the klystron is 0.1% amplitude stability, this is not achieved on a pulse-to-pulse basis.

It was established that the amplitude and phase stability of the 50 MW klystron at Xbox1 is not sufficient to meet a standard of 0.1% amplitude stability and  $1^\circ$  phase stability without further development.

A sensitivity analysis was performed on the klystron at Xbox1. This involved varying the input parameters one at a time and measuring the response at the klystron output. In particular the study focused on the pulse-to-pulse phase stability. This was possible as Xbox1 has the capability to record both phase and amplitude before and after the klystron as well as measuring the modulator voltage. The phase shift across the klystron increases linearly with modulator voltage and is insensitive to the RF pulse length. The phase shift response to the RF power level is logarithmic with the exact parameters of the fit being simultaneously dependent on the modulator voltage. Thus the effects of the RF power level and the modulator voltage cannot be decoupled. Similarly, the pulse-to-pulse phase stability of the klystron is responsive to the modulator voltage, RF power level and RF pulse length. The stability increases linearly with pulse length and decreases linearly with modulator voltage. The gradient of these effects are 0.0033 and -0.0031 so the two parameters have essentially equal and opposite effects. The measurements of the modulator voltage ripple exhibit ripple over the flat top region. It is proposed here that the ripple is causing voltage variations across the klystron output phase. A correction was applied to each individual pulse in post processing which increased the stability of the phase leaving the klystron. The modulator voltage could be an important parameter to be improved to enhance klystron stability.

## Chapter 6

# Single Path Inteferometry for High Precision Phase Measurements of Phase Shifts in X-Band Waveguide Networks

### 6.1 Introduction

In an accelerator facility it is common for the high power RF source to be located a short distance away from the beam line and for a single klystron can be used as the source for multiple accelerating structures [118]. In these cases the RF source and the accelerating structures are coupled by lengths of waveguide. This waveguide network will be subject to vibrations, ground movement and temperature changes. These disturbances alter the phase velocity of the RF due to changes in the physical dimensions of the waveguide. This results in a varying phase shift between the RF leaving the klystron and the RF arriving at the accelerating structures. This phase effect alters the synchronism between the RF and the beam resulting in sub-optimal beam acceleration. Characterisation of the magnitude and timescale of these disturbances is required to determine if and how corrections should be made.

The length of the high power waveguide network which connects Xbox1 and CLEAR is approximately 30 m. For the existing high power network, installed prior to 2021, RF signals are sampled immediately after the pulse compressor and also at the end of the waveguide network just before input to the accelerating structures. As a local synchronised phase reference is not available at the two ends of the waveguide network then disturbances to the network are not determined by

available measurements in an absolute sense. The installation of a local synchronised phase reference would allow disturbances to be characterised. However, due to the short RF pulse lengths and modulation during pulse compression such measurements would not allow correction to be made on a timescale less than the pulse repetition rate which is 50 Hz. Single path interferometry along the high power RF path is proposed as a method to both characterise environmentally driven phase variations and also enable continuous correction hence constant phase delivery [119]. The phase of reflected pulses is compared with the phase of a master oscillator at the input of the waveguide network.

The high power RF path is a mix of WR90 waveguide and low loss over-moded circular waveguide. The interferometer must be fully compatible and in no way detrimental to the delivery of high power pulses. The method employed measures waveguide length at a slightly different frequency and a much higher pulse repetition rate than the high power pulses. The frequency of the measurement pulses is chosen so they are almost fully reflected by the Linac acceleration structure but can propagate freely through all sections of the waveguide network. The implementation and experiments described here provide a proof of principle. As well as being relevant to the CLIC project, this technique described will be of interest to the Free Electron Laser community where femto-second synchronism of high power short pulse linacs is required [118] [120]. One useful property of FELs is their ability to achieve microbunching of the electrons in the beam. This is best achieved if the electrons have identical energies leaving the LINAC. Therefore, the greater the LINAC RF stability, a greater degree of microbunching can be achieved. Thus, the RF output from the klystron amplifiers is of critical importance.

## 6.2 Theory of Operation

The proposed measurement method requires that a number of low power RF pulses be injected into the waveguide in between subsequent high power pulses. The length of the low power pulses needs to be sufficient for an accurate measurement of phase to be made. A suitable pulse length allowing accurate measurement of phase could be just a few microseconds depending on the precision in femto-seconds that is required at the structure. Johnson noise is the ultimate limiting factor. In order that measurements are not affected by multiple reflections along the full network, then for pulse lengths longer than a few hundred nanoseconds a circulator at the source of

the low power pulse is required. The repetition rate of the low power pulses needs to be sufficient to track disturbances and hence depends on how quickly phase is changing with respect to the precision required. A repetition rate in the range 1 kHz to 5 kHz is planned for the measurement system.

A significant challenge with our interferometric measurement proposal is the requirement of a method for injecting both high power and low power pulses into the same network whilst keeping the low power source isolated from the high power source. Effectively a diplexer is needed. One requires minimal absorption or reflection of the high power pulses through the injection network and the whole network must tolerate extremely high power levels.

The low power measurement pulse travels through the injection network, then the waveguide network, reflects from the accelerating structure then travels back through the waveguide network, through the injection network back to the point of measurement where it must have sufficient amplitude to be measured accurately. A modest loss can be tolerated but reflections in the waveguide network must be minimised as they introduce reflections which result in errors in determining the phase change for the whole transmission length. Reflection from intermediate impedance mismatches on the network arrive back at the measurement point with a phase that does not depend on the full length of the measurement and hence contaminates the measurement of the full length.

The operating frequency of the CLIC accelerating structure is 11.9942 GHz and at this frequency these structures reflect less than 0.01% of their input power. They become over 95% reflecting at an offset frequency of approximately  $-50$  MHz. Some of the high power components used in the waveguide network have relatively narrow bandwidths. The available bandwidth for the measurement frequency around the high power frequency is primarily limited by the presence of a jog mode converter. A jog mode converter is the name used to describe a mode converter where the conversion happens inline (as opposed to being a bend), in this case a taper and dogleg shape converts rectangular mode to the circular mode.

The mode converter from the rectangular TE<sub>01</sub> mode to the circular TM<sub>01</sub> mode, shown in Figure 6.1, has a bandwidth of just 110 MHz for  $-30$  dB reflection [121]. The 'jog converter' is a compact mode transducer, consisting of two oppositely oriented  $\pm 45^\circ$  bends, separated by a very short phasing section, which gives complete conversion between TE<sub>10</sub> and TE<sub>20</sub> [122].

An offset frequency for the measurement pulse of  $-55$  MHz satisfies the bandwidth criterion of the waveguide network and the reflection criterion at the accelerating structure. The chosen measurement frequency is therefore near  $11.9392$  MHz.

A typical high power pulse is  $50$  MW and is supplied by a klystron. For an accelerating cavity with typical a reflection coefficient of  $-43$  dB at the high power operating frequency will have a returning pulse magnitude of  $2.5$  kW in the absence of waveguide losses. In order for the receiver to handle reflected pulses from the klystron and reflected measurement pulses then ideally the measurement pulse need to be a few kW. The klystron cannot be configured to give high repetition low power pulses. The measurement pulse for our system is therefore generated using a signal generator and then amplified using a TWT. From this point forward the measurement pulses will be usually be referred to as the 'TWT' pulses and the high power pulses the as 'klystron' pulses. The output power from the TWT available for this experiment is  $1$  kW. In order to handle full reflection of a  $50$  MW pulse in the event that a vacuum breakdown occurs in the accelerating structure or the waveguide network, then  $60$  dB couplers are routinely used for sampling signals. A  $50$  MW pulse that is fully reflected could potentially deliver a  $50$  W pulse after the directional couplers. After attenuation in the waveguide system, reflected TWT pulses were expected to have power levels above  $500$  W hence the signal after a  $60$  dB directional coupler would be of the order of  $0.5$  mW =  $-3$  dBm. The measurement electronics must be optimised for receiving signals in the range  $-3$  dBm to  $1$  dBm whilst not being susceptible to damage from  $47$  dBm pulses.

The interferometer implementation is complicated by the general availability of high power X-band components and the use of SLAC flanges at Xbox1 which are gendered. One method that could be used to inject two different frequencies would be a magic tee. However, a high power X-band magic tee was not available. An alternative four port device is a quadrature hybrid. This is slightly more complex as it induces a  $90^\circ$  shift between the output ports depending on the input port used. When pulsing into either port 1 or port 4 of the quadrature hybrid the power will be split between port 2 and 3 with a quadrature phase shift between them. This power will need to be recombined before injection into the waveguide network, this would be true for both the magic tee and hybrid. The S-matrix for the perfect quadrature hybrid is:

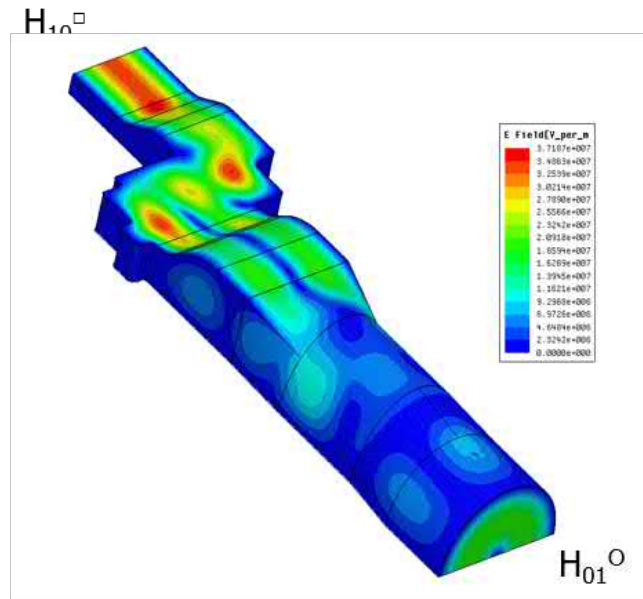


FIGURE 6.1: The Electric Field Profile of the Jog Mode Converter which converts rectangular WR90 to Circular Waveguide [121]

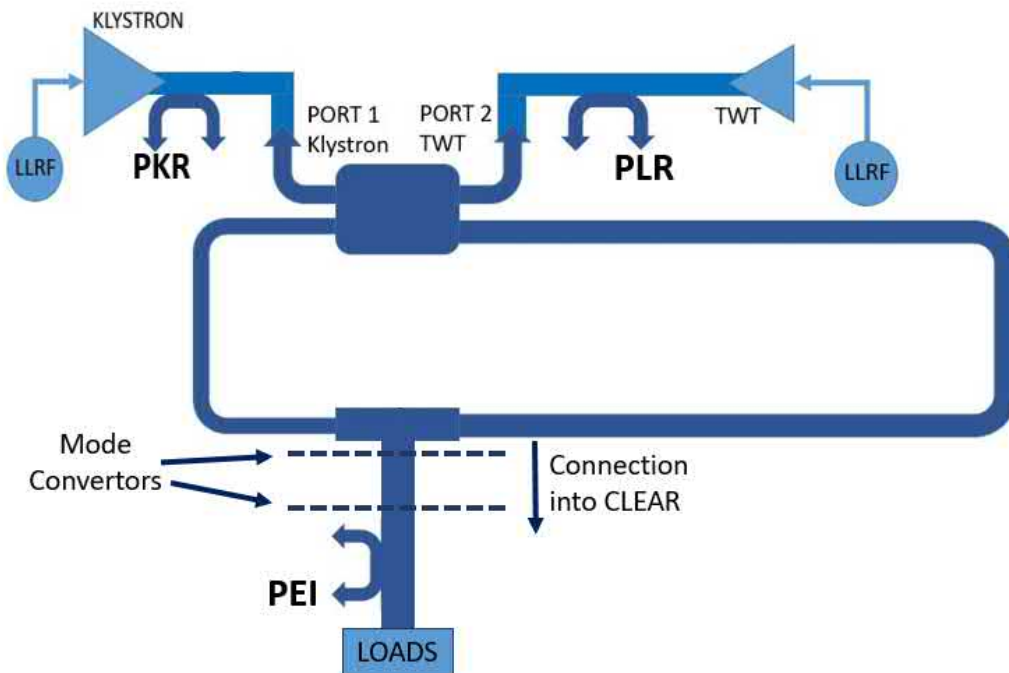


FIGURE 6.2: Schematic showing the proposed integration of the interferometer at Xbox1

$$S_{Hybrid} = \begin{bmatrix} 0 & \frac{-j}{\sqrt{2}} & \frac{-1}{\sqrt{2}} & 0 \\ \frac{-j}{\sqrt{2}} & 0 & 0 & \frac{-1}{\sqrt{2}} \\ \frac{-1}{\sqrt{2}} & 0 & 0 & \frac{-j}{\sqrt{2}} \\ 0 & \frac{-1}{\sqrt{2}} & \frac{-j}{\sqrt{2}} & 0 \end{bmatrix} \quad (6.1)$$

The high power component available for recombination is a H-plane tee, this device will recombine the power completely when the input into the two sidearms are in-phase. The S-matrix for the perfect H-plane tee is:

$$S_{Tee} = \begin{bmatrix} \frac{1}{2} & \frac{-1}{2} & \frac{1}{\sqrt{2}} \\ \frac{-1}{2} & \frac{1}{2} & \frac{1}{\sqrt{2}} \\ \frac{1}{\sqrt{2}} & \frac{1}{\sqrt{2}} & 0 \end{bmatrix} \quad (6.2)$$

Therefore a system is required which will correct for the quadrature phase shift from the hybrid at both frequencies in order for the split power to correctly recombine at the tee. Two waveguide arms of differing length will be used to create a delay line which will induce a 90° phase advance between the two paths. The proposed high power implementation is shown in Figure 6.2. The interferometer is placed in between the pulse compressor and the start of the long waveguide network. A secondary TWT and LLRF system is used to generate the ‘phase measurement’ pulses which enter port 4 while the klystron pulses into port 1.

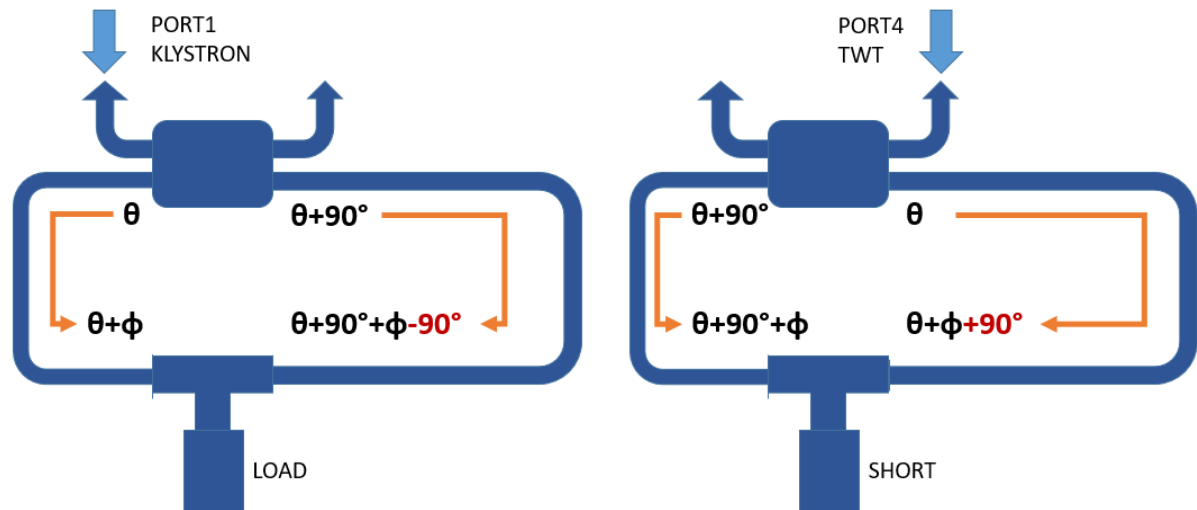


FIGURE 6.3: Interferometer Schematic demonstrating the required phase shift at both the Klystron Frequency and the TWT Frequency

Assuming the klystron pulses enter into port 1 of the hybrid and are split with the  $90^\circ$  phase shift appearing on port 3. Then the path difference between the two arms must introduce a phase shift of  $-90^\circ$  or  $270^\circ$  at 11.9942 GHz. The second frequency is introduced into the system using port 4 of the hybrid, in this case the quadrature phase shift will move onto port 4. The same process applies here, the difference in path length between the hybrid and the combiner must either gain  $90^\circ$  or gain  $270^\circ$  at the second frequency. This is visualised in Figure 6.3. There are two options, the extra length adjacent to port 1, shown in Figure 6.3, or the extra length adjacent to port 4, not shown. Both give valid solutions which are extremely similar.

The path length in WR90 waveguide must satisfy the requirements for phase advance at both frequencies simultaneously. An exact path length exists which will induce the correct phase shift at both frequencies, the length will be an exact number of cycles of each frequency plus or minus a quarter wavelength at the respective frequencies. This exact length is dependent on the second frequency which can be selected. Provided it remains within the restraints of the high power system. The TWT frequency must be within the 110 MHz bandwidth of the mode-convertors. In addition, the second frequency must be suitably close to the CLIC frequency so that the IF is sufficiently small that IQ sampling can be performed with the available digitizers at Xbox1.

A  $90^\circ$  phase shift at 11.9942 GHz is a path length change of 6.25 mm. As the components in the interferometer must be symmetrical, this phase shift will be added as part of two straight sections, shown in Figure 6.2, which will each introduce  $45^\circ$ ,

this is approximately 3.125 mm. The lengths of waveguide between the quadrature Tee and the combiner Tee must be maintained to micron accuracy in order to minimize reflection at the combiner Tee. Fine control and maintenance of path length will be achieved by temperature adjustment and control of the long waveguide arms.

In order for this measurement to be successful, any unwanted phase shifts induced by the interferometer must be reduced or characterized. The temperature of the waveguide affects the phase shift induced between the two arms which reduces the recombination at the tee.

When pulsing from the klystron, the RF power should be split by the hybrid and recombined at the tee recovering full amplitude, as though the interferometer is invisible to the high power pulses. When pulsing into the TWT port the signal should also split and recombine without loss. Any reflections at the tee due to incorrect phasing will direct power back to the hybrid and then back to the klystron or TWT. Reflections of this nature should be minimized to the limit of detection. The interferometer system should never be operated at high power when the arms are not correctly phased. Hence Xbox1 should not be operated at high power before the interferometer has reached its operating temperature.

### 6.3 Determining TWT Frequency and Path Length

There will be identical waveguide path lengths where the klystron frequency can rotate through an integer number of wavelengths  $m$  plus one quarter and the TWT frequency can rotate through an integer number of wavelength  $n$  minus a quarter. For a given klystron frequency and a given choice of the number of complete wavelengths, the TWT frequency is prescribed. The condition for perfect recombination at both frequencies is therefore  $n + 0.5 = m$ .

It has been previously noted that there are some limitations on the choice of the TWT frequency so the TWT frequency needs to be within  $\pm 55\text{MHz}$  of the CLIC RF frequency. As the two frequencies are so close together their wavelengths will be similar. and the values of  $m$  and  $n$  will be large. The shortest additional waveguide lengths for chosen frequencies will occur either for  $n = m$ ,  $n=m+1$  or  $m=m-1$ . To convert to a physical length the frequencies will be converted to the guide wavelength in WR90 waveguide. Guide wavelength is defined as the distance between two equal phase planes inside the waveguide. The guide wavelength is a function of operating frequency and the lower cutoff wavelength, and is always longer than the wavelength in free-space.

The equation for determining the guide wavelength with respect to the frequency,  $f$ , and the dimensions of the waveguide,  $a$ , is [119]:

$$\lambda_{\text{Guide}} = \frac{c}{f} \cdot \frac{1}{\sqrt{1 - \left(\frac{c}{2a \cdot f}\right)^2}} = \frac{\lambda}{\sqrt{1 - \left(\frac{\lambda}{\lambda_c}\right)^2}} \quad (6.3)$$

For rectangular WR90 waveguide the width of the waveguide is represented by  $a$ , this is 22.86 mm and the exact RF frequency is 11.9942 GHz. The spatial wavelength of the CLIC RF frequency in WR90 is 0.029 850 5 m.

Figure 6.4 corresponds to the interferometer layout of Figure 6.3 but defines variables for the waveguide lengths and the wavelengths. The long path is shown as  $x_2$  but one could also make  $x_1$  the long path. These cases are different algebraically as the system is not symmetrical because the wavelengths are different.

At the klystron frequency pulsing into port 1, the phase shift induced by each of the two paths ( $x_1$  and  $x_2$ ) are described by:

$$\theta_{\text{Kly1}} = \frac{\pi}{2} + \frac{2\pi x_1}{\lambda_1} \quad (6.4)$$

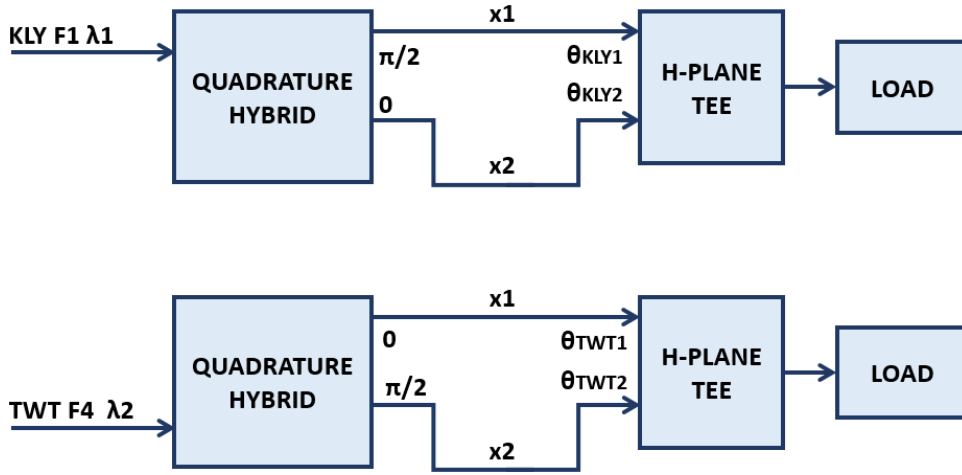


FIGURE 6.4: Diagram defining variable for the additional length calculation. Note lack of symmetry in interchange of input ports (F1 and F4)

$$\theta_{2Kly} = \frac{2\pi x_2}{\lambda_1} \quad (6.5)$$

Note that path 1 induces an extra  $\frac{\pi}{2}$  phase shift due to the quadrature hybrid. So the difference in phase between the RF arriving at the tee is:

$$\Delta x = x_1 - x_2$$

$$\Delta\theta = \theta_{Kly1} - \theta_{Kly2} = \frac{\pi}{2} - \frac{2\pi}{\lambda_1} \Delta x = 2\pi m \quad (6.6)$$

Where  $m$  has already been defined as the number of whole wavelengths in the difference of waveguide lengths for the klystron frequency. Similarly, at the second frequency (TWT) and pulsing into port 4, the phase shift over the two paths is:

$$\theta_{TWT1} = \frac{2\pi x_1}{\lambda_2} \quad (6.7)$$

$$\theta_{TWT2} = -\frac{\pi}{2} + \frac{2\pi x_2}{\lambda_2} \quad (6.8)$$

The extra  $\frac{\pi}{2}$  phase shift has now swapped ports, so the difference in phase between the RF arriving at the tee is:

$$\Delta\theta = \theta_{TWT1} - \theta_{TWT2} = \frac{\pi}{2} - \frac{2\pi}{\lambda_2} \Delta x = 2\pi n \quad (6.9)$$

where  $n$  has already been defined as the number of whole wavelengths in the difference of waveguide lengths for the TWT frequency.

The difference in length between the two paths,  $\Delta x$ , is determined such that both of the phase difference equations 6.6 and 6.9 are satisfied and this gives:

$$\Delta x = \lambda_1 \left( m + \frac{1}{4} \right) = \lambda_2 \left( n - \frac{1}{4} \right) \quad (6.10)$$

The smallest additional length might occur under one of three scenarios;  $m = n$ ,  $m = n + 1$ , or  $m = n - 1$ , giving three different solutions. The klystron frequency is already determined, both  $m$  and  $n$  must be determined in order to find a suitable TWT frequency within the desired bandwidth.

The length difference is eliminated from equation 6.10 and the equation is rearranged to find  $n$ . For the case where  $m = n$ :

$$\lambda_1 \left( n + \frac{1}{4} \right) = \lambda_2 \left( n - \frac{1}{4} \right) \quad (6.11)$$

$$n = \frac{1}{4} \left( \frac{\lambda_2 + \lambda_1}{\lambda_2 - \lambda_1} \right) \quad (6.12)$$

For the case where  $m = n + 1$ :

$$\lambda_1 \left( n + \frac{5}{4} \right) = \lambda_2 \left( n - \frac{1}{4} \right) \quad (6.13)$$

$$n = \frac{5\lambda_1 + \lambda_2}{4(\lambda_2 - \lambda_1)} \quad (6.14)$$

Finally, for the case where  $m = n - 1$ :

$$\lambda_1 \left( n + \frac{3}{4} \right) = \lambda_2 \left( n - \frac{1}{4} \right) \quad (6.15)$$

$$n = \frac{3\lambda_1 + \lambda_2}{4(\lambda_1 - \lambda_2)} \quad (6.16)$$

$n$  must be a positive integer as the waveguide cannot have a negative length. Equations 6.12 and 6.14 gives valid solutions when the wavelengths are close only if  $\lambda_2 > \lambda_1$  whilst Equation 6.16 gives a valid solution for close wavelengths when  $\lambda_1 > \lambda_2$ . It is apparent that Equations 6.12 and 6.16 give solutions with the smallest value of  $n$  and hence the shortest excess waveguide. Solution 6.14 and other solutions

have much larger values of  $n$  and hence longer waveguide lengths so will not be of interest here. If  $\lambda_1$  (feed with zero phase shift to long leg) corresponds to the high power pulse with a shorter wavelength than the measurement pulse then equation 6.12 determines  $n$  and hence the additional length of waveguide.

Note that  $\lambda_1$  corresponds to the top diagram in figure 6.4 where power is injected such that zero phase shift goes to the long leg and  $\pi/2$  phase shift goes to the short leg. One also sees that  $\lambda_2$  corresponds to the bottom diagram in figure 6.4 where power is injected such that zero phase shift goes to the short leg and  $\pi/2$  phase shift goes to the long leg. A lower TWT frequency is required and hence longer wavelength for the measurement pulse. One of the two solutions 6.12 and 6.16 must be selected to get a lower frequency for the measurement pulse dependent on whether high power is injected to port 1 or port 4. The other solution can then be used when two sources (klystron and TWT) are swapped so that  $\lambda_2$  corresponds to the top figure instead of the bottom figure. In this case 6.12 becomes:

$$\lambda_{2s} \left( n + \frac{1}{4} \right) = \lambda_{1s} \left( n - \frac{1}{4} \right) \quad (6.17)$$

There is a second set of solutions which are derived from explicitly changing the phase shifts on hybrid. These solutions are detailed in appendix C.

Once the guide wavelength of the klystron frequency in WR90 is known,  $m$  is set to an integer value and the TWT frequency is swept in order to find a frequency where  $n - 0.5$  is close to an integer to within three significant figures. When the TWT frequency is known the path length can be found and the intermediate frequency is simply the difference between the Xbox1 local oscillator and the TWT frequency.

The frequency offset is relative to the main CLIC frequency of 11.9942 GHz, this is noted to ensure the second frequency remains inside the bandwidth of the mode convertors. Increasing the difference between the klystron frequency and the TWT frequency (within the bandwidth of the mode convertor) will reduce the path length but increases the IF frequency to be sampled. Formulas are evaluated for differing values of  $n$  expected to give the TWT frequency within the required bandwidth. Two cases will be shown in this work, one for high power tests and one for low power tests, the parameters for both cases are summarised in Table 6.3.

Filling Medium	Frequency (GHz)	$n_{TWT}$	$\delta L$ (m)
Air	11.92635	65	1.947734
Vacuum	11.93911	76	2.276097

As the system will be symmetrical the difference in path length will be achieved using two pieces of WR90 waveguide, each length will be heated to continuously correct the length as will be discussed in the next section. The frequency offset is slightly greater than 55 MHz but it is close enough that the power reduction due to the mode converters will be very small.

## 6.4 Phase Changes in the Waveguide due to Temperature

The waveguide network between Xbox1 and the accelerating structures at CLEAR is constructed from two different waveguide types, approximately 10 m of WR90 rectangular waveguide and 20 m of circular over-moded waveguide. The over-moded waveguide utilises the TE<sub>01</sub> mode which exhibits particularly low loss because the magnetic field distribution of the mode generates lower current levels on the walls of the waveguide than the other waveguide modes. Therefore, a circular waveguide carrying this mode is commonly used when signals are sent over relatively long distances

Both types of waveguide are sensitive to changes in temperature. Thermal expansion and contraction of the copper changes the dimensions of the waveguide which changes the phase velocity and guide wavelength of the propagating RF. The copper will expand linearly according to:

$$\Delta L = \alpha L \Delta T \quad (6.18)$$

Where  $\Delta L$  is the expansion in mm,  $\alpha$  is the coefficient of linear expansion, which has units of  $\text{ppm}^\circ\text{K}^{-1}$ ,  $L$  is the original length in m, and  $\Delta T$  is the change in temperature in  $^\circ\text{C}$ . Over the course of one day the temperature can typically vary by  $10^\circ$ . The thermal expansion coefficient of pure copper is  $16 \text{ } \mu\text{m per}^\circ\text{K}$  at ambient temperatures (approximately  $23^\circ$ ).

The interferometer is designed to measure thermal and environmental changes in the waveguide network. If the diplexing section of the interferometer also expands and contracts with the environmental changes then this will negate the measurement of the waveguide length to the structure. Hence, the interferometer, specifically the path length, will need to be thermally stabilised and isolated from the environment. This will ensure changes in the interferometer will not be conflated with changes in the length of the waveguide.

Guide wavelength was defined in Equation 6.3 in Section 6.3. The guide wavelength depends on  $a$ , the dimension of the broad wall of the waveguide. This dimension will expand when heated. For WR90 the width of the WR90 waveguide is 22.86 mm. One side of the interferometer, the 'short' arm, is connected to a cooling system. The other side, the 'long' arm is heated using heating tapes and thermally insulated. The two straight pieces of waveguide making up the path difference can be heated up to 100° C using the heating tapes, the total heated length is 1.948 m. The phase can be shifted through approximately an eighth of the wavelength by adjusting the temperature of the 'long' arms by up to 100°C.

One quarter wavelength at 11.939 85 GHz is 6.25 mm and this is split between the two arms, so 3.14 mm per arm. This must be kept exact in order for the recombination to work correctly. It is likely that manufacturing errors could have a significant effect on the recombination. Controlling the temperature up to 100° C is ample to be able to account for any errors due to manufacturing tolerances and to stabilise the length of the waveguide.

## 6.5 System Simulations

The behaviour of the interferometer can be predicted by solving for all of the forward and reflected signals using simultaneous equations. The equations will be formulated as a matrix with dependency on path lengths of the interferometer arms and the path length to the load (cavity). Matrix elements can also be given frequency dependency. The system will be solved using matrix inversion. The system with all signals is shown in Figure 6.5.

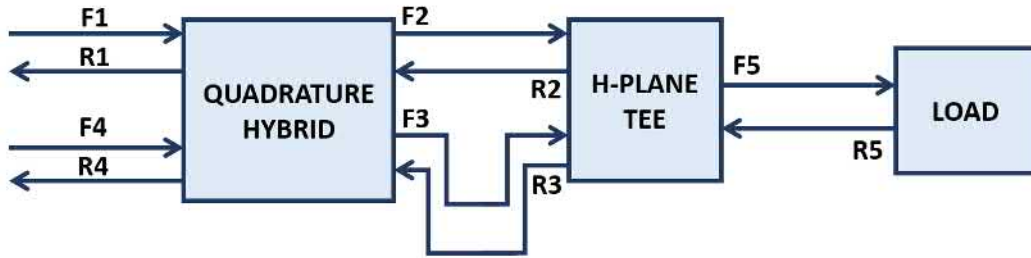


FIGURE 6.5: Diagram of the interferometer as used in the simulation. The matrix elements correspond to the forward and reflected signals at different point in the system as indicated here

Each arm of the interferometer arms has a different phase advance between the hybrid and the combiner. Let  $S_H$  be the s-matrix for the hybrid,  $S_T$  be the s-matrix for the tee and  $S_L$  be the s-matrix for the load. The inputs to the hybrid are F1 and F4. When pulsing into port 1,  $F1 \neq 1$  and  $F4 = 0$ . When pulsing into port 4 the reverse is true. The equations which describe the the behaviour at the hybrid, tee and line are shown in Equations 6.19, 6.20 and 6.21 respectively:

$$\begin{bmatrix} R1 \\ F2 \\ F3 \\ R4 \end{bmatrix} = [S_H] \times \begin{bmatrix} F1 \\ R2 \cdot \exp(j\varphi_2) \\ R3 \cdot \exp(j\varphi_3) \\ F4 \end{bmatrix} \quad (6.19)$$

$$\begin{bmatrix} R2 \\ R3 \\ F5 \end{bmatrix} = [S_T] \times \begin{bmatrix} F2 \cdot \exp(j\varphi_2) \\ F3 \cdot \exp(j\varphi_3) \\ R5 \cdot \exp(j\varphi_5) \end{bmatrix} \quad (6.20)$$

$$R5 = S_{LF5} \cdot \exp(j\varphi_5) \quad (6.21)$$

Where  $\varphi_n$  is the phase advance on the  $n^{th}$  line in Figure 6.5,  $\varphi_3$  is phase advance on the temperature adjustable long arm in the interferometer and  $\varphi_5$  is the phase advance on the line length to be measured. For an input at F4 the length of the long arm must be adjusted to set R1 to zero implying correct recombination.

The essence of the dual frequency operation is that line 3 must gain  $90^\circ$  when driven from one port (F1 or F4) but lose  $90^\circ$  when driven from the other port (F4 or F1). The method for calculating the additional line length required for the exact phase shifting was described in section 6.3. Inspection of Figure 6.5 tells one that the full interferometer system can be described by a  $9 \times 9$  matrix, M, with one input port and nine unknowns.

$$M = \begin{bmatrix} S_{11} & S_{12} & \cdots & S_{1n} \\ S_{21} & S_{22} & \cdots & S_{2n} \\ \vdots & \vdots & \ddots & \vdots \\ S_{n1} & S_{n2} & \cdots & S_{nn} \end{bmatrix}$$

The output of interest is the reflected signal at port 1 and port 4 of the hybrid with respect to the difference in path length and the length specified here as  $\varphi_5$ . For this calculation the two input frequencies must already be known, these were calculated in Section 6.3.

The terms in the matrix M are given by the matrix elements of the individual responses of the hybrid quadrature coupler, the tee and the load. The S-matrix of an ideal hybrid and h-plane tee were detailed in equations 6.1 and 6.2. For a real component there will be losses so the S-matrices are described by the following matrices which have been written in a symmetrical form to obey the reciprocity theorem:

$$S_{Hybrid} = -\frac{1}{\sqrt{2}} \cdot \begin{bmatrix} t_{11} & t_{12} & t_{13} & t_{14} \\ t_{12} & t_{22} & t_{23} & t_{24} \\ t_{13} & t_{23} & t_{33} & t_{34} \\ t_{14} & t_{24} & t_{34} & t_{44} \end{bmatrix} \quad (6.22)$$

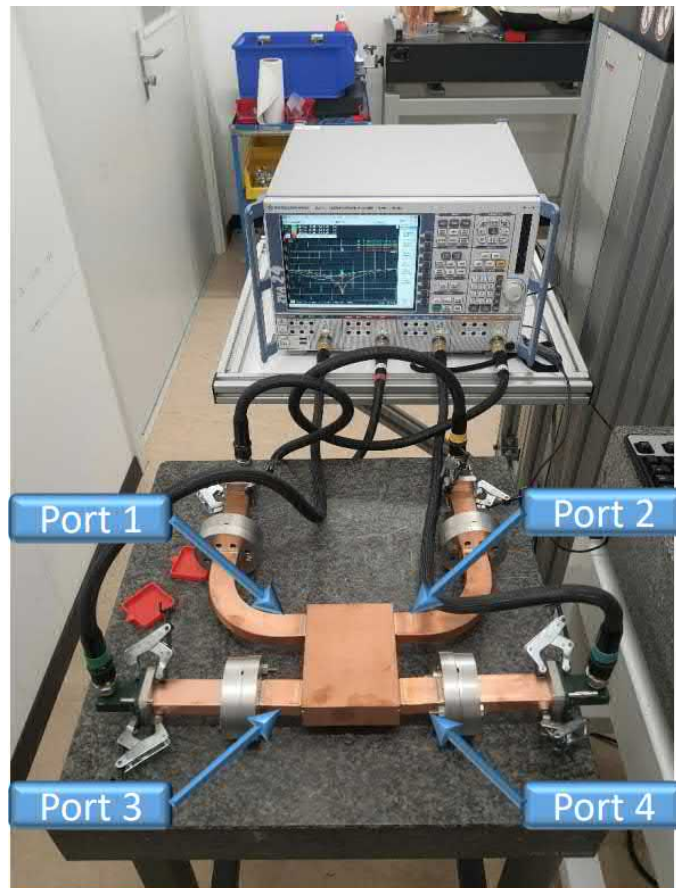


FIGURE 6.6: Hybrid during S-parameter Measurement in the RF Lab at CERN

$$S_{Tee} = \frac{1}{2} \cdot \begin{bmatrix} r_{11} & r_{12} & r_{13} \\ r_{12} & r_{22} & r_{23} \\ r_{13} & r_{23} & r_{33} \end{bmatrix} \quad (6.23)$$

Where  $t_1 \approx 0, t_4 \approx 0, t_2 \approx j, t_3 \approx 1$  and  $r_1 \approx 1, r_2 \approx -1, r_3 \approx 1.414, r_4 \approx 0$ . For convenience it is desirable to include frequency response for terms in the S matrices in a simple way. It was found that all the curves in Figure 6.7 can be accurately fitted with first order band-stop filters. The filters are characterised by a resonant frequency of the parallel arm, resistance in the parallel arm and a series resistance. The S-parameters of the high power hybrid (manufactured by CINEL) were measured on a Rohde and Schwarz ZVA24 4 port VNA. The amplitude response of the hybrid is shown in Figure 6.7.

The hybrid, tee and load were measured to obtain their s-parameters to be used in the simulations from Section 6.5. The parameters for the measurements are shown in Table 6.1 along with an image of the hybrid measurement in Figure 6.6. The span was changed for each component to reflect the expected bandwidth.

VNA	Rohde and Schwarz ZVA 24 (4-ports)
Calibration	TRL X-Band
Number of points	10001
Resolution BW	10kHz
Temperature	21°C
Center Frequency	11.992 GHz

TABLE 6.1: RF Measurement Settings Setup

The equations for the hybrid, tee and load (from Equations 6.19, 6.20 and 6.21) are formed into the matrix equation. Then for an input signal being injected into port 1 the matrix equation becomes:

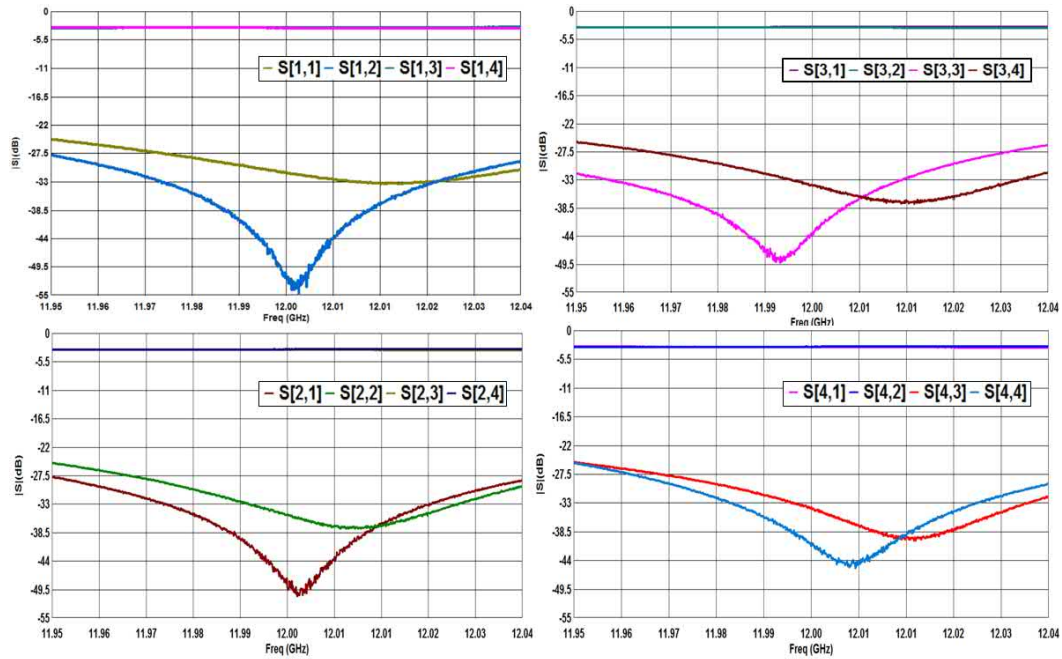


FIGURE 6.7: Measured Magnitude S-Parameters of High Power X-Band Hybrid produced by CINEL

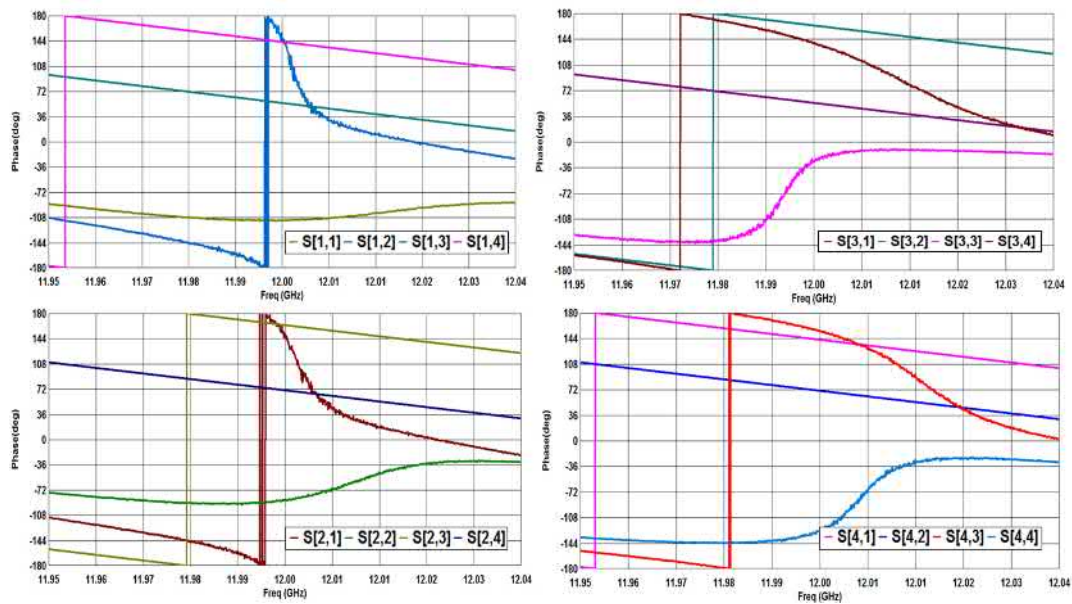


FIGURE 6.8: Measured S-Parameters: Phase (°) Response of the Hybrid

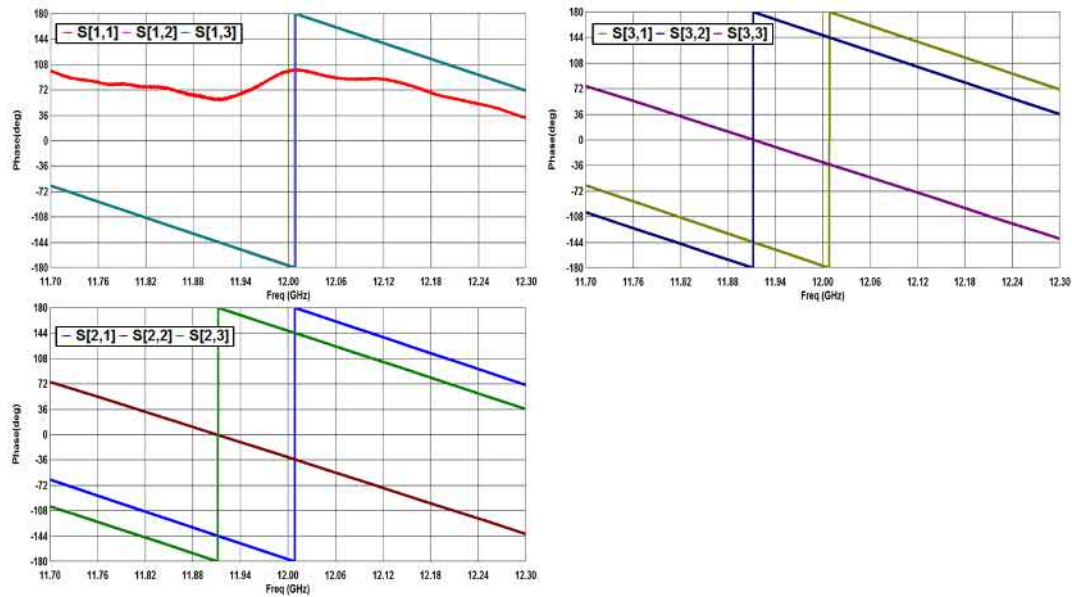


FIGURE 6.9: Measured S-Parameters: Magnitude (dB) Response of the H-Plane Tee

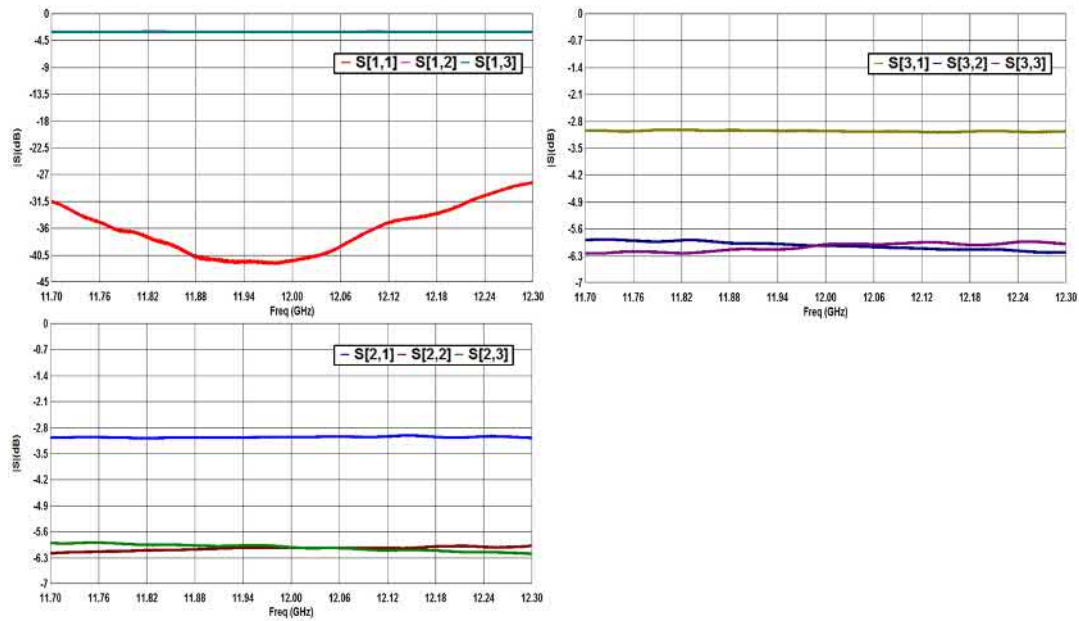


FIGURE 6.10: Measured S-Parameters: Phase (°) Response of the H-Plane Tee

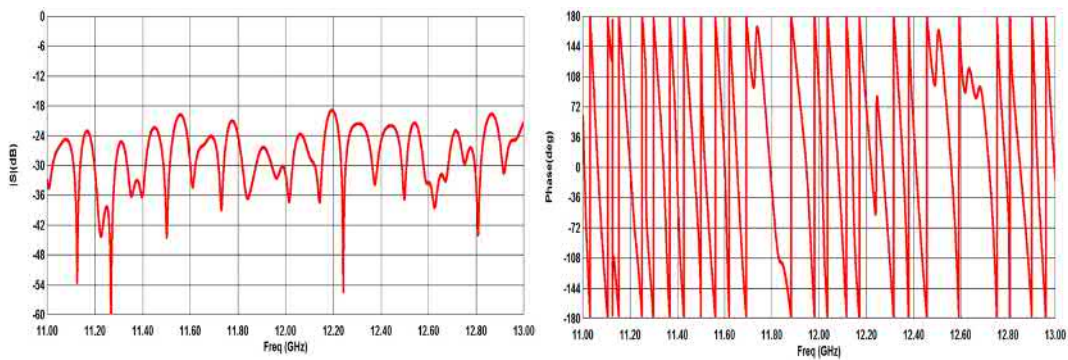


FIGURE 6.11: Measured S-Parameters: Magnitude (dB) and Phase (°) Response of a Low Power X-band Load

$$\begin{bmatrix}
 0 & t_{12}e^{j\varphi_2} & 0 & t_{13}e^{j\varphi_3} & t_{11} & 0 & 0 & 0 & \sqrt{2} \\
 \sqrt{2} & t_{22}e^{j\varphi_2} & 0 & t_{23}e^{j\varphi_3} & t_{12} & 0 & 0 & 0 & 0 \\
 0 & t_{23}e^{j\varphi_2} & \sqrt{2} & t_{33}e^{j\varphi_3} & t_{13} & 0 & 0 & 0 & 0 \\
 0 & t_{24}e^{j\varphi_2} & 0 & t_{34}e^{j\varphi_3} & t_{14} & \sqrt{2} & 0 & 0 & 0 \\
 r_{11}e^{j\varphi_2} & -2 & r_{12}e^{j\varphi_3} & 0 & 0 & 0 & 0 & r_{13}e^{j\varphi_5} & 0 \\
 r_{21}e^{j\varphi_2} & 0 & r_{22}e^{j\varphi_3} & -2 & 0 & 0 & 0 & r_{23}e^{j\varphi_5} & 0 \\
 r_{31}e^{j\varphi_2} & 0 & r_{32}e^{j\varphi_3} & 0 & 0 & 0 & -2 & r_{33}e^{j\varphi_5} & 0 \\
 0 & 0 & 0 & 0 & 0 & 0 & S_L e^{j\varphi_5} & -1 & 0 \\
 0 & 0 & 0 & 0 & 1 & 0 & 0 & 0 & 0
 \end{bmatrix}
 \begin{bmatrix}
 F2 \\
 R2 \\
 F3 \\
 R3 \\
 F4 \\
 R4 \\
 F5 \\
 R5 \\
 R1
 \end{bmatrix}
 =
 \begin{bmatrix}
 -t_{14}F1 \\
 -t_{24}F1 \\
 -t_{34}F1 \\
 -t_{44}F1 \\
 0 \\
 0 \\
 0 \\
 0 \\
 0
 \end{bmatrix}$$

### 6.5.1 Dependence on Difference in Path Length

The change in the reflected amplitude will be predicted as a function of the difference in path length between the two waveguide arms. For this calculation the klystron frequency is 11.9942 GHz and the TWT frequency is set to 11.9391 GHz, this was calculated in Section 6.3.

Although the load should reject across a broad bandwidth which covers both frequencies, in this simulation a quasi-load will be used which is set to absorb the the incident power at 11.9942 GHz and reject the power at 11.9391 GHz. The full code for the system simulation can be found in Appendix D

The input parameters for the simulation are shown in Table 6.2. The difference in the drive amplitudes is simply for demonstration, for a 10 MW klystron pulse and a 1 kW TWT pulse then the actual drive ratio is  $\sqrt{10000} = 100$ .

WR90 Width	22.86	mm
Speed of light	$2.99792458 \cdot 10^8$	m \ s
Filling Medium	Vacuum	
Frequency 1	11.9942	GHz
Frequency 4	11.9391	GHz
Drive Amplitude 1	100	
Drive Amplitude 2	1	
WR90 Waveguide Losses	0.0985	dB/m
Load S11 @ F1	-34.13dB -145.26°	
Load S11 @ F2	-0.78dB -42.69°	
Length 2	0.600	m
Length 5	19.995	m

TABLE 6.2: Parameters used for high power simulations of the interferometer Network presented in Figures 6.12 and 6.14

Figure 6.12 shows the proportion of the reflected signal which returns to both of the hybrid input ports (Port 1 and Port 4 in figure 6.5) when pulsing into port 1 at 11.9942 GHz. The ideal case occurs when all of the power is reflected back to port 1 and as little power as possible is leaked onto port 4. This occurs when the difference in path length is 2.276 097 m. A change in length on the order of several millimetres has a significant change on the transmission and reflection.

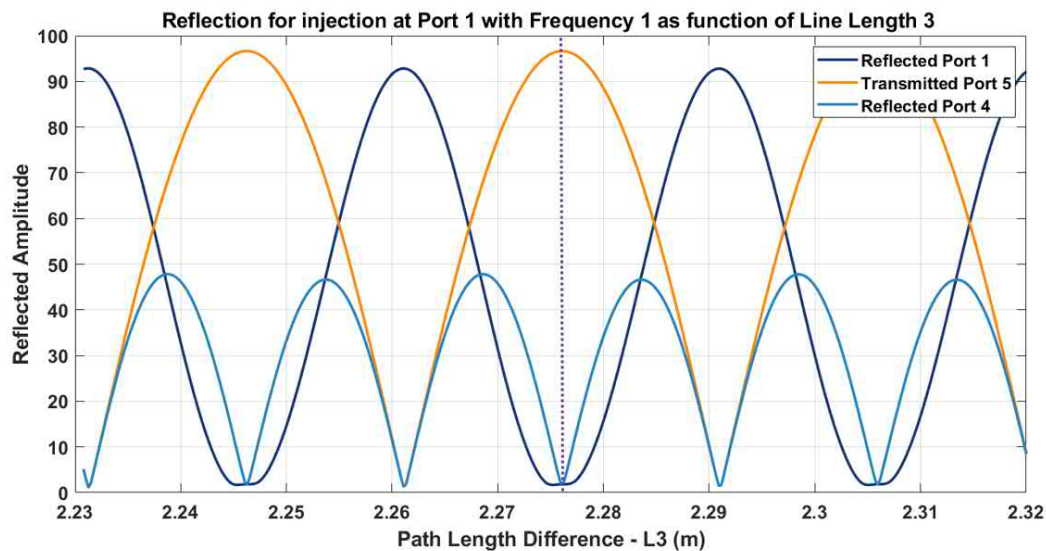


FIGURE 6.12: Simulation of Transmitted Amplitude at Port 5, and Reflected Amplitude at both Hybrid Input ports (Port 1 and Port 4) when pulsing into Port 1 at the klystron frequency (F1) with respect to Length 3

When pulsing into port 4 is it desirable that all of the power is directed back to port 4 and port 1 should be isolated. This occurs when the difference in path length is 2.276 097 m as shown in Figure 6.12 by the purple line. When the path length is not correct more power is diverted to port 4. The reflection to both ports is small in magnitude as the load is set so absorb power at this frequency.

When pulsing into port 4 at the correct frequency the reverse effect observed, this is shown in Figure 6.14.

Similarly, when the difference in path length is 2.276 097 m (purple line) all of the power is diverted back to port 4. In this figure the amplitude of the reflected signals is much larger because the simulation is setup to reflect a large percentage of the power at this frequency.

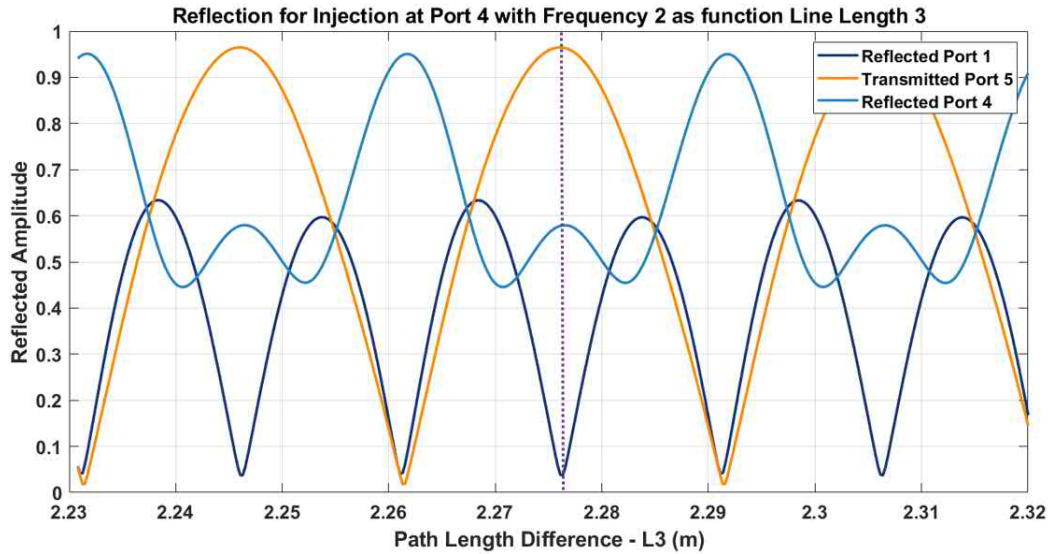


FIGURE 6.13: Simulation of Transmitted Amplitude at Port 5, and Reflected Amplitude at both Hybrid Input ports (Port 1 and Port 4) when pulsing into Port 4 at the Frequency 4 with varying Length 3

### 6.5.2 Dependence on Frequency

In the following simulations the length of L3 is maintained at 2.276 097 m for optimum transmission of forward power, the injection frequency is swept at both input ports. In Figure 6.14 frequency 1 is swept and the injection port is port 1.

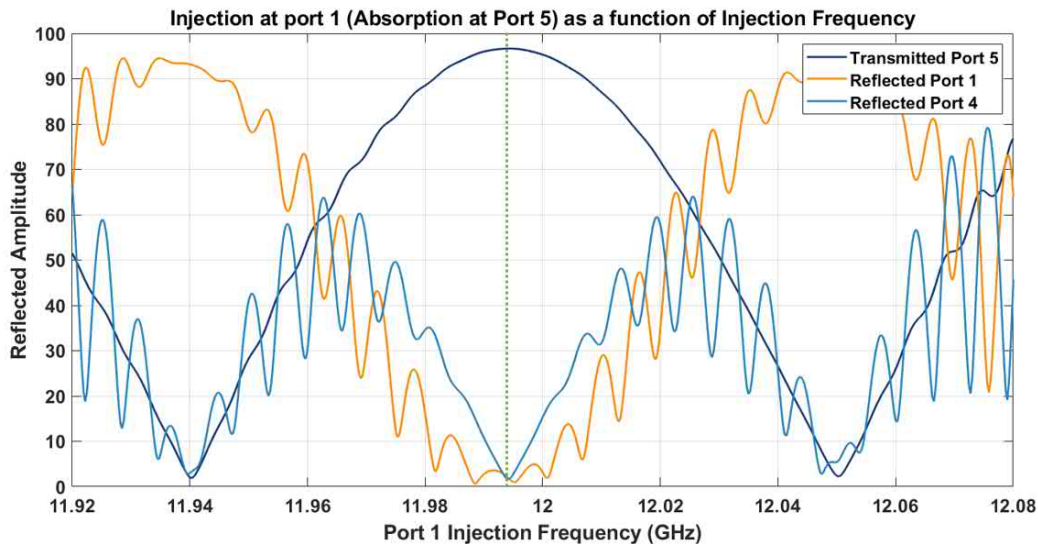


FIGURE 6.14: Simulation of Transmitted Amplitude at Port 5 and Reflected Amplitude at both Hybrid Input ports (Port 1 and Port 4) when pulsing into Port 1 as a function of Frequency 1

In Figure 6.14, optimum transmission of the power from port 1 is achieved when frequency 1 is 11.9942 GHz, as indicated by the green line. The high frequency oscillations are due to the interference of reflections when the frequencies are not ideal.

In Figure 6.15 the signal is injected onto port 4 and the frequency is swept. optimum transmission of the power from port 4 is achieved when frequency 4 is 11.9391 GHz, as indicated by the red line. At 11.9942 GHz the power is not transmitted.

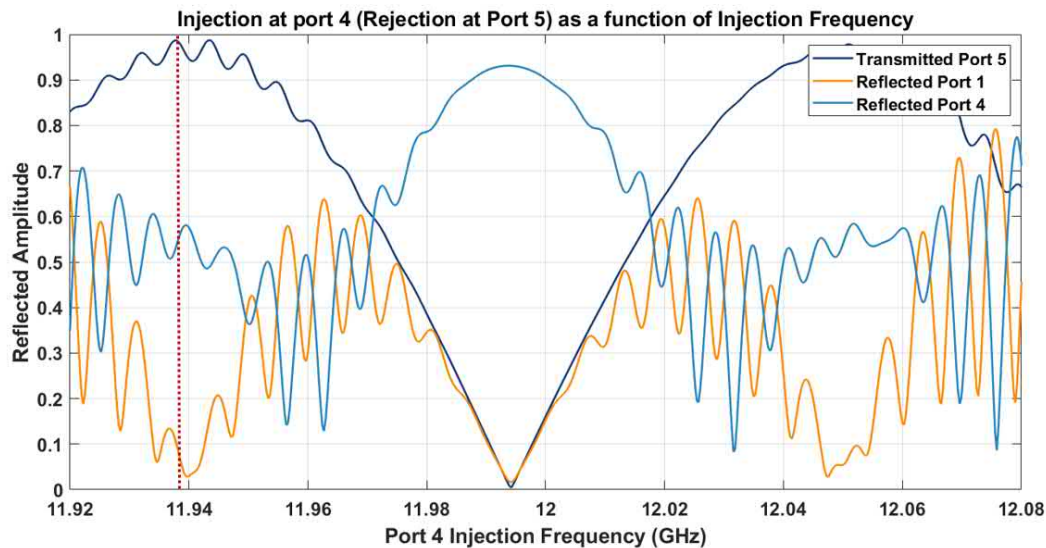


FIGURE 6.15: Simulation of Transmitted Amplitude at Port 5 and Reflected Amplitude at both Hybrid Input ports (Port 1 and Port 4) when pulsing into Port 4 as a function of Frequency 4

### 6.5.3 Dependence on Length to Load

The reflected phase at port 4 is designed to respond to changes in the length of line 5 as defined in Figure 6.5. Provided the difference in path length between the two arms is constant and correct then maximum power is transferred through the interferometer at both injection frequencies.

The TWT pulses will be reflected at the accelerating structures and will return back to port 4 of the hybrid. Provided the system is tuned, the amplitude response at both port 1 and port 4 is relatively unresponsive to the changing length of line 5, this is shown in Figure 6.16.

In Figure 6.17, the signal is injected to port 4 at the frequency 4 and the reflected phase at both ports is shown.

The reflected phase response at port 4 is sensitive to changes in the length of line 5. The change of the reflection at port 4 is  $2.023^\circ$  per degree on line 5. The expected value is  $2^\circ$  per degree on line 5. The difference is due to unwanted reflections arising from imperfect components. However, despite this imperfection the reflected phase

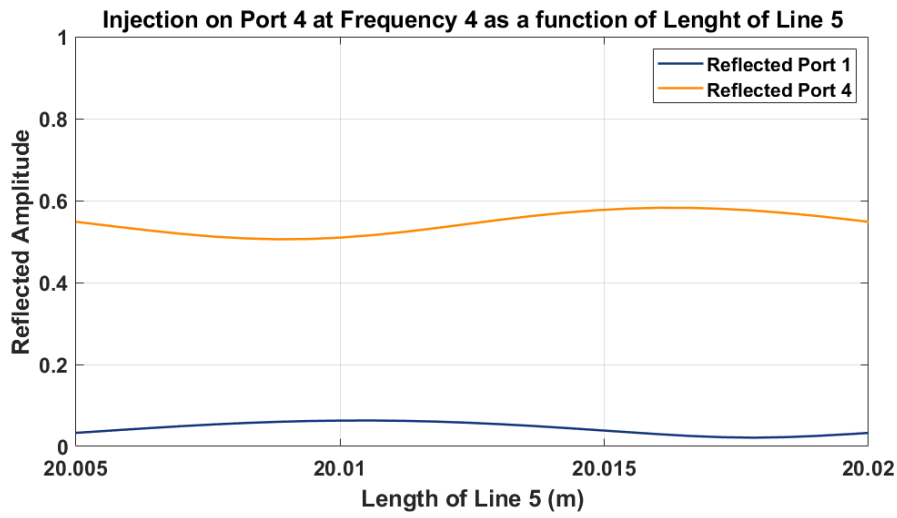


FIGURE 6.16: Simulation of Reflected Amplitude at Port 1 and Port 4 when the length of Line 5 is changed, input signal is injected into Port 4 at Frequency 4

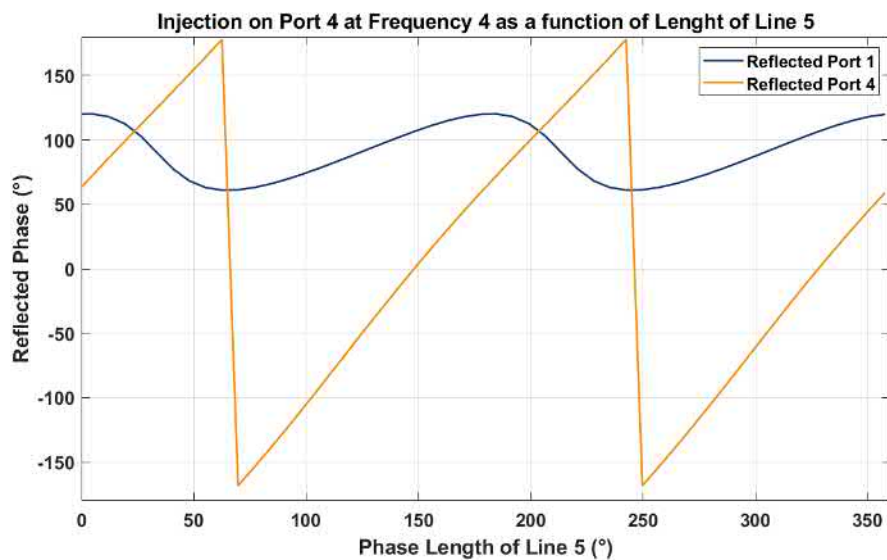


FIGURE 6.17: Simulation of Reflected Phase at Port 1 and Port 4 when the length of Line 5 is changed, input signal is injected into Port 4 at Frequency 2

at port 4 of the hybrid can be used to measure phase changes in the waveguide network.

The reflected phase at port 1 also shows a small phase variation. However, it is not single valued, such that a measurement of reflected phase does not uniquely determined the line length. The reflected phase on the wrong port depends on imperfections in the components and has a complex dependency on all the line lengths.

The system simulation has been used to estimate the effect of changing the length of L3 on the measurement of L5 as shown in Figure 6.18. In the figure, the ideal tuning is represented by the purple signal in the centre (L3 = 2.276 097 m).

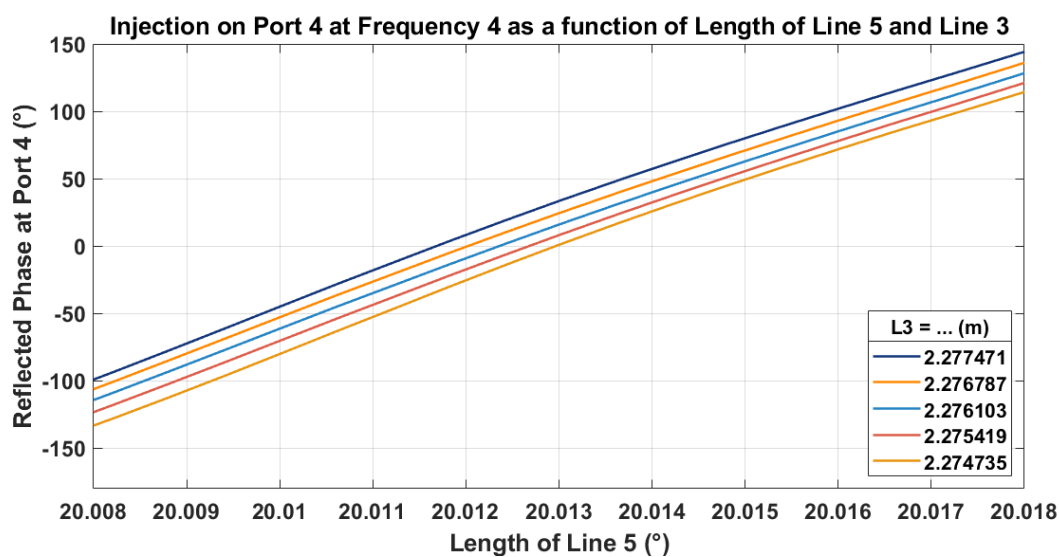


FIGURE 6.18: Simulation of Phase of the Reflection at Port 4 of the Hybrid vs the Phase of the Reflection from Line 5 with changing Path Difference of the Inteferometer Arms (length of L3). The ideal length of L3 is 2.276 097 m

When the length of line 3 changes, this changes the phase of the reflection returning to port 4 of the hybrid. In Figure 6.18 the path difference between each trace is 0.684 mm which corresponds to a temperature change of line 3 of 18.6°C for a waveguide length of 2.3 m and a phase shift of 7.4°.

These phase changes will cause an error on the reading of the reflected phase from line 5. A temperature change of 0.1°C will change the length of line 3 by 0.003 68 mm. This would shift the measured phase at port 4 by 0.041° according to Figure 6.18 which would create an error on the reflected phase measurement.

Without knowing what phase changes can be expected from the waveguide network at Xbox1, it is reasonable to assume that the system can be stabilised to within 1° C as this is achieved in other areas of the Xbox systems such as the pulse compressor cooling circuit.

## 6.6 Low Power Tests

Experimental validation was planned in two stages starting with low power tests before proceeding to high power test. Components required for the interferometer as set out in Figure 6.2 were sourced and characterised. The numbering convention for the ports is maintained from the previous sections, the definition can be found in Figure 6.5.

The system was assembled and tested in the RF measurements lab with the components in air. The low power system was validated in two steps. Firstly, a load is used on the output to replicate the long waveguide network. Secondly, a short is used on the output to replicate a reflected signal. The low power test is also used to characterise the thermal stability of the interferometer.

The interferometer system should be 'invisible' to high power klystron pulses entering into port 1, at the klystron frequency (frequency 1) the reflection should be minimised and the transmission maximised. The high power, vacuum frequency of 11.9942 GHz is converted to 11.9907 GHz as the low power measurements are made while the system is in air. The RF frequency scales with the square root of relative permittivity, which is 1.00059 for air and 1 for vacuum.

Two straight sections of WR90 waveguide are used to create the path length difference, their lengths are 0.972 m and 0.973 m so a total path difference between the arms of 1.945 m. In this case, the analytical calculation give the second frequency as 11.9263 GHz with extra lengths 1.9477 m and the number of wavelengths is  $n = 65$ .

The interferometer S-parameters must remain consistent during operation to minimise phase changes induced by the interferometer itself. When the system is not thermally optimised the phase advance between the two arms is not correct. This results in incorrect recombination of the power at the h-plane tee and a portion of the power is reflected back to the hybrid from the tee. In the high power system it will not be possible to calibrate the interferometer by directly measuring the S-parameters using a VNA. Instead, the S-parameters of the interferometer will be maintained by ensuring the system reaches exactly the same temperature each time it is operated and monitoring the reflected amplitude at the input port.

The full thermal stabilisation system and the position of the RTD temperature probes are shown in figure 6.19. Heating tapes are coiled around the 'long' arms which are then covered in insulation material. The 'short' arm has four cooling

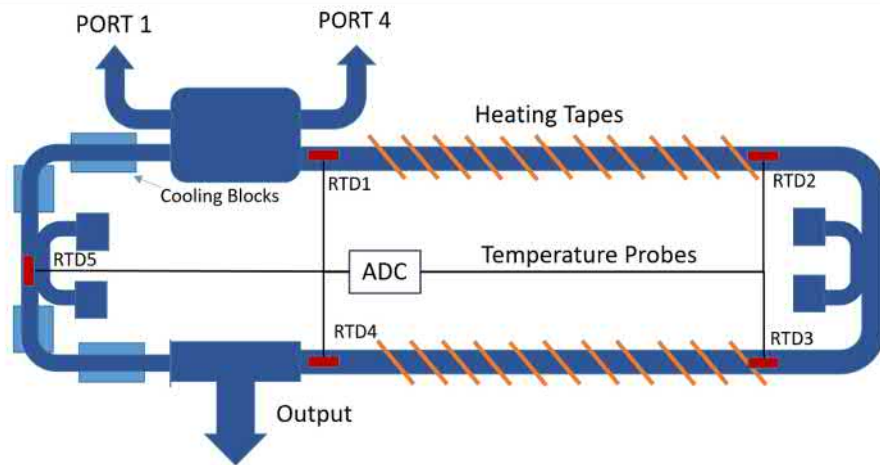


FIGURE 6.19: Schematic showing the interferometer with the position of the RTD (resistance temperature detector) temperature probes, heating tapes and cooling blocks

blocks attached to a chiller which circulates cooling water at  $20^{\circ}$ , there is also a temperature probe here.

Thermal stabilisation is achieved by heating the 'long' arm of the interferometer to increase the path length due to expansion of the copper. The 'short' arm is also held at a constant temperature using water cooling, this ensures that the temperature difference between the two arms (thus the difference in path length) is maintained. The temperature is controlled by adjusting the duty cycle of the heating tapes. Figure 6.20 shows the stabilised temperatures. Four temperature probes are placed on the 'long' arm on the waveguide surface, below the heating tapes and insulation. These are RTD's 1-4 in Figure 6.20, RTD5 is placed on a cooling block. It was found that there is a reduction in the temperature along the length of the heating tapes. RTD's 2 and 3 are placed closer to the power source for the heating tapes which is why their temperatures are slightly higher.

The average standard deviation of the waveguide temperatures is  $\pm 0.0123^{\circ}$ .

Figure 6.21 shows the waveguide temperature with respect to duty cycle. The difference between the upper and lower temperatures is the same as was shown in Figure 6.20, the difference between the probes located close to the power source of the heater and those at the opposite end (1.1 M away).

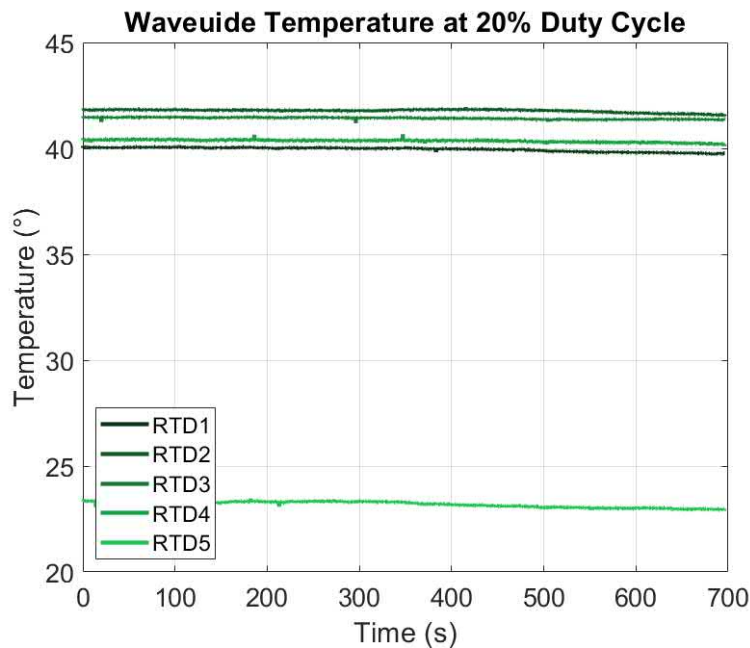


FIGURE 6.20: Waveguide Surface Temperatures measured using PT100 probes when the heating systems is set at 20% Duty Cycle (Right). The probes 1-4 are placed on the heated arms and probe 5 is placed on the short arm which is stabilised using a water cooling system

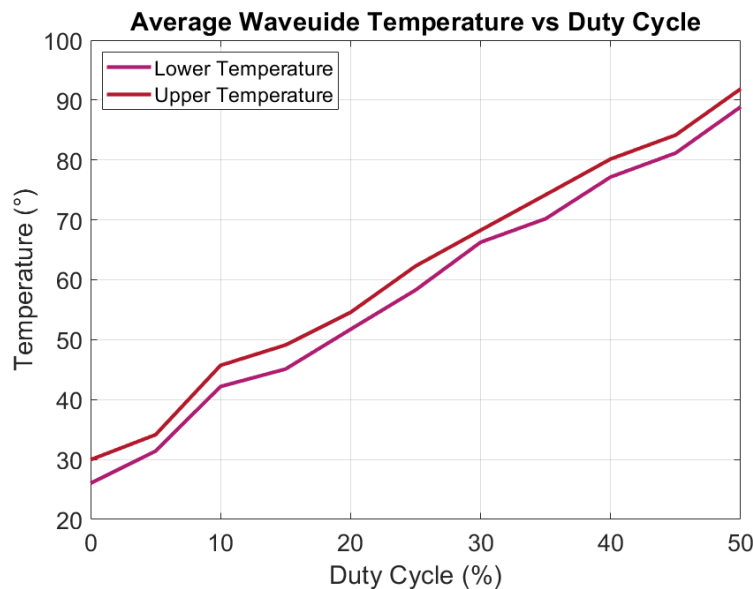


FIGURE 6.21: The Upper and Lower Temperatures of the Waveguide vs Heater Duty Cycle. The upper temperature is taken from the two probes placed at the start of the heating tapes (close to the power source) and the lower temperature is taken from the two probes placed at the opposite end of the arm ( 1 m away from the power source)

### 6.6.1 Loaded Output

The system was measured using a Rhode and Schwarz two-port VNA, which will allow measurement of the full frequency response. In Figure 6.22, the VNA ports are connected to port 1 and port 5 (the output), This provides the S51 and S11 of the system at optimal temperature. The purple dot shows the maximum transmission (S51) through the system at 11.9907 GHz. The S11, the reflection is very small at 11.9907 GHz, this is indicated by the position of the red dot.

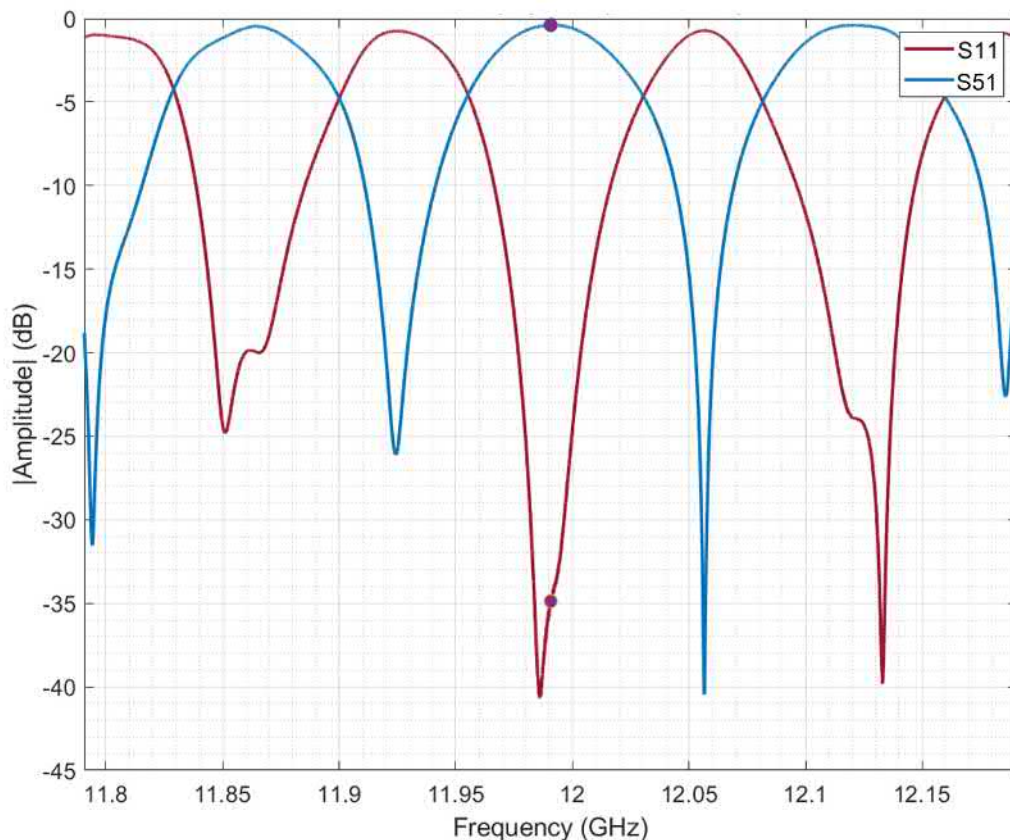


FIGURE 6.22: Measured Transmission (S51) and Reflection (S11) taken from the VNA when pulsing into port 1 vs Injection Frequency. The temperature of the arms is set at 40°(% duty cycle)

The simulations from Section 6.5 were repeated, the same methodology was used but the injection frequency was swept. The input parameters for the simulation are summarised in Table 6.3.

Figure 6.23 shows the simulated transmission (S51) and Reflection (S11) when pulsing into port 1 at with respect to the injection frequency into port 1.

WR90 Width	22.86	mm
Speed of light	$2.99792458 \cdot 10^8$	m \ s
Filling Medium	Air	
Drive Amplitude 1	1	
Drive Amplitude 2	1	
WR90 Waveguide Losses	0.0985	dB/m
Load S11	0	
Length 2	0.600	m
Total Length 3	2.51782	m
Length Difference	1.91782	m
Length 5	19.995	m

TABLE 6.3: Parameters used for Low Power Simulations of the Interferometer Network vs Injection Frequency

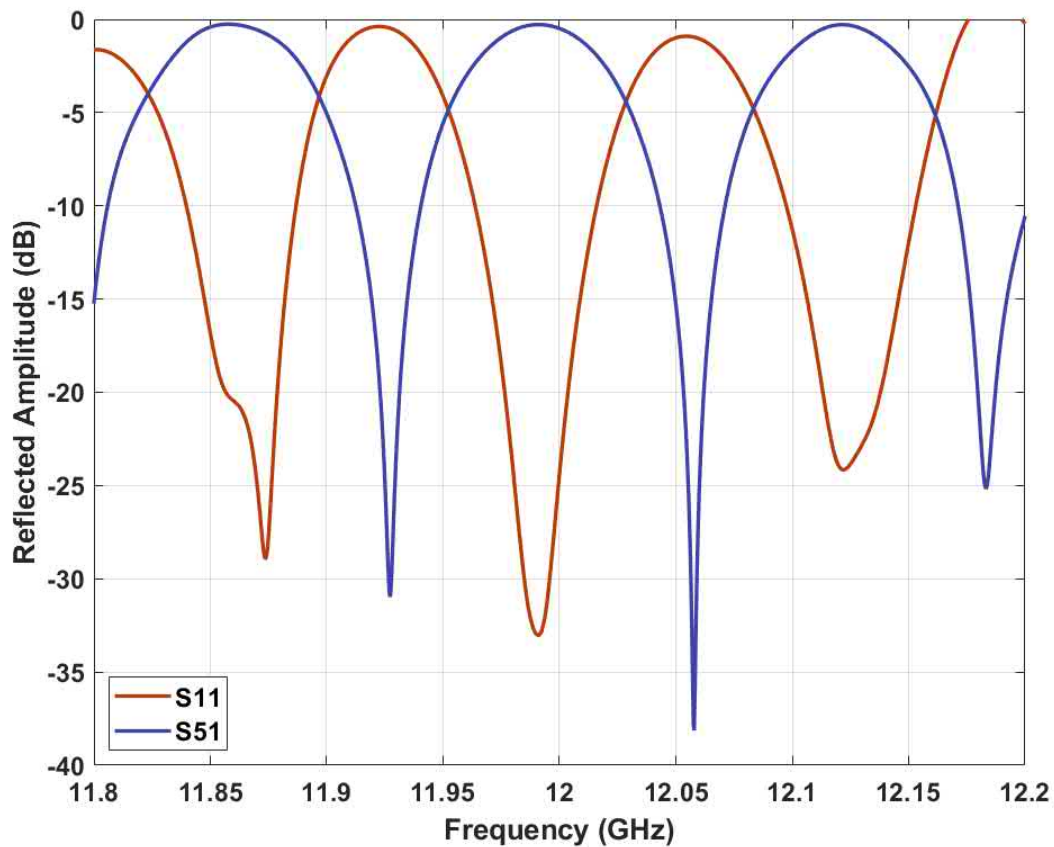


FIGURE 6.23: Simulated transmission (S51) and Reflection (S11) when pulsing into port 1 at vs Injection Frequency

When pulsing into port 4 the S-parameters are reversed with respect to pulsing into port 1. The S-parameters shown in Figure 6.24 are measured between port 4 and port 5 (S44 and S54) when injecting into port 4 when the system was thermally stabilised. As the frequency difference between the klystron pulses and the TWT pulses is constant, optimising the klystron pulse transmission using temperature will simultaneously optimise the TWT pulse transmission.

In Figure 6.24 the purple markers are the klystron frequency, which are now exhibiting maximum reflection and minimum transmission. The TWT frequency could be the node either above or below the klystron frequency, as shown by the yellow markers in figure 6.24. At 11.9263 GHz the transmission is 0.76 dB and the reflection is  $-25.52$  dB.

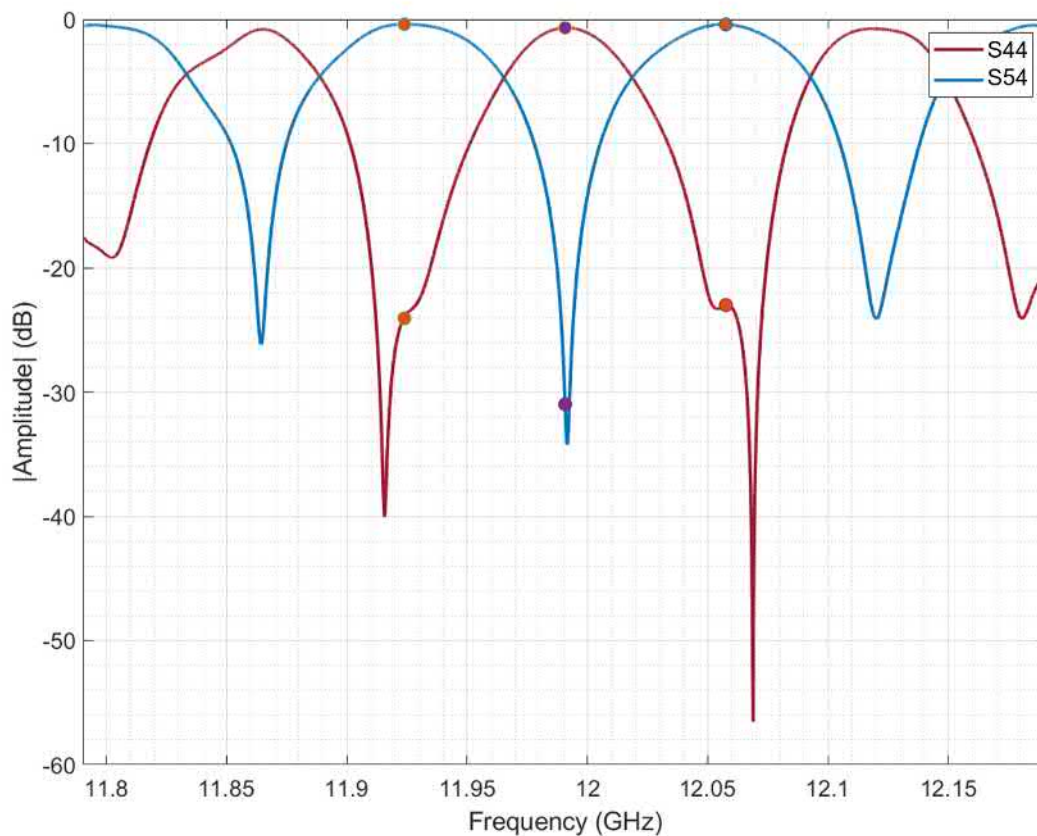


FIGURE 6.24: Measured transmission (S41) and Reflection (S44) when pulsing into port 4 vs Injection Frequency. Temperature of the long arm is set at  $40^{\circ}$

The measured frequency response from Figure 6.24 is in agreement with simulated results which are shown below in Figure 6.25. The simulation used the parameters from Table 6.3 with injection into port 4 with varying input frequency.

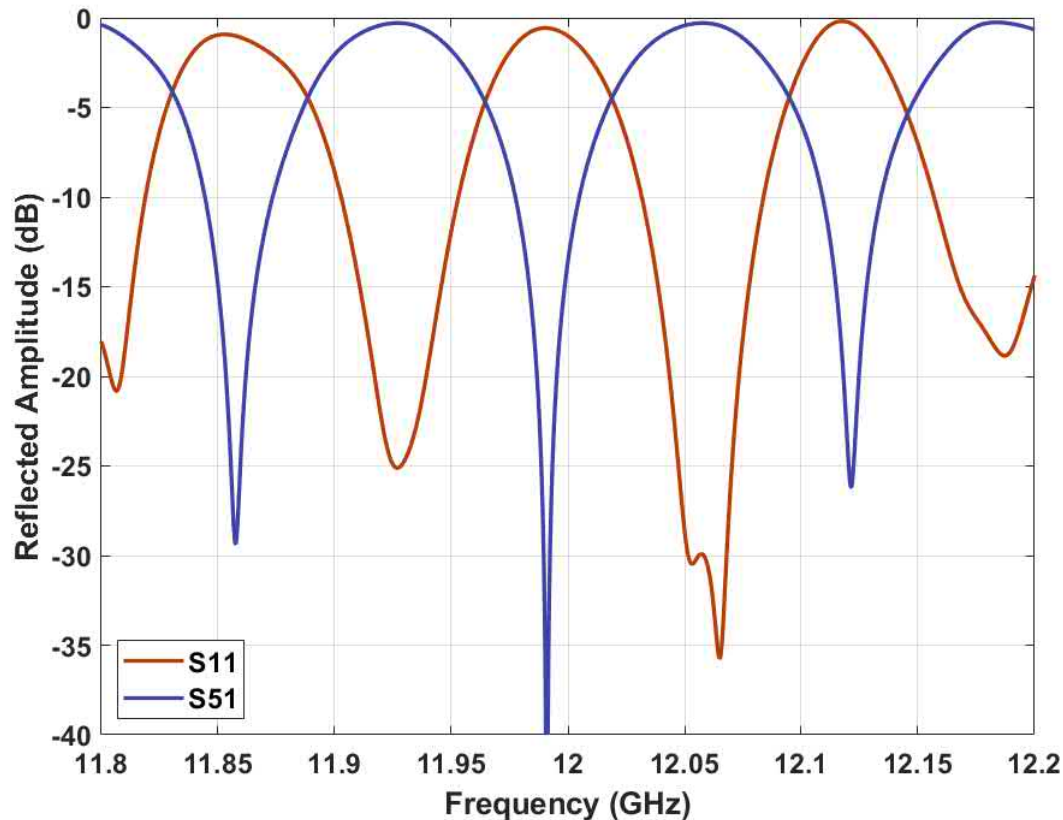


FIGURE 6.25: Simulated transmission (S41) and Reflection (S44) when pulsing into port 4 vs Injection Frequency

### 6.6.2 Shorted Output

Measurement of the phase of the waveguide network at the output is achieved by measuring the phase of the reflected TWT signal returning to port 4 of the hybrid. In order to simulate reflections to port 5 in the low power setup a short is placed on the output of the interferometer to reflect the input signal back to the hybrid. The VNA is connected to port 1 and port 4 of the hybrid to monitor the reflection at both ports. During the measurements the interferometer was thermally stabilised. The reflected phase from the short placed on port 5 is varied using a dial which changes the internal length, the phase of the reflection can be varied through  $180^\circ$  using this method. The following sections show the individual phase and amplitude responses for each port in more detail. Figure 6.26 shows the phase of the reflection at port 1 (S11) of the hybrid with respect to the changing phase of the reflection from the short at port 5.

At the klystron frequency the phase response is sensitive to the changing phase at the short. However, the phase in the region of the TWT frequency (11.9263 GHz) remains constant. Conversely, Figure 6.27 shows the phase of the reflection at port

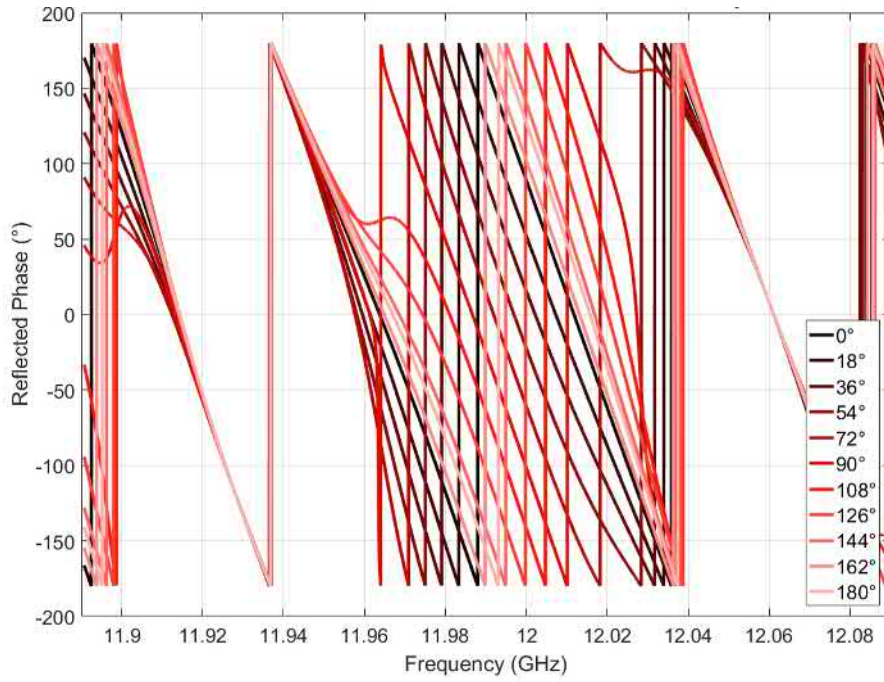


FIGURE 6.26: Measure change in phase detected at Port 1 (S11) with respect to the phase of the reflection from the short on the output controlled by the position of the moveable short

4 of the hybrid. The phase at the klystron frequency remains constant whereas the phase at the TWT frequency is sensitive to the changing phase at the short.

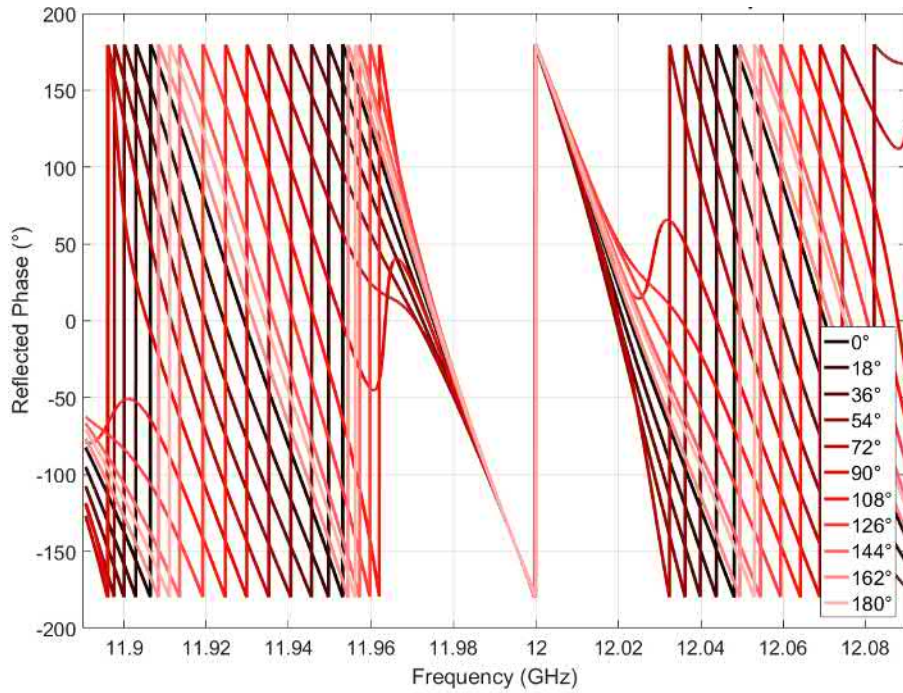


FIGURE 6.27: Measured change in phase at port 4 (S44) with respect to the phase of the reflection from the short on the output

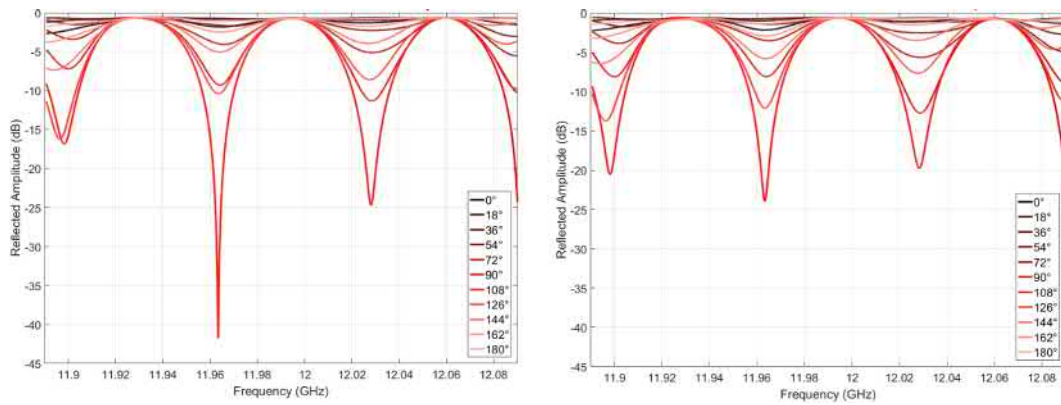


FIGURE 6.28: Measured change in amplitude when pulsing into Port 1, (Left, S11) and pulsing into port 4, (Right, S44) with respect to the phase of the reflection from the short which is connected to Port 5 (Output port)

This is beneficial to the interferometer experiment as the port 4 phase measurement is not affected by the amplitude and is only responsive in phase. This is shown in Figure 6.28 which show the reflected amplitude at when pulsing into port 1 and port 4 respectively. When the system is optimised the system will correctly recombine both frequencies, hence the reflected amplitude at both frequencies is minimised. When there is a complete short and both frequencies are reflected then a standing wave pattern appear as shown in Figure 6.28.

With the short on port 5 and injection of port 4, the reflected phase and amplitude at port 1 and port 4 at 40° are shown in Figure 6.29. When the phase of the

reflection from the short on port 5 is varied through  $180^\circ$ , only the phase at port 4 responds proportionally. The return phase at port 1 exhibits minimal response. The reflected amplitude variation the amplitude variation is very small, at both port 1 the amplitude varies by approximately 0.2 dB, even less for port 4.

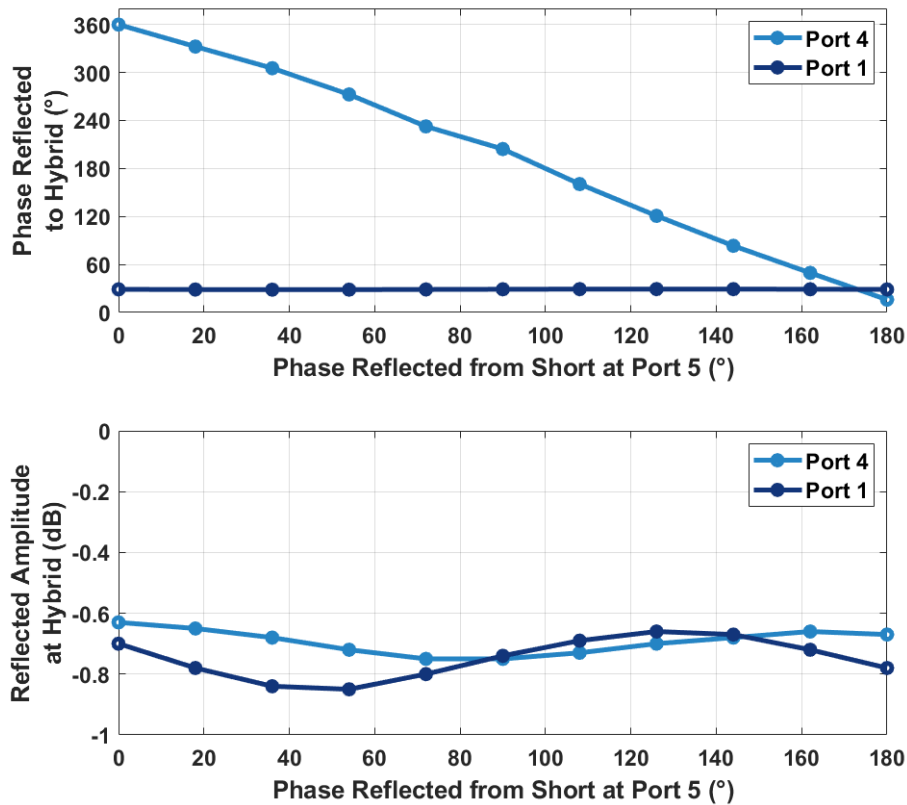


FIGURE 6.29: For injection on port 4, Measured Phase (Top) and Amplitude (Bottom) Response at when pulsing into port 4 vs Reflected Phase at Load at  $40^\circ$

When the interferometer is thermally tuned the reflected phase at the injection port changes linearly in response to the line length, only when using the correct injection frequency for each port. In all cases the reflected amplitude at both injection frequencies and ports remains relatively unchanged.

It is important to emphasise that reflection at either input port does not reveal the length of line 5 unless observed at the correct frequency for the port in question.

### 6.6.3 Thermal Effects

During operation it will not be possible to continuously monitor the S-parameters using the VNA to conform if the long leg of the interferometer is thermally tuned. It is important to wait until the interferometer is tuned before pulsing from the klystron so that large reflections are not sent back to the klystron from the interferometer. In the high power installation a directional coupler will be placed before port 1, this

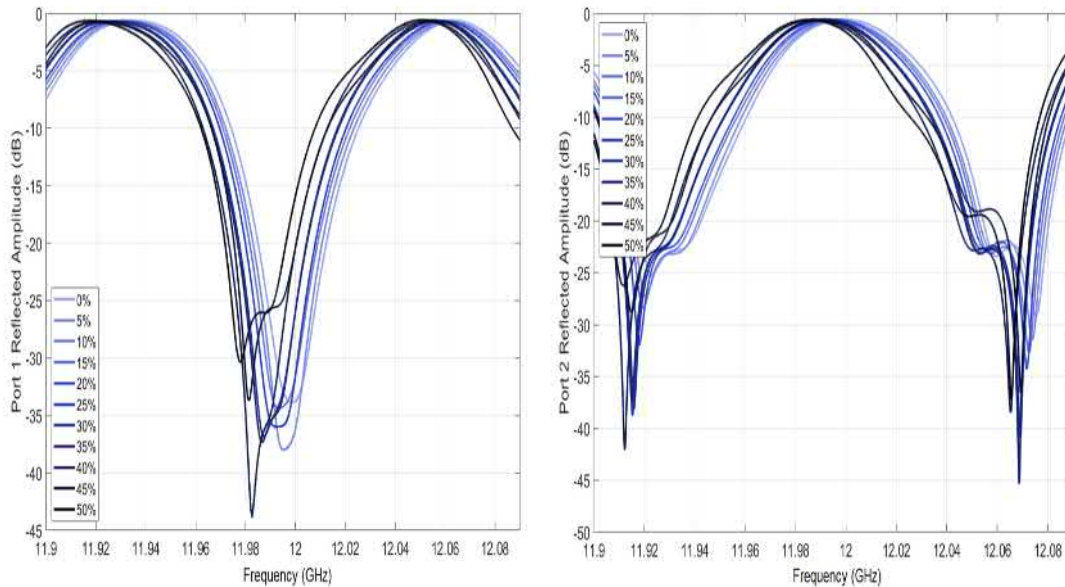


FIGURE 6.30: Measured reflected amplitude at Port 1 (Left) and Port 4 (Right) when injecting into port 4 with a short on line 5, vs varying duty cycle

will measured the forward and reflected power from the TWT port. The low power 1 kW TWT pulses can be used to determine if the inteferometer can be thermally tuned before commencing with the high power klystron pulses. Using a low power pulse, the forward and reflected signals can be monitored. As the temperature of the inteferometer reaches its optimum. For pulsing into port 4 (TWT) the ratio of the return signal on port 1 to port 4 reduces to zero as the inteferometer approaches the optimum temperature.

Phase changes due to the temperature of the inteferometer will also change the reflected phase at port 4. Figure 6.30 shows how the reflected amplitude at port 1 (Left) and port 4 (Right) change relative to the duty cycle of the heaters.

Figure 6.31 shows how the reflected phase at port 4 changes with the duty cycle of the heaters. The changing phase with duty cycle, particularly at port 4, is an important consideration as the purpose of the inteferometer is to measure phase changes at this port with a very high accuracy. Any phase changes resulting from a changing duty cycle will directly mask phase changes that we are looking to detect. A change of 5% in the duty cycle changes the temperature by an average of 6° C.

Figure 6.32 shows the reflected phase at port 4 with respect to the phase at the short, the error bars represent thermal stabilisation to within 1°C.

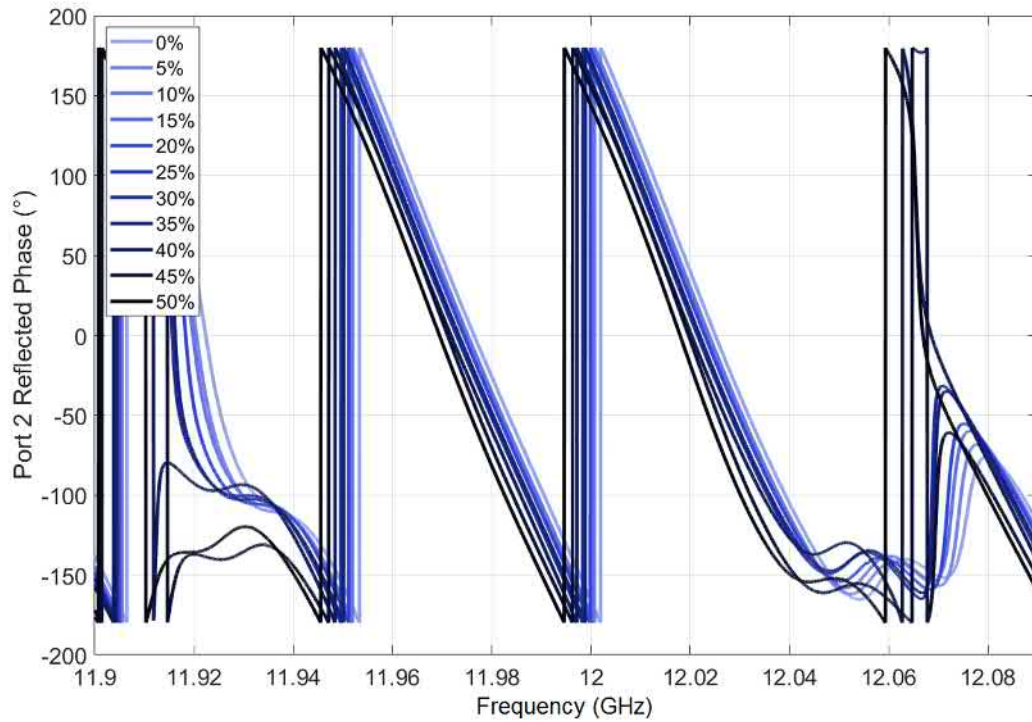


FIGURE 6.31: Measurement of the reflected phase at port 4 when injecting into port 4 with a short on line 5, vs varying duty cycle

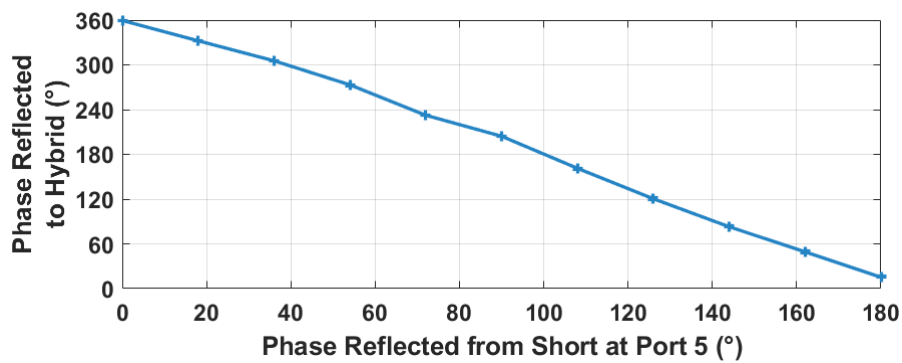


FIGURE 6.32: Reflected Phase at port 4 when injecting into port 4 with shorted on line 5, with 20% Duty Cycle (approximately 40°) with Error Bars

## 6.7 High Power Implementation

The interferometer was transferred from the RF measurement lab to Xbox1 and assembled in the CTF2 klystron gallery; the pulse compressor was removed and the klystron connected to port 1. A high power load was connected to port 4 and the full system was placed under vacuum. The system is shown in Figure 6.33 including all the electronics, cooling circuits, chiller and insulation. The waveguide system still retains the same fundamental layout as was shown in Figure 6.11. The waveguide section is shown in more detail in Figure 6.33 alongside the 3D drawing in Figure 6.34 and a diagram of the installation in Figure 6.2.

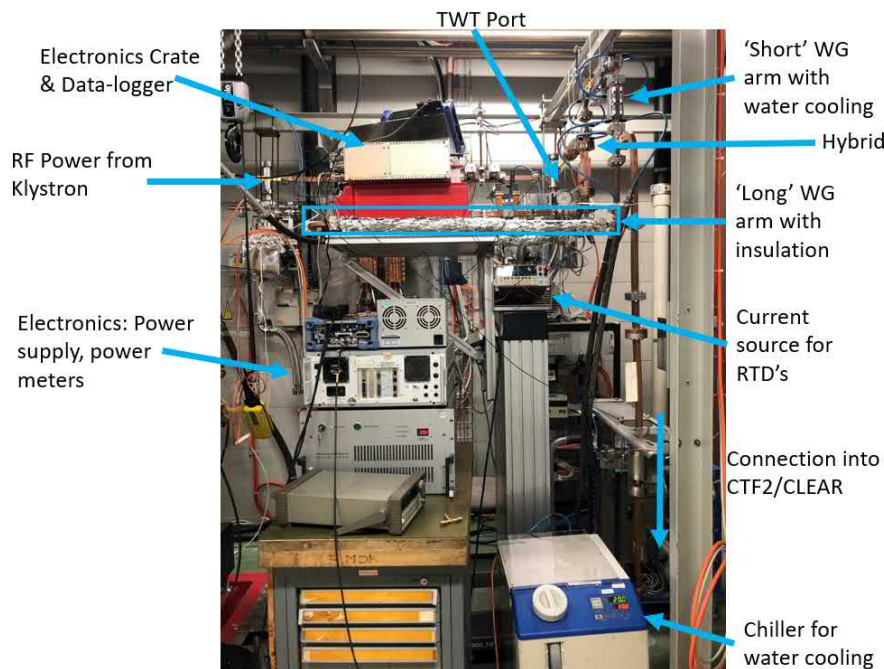


FIGURE 6.33: A photograph of the interferometer installation at Xbox1 with all electronics, cooling circuits and insulation

Under vacuum the klystron frequency is 11.9942 GHz and the TWT frequency is 11.9391 GHz. Due to the the lower frequency as measured during the low power test, being outside the frequency of the jog mode convertors at Xbox1, two extra waveguide elbows were added into the network compared to the low power test setup. The total electrical length of the two bends is 0.324 m, thus the total path length difference is 2.271 m to the nearest millimetre. This is in agreement with the results from the simulation in Section 6.5 which required a path length of 2.276 097 m for frequencies of 11.9942 GHz and 11.9391 GHz.

The exact path difference can not be known to a higher degree of accuracy due to the number of unknowns in the system. The temperature stabilisation system is

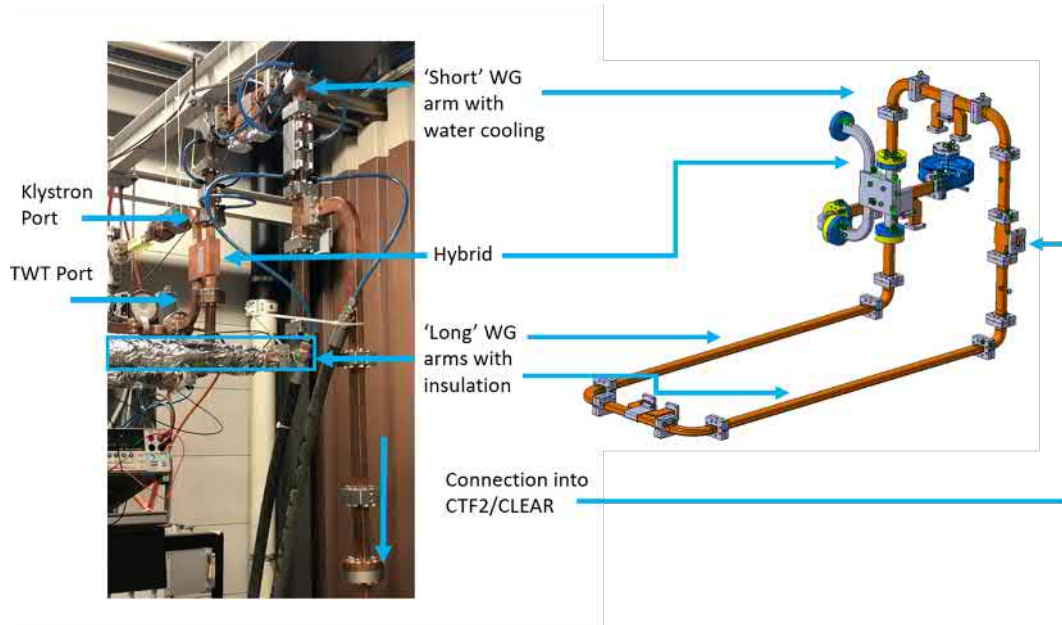


FIGURE 6.34: Interferometer WG installation at Xbox1 in the CTF2 Klystron Gallery (Left) and the 3D Design for the installation (Right)

	RTD1	RTD2	RTD3	RTD4	RTD5
Mean Temp (°C)	84.035	84.510	81.980	82.102	20.510
Standard Deviation (°C)	0.0891	0.128	0.0879	0.0927	0.1023

TABLE 6.4: Mean Temperature and Standard Deviation of the Thermal Stabilisation of the Waveguide Loop

used to precisely control the difference in path length.

Figure 6.35 shows the thermal stability of the waveguide loop. There are two probes on each arm of the waveguide loop, two of the temperature probes are approximately 2°C lower as they are further away from the heat source. The fifth temperature probe is placed on the short arm of the waveguide loop which is stabilised at 20°C using a water-cooling circuit. The mean and standard deviation of the stabilised resistance temperature detectors, RTDs, are shown in Table 6.4.

From Table 6.4, the measured thermal stability of the waveguide loop is on the order of 0.1°C.

### 6.7.1 Klystron Pulses

In the same way as in the lab setup, the temperature stabilisation system must be swept in order to find the new minimum reflection point of the system. As the temperature changes, the amplitude of the signals was measured at three points using a power meter connected to a patch panel.

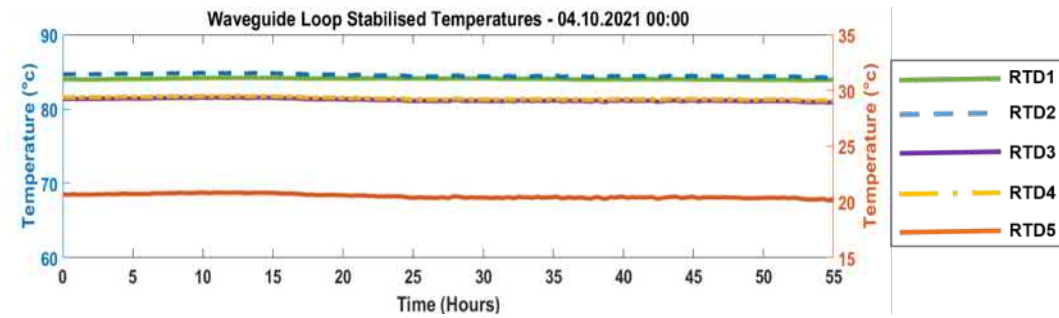


FIGURE 6.35: The waveguide loop is thermally stabilised at 84°C, the stabilisation of the waveguide loop was measured over 50 hours. RTD's 1-4 are plotted on the scale on the left (Blue) and RTD5 is plotted on the scale on the right (Orange)

It was found that when the system is at 84°C the reflection is minimised when pulsing into the klystron port, this is shown in Figure 6.36. The input power at port 1 is 15 MW.

The measured results show the reflected power is directed back to the klystron port when the system is tuned, thereby isolating the TWT port from reflections. This is the desired behaviour and is consistent with what was observed in the low power measurements and simulation. The total portion of reflected power is low (approximately 2%) as any power transmitted through the systems at both frequencies is absorbed by the load. This is confirmed by considering the power incident at the load, this is shown in Figure 6.37.

The heater tapes can change the temperature of the waveguide arms in the range of 20 °C to 100 °C. Using the formula for linear expansion of copper from 6.18 this should equate to an increase in length of approximately 4 mm. Power is injected into the klystron port at 11.9942 GHz while the heater tapes are varied through their full range and the power is recorded at three points in the network. The reflected power at the klystron and TWT ports are shown in Figure 6.36 and the forward power incident at the load is shown in Figure 6.37.

For an incident power of 15 MW, as the heating begins, the interferometer is not tuned and there are internal reflections in the system which prevent power from being transmitted through to the load, which is currently taking the place of the TWT which would be on port 4. The results from Figure 6.36 are in agreement with the simulation from section 6.5 which exhibited the same behaviour when adjusting the path difference between the arms. As the arms are heated more of the power is directed back to port 1 and port 4 becomes isolated. Upon approaching the optimal temperature the interferometer begins to transmit more power through to the load,

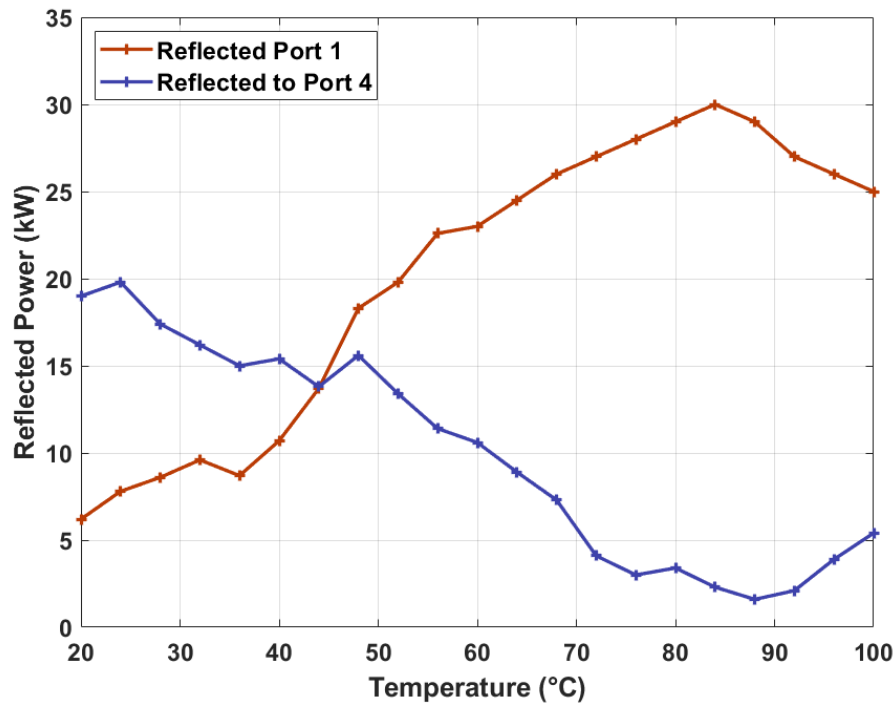


FIGURE 6.36: Left: Reflected Power at the Klystron Port and the TWT Port vs Temperature when pulsing into Port 1 (Klystron Port) at 11.9942 GHz.

as observed in Figure 6.37. At the optimum temperature the losses in the system are minimised to approximately the resistive losses in the waveguide. From Figure 6.36, at 84°C the return loss of the load is calculated to be approximately  $-34.8$  dB due to:

$$ReturnLoss(dB) = -20\log|\Gamma|$$

Where:

$$\Gamma = \sqrt{\frac{ReflectedPower(\%)}{100}}$$

It would be theoretically possible to use the returning pulses at the klystron port to measure the changing phase of the line. However, as a good accelerating structure reflects a small fraction of the incident power, then power returning from the load is similar in magnitude to power reflected from the interferometer due to imperfections in the hybrid quadrature coupler and the combiner tee. This extra reflection masks the measurement. Furthermore, the pulse length will be less than 250 ns. The precision of the measurement of the phase of the klystron pulses is limited by the phase jitter induced by the klystron itself, which was shown in Chapter 5.

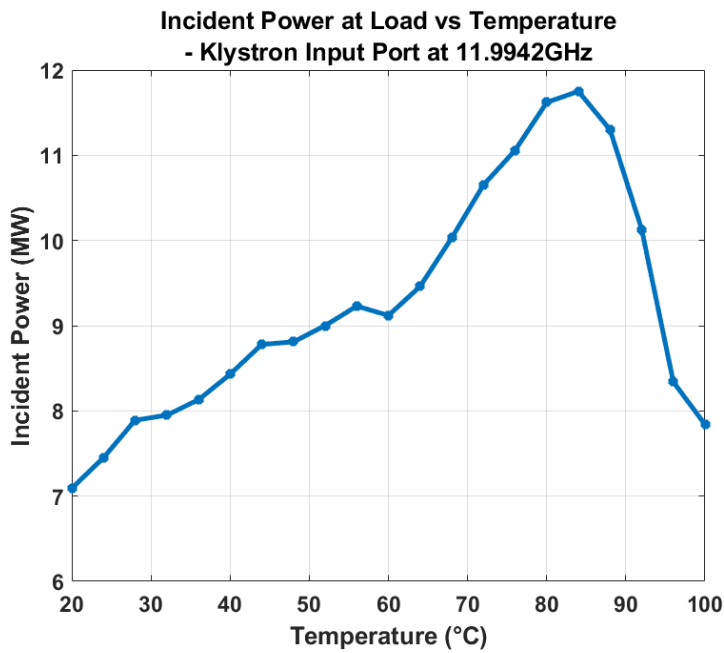


FIGURE 6.37: Forward Power at the load vs Temperature when pulsing into the Klystron Port at 11.9942 GHz

### 6.7.2 TWT Pulses

It was not possible to simultaneously test the klystron and TWT ports due to lack of suitable high power RF window to separate the vacuum section from the TWT. The TWT output port operates in air while the klystron must operate under vacuum. Hence, the TWT was pulsed into the system separately under air. The corrected frequencies for operating in air are 11.9907 GHz and 11.9364 GHz for the klystron and TWT respectively.

Power is injected into the TWT port at 11.9364 GHz at 60 dBm while the heater tapes are varied through their full range. It was not possible to measure the incident power at the load, the total attenuation between the directional couplers at the load and the measurement port at Xbox1 is  $-110.8$  dB, hence the power at the load was too low to measure. Furthermore, the load is located in the CLEAR LINAC facility and therefore not accessible during operation. The reflected power at the klystron and TWT ports are shown in Figure 6.36.

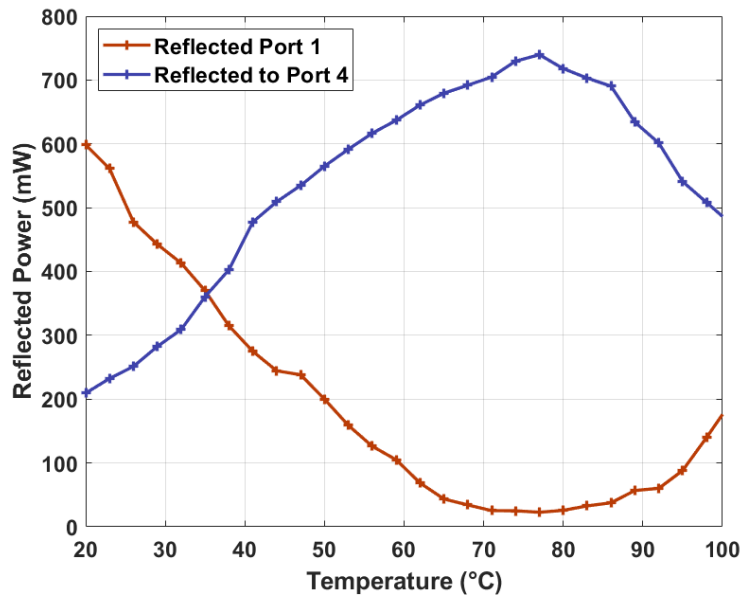


FIGURE 6.38: Left: Reflected Power at the Klystron Port and the TWT Port vs Temperature when pulsing into port 4 at 11.9364 GHz

The change from vacuum to air requires readjusting the optimum temperature to 76 °C. The measured results show the reflected power is directed back to the TWT port when the system is tuned to the correct temperature. This is the desired behaviour and is consistent with what was observed in the low power measurements and simulations. From Figure 6.38, at 76 °C the return loss of the load is calculated to be approximately  $-29.0$  dB. The reflection is higher than what was previously measured for the klystron pulses, this indicates that some of the power is being reflected from the mode convertors (due to pulsing at a frequency outside their bandwidth) as well as the load.

In order to test the system’s ability to measure reflected phase in its current state it was necessary to induce a reflection along the line so that the reflected TWT pulses can be measured at the interferometer. Consequently, for this particular experiment the TWT frequency was adjusted in order to lie just outside the bandwidth of the mode convertors. The change in frequency will sacrifice some of the transmission efficiency of the system but is necessary to be able to detect reflected power. In air the mode convertor band-edge is 11.9357 GHz so the TWT frequency was set as 11.9347 GHz. This gives around 10 m of bare WR90 rectangular waveguide which can be used for the phase measurement.

In order to make very precise phase measurements the noise level of the acquisition system should be suitably low. The phase measurement are expected to change over long periods of time, longer than individual pulses. Hence the TWT phase

measurement is collected by averaging over a full pulse. This pulse length will be much longer than the CLIC RF pulses, in these measurements the pulse length was set to 500 ns.

The low phase noise sampling clock and the Xbox1 LO generated using the up-converter will be used during the down-conversion and acquisition, these were detailed in Chapter 3. For a path length difference of 2.276 097 m and the system in vacuum, the TWT frequency is 11.9347 GHz so when mixed with the local oscillator from Chapter 3 the IF is 127.9 MHz so the Nyquist is 266 MHz. These signals can be non-IQ sampled using the NI5162 ADCs at Xbox1 with an oversampling rate of 3. This pulse length of the interferometer calibration pulse will be much longer than the CLIC RF pulses, in these measurements the pulse length was set to 500 ns.

The TWT pulses have much less phase jitter with respect to the klystron pulses, this is shown in Figure 6.39. There are two reasons for the reduction in phase jitter. Firstly, the klystron is the most significant contributor to the phase jitter and is not included in this signal chain. Secondly the TWT pulses are over-sampled at a higher rate and the RF pulses are much longer, (500 ns), so averaging across a much longer pulse significantly reduced the phase jitter. The TWT pulses have a standard deviation in the phase of  $0.1075^\circ$ , therefore a  $5\sigma$  accuracy is  $0.5375^\circ$ .

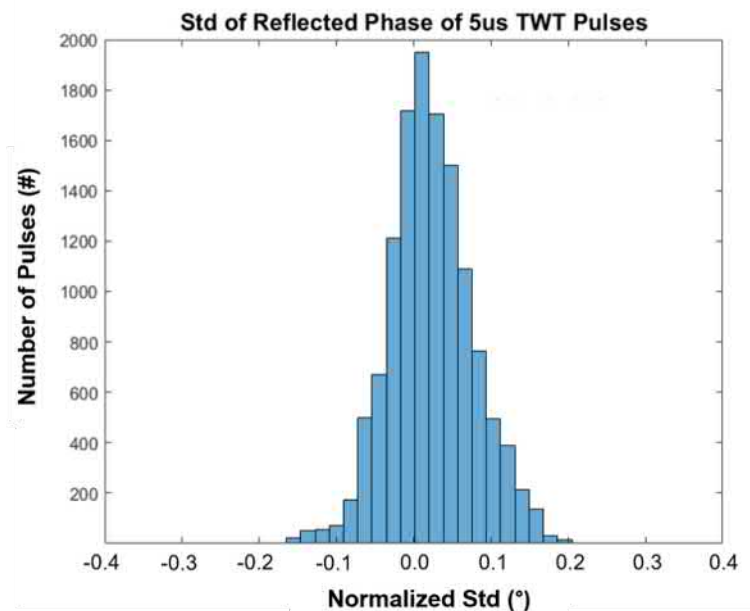


FIGURE 6.39: Normalized Standard Deviation of the Reflected Phase of the TWT pulses

The reflected phase at the TWT exhibits phase changed over two distinct timescales. There are ‘fast’ oscillations which are on the order of 20 minutes. These are attributed to temperature changes due to the air conditioning in the klystron gallery and the

oscillations are consistent with those which were previously observed on the output phase from the klystron. Secondly, the reflected phase from the TWT also exhibits 'slow' phase changes which take place over the course of the day.

There are two types of temperature measurement available from the Xbox1. There is a PT100 thermocouple placed onto the un-insulated copper WR90 waveguide in the CTF2 klystron gallery. In addition, there are ambient air temperature probes in various point through the klystron gallery and CTF2 bunker, an example of the air temperatures is shown in Figure 6.40.

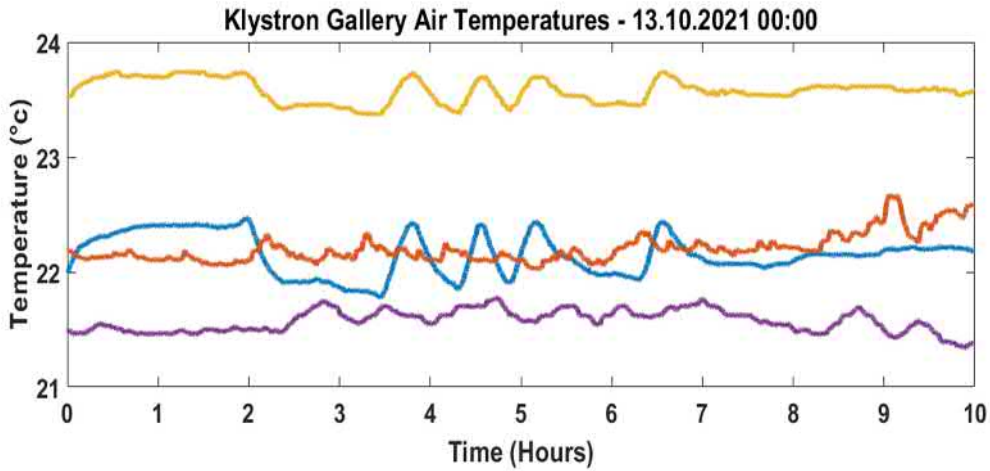


FIGURE 6.40: Air Temperatures in the CTF2 Klystron Gallery where the Xbox1 Klystron and Inteferometer is located

The reflected phase exhibits an oscillation on a time scale of approximately 20 minutes which can be correlated with air temperature in the klystron gallery, in particular the feedback loop of the air conditioning. During a time period where both the air conditioning and the reflected phase are oscillating a sample of the data was taken spanning several hours. A sine function with an angular shift and is fitted to each time series in order to find the time period of the oscillations and the overall gradient. The function of the fit is:

$$y_{Fit} = \beta_1 + \beta_2 \cdot \cos\left(\frac{2\pi}{dt \cdot p}\right) + \sin\left(\frac{2\pi}{dt \cdot p}\right) - (\rho \cdot t) \quad (6.24)$$

Where  $\beta$  are the co-efficient of the fitted function,  $dt$  is the time between samples,  $p$  is the period and  $\sigma$  is the slope. For the air temperature the time period is 22.92 minutes and the slope is 60.1 u°C per minute. For the reflected phase shift the time period is 23.75 minutes and the slope is 66.7 u° per minute. The oscillations of both the air temperature; the reflected phase and the fitted functions are shown in Figure 6.41.

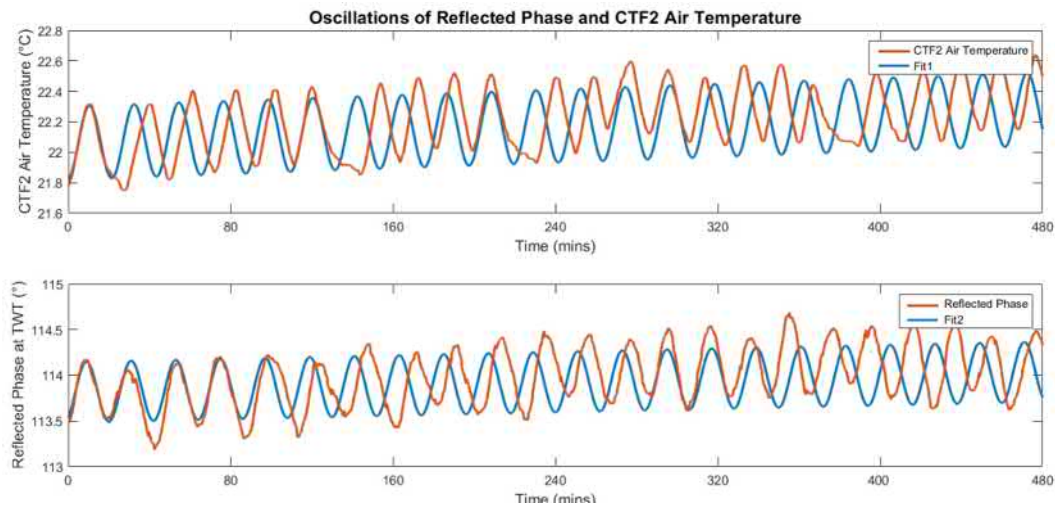


FIGURE 6.41: Oscillations with a short time period (on the order of 2 minutes, compared with 24 hour oscillation) in CTF2 Air Temperature and Reflected Phase and the fitted function for each

Over a period of several days a longer oscillation can be observed, the time period is approximately 24hours. The reflected phase is low pass filtered in order to remove the short term oscillations. Figure 6.42 shows a clear correlation between the reflected phase and the WR90 surface temperature as measured by the PT100 thermocouple placed on the surface. Figure 6.42 also shows the temperature of the thermally stabilised section of waveguide over the same time period which are impervious to the daily oscillation cycle.

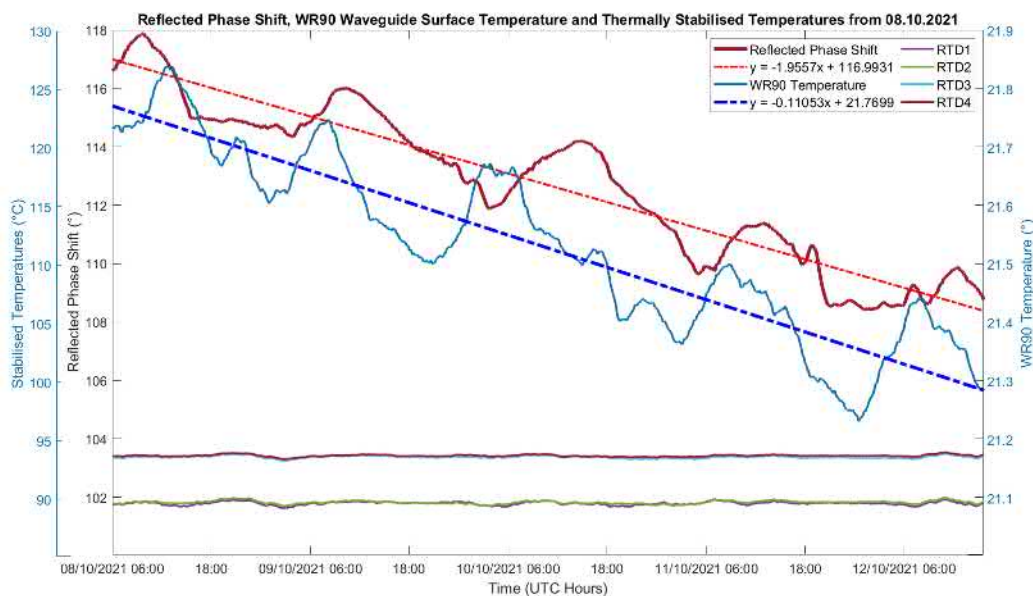


FIGURE 6.42: Reflected Phase, WR90 Copper Surface Temperature and Stabilised Temperatures vs Time from 08.10.2021

The relationship between the reflected phase and copper surface temperature is shown in Figure 6.43, this is calculated by comparing the gradient of the phase

and temperature using a sliding window. The window for the temperature can be larger than the phase window as the temperature is a much slower changing property. Several window sizes were compared but the optimal ratio between the phase averaging window and the temperature averaging window is 1:1.9. The R-squared value, is the square of the correlation which is a measure of the proportion of variation in the dependent variable that can be attributed to the independent variable, in this case the correlation is very high and  $R^2 = 0.9077$ . The linear fit shows that a change in phase of  $1^\circ$  corresponds to a change in surface temperature of  $1.4919^\circ\text{C}$ .

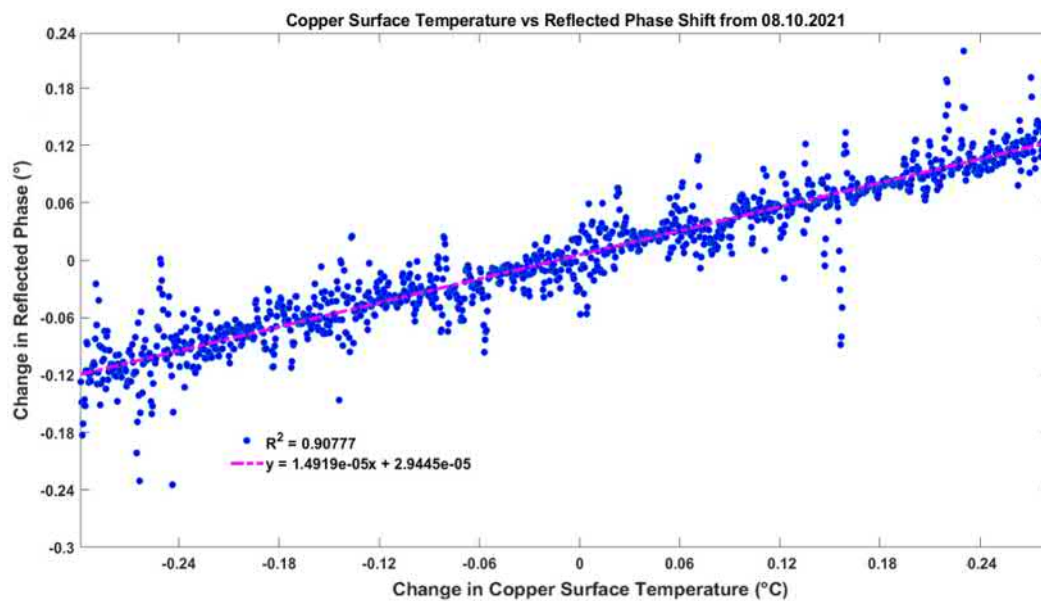


FIGURE 6.43: Correlation between change in reflected phase measured using the PXI and change in copper surface temperature measured using a PT100 probe on the bare copper in the gallery

Thermal expansion and contraction of the copper changes the dimensions of the waveguide, which changes the phase velocity and guide wavelength of the propagating RF. The linear expansion of copper was described in Equation 6.18 in Section 6.4. In this experiment the TWT pulses were intended to be reflected by the mode converters rather than the load. The Xbox1 waveguide network spans three different areas: the CTF2 klystron gallery, the CTF2 bunker and the CT3 LINAC bunker. These areas will all have different temperature profiles which means the phase shift may not be exact or consistent along the entire line, in addition the cables returning from these sections will also expand and contract differently. Expansion of cables has not been considered in this work.

## 6.8 Conclusion

### 6.8.1 Low Power Tests

The results of the low power tests shows that the interferometer operates as predicted. When the difference in path length between the two arms is correctly phased the forward power from both ports is correctly recombined and the full power can be transmitted forward through the interferometer section.

The low power tests demonstrate that when the path difference is correct and the signal is reflected back to the interferometer from the output port using a short, the power will be directed back to the injection port and the second input port is isolated.

When the phase of the short is changed the reflected amplitude is relatively unresponsive at both ports and both frequencies. However, the reflected phase responds linearly only at the correct port and frequency. The reflected phase at port 4 will be monitored to identify changes in the long waveguide network, the sensitivity of the phase response at this port is  $1.9^\circ$  per degree of phase shift at the short. The system will be stabilised thermally and isolated from the environment to reduce phase changes from the interferometer itself. Changing the temperature of the interferometer by  $1^\circ\text{C}$  is significant enough to mask small phase changes in the range of  $0.5^\circ$  in the waveguide network.

### 6.8.2 High Power Results

The frequencies and filling medium can be changed and the system can be re-calibrated. However, it is crucial the klystron is not pulsed until the system has reached the desired temperature otherwise significant power is directed back to the TWT port which will damage the TWT, there are several mechanisms in place to prevent this.

Reflected signals at the klystron port are not long enough in duration to be able to provide a very accurate phase measurement and the phase jitter from the klystron is a significant.

The TWT pulse measurement is much higher precision due to the long phase length. The TWT pulses were down-converted using the low phase noise LLRF system at Xbox1 and digitised using the NI5162 ADC. The TWT pulses were reflected from the mode convertors by pulsing outside their bandwidth, the frequency of the

TWT signals is changed using the NI5793 signal generator card in the PXI, and this is synchronised with the CLEAR master oscillator.

There is a strong linear relationship between the phase shift and the temperature. A temperature change of 1 °C corresponds to a phase shift of 1.5°. Simple analysis predicts 2°. Detailed simulation indicated 1.9° given the imperfect components.

The changes in the reflected phase from the TWT can be separated into two distinct profiles with differing time periods. There is an oscillation with a time period of approximately 24 hours which corresponds to a day night cycle and is correlated to the WR90 surface temperature in the klystron gallery.

Additionally, there are short term phase shifts which are caused by the air conditioning in the klystron gallery, both the air conditioning cycle and the phase shift cycle have a time period of approximately 23 minutes. There may be other environmental effects on the waveguide (such as ground motion or vibrations from equipment) but they were not studied in this work.

The interferometer is successful as a proof of principle; the system demonstrates a method for diplexing two pulses of differing frequencies into a single waveguide network. The secondary pulse can be used to monitor the changing length of the waveguide network and stabilise the phase arriving at an accelerating structure using a feed-forward system acting on the phase leaving the klystron.

## Chapter 7

# Conclusion

This thesis outlines the work which was undertaken to upgrade the first high power X-band test stand at CERN, Xbox1. The development of the new X-band LLRF system was followed from inception to completion and a custom cavity filter was designed and implemented. The newly developed LLRF system with improved phase stability was characterised and utilised to commission (RF conditioning) a 50 MW klystron. The phase stability of the klystron was studied using the new LLRF system. Finally, a single path interferometer was designed and constructed from WR90 waveguide. The interferometer was used to pulse a secondary frequency into the waveguide network at Xbox1 in order to measure small phase changes in the network which occur as a result of the changing environment.

### Relevance

In any accelerator it is important to maintain beam quality by controlling the phase of RF powering the accelerating structures. The stability of the RF power source is a particularly important metric in LINAC applications. Phase and amplitude errors from the RF will result in energy errors, causing emittance blow-up and luminosity reduction of the accelerated beam in a LINAC.

The thesis work is especially relevant to 'klystron based CLIC' and to the use of crab cavities in the CLIC beam delivery system. This is the working mode of a proposed CLIC low energy machine powered using klystrons rather than a drive beam. Two clear advantages of a klystron-based design over a two-beam design at low energy are that the technical development of full RF unit prototypes is essentially complete and thus can be tested easily.

It is particularly important in CLIC to guarantee the synchronisation between crab cavities and to preserve luminosity. Regulation of the field phase in accelerating structures is an important parameter that controls performance, especially in

machines like FELs.

The stability of the free electron laser output is primarily determined by the stability of the electron beam, and the stability of the electron beam based on RF linac is mainly determined by the stability of the microwave source. According to FEL theory, to realise the saturation output of FEL and to get better FEL spectrum purity, the amplitude and phase stability of RF power must be very high.

A phase error induced by the LLRF that controls the X-band structure directly affects beam quality, particularly in the aforementioned machines. Furthermore, phase noise added during down-conversion directly will appear as jitter on the RF pulses, resulting in an incorrect instantaneous measurement of the RF phase at the accelerating structure.

Moreover, there is a requirement at Xbox1 to synchronise the RF pulses with a beam in accelerating structures that are more than 30 m away. It is a common modality for the RF source to be separated from the RF cavity and hence the power delivery system contains stretches of waveguide which are vulnerable to environmental changes.

### Summary of Results

The single-sideband up-converter and cavity filter combination produced significantly lower phase-noise than the X-Band PLL. The average reduction in phase noise close to the carrier (up to 10 kHz) is 40.64 dBm. The improvement in phase noise from the single side-band up-converter is maintained through the down-conversion chain. The up-converter utilised a custom designed cavity filter which was designed in this work.

The up-converter and the PLL were both used as the 11.8068 GHz local oscillator source for down-conversion of the X-band signals. The improvement in the phase noise of the up-converter translates to a reduction in the intra-pulse phase stability of the reference channel. The average intra-pulse phase stability of the reference channel is reduced by  $0.385^\circ \pm 0.027^\circ$ .

The pulse-to-pulse phase stability of the TWT and klystron was measured and it does not achieve the  $1^\circ$  phase stability target set in this work. As with the phase stability, the amplitude stability also worsens after the TWT and again after the klystron. The desired amplitude stability leaving the klystron is 0.1% amplitude jitter, this is not achieved on a pulse-to-pulse basis at Xbox1.

The sensitivity of the klystron output phase to several input parameters was measured using one-at-a-time sensitivity analysis. The phase instability is greatest when operating at high modulator voltages and low RF power levels. The modulator voltage ripple can be correlated with a ripple on the phase leaving the klystron. Even with this correction applied in post processing, the klystron does not provide sufficient phase stability to meet the CLIC requirements for the stability of the phase arriving at the accelerating structures. Therefore, a feedback system will be required in order to adjust the phase leaving the klystron in order to stabilise the phase arriving at the structure.

A proof-of-principle experiment was devised to allow injection of two independent pulses at differing frequencies into a single waveguide network. The method successfully uses single path interferometry to diplex a 'phase measurement pulse' into the Xbox1 network which is used to measure the phase stability of the line.

The results of the low power tests show that the interferometer operates as predicted in the simulation. The low power tests demonstrate that when the path difference is correct, any reflected power is directed back to the original input port and the second input port is isolated. The reflected phase responds proportionally only at the correct port and frequency. The sensitivity of the phase response at this port is  $1.9^\circ$  per degree of phase shift at the short.

The system was successfully transferred from the lab and installed into the high power network at Xbox1. A TWT was used to inject pulses at the second frequency over the course of several days. The detected phase changes in the reflected phase from the TWT can be separated into two distinct profiles with differing time periods.

### **Future Work**

The LLRF system at Xbox1 has improved phase noise stability due to the redesign and improved local oscillator. However, a full characterisation of the LLRF including the signal processing could be completed. In particular a study of the ADC conversion errors and their effect on the quality of the measurements. Signal processing techniques were also not studied in detail in this work. For example in the PXI acquisition code there is an FIR filter which has not been optimised in this work. Also complex signal processing techniques implemented on the phase and amplitude data was not considered. It is possible that more information can be extracted from the measured signals than has been elucidated here.

At X-band frequencies the wavelength is on the order of 2.5 cm which is on a similar order of magnitude with several components, connectors or spaces in the LLRF crate. Hence it was a concern whether there is radiated coupling or leaking inside the crate. A small but simple experiment would be to add RF shielding tape in and around the LLRF crate and re-measure the phase noise in particular.

Along a similar theme the thermal stability of the LLRF crate and the PXI was not considered here. For example, it is known that in the summer the PXI crate at Xbox3 is liable to overheating and hence a chiller system was implemented. The temperature variations measured in Chapter 6 will also effect the RF high power cables, low power cables and even the sensitive components in the LLRF crate (alongside internal heating from the crate itself). These thermal drifts can likely be measured via a high precision measurements of the reference channel.

The acquisition uses an IQ sampling, where the sampling signal is four times the frequency of the measurement signal. However, higher order frequencies in the system which are multiples of the IF will be aliased. An alternative method would produce a clock at a frequency close to a multiple of four. This can be easily implemented by changing the division ratio of the divider or by changing the tuning word of the DDS (both very simple operations). A study of the acquired signals using the non-IQ sampling scheme would be of interest in trying to identify high order modes propagating in the system. It is known that these frequencies exist in the system because their magnitude has been measured at the klystron output using a power meter.

Since the conception of the new LLRF and the development of the other two X-band test stands there have been advances in the PXI cards available. Hence the system could be easily improved by using purchasing new ADCs. For the same sampling speed these have many more bits. Also a greater sampling rate would increase the level of oversampling leading to shorter sampling bins and hence more resolution in the time domain. This would be particularly useful when examining features such as the rising edge of pulses where the timescale is so short.

More importantly perhaps, the RF generator card can also be replaced by a new model with more bits and possibly an improved internal oscillator. This would easily improve the phase noise of the transmitter as the RF generator card was the highest contributor to the phase noise.

All of the above tests would serve the purpose of completely characterising the low power and control section of the system at Xbox1. The conceivable errors can

be known and mitigated such that the quality of the phase and amplitude at low powers is improved.

It is crucial to improve the stability of the phase leaving the klystron in order to be able to meet the CLIC requirements. All of the above tests would serve the purpose of completely characterising the low power and control section of the system at Xbox1. The conceivable errors can be known and mitigated such that the quality of the phase and amplitude at low powers is improved.

There are several suggestions for methods to improve the high power stability. From this work, one clear solution is to improve the modulator stability, as it was shown that the ripple on the modulator voltage has a detrimental effect on the phase leaving the klystron. Furthermore, the reproducibility of the modulator voltage can be improved.

Secondly, implementation of a feedback loop operating on the klystron. Currently, at Xbox1, there are continuous measurements of several vital parameters; namely, the input and output phase and amplitude, the modulator voltage and the pulse length. These measurements can be used to design an algorithm which can adjust the output of the klystron phase and amplitude. It could even be helpful to add additional environmental measurements into the PXI system. These would include: ambient air temperatures, copper surface temperatures and cooling water flow rates inside the klystron and modulator system.

The study of the klystron can be furthered by studying the amplitude stability. It is possible that the input amplitude jitter is linked to the phase stability in a way that has not been elucidated here.

Originally, the interferometer was designed for implementation into Xbox1 with an accelerating structure. It was designed so that the klystron pulses were transmitted into the accelerating structure and the TWT pulses were totally reflected. The interferometer can be implemented at Xbox1 alongside the klystron with an accelerating structure, or other filtering component, replacing the loads, as was the intended operation. In addition, the installation of a high power RF window would allow both the TWT and the klystron to operate simultaneously with their pulses interleaved. This would prove that the TWT and klystron can be operated in parallel without interference.

It is evident that the interferometer needs to be thermally stable in order to detect phase changes in the waveguide. It is important to develop a control system to be able to maintain the thermal stabilisation of the interferometer to the order of  $0.1^{\circ}\text{C}$ .

The interferometer can be used to implement a feedback and control algorithm which will correct the changing phase in the waveguide network. This would require an additional programmable phase shifter to be integrated into the network. Ideally, the feedback system would be integrated into the PXI system for real time control. The high power, WR90 phase shifter which was tested at the Xboxes would be an ideal candidate and could be controlled using a motor connected to the PXI.

# Bibliography

- [1] L. Evans and P. Bryant, “LHC Machine”, *Journal of Instrumentation*, vol. 3, no. 8, S08001, Aug. 2008. DOI: 10.1088/1748-0221/3/08/S08001.
- [2] C. Quigg, “The coming revolutions in particle physics”, vol. 298, no. 2, Jan. 2008, ISSN: 0036-8733. DOI: 10.1038/scientificamerican0208-46. [Online]. Available: <https://www.osti.gov/biblio/987233>.
- [3] W. Scandale, “Status of the LHC and possible scenarios for the luminosity upgrade”, *Italian Phys. Soc. Proc.*, vol. 92, pp. 3–18, 2006.
- [4] W. H. B. Muratori, “Concept of luminosity”, CERN, Tech. Rep., 2006.
- [5] M. Aicheler, U. Ruhr, P. Burrows, M. Draper, and et al, “A multi-TeV linear collider based on CLIC technology: CLIC conceptual design report”, European Organization For Nuclear Research, Tech. Rep., 2012.
- [6] G. Riddone, D. Gudkov, A. Samoshkin, and A. Solodko, “CLIC Two-Beam Module for the CLIC Conceptual Design and Related Experimental Program”, *Conf. Proc. C*, vol. 110904, C. Petit-Jean-Genaz, Ed., pp. 1003–1005, 2011.
- [7] T. Higo, *Performance of CLIC prototype accelerator structures tested at nexteF*, Presentation, Feb. 2014.
- [8] “The European Strategy for Particle Physics Update 2013. La stratégie européenne pour la physique des particules Mise à jour 2013. 16th Session of European Strategy Council”, 2013. [Online]. Available: <https://cds.cern.ch/record/1567258>.
- [9] R. Poeschl, “Future colliders - linear and circular”, *Proceedings of An Alpine LHC Physics Summit — PoS(ALPS2018)*, 2018. DOI: 10.22323/1.330.0042. [Online]. Available: <http://dx.doi.org/10.22323/1.330.0042>.
- [10] T. Golling, M. Hance, and P. Harris, “Beyond the standard model phenomena: physics at a 100 TeV”, *CERN Yellow Report*, no. CERN-TH-2016-111. CERN-TH-2016-111. CERN-ATS-2016-004. 3, 441–634. 197 p, 2016. DOI: 10.23731/

- CYRM-2017-003.441. [Online]. Available: <https://cds.cern.ch/record/2158187>.
- [11] *Cepc conceptual design report: Volume 1 - accelerator*, 2018. arXiv: 1809.00285 [physics.acc-ph].
- [12] D.Brandt, H.Burkhardt, M.Lamont, S. Myers, and J.Wenninger, "Accelerator physics at lep", European Organization For Nuclear Research, Tech. Rep., 2000.
- [13] S. Geer, "Muon colliders and neutrino factories", FermiLab, Tech. Rep., 2012.
- [14] T. Behnke, J. E. Brau, B. Foster, J. Fuster, M. Harrison, J. M. Paterson, M. Peskin, M. Stanitzki, N. Walker, and H. Yamamoto, *The international linear collider technical design report - volume 1: Executive summary*, 2013. arXiv: 1306.6327 [physics.acc-ph].
- [15] P. Roloff, R. Franceschini, U. Schnoor, and A. Wulzer, *The compact linear  $e^+e^-$  collider (clic): Physics potential*, 2018. arXiv: 1812.07986 [hep-ex].
- [16] "CTF2 design report: the CLIC test facility. CERN. Geneva", CERN, Geneva, Tech. Rep. CERN-PS-96-014-LP. CLIC-Note-304, 1996. [Online]. Available: <https://cds.cern.ch/record/307310>.
- [17] R Corsini, A Ferrari, L. Rinolfi, P Royer, and F. A. Tecker, "Experimental results on electron beam combination and bunch frequency multiplication", *Phys. Rev. Spec. Top. Accel. Beams*, vol. 7, no. 4, p. 040101, 2004. DOI: 10.1103/PhysRevSTAB.7.040101. [Online]. Available: <http://cds.cern.ch/record/909123>.
- [18] D. Schulte, A. Grudiev, P. Lebrun, G. McMonagle, I. Syratchev, and W. Wuenesch, "Status of the Exploration of an Alternative CLIC First Energy Stage Based on Klystrons", in *4th International Particle Accelerator Conference*, 2013, TUPME049.
- [19] H. H. Braun, "CLIC progress towards Multi-TeV Linear Colliders.", 2005. [Online]. Available: <https://cds.cern.ch/record/879700>.
- [20] M Brugger and et al, "The CLEAR facility at CERN", 2016.
- [21] R. Corsini, "Final Results From the Clic Test Facility (CTF3)", no. CERN-ACC-2017-130. CLIC-Note-1113, TUZB1. 6 p, 2017. DOI: 10.18429/JACoW-IPAC2017-TUZB1. [Online]. Available: <http://cds.cern.ch/record/2289699>.

- [22] R. Ruber, V. Ziemann, T. Ekelöf, A. Palaia, W. Farabolini, and R. Corsini, "The CTF3 Two-beam Test Stand", *Nucl. Instrum. Meth.*, vol. A729, pp. 546–553, 2013. DOI: 10.1016/j.nima.2013.07.055.
- [23] R. Corsini, "Clic r d: Technology, test facilities and future plans", *Nuclear Physics B - Proceedings Supplements*, vol. 154, no. 1, pp. 137–145, 2006, Proceedings of the High Intensity Frontier Workshop, ISSN: 0920-5632. DOI: <https://doi.org/10.1016/j.nuclphysbps.2006.01.053>. [Online]. Available: <https://www.sciencedirect.com/science/article/pii/S0920563206000661>.
- [24] D. P. Pritzkau, "RF pulsed heating", PhD thesis, Stanford U., 2001.
- [25] A. Grudiev, D. Schulte, and W. Wuensch, "Optimum frequency and gradient for the clic main linac accelerating structure", Jan. 2006.
- [26] A. Grudiev and W. Wuensch, "Design of the clic main linac accelerating structure for clic conceptual design report", Jan. 2010.
- [27] A. Descoeurdes, Y. Levinsen, S. Calatroni, M. Taborelli, and W. Wuensch, Eds., *Investigation of the DC Vacuum Breakdown Mechanism*, Physical Review - Special Topics-Accelerators and Beams, CERN, 1211 Geneva 23, Switzerland: European Organization For Nuclear Research, Sep. 2009.
- [28] V. Pirozhenko, "Efficient traveling-wave accelerating structure for linear accelerators", *EPAC 2008 - Contributions to the Proceedings*, Jan. 2008.
- [29] R. H. Miller, "Comparison of Standing Wave and Traveling Wave Structures", in *13th International Linear Accelerator Conference*, 1986, TU2–4.
- [30] F. Gerigk, *Cavity types*, 2011. arXiv: 1111.4897 [physics.acc-ph].
- [31] P. Schmueser, "Basic principles of RF superconductivity and superconducting cavities", in *CERN Accelerator School and DESY Zeuthen: Accelerator Physics*, Sep. 2003, pp. 183–202.
- [32] W. D. Kilpatrick, "Criterion for vacuum sparking designed to include both rf and dc", *Review of Scientific Instruments*, vol. 28, no. 10, pp. 824–826, 1957. DOI: 10.1063/1.1715731. eprint: <https://doi.org/10.1063/1.1715731>. [Online]. Available: <https://doi.org/10.1063/1.1715731>.
- [33] E. Tanabe, J. Wang, and G. Loew, "Voltage breakdown at x-band and c-band frequencies", 1986.

- [34] A. Grudiev, S. Calatroni, and W. Wuensch, "New local field quantity describing the high gradient limit of accelerating structures", *Phys. Rev. ST Accel. Beams*, vol. 12, p. 102001, 10 2009. DOI: 10.1103/PhysRevSTAB.12.102001. [Online]. Available: <https://link.aps.org/doi/10.1103/PhysRevSTAB.12.102001>.
- [35] X. Wu, J. Shi, H. Chen, J. Shao, T. Abe, T. Higo, S. Matsumoto, and W. Wuensch, "High-gradient breakdown studies of an X-band Compact Linear Collider prototype structure", *Phys. Rev. Accel. Beams*, vol. 20, no. 5, p. 052001, 2017. DOI: 10.1103/PhysRevAccelBeams.20.052001.
- [36] B. Woolley, "High power x-band rf test stand development and high power testing of the clic crab cavity", English, PhD thesis, Lancaster University, 2015.
- [37] B. Woolley, "High power x-band rf test stand development and high power testing of the clic crab cavity", PhD thesis, Lancaster university, 2015.
- [38] R. Rajamäki, "Vacuum arc localization in clic prototype radio frequency accelerating structures", PhD thesis, Aalto university school of electrical engineering, Mar. 2016.
- [39] S. Matsumoto, M. Akemoto, S. Fukuda, T. Higo, N. Kudoh, H. Matsushita, and H. Nakajima, "Nextef : 100mw x-band test facility in kek", Jan. 2008.
- [40] F Peauger, A Hamdi, S Curt, S Doebert, G McMonagle, G Rossat, K. Schirm, I Syrathev, L Timeo, S Kuzikhov, A. Vikharev, A Haase, D Sprehn, A Jensen, E. Jongewaard, C. Nantista, and A Vlieks, "A 12 GHZ RF Power source for the CLIC study", no. CERN-ATS-2010-196, 4 p, 2010. [Online]. Available: <https://cds.cern.ch/record/1287901>.
- [41] P Wilson, Z. D. Farkas, and R. D. Ruth, "SLED II: A New Method of RF Pulse Compression", *Proceedings of the Linear Accelerator Conference*, pp. 546–553, 1990.
- [42] G. Caryotakis, "Developent of x-band klystron technology at slac", SLAC, Tech. Rep., 2009.
- [43] A Fiebig and C Schieblich, "A SLED type pulse compressor with rectangular pulse shape", no. CERN-PS-90-13-RF, 4 p, 1990. [Online]. Available: <https://cds.cern.ch/record/209756>.

- [44] G. Istee, "Guglielmo marconi and the history of radio. part i", vol. 7, pp. 45–56, Jan. 1991.
- [45] E. Schoenherr, *The digital revolution*, <https://web.archive.org/web/20081007132355/http://history.sandiego.edu/gen/recording/digital.html>, May 2004.
- [46] O. Ugweje, "Radio frequency and wireless communications", in. Apr. 2004, ISBN: 9780471482963. DOI: 10.1002/047148296X.tie151.
- [47] A. W. Chao, K. H. Mess, M. Tigner, and F. Zimmermann, *Handbook of accelerator physics and engineering; 2nd ed.* Singapore: World Scientific, 2013. DOI: 10.1142/8543. [Online]. Available: <https://cds.cern.ch/record/1490001>.
- [48] T. Roupael, "Wireless receiver architectures and design: Antennas, rf, synthesizers, mixed signal, and digital signal processing", *Wireless Receiver Architectures and Design: Antennas, RF, Synthesizers, Mixed Signal, and Digital Signal Processing*, pp. 1–488, Jan. 2014.
- [49] P. Horowitz and W. Hill, *The art of electronics; 3rd ed.* Cambridge: Cambridge University Press, 2015. [Online]. Available: <https://cds.cern.ch/record/1981307>.
- [50] T Schilcher, "RF applications in digital signal processing", 2008. DOI: 10.5170/CERN-2008-003.249. [Online]. Available: <https://cds.cern.ch/record/1100538>.
- [51] P. Delos, "Iq, image reject single sideband mixer primer", Marki Microwave Technical Articles, Tech. Rep., 2018.
- [52] P. O. Mark Curtin, "Phase-locked loops for high-frequency receivers and transmitters", Analog Dialogue 33-3, Tech. Rep., 1999.
- [53] E. Y. L. Matthaei George; Jones, *Microwave filters, impedance-matching networks, and coupling structures*. Dedham, Massachusetts: Artech House Books, 1980, ISBN: 0-89006-099-1.
- [54] A. Scheinker, C. Emma, A. L. Edelen, and S. Gessner, *Advanced control methods for particle accelerators (acm4pa) 2019 workshop report*, 2020. arXiv: 2001.05461 [physics.acc-ph].
- [55] *Fundamentals of rf and microwave power measurements - part1*, Keysight, Apr. 2000.
- [56] V. Aleinikov, I. Borina, A. Krylov, and S. Pachtchenko, "Using labview to build distributed control system of a particle accelerator", Oct. 2017.

- [57] J. J. Carr, *Practical radio frequency test and measurement: a technician's handbook*. Boston, MA: Newnes, 1999. [Online]. Available: <https://cds.cern.ch/record/441933>.
- [58] U. Mavric and G. Jug, "Design approaches for the x band llrf system", *Nuclear Instruments Methods in Physics Research Section A-accelerators Spectrometers Detectors and Associated Equipment - NUCL INSTRUM METH PHYS RES A*, vol. 657, pp. 22–26, Nov. 2011. DOI: 10.1016/j.nima.2011.05.027.
- [59] L. Zhao, X. Gao, X. hu, S. Liu, and Q. An, "Beam position and phase measurement system for the proton accelerator in ads", *IEEE Transactions on Nuclear Science*, vol. 61, Jan. 2014. DOI: 10.1109/TNS.2013.2291779.
- [60] Y. Cheng-Ke, D. Zhi-Min, L. Jian-Fei, Z. Yu-Bin, Z. Tong-Xuan, F. Ze-Chuan, and L. Wei-Qing, "A non-IQ sampling controller in low level RF system", *Chinese Physics C*, vol. 32, no. 10, pp. 852–856, 2008. DOI: 10.1088/1674-1137/32/10/018. [Online]. Available: <https://doi.org/10.1088/1674-1137/32/10/018>.
- [61] S. R. Kurtz, "Mixers as phase detectors", The Communications Edge, Tech. Rep., 1978.
- [62] P. L. Lui, "Passive intermodulation interference in communication systems", *Electronics Communication Engineering Journal*, vol. 2, no. 3, pp. 109–118, 1990.
- [63] S. Tenney, "Rf transmitter measurements every engineer should know", Tech. Rep., Jul. 2019.
- [64] CustomMMIC, "Addressing phase noise challenges in radar and communication systems", CustomMMIC, Tech. Rep., 2018.
- [65] J. B. Johnson, "Thermal agitation of electricity in conductors", *Phys. Rev.*, vol. 32, pp. 97–109, 1 1928. DOI: 10.1103/PhysRev.32.97. [Online]. Available: <https://link.aps.org/doi/10.1103/PhysRev.32.97>.
- [66] N. Roberts, "Phase Noise and Jitter – A Primer for Digital Designers", *EEdesign*, 2015. DOI: <http://www.eedesign.com>.
- [67] M. R. Khanzadi, D. Kuylenstierna, T. Eriksson, and H. Zirath, "Calculation of the performance of communication systems from measured oscillator phase noise", *Circuits and Systems I: Regular Papers, IEEE Transactions on*, vol. 61, May 2013. DOI: 10.1109/TCSI.2013.2285698.

- [68] D. Owen, "Good practice guide to phase noise measurement", Pickering Interfaces, Tech. Rep., 2004.
- [69] E. Rubiola and V. Giordano, "Correlation-based phase noise measurements", *Review of Scientific Instruments*, vol. 71, no. 8, pp. 3085–3091, 2000. DOI: 10.1063/1.1304871. [Online]. Available: <https://doi.org/10.1063/1.1304871>.
- [70] E. Rubiola and R. Brendel, "The AM noise mechanism in oscillators", *IEEE*, 2009. [Online]. Available: <http://rubiola.org/pdf-articles/conference/2009-ifcs-oscillator-AM-noise.pdf>.
- [71] T. J. Bress, "Effective labview programming", in. NTS Press., 2013, ISBN: 978-1-934891-08-7.
- [72] D Rémi, *The maturity of visual programming*, <https://www.craft.ai/blog/the-maturity-of-visual-programming>, Sep. 2015.
- [73] J. Travis, "Labview for everyone: Graphical programming made easy and fun (3rd ed.)", in. Prentice Hall, 2006, ISBN: 0131856723.
- [74] C. Salzmann, D. Gillet, and P. Huguenin, "Introduction to real-time control using labview with an application to distance learning", *Int J Eng Educ*, vol. 16, Jan. 2000.
- [75] T. Fountain, A. McCarthy, and F. Peng, "Pci express: An overview of pci express, cabled pci express, and pxi express", 2005.
- [76] I. B. Fernández, "Advanced techniques for diagnostics and control applied to particle accelerators", PhD thesis, University of the Basque Country, 2015.
- [77] J. Serrano, P. Alvarez, M. Lipinski, and T. Wlostowski, "Accelerator Timing Systems Overview", *Conf. Proc. C*, vol. 110328, T. Satogata and K. Brown, Eds., pp. 1376–1380, 2011.
- [78] M. E. Angoletta, S. Albright, A. Findlay, M. Haase, S. Hancock, M. Jaussi, J. Molendijk, M. Paoluzzi, and J. Sanchez-Quesada, "The New LEIR Digital Low-Level RF System", in *8th International Particle Accelerator Conference*, 2017, THPAB144. DOI: 10.18429/JACoW-IPAC2017-THPAB144.
- [79] *Ni pxi timing and synchronization design advantages*, <https://www.ni.com/en-gb/innovations/white-papers/11/ni-pxi-timing-and-synchronization-design-advantages.html>, Apr. 2019.

- [80] T. Higo, T. Abe, Y. Arakida, Y. Higashi, S. Matsumoto, T. Shidara, T. Takatomi, M. Yamanaka, A. Grudiev, G. Riddone, and W. Wuensch, "Comparison of High Gradient Performance in Varying Cavity Geometries", WEPFI018. 3 p, 2013. [Online]. Available: <https://cds.cern.ch/record/2110690>.
- [81] C. Adolphsen, "Normal-conducting rf structure test facilities and results", in *Proceedings of the 2003 Particle Accelerator Conference*, vol. 1, 2003, 668–672 Vol.1. DOI: 10.1109/PAC.2003.1289005.
- [82] A. Schnase *et al.*, "J-PARC RCS Non-linear Frequency Sweep Analysis", *Conf. Proc. C*, vol. 0806233, I. Andrian and C. Petit-Jean-Genaz, Eds., MOPC120, 2008.
- [83] G. Jug and A. Koiek, "Libera llrf - development and tests", 2010.
- [84] G. D'Auria, M. El-Ashmawy, A. Rohlev, M. Scafaru, C. Serpico, A. Turchet, and D. Wang, "The X-band System for the FERMI@ELETTRA FEL Project", *Conf. Proc. C*, vol. 100523, A. Noda, C. Petit-Jean-Genaz, V. R. W. Schaa, T. Shirai, and A. Shirakawa, Eds., TUPE015, 2010.
- [85] S. Levantino, L. Romano, S. Pellerano, C. Samori, and A. L. Lacaíta, "Phase noise in digital frequency dividers", *IEEE Journal of Solid-State Circuits*, vol. 39, no. 5, pp. 775–784, 2004. DOI: 10.1109/JSSC.2004.826338.
- [86] E. Rubiola, "Phase noise and frequency stability in oscillators", *Phase Noise and Frequency Stability in Oscillators*, Nov. 2008. DOI: 10.1017/CB09780511812798.
- [87] W. Kester, "Converting oscillator phase noise to time jitter", Jan. 2005.
- [88] T. Schilcher, "RF applications in digital signal processing", in *CERN Accelerator School: Specialized Course on Digital Signal Processing*, 2008.
- [89] S. Simrock, M. Hoffmann, F. Ludwig, M. K. Grecki, and T. Jezynski, "Considerations for the choice of the intermediate frequency and sampling rate for digital RF control", *Conf. Proc. C*, vol. 060626, C. Prior, Ed., pp. 1462–1464, 2006.
- [90] C. J. Grebenkemper, "Local oscillator phase noise and its effect on receiver performance", 2000.
- [91] C. Slattery, "Direct digital synthesis ( dds ) controls waveforms in test , measurement , and communications", 2005.

- [92] C. E. Calosso, Y. Gruson, and E. Rubiola, "Phase noise and amplitude noise in dds", in *2012 IEEE International Frequency Control Symposium Proceedings*, 2012, pp. 1–6. DOI: 10.1109/FCS.2012.6243619.
- [93] D. M. Pozar, *Microwave engineering*, ser. Addison-Wesley series in electrical and computer engineering. Addison-Wesley, 1990, ISBN: 0201504189.
- [94] S. A. Maas, *Microwave mixers*, 2nd ed., ser. The Artech House microwave library. Artech House, 1992, ISBN: 0890066051.
- [95] M. Curtin and P. O'Brien, "Phase-locked loops for high-frequency receivers and transmitters – part 1 by", 1999.
- [96] D. Banerjee, *PLL performance, simulation and design*. Dog Ear Publishing, 2006.
- [97] Analog Devices, *Adisimpll*, version 0.20.2, Aug. 29, 2022. [Online]. Available: <https://www.analog.com/en/design-center/adisimpll.html>.
- [98] B. C. Henderson and J. A. Cook, *Image-reject and single-sideband mixers*, 1985. [Online]. Available: [http://www.triquint.com/prodserv/tech\\_info/docs/WJ/ImageRej\\_n\\_SSB\\_mixers.pdf](http://www.triquint.com/prodserv/tech_info/docs/WJ/ImageRej_n_SSB_mixers.pdf).
- [99] D. Natarajan, "A practical design of lumped, semi-lumped and microwave cavity filters", *Lecture Notes in Electrical Engineering*, vol. 183, pp. 1–157, Oct. 2013. DOI: 10.1007/978-3-642-32861-9\_1.
- [100] F. J. Williams Arthur B; Taylors, *Electronic Filter Design Handbook*. New York: McGraw Hill, 1988, ISBN: 0-07-070434-1.
- [101] A. Technologies, "Network analyser basics", p. 9, 2004. [Online]. Available: <http://cp.literature.agilent.com/litweb/pdf/5965-7917E.pdf>, (accessed: 04.01.2022).
- [102] R Anderson-Sprecher, "Model comparisons and r 2", *The American Statistician*, vol. 48, no. 2, pp. 113–117, 1994. DOI: 10.1080/00031305.1994.10476036. eprint: <https://doi.org/10.1080/00031305.1994.10476036>. [Online]. Available: <https://doi.org/10.1080/00031305.1994.10476036>.
- [103] F. D. Ramos. [Online]. Available: <https://cnc-proto.eu/>.
- [104] M. G. (2016). Status of the x-band klystron, [Online]. Available: [https://indico.cern.ch/event/449801/contributions/1945391/attachments/1212885/1769662/clic\\_workshop\\_2016.pdf](https://indico.cern.ch/event/449801/contributions/1945391/attachments/1212885/1769662/clic_workshop_2016.pdf). (accessed: 08.12.2021).

- [105] C. Huang, C. Burkhart, M. Kemp, B. Morris, T. Beukers, R. Ciprian, and M. Nguyen, "Development of a modulator pulse stability measurement device and test results at slac", in *2011 IEEE Pulsed Power Conference*, 2011, pp. 1526–1529. DOI: 10.1109/PPC.2011.6191676.
- [106] P. R. Maus, "Phase and amplitude stability of a pulsed RF system on the example of the CLIC drive beam LINAC", Presented 01 Mar 2017, 2016. [Online]. Available: <https://cds.cern.ch/record/2274101>.
- [107] P. McIntosh, R. Akre, R. Boyce, P. Emma, A. Hill, and C. Rago, "Overview of the RF Systems for LCLS", 3 p, 2005. [Online]. Available: <https://cds.cern.ch/record/894839>.
- [108] K. Czuba, K. Antoszkiewicz, S. Simrock, and H. Weddig, "The RF Phase Reference Distribution System Concept for the European XFEL", in *Particle Accelerator Conference (PAC 09)*, 2010, WE5PFP102.
- [109] Z. Geng *et al.*, "RF Jitter and Electron Beam Stability in the SwissFEL Linac", in *39th International Free Electron Laser Conference*, 2019, WEP037. DOI: 10.18429/JACoW-FEL2019-WEP037.
- [110] W. C. Nunnally and T. G. Engel, "Review of klystron modulator technology for particle accelerators", in *Digest of Technical Papers. 12th IEEE International Pulsed Power Conference. (Cat. No.99CH36358)*, vol. 2, 1999, 967–970 vol.2.
- [111] M. Pande and P. Singh, "Study of rf breakdown and multipacting in accelerator components", in *2014 International Symposium on Discharges and Electrical Insulation in Vacuum (ISDEIV)*, 2014, pp. 105–108. DOI: 10.1109/DEIV.2014.6961630.
- [112] C. Salmer, P. Eudeline, and P.-A. Rolland, "Pulse to pulse stability of solid state transmitter module for radars application", *1998 28th European Microwave Conference*, vol. 2, pp. 79–84, 1998.
- [113] P. Mcintosh, R. Akre, R. Boyce, P. Emma, A. Hill, and C. Rago, "Overview of the rf systems for lcls", Jun. 2005, pp. 2753 –2755. DOI: 10.1109/PAC.2005.1591254.
- [114] M. B. Trimale and Chilveri, "A review: Fir filter implementation", in *2017 2nd IEEE International Conference on Recent Trends in Electronics, Information Communication Technology (RTEICT)*, 2017, pp. 137–141. DOI: 10.1109/RTEICT.2017.8256573.

- [115] B. Beutner and S. Reiche, "Sensitivity and tolerance study for the swissfel", in *Proc. 32nd Int. Free Electron Laser Conf. (FEL'10)*, (Malmö, Sweden), 2010, pp. 437–440. DOI: <https://epaper.kek.jp/FEL2010/papers/wepb17.pdf>.
- [116] "Pulse to Pulse Stability of Solid State Transmitter Module for Radars Application", P. R. P. Salmer C; Eudeline, Ed., 1998.
- [117] A. Saltelli, "Sensitivity analysis for importance assessment", *Risk Analysis*, vol. 22, no. 3, pp. 579–590, 2002. DOI: <https://doi.org/10.1111/0272-4332.00040>. eprint: <https://onlinelibrary.wiley.com/doi/pdf/10.1111/0272-4332.00040>. [Online]. Available: <https://onlinelibrary.wiley.com/doi/abs/10.1111/0272-4332.00040>.
- [118] J. W. Kim, F. Oemer-Ilday, F. X. Kaertner, O. Muecke, and M. Perrott, "Large-Scale Timing Distribution and RF-Synchronization for FEL Facilities", 2004. [Online]. Available: <https://cds.cern.ch/record/931691>.
- [119] P Hariharan, *Basics of Interferometry 2nd Edition*. Academic Press, 2006.
- [120] S. Schulz *et al.*, "Few-Femtosecond Facility-Wide Synchronization of the European XFEL", in *39th International Free Electron Laser Conference*, Sep. 2019. DOI: 10.18429/JACoW-FEL2019-WEB04.
- [121] S. Yeddulla Muralidhar; Tantawi, "Analysis of a compact circular te<sub>0,1</sub> - rectangular te<sub>0,2</sub> waveguide mode converter", in *2007 IEEE Particle Accelerator Conference (PAC)*, 2007, pp. 587–589. DOI: 10.1109/PAC.2007.4440287.
- [122] S. Tantawi, G. Bowden, Z. Farkas, J. Irwin, K. Ko, N. Kroll, T. Lavine, Z. Li, R. Loewen, R. Miller, C. Nantista, R. Ruth, J. Rifkin, A. Vlieks, P. Wilson, C. Adolphsen, and J. Wang, "Multimoded rf delay line distribution system for the next linear collider", *AIP Conference Proceedings*, vol. 472, Jul. 1999. DOI: 10.1103/PhysRevSTAB.5.032001.

## Appendix A

# Simulation Results from Two Cavity Tuning

Cavity	Insertion (mm)	Cavity	Insertion (mm)	S11 Min (dB)	S11 Min Frequency (GHz)	S21 Max (dB)	S21 Min Frequency (GHz)
1	1.40	7	1.75	-7.52	11.638	-13.20	11.785
2	1.40	7	1.75	-25.50	11.866	-33.00	11.864
3	2.80	7	3.50	-10.38	11.654	-17.41	11.664
4	1.40	7	2.30	-28.23	11.834	-11.86	11.797
5	1.14	7	1.42	-26.14	11.798	-5.59	11.757
6	2.54	7	1.24	-27.18	11.905	-12.65	11.895
1	4.68	6	1.40	-17.57	11.714	-133.91	11.670
2	5.84	6	6.45	-7.12	11.764	-35.91	11.678
3	4.36	6	1.25	-29.43	11.785	-14.05	11.876
4	2.20	6	4.25	-29.96	11.830	-15.19	11.805
5	2.65	6	4.35	-20.89	11.962	-12.09	11.795
1	1.21	5	3.42	-27.79	11.767	-18.33	11.756
2	2.54	5	1.02	-5.78	11.782	-4.75	11.765
3	2.98	5	3.54	-24.88	11.689	-30.13	11.900
4	1.87	5	1.65	-12.75	11.793	-20.65	11.801
1	3.37	4	2.54	-8.95	11.890	-20.27	11.768
2	2.17	4	3.03	-7.23	11.861	-12.34	11.784
3	2.34	4	3.12	-14.65	11.812	-15.67	11.794
1	3.36	3	1.04	-19.00	11.753	-20.27	11.714
2	1.40	3	1.98	-15.67	11.795	-12.34	11.795
1	1.75	2	5.42	-5.42	11.657	-15.67	11.774

TABLE A.1: Tuning Results from Two Cavity Tuning

## Appendix B

# Full Calibration Results for NI5162A and NI5162B

Correction	
NI5162A CH0	NI5162B CH0
$y = 1.065 \cdot x + 0.061 - 0.0014$	$y = 1.032 \cdot x + 0.042 - 0.0017$
NI5162A CH1	NI5162B CH1
$y = 1.029 \cdot x + 0.091 - 0.0009$	$y = 1.038 \cdot x + 0.073 - 0.0029$
NI5162A CH2	NI5162B CH2
$y = 1.102 \cdot x + 0.075 - 0.0010$	$y = 1.091 \cdot x + 0.039 - 0.0009$
NI5162A CH3	NI5162B CH3
$y = 1.063 \cdot x + 0.075 - 0.0029$	$y = 1.087 \cdot x + 0.047 - 0.0029$

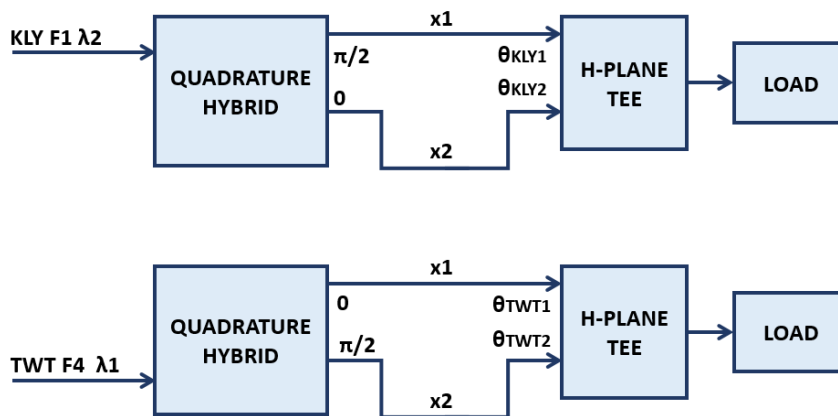
TABLE B.1: Corrections for NI5162A and NI5162B where  $x$  is the measured voltage on the channel (ADC Counts) and  $y$  is the adjusted voltage (ADC Counts)

Error with respect to the Reference (NI5162A CH0) ( $mV_{rms}$ )		
NI5162B CH0		
	Before Correction	After Correction
Mean (V)	2.103	0.248
$\sigma$ (V)	1.578	0.132
NI5162A CH1		
	Before Correction	After Correction
Mean (V)	2.093	0.284
$\sigma$ (V)	1.782	0.194
NI5162B CH1		
	Before Correction	After Correction
Mean (V)	2.123	0.304
$\sigma$ (V)	1.793	0.216
NI5162A CH2		
	Before Correction	After Correction
Mean (V)	2.156	0.194
$\sigma$ (V)	1.697	0.205
NI5162B CH2		
	Before Correction	After Correction
Mean (V)	2.302	0.297
$\sigma$ (V)	1.856	0.254
NI5162A CH3		
	Before Correction	After Correction
Mean (V)	1.994	0.245
$\sigma$ (V)	0.928	0.158
NI5162B CH3		
	Before Correction	After Correction
Mean (V)	2.435	0.301
$\sigma$ (V)	1.782	0.234

TABLE B.2: Error for each Channel with respect to the Reference Channel (NI5162A CH0) ( $mV_{rms}$ )

## Appendix C

# Explicitly Changing Phase Shifts on the Hybrid



When pulsing frequency 1 into path 1 the phase shift is:

$$\theta_1 = \frac{2\pi x_1}{\lambda_1}$$

For frequency 1 pulsing into path 2 the phase shift is:

$$\theta_2 = \frac{\pi}{2} + \frac{2\pi x_2}{\lambda_1}$$

The phase difference is therefore:

$$\Delta\theta = \theta_2 - \theta_1 = \frac{\pi}{2} + \frac{2\pi}{\lambda_1} \Delta x = 2\pi m$$

Conversely, when pulsing frequency 2 into path 1 the phase shift is:

$$\theta_1 = \frac{\pi}{2} + \frac{2\pi x_1}{\lambda_2}$$

For frequency 1 pulsing into path 2 the phase shift is:

$$\theta_2 = \frac{2\pi x_2}{\lambda_2}$$

The phase difference is therefore:

$$\Delta\theta = \theta_2 - \theta_1 = \frac{\pi}{2} + \frac{2\pi}{\lambda_2}\Delta x = 2\pi n$$

Where both m and n must be positive integers. A value of  $\Delta x$  must be found so that both phase difference equations are satisfied. Eliminate the path difference to give:

$$\Delta x = \lambda_1 \left( m - \frac{1}{4} \right) = \lambda_2 \left( n + \frac{1}{4} \right)$$

The smallest additional length occurs for the cases;  $m=n$ ,  $m=n+1$  or  $m=n-1$ . This produces three solutions:

$$\lambda_1 \left( n - \frac{1}{4} \right) = \lambda_2 \left( n + \frac{1}{4} \right)$$

$$\lambda_1 \left( n + \frac{3}{4} \right) = \lambda_2 \left( n + \frac{1}{4} \right)$$

$$\lambda_1 \left( n - \frac{5}{4} \right) = \lambda_2 \left( n + \frac{1}{4} \right)$$

The first equation is as before with  $\lambda_1$  and  $\lambda_2$  interchanged. The 2nd equation above maps to the 3rd previously with n replaced with n-1 and  $\lambda_1$  and  $\lambda_2$  interchanged. The third equation above maps to the 2nd previously with n replaced with n+1 and  $\lambda_1$  and  $\lambda_2$  interchanged.

## Appendix D

# Code for System Simulation

```

c   Stabilised line model
c   *****
c
c   Input high power pulses of frequency frq1 at F4 or F1
c   Input low power pulses of frequency frq2 at F1 or F4
c
c   Swapping F1 and F4 is not symmetrical as F2 and F3
c   have short and long lines respectively
c
c   For an input at F1 the long path 3 must be adjusted
c   until R4 is zero.
c   The phase of the reflection R1
c   then gives the length of line 5.
c
c   For an input at F4 the long path 3 must be
c   adjusted to set R1 to zero.
c   The phase of the reflection R4 then also
c   gives the length of line 5.
c
c   Let phase changes on line 3 at the two frequencies be ph1 and ph4
c   Our S matrix for the Quad Hybrid gives input
c   from line1 needing line 3 to lose pi/2
c   Our S matrix for the Quad Hybrid gives input from
c   line4 needing line 3 to gain pi/2
c   let x3-x2 be the extra length of line 3 over line 2
c   let w1 and w2 be the wavelengths of the two

```

```

c   frequencies in the waveguide.
c   phase = w*t - k*x hence note the minus signs
c   this gives

c   ph1 = -2*pi*(x3-x2)/wl1 = -pi/2 + 2*pi*n
c   ph2 = -2*pi*(x3-x2)/wl2 = +pi/2 + 2*pi*m
c   where m and n are integers

c   hence need (x3-x2) = wl1*(m - 0.25) = wl2*(n + 0.25)

c   for the shortest lines m will differ from n by 0, +1 and -1
c   for wl1>wl2  wl2=wl1*(4n-1)/(4n+1)
c   for wl2>wl1  wl2=wl1*(4n+3)/(4n+1)
c   for wl1<wl2  wl2=wl1*(4n-5)/(4n+1)

c   choosing frq1 hence wl1 and a value for n sets wl2 and hence frq2

c   The diagram defines a system with one input and
c   9 unknowns hence is solved by inverting
c   a 9x9 matrix.
c   this program set up the matrix and the solves it with
c   the routines lubksb, ludcmp

integer jvar
parameter(jvar=9)

c   Matrix index labels
c   1=F02, 2=R02, 3=F03, 4=R03, 5=F01 or F04, 6=R01 or R04,
7=F05,
c   8=R05, 9=R04, or R01

complex*16 M(jvar, jvar), A(jvar, jvar)
complex*16 x(jvar), y(jvar)
complex*16 chk(jvar)
complex*16 t11, t22, t33, t44, t12, t13, t14, t23, t24, t34

```

```

complex*16 SL1, SL2
complex*16 r1, r2, r3, r4
complex*16 phi2, phi3, phi5

complex*16 j

real*8 value
real*8 pi, tpi, rt2, one, two, zero
real*8 phi2_deg, phi3_deg, phi5_deg, phi_diff
c real*8 ph21_deg, ph22_deg

real*8 phase6, phase9
real*8 phase6_deg, phase9_deg
real*8 mag6, mag7, mag9, xr6, xr7, xr9, xi6, xi7, xi9
c the outputs of interest are X(6) and X(9) which are R01 and R04
c a further output of interest is X(7) which is F05

real*8 frq1, frq2, wl1, wl2, ghz, ghz1, ghz2, frqG
real*8 lgth2, lgth3, lgth5, extra_lgth, lgth_diff
real*8 length5, dlgth3
real*8 d, alpha
real*8 aa, cc, cvac, cair
real*8 DRV1, DRV2
real*8 fi14, r1i14, r2i14, fi23, r1i23, r2i23
real*8 fr11, r1r11, r2r11, fr22, r1r22, r2r22
real*8 fr33, r1r33, r2r33, fr44, r1r44, r2r44
real*8 ss, coef

character*1 ch
character*128 anything

integer indx(jvar)
integer j1, j2, j3, j4
integer nw1, nw2, n3, ntest
integer ierr, ierr2, iadj

```

```

integer nwr1, nwr2

logical lf1, l_very_good, lwrite_matrix

intrinsic abs, exp, sin, cos, real, aimag, asin, atan, sqrt,
+          log10, sign

external lubksb, ludcmp
c external check

j      = (0.0d00,1.0d00)
pi     = 4.0d00*atan(1.0d00)
tpi    = 2.0d00*pi
rt2    = sqrt(2.0d00)
one    = 1.0d00
two    = 2.0d00
zero   = 0.0d00

ierr2 = 0

l_very_good = .true.
c The is an option to read inputs from a file. The built in values
c that can be used by default are for near perfect components.

lwrite_matrix = .false.
c During testing it was handy to write out the matrix.

open(unit=46,file='outdat_stabline.txt',status='replace')

print*, 'Do you want to read the input from a file? (y/n)'
read(*,900) anything
900 format(a)
do 300 j1=1,10
  ch=anything(j1:j1)
  if(ch.eq.'y'.or.ch.eq.'Y') then

```

```
        l_very_good=.false.
        open(unit=45,file='indata_stabline_nn.txt',status='old')
        go to 301
    end if
300  continue

301  cvac = 2.99792458d08
    cair = cvac/sqrt(1.00059)
c    speed of light

c    frequencies Hz
c    *****
    if(l_very_good) then
        cc = cvac
        frq1 = 11.9942d9
        frq2 = 11.939823d9
c    frq1 must be exact, frq2 should be an estimate
        iadj = 1
    else
        read(45,900) anything
        do 319 j1=1,10
            ch=anything(40+j1:40+j1)
            if(ch.eq.'r'.or.ch.eq.'R') then
                cc = cair
                print*,'vel light in air=',cair
                write(*,736)
                write(46,736)
736         format('Medium is air')
                go to 321
            end if
            if(ch.eq.'v'.or.ch.eq.'V') then
                cc=cvac
                write(*,737)
                write(46,737)
737         format('Medium is vacuum')
```

```

        go to 321
    end if
319  continue
    cc=cvac

321  read(45,900) anything
    read(anything(41:),*,err=3000) frq1 , frq2
    read(45,900) anything
    read(anything(41:),*,err=3000) iadj
    end if
    ghz1 = frq1*1.0d-9
    ghz2 = frq2*1.0d-9
    if((iadj.ne.1).and.(iadj.ne.2)) iadj = 1
    write(*,800) ghz1 , ghz2
    write(46,800) ghz1 , ghz2
    write(46,790)
800  format('frequencies (Hz) ',f13.9,' GHz',4x,f13.9,' GHz')
790  format('frequency 1 has zero phase shift to the longer line')
    write(*,789) iadj
    write(46,789) iadj
789  format('frequency ',i1,' will be adjusted for exact cancellation')
    write(46,788)
788  format('      ')

c    waveguide WR90 TE10 mode
c    *****
    aa = 0.02286d00
c    waveguide width determine the wavelength

w11 = one/sqrt((frq1/cc)**2 - (0.5d00/aa)**2)
w12 = one/sqrt((frq2/cc)**2 - (0.5d00/aa)**2)

```

```

    if (iadj.eq.1) then
      write(*,918) w11, w12
      write(46,918) w11, w12
918  format('estimation for wavelength 1 = ', f8.6,
+         ' m wavelength 2 = ',f8.6,' m')
      write(46,788)
    else
      write(*,9181) w11, w12
      write(46,9181) w11, w12
9181 format('wavelength 1= ', f8.6,
+         ' m estimation for wavelength 2 = ',f8.6,' m')
      write(46,788)
    end if

    if (w12.gt.w11) then

c     zero phase to long arm formula
c     *****
nw = 0.25d00*(w12 + w11)/(w12 - w11)
w12 = w11*(4.0d00*nw + 1.0d00)/(4.0d00*nw - 1.0d00)
extra_lgth = (nw - 0.25d00)*w12

    else

c     zero phase to long arm formula with n-> n+1
c     *****
nw = 0.25d00*(3.00d00*w12-w11)/(w11-w12)
w12 = w11*(4.0d00*nw + 1.0d00)/(4.0d00*nw + 3.0d00)
extra_lgth = (nw + 0.75d00)*w12

    end if

    write(*,791) nw
    write(46,791) nw
91  format('additional number of wavelengths for long path =', i5)

```

```

    if (iadj.eq.2) then
      frq2 = cc*sqrt((one/wl2)**2+(0.5 d00/aa)**2)
      ghz=1.0d-09*frq2
      write(*,919) ghz
      write(46,919) ghz
919   format('adjusted frequency 2 = ', f10.6, ' GHz')
    else
      frq1 = cc*sqrt((one/wl1)**2+(0.5 d00/aa)**2)
      ghz=1.0d-09*frq1
      write(*,979) ghz
      write(46,979) ghz
979   format('adjusted frequency 1 = ', f10.6, ' GHz')
    end if

    write(*,920) wl1, wl2
    write(46,920) wl1, wl2
920   format('wavelength 1 = ', f8.6, ' m    wavelength 2 = ', f8.6, ' m')

    write(46,788)
    if (l_very_good) then
      lgth2 = 0.10d00
    else
      read(45,900) anything
      read(anything(41:),*,err=3000) lgth2
    end if
    write(*,801) lgth2
    write(46,801) lgth2
801   format('short leg length = ', f9.5, ' m')

    lgth3 = lgth2 + extra_lgth
    write(*,921) lgth3, extra_lgth
    write(46,921) lgth3, extra_lgth
921   format('optimal length long leg = ', f9.5, ' m',
+           ' extra length=', f9.5, ' m' )

```

```

c      ph21_deg = 180.0d00*lgth2/(pi*w11)
c      ph22_deg = 180.0d00*lgth2/(pi*w12)
c      write(*,933) ph21_deg, ph22_deg
c      write(46,933) ph21_deg, ph22_deg
c933  format('Phase line2 for w11=', f7.2,
c      +      ' Phase line2 for w12=', f7.2)

print*, 'Do you want to adjust the extra length? (y/n)'
read(*,900) anything
do 309 j1=1,10
  ch=anything(j1:j1)
  if(ch.eq.'y'.or.ch.eq.'Y') then
    print*, 'How many mm do you wish to add?'
    read(*,*) dlgth3
    lgth3 = lgth3 + dlgth3*1.0d-3
    extra_lgth = extra_lgth + dlgth3*1.0d-3
    write(*,922) lgth3, extra_lgth
    write(46,922) lgth3, extra_lgth
922  format('modified length long leg = ', f9.5, ' m',
+      ' extra length=', f9.5, ' m' )
    go to 310
  end if
309  continue

c      Quadrature Hybrid
c      *****
310  write(46,788)
    write(46,787)
787  format('Coefficients for quadrature hybrid tee')
    if(l_very_good) then
      t11 = zero
      t22 = zero

```

```

t33 = zero
t44 = zero
t14 = zero
t23 = zero
t12 = -j
t34 = -j
t13 = -one
t24 = -one
else
  read(45,900) anything
  read(anything(41:),*,err=3000) fi14 , r1i14 , r2i14
  read(45,900) anything
  read(anything(41:),*,err=3000) fi23 , r1i23 , r2i23
c   fixy = frequency of bandstop for isolation ,
c   r1ixy and r2ixy are series and parallel resistances
  read(45,900) anything
  read(anything(41:),*,err=3000) fr11 , r1r11 , r2r11
  read(45,900) anything
  read(anything(41:),*,err=3000) fr22 , r1r22 , r2r22
  read(45,900) anything
  read(anything(41:),*,err=3000) fr33 , r1r33 , r2r33
  read(45,900) anything
  read(anything(41:),*,err=3000) fr44 , r1r44 , r2r44
  read(45,900) anything
  read(anything(41:),*,err=3000) t12 , t13 , t24 , t34
c   the ~3dB couplings
end if
write(*,8031) t12 , t34
write(*,8032) t13 , t24
write(46,8031) t12 , t34
write(46,8032) t13 , t24
8031 format('t12 , t34 ',2(' (',1pe11.4,2x,1pe11.4,')'))
8032 format('t13 , t24 ',2(' (',1pe11.4,2x,1pe11.4,')'))

c   H plane Tee

```

```

c      *****
      write(46,788)
      write(46,786)
786   format('Coefficients for H-plane tee')
      if(l_very_good) then
          r1 = one
          r2 = -one
          r3 = rt2
          r4 = zero
      else
          read(45,900) anything
          read(anything(41:),*,err=3000) r1, r2, r3, r4
      end if
      write(*,8041) r1, r2
      write(46,8041) r1, r2
      write(*,8042) r3, r4
      write(46,8042) r3, r4
8041  format('r1, r2 ',2('(',1pe11.4,2x,1pe11.4,')'))
8042  format('r3, r4 ',2('(',1pe11.4,2x,1pe11.4,')'))

c      Load
c      ****
      write(46,788)
      write(46,785)
785   format('Reflection coefficients for load 1 and load 2')
      if(l_very_good) then
          SL1 = (0.10d00, 0.0d00)
          SL2 = (0.99d00, 0.0d00)
      else
          read(45,900) anything
          read(anything(41:),*,err=3000) SL1, SL2
      end if
      write(*,805) SL1, SL2
      write(46,805) SL1, SL2

```

```

805   format('SL1&SL2  ',2(' (',1pe11.4,2x,1pe11.4,')'))

c     Drive
c     ****
      if (l_very_good) then
          DRV1 = 1.0d00
          DRV2 = 1.0d00
      else
          read(45,900) anything
          read(anything(41:),*,err=3000) DRV1, DRV2
      end if
      write(46,788)
      write(46,784)
784   format('Drive coefficients for input frequencies 1 & 2')
      write(*,806) DRV1, DRV2
      write(46,806) DRV1, DRV2
806   format('Drives      ', 1pe11.4,2x,1pe11.4)

      if (l_very_good) then
          alpha = 0.0d00
      else
          read(45,900) anything
          read(anything(41:),*,err=3000) alpha
      end if
      write(46,718) alpha
718   format('WG loss    ', 1pe11.4)

      if (l_very_good) then
          length5 = 10.0d00
      else
          read(45,900) anything
          read(anything(41:),*,err=3000) length5
      end if
      write(46,719) length5
719   format('Length5    ', 1pe11.4)

```

```

    if (.not.l_very_good) then
        close (unit=45,status='keep')
    end if

c    open files for outputs – see headers for contents
c    *****
    open(unit=41,file='FF1_phi3.txt',status='replace')
    open(unit=42,file='FF4_phi3.txt',status='replace')
    open(unit=43,file='FF1_phi5.txt',status='replace')
    open(unit=44,file='FF4_phi5.txt',status='replace')
    open(unit=47,file='Tmatrix.txt',status='replace')

9901 format(' freq      ',2x,' line_phase ',6x,' mag_R4 ',4x,' ph_R4 ',4x,
+         ' mag_F5 ',4x,' ph_F5 ',4x,' mag_R1 ',4x,' ph_R1 ',2x,' lin5_lgth ',
+         2x,' wavelgth ')

9902 format(' freq      ',2x,' line_phase ',6x,' mag_R1 ',4x,' ph_R1 ',4x,
+         ' mag_F5 ',4x,' ph_F5 ',4x,' mag_R4 ',4x,' ph_R4 ',2x,' lin5_lgth ',
+         2x,' wavelgth ')

9903 format(' freq      ',6x,' lgth5 ',4x,' mag_R4 ',4x,' ph_R4 ',3x,
+         ' mag_F5 ',4x,' ph_F5 ',3x,' mag_R1 ',4x,' ph_R1 ')

9904 format(' freq      ',6x,' lgth5 ',4x,' mag_R1 ',4x,' ph_R1 ',3x,
+         ' mag_F5 ',4x,' ph_F5 ',3x,' mag_R4 ',4x,' ph_R4 ')

9907 format(' freq      ',9x,' t11 ',8x,' t22 ',8x,' t33 ',8x,
+         ' t44 ',8x,' t14 ',8x,' t23 ')

    write(41,9901)
    write(42,9902)
    write(43,9903)

```

```

write(44,9904)
write(47,9907)

c vary frequency
c *****
n3 = 1600
do 3 j3 = 1,n3
  lgth_diff = extra_lgth
  lgth3 = lgth2 + lgth_diff
  wl = wl2 + (j3 - 701)*(wl1-wl2)/(n3-1400)
  frqG = (cc/1.0d09)*sqrt(one/wl**2+(0.5d00/aa)**2)

do 4 j4 = 1, 80
  lgth5 = length5 + 0.02d00*(j4 - 1)*wl2
c length to load ultimately must be kept a fixed number of drive
c frequency wavelengths so use wl2 rather than wl
c loop on j4 is used to see phase changes at
c both frequencies when lgth5 is varied.

do 5 j5 = 1,2
c switch injection port
  if(j5.eq.1) then
    LF1 =.true.
  else
    LF1 = .false.
  end if

  if(l_very_good) then
    t11 = zero
    t22 = zero
    t33 = zero
    t44 = zero
    t14 = zero
    t23 = zero
  else

```

```

c      evaluate frequency dependent hybrid tee coefs for isolated ports
      ss = (frqG/fi14-fi14/frqG)
      t14 = (R1i14+j*ss)/(R2i14+j*ss)
      ss = (frqG/fi23-fi23/frqG)
      t23 = (R1i23+j*ss)/(R2i23+j*ss)

c      evaluate frequency dependent hybrid tee coefs for relection
      ss = (frqG/fr11-fr11/frqG)
      t11 = (R1r11+j*ss)/(R2r11+j*ss)
      ss = (frqG/fr22-fr22/frqG)
      t22 = (R1r22+j*ss)/(R2r22+j*ss)
      ss = (frqG/fr33-fr33/frqG)
      t33 = (R1r33+j*ss)/(R2r33+j*ss)
      ss = (frqG/fr44-fr44/frqG)
      t44 = (R1r44+j*ss)/(R2r44+j*ss)
end if

      phi2 = (tpi/wl+j*alpha)*lgth2
      phi3 = (tpi/wl+j*alpha)*lgth3
      phi5 = (tpi/wl+j*alpha)*lgth5
c      phase gains depend on the actual wavlength

      phi2_deg = Real(180.0d00*phi2/pi)
      phi3_deg = Real(180.0d00*phi3/pi)
      phi5_deg = Real(180.0d00*phi5/pi)
      phi_diff = phi3_deg - phi2_deg

c      Set Matrix coefficients
c      *****
c      set all to zero and then over write the no zero elements
do 100 j1=1,jvar
  do 101 j2=1, jvar
    M(j1 , j2)=0.0d00
101  continue
      Y(j1)=0.0d00

```

```

100      continue

      if (LF1) then
c        frequency1
          Y(1)=- t11 *DRV1
          Y(2)=- t12 *DRV1
          Y(3)=- t13 *DRV1
          Y(4)=- t14 *DRV1
        else
c        frequency2
          Y(1)=- t14 *DRV2
          Y(2)=- t24 *DRV2
          Y(3)=- t34 *DRV2
          Y(4)=- t44 *DRV2
        end if

c      Equation 1 quadrature Hybrid
c      *****
M(1 ,2)  =  t12 *exp(j *phi2)
M(1 ,4)  =  t13 *exp(j *phi3)
      if (LF1) then
          M(1 ,5) =  t14
          M(1 ,9) =  rt2
        else
          M(1 ,5) =  t11
          M(1 ,6) =  rt2
        end if

M(2 ,1)  =  rt2
M(2 ,2)  =  t22 *exp(j *phi2)
M(2 ,4)  =  t23 *exp(j *phi3)
      if (LF1) then
          M(2 ,5) =  t24
        else
          M(2 ,5) =  t12

```

```

end if

M(3,2) = t23*exp(j*phi2)
M(3,3) = rt2
M(3,4) = t33*exp(j*phi3)
if (LF1) then
  M(3,5) = t34
else
  M(3,5) = t13
end if

```

```

M(4,2) = t24*exp(j*phi2)
M(4,4) = t34*exp(j*phi3)
if (LF1) then
  M(4,5) = t44
  M(4,6) = rt2
else
  M(4,5) = t14
  M(4,9) = rt2
end if

```

```

c      Equation 2 E plane Tee
c      *****
M(5,1) = r1*exp(j*phi2)
M(5,2) = -2.0d00
M(5,3) = r2*exp(j*phi3)
M(5,8) = r3*exp(j*phi5)

M(6,1) = r2*exp(j*phi2)
M(6,3) = r1*exp(j*phi3)
M(6,4) = -2.0d00
M(6,8) = r3*exp(j*phi5)

M(7,1) = r3*exp(j*phi2)
M(7,3) = r3*exp(j*phi3)

```

```

M(7,7) = -2.0d00
M(7,8) = r4*exp(j*phi5)

c      Equation 3 Load
c      *****
c      assumes cavity is tuned to 11.9942GHz
c      SL1 is reflection at 11.9942 GHz and SL2 is reflection at offset 0.05
value = (one-abs(SL1))/(one-abs(SL2))
if (value.gt.0.0d00) then
  coef = 0.055d00/sqrt(log(value))
else
  coef = 0.055d00
end if
M(8,7) = (one-(one-SL1)*exp(-((frqG-11.9942d00)/coef)**2))
+      *exp(j*phi5)
M(8,8) = -1.0d00

c      Equation 4 no feed on other port
c      *****
M(9,5) = 1.0d00

if (lwrite_matrix) then
c      only used for testing
open(unit=45,file='matrix.txt',status='replace')
do 106 j1=1,jvar
  do 105 j2=1, jvar
    write(45,*) 'M ', j1, j2, M(j1,j2)
105    continue
    write(45,*) 'Y ', j1, Y(j1)
106  continue
  close(unit=45,status='keep')
end if

c      Solve the matrix equation MX=Y for the unknown vector X
c      *****

```

```

call ludcmp(M,A,jvar ,indx ,d ,ierr )
if(ierr.eq.1) go to 3000
call lubksb(A,jvar ,indx ,y ,x)

if((j3.eq.n test ).and.(j4.eq.1)) then
  call check(m,x,y,chk,jvar )
  write(*,*) '      '
  write(*,955)  chk(1), chk(2), chk(3)
  write(*,956)  chk(4), chk(5), chk(6)
  write(*,957)  chk(7), chk(8), chk(9)
955  format('chk1-3 ',3(' ',1pe12.5,', ',1pe12.5,', '))
956  format('chk4-5 ',3(' ',1pe12.5,', ',1pe12.5,', '))
957  format('chk7-9 ',3(' ',1pe12.5,', ',1pe12.5,', '))
  write(*,*) '      '
end if

mag6=abs(x(6))
if(mag6.ge.0.0d00)then
  xr6=real(x(6))
  xi6=aimag(x(6))
  if(xr6.ge.0.0d00)then
    phase6=asin(xi6/mag6)
  else
    if(xi6.ge.0.0d00)then
      phase6=pi-asin(xi6/mag6)
    else
      phase6=-pi-asin(xi6/mag6)
    end if
  end if
  phase6_deg = phase6*180.0d00/pi
else
  phase6=2000.0d00
  phase6_deg = 2000.0d00
  print*, 'No output on 6'
  ierr2=ierr2+1

```

```
end if

mag7=abs(x(7))
if (mag7.ge.0.0d00) then
  xr7=real(x(7))
  xi7=aimag(x(7))
  if (xr7.ge.0.0d00) then
    phase7=asin(xi7/mag7)
  else
    if (xi7.ge.0.0d00) then
      phase7=pi-asin(xi7/mag7)
    else
      phase7=-pi-asin(xi7/mag7)
    end if
  end if
  phase7_deg = phase7*180.0d00/pi
else
  phase7=2000.0d00
  phase7_deg = 2000.0d00
  print*, 'No output on7'
  ierr2=ierr2+1
end if

mag9=abs(x(9))
if (mag9.ge.0.0d00) then
  xr9=real(x(9))
  xi9=aimag(x(9))
  if (xr9.ge.0.0d00) then
    phase9=asin(xi9/mag9)
  else
    if (xi9.ge.0.0d00) then
      phase9=pi-asin(xi9/mag9)
    else
      phase9=-pi-asin(xi9/mag9)
    end if
  end if
end if
```

```

        end if
        phase9_deg = phase9*180.0d00/pi
    else
        phase9=2000.0d00
        phase9_deg = 2000.0d00
        print*, 'No output on9'
        ierr2=ierr2+1
    end if

c      write outputs to one of four files
c      *****

    if (j4.eq.1) then
        write(47,9997) frqG, abs(t11),abs(t22),abs(t33),abs(t44),
+                abs(t14),abs(t23)
9997    format(f10.6,6(2x,f9.7))

        if(LF1)then
            write(41,991) frqG, phi_diff, mag6, phase6_deg,
+                mag7,phase7_deg, mag9,phase9_deg, lgth5, wl
        else
            write(42,991) frqG, phi_diff, mag6, phase6_deg,
+                mag7,phase7_deg, mag9,phase9_deg, lgth5, wl
        end if
    end if
991    format(f10.6,5x,f7.1,2x,3(2x,f8.4,2x,f7.2),2x,f9.2,2x,f9.7)

nwr1 = 701
nwr2 = n3-699
if ((j3.eq.nwr1).or.(j3.eq.nwr2)) then
    if(LF1)then
        write(43,997) frqG, lgth5,mag6,phase6_deg,
+                mag7,phase7_deg,mag9,phase9_deg
    else

```

```

        write(44,997) frqG , lgth5 ,mag6,phase6_deg ,
+           mag7,phase7_deg ,mag9,phase9_deg
        end if
    end if

997    format(f10.6,3x,f8.5,3(2x,f8.4,2x,f7.2))

        if(ierr2.gt.30) go to 3000

5        continue
4        continue

        if((j3.eq.nwr1).or.(j3.eq.nwr2)) then
            write(43,998)
            write(44,998)
        end if
998    format('    ')

3        continue

        close(unit=41,status='keep')
        close(unit=42,status='keep')
        close(unit=43,status='keep')
        close(unit=44,status='keep')
        close(unit=47,status='keep')
        close(unit=46,status='keep')

        stop

3000    print*, 'Calculation incomplete'
        close(unit=41,status='keep')
        close(unit=42,status='keep')
        close(unit=43,status='keep')
        close(unit=44,status='keep')
        close(unit=47,status='keep')

```

```

close ( unit=46, status='keep' )

stop
end

SUBROUTINE check(m,x,y,chk,jvar)
c *****
integer    jvar
complex*16 m(jvar,jvar),x(jvar),y(jvar),chk(jvar)
integer    j1,j2

do 1 j1=1,jvar
    chk(j1)=-y(j1)
    do 2 j2=1,jvar
        chk(j1)=chk(j1)+M(j1,j2)*x(j2)
2    continue
1    continue

c    valid solution when chk is zero for all j1

end

SUBROUTINE lubksb(a,jvar,indx,y,x)
c *****
integer    jvar
integer    indx(jvar)
complex*16 a(jvar,jvar),x(jvar),y(jvar),b(100)
integer    j1,j2,j3,j4
complex*16 sum

intrinsic abs

do 10 j1=1,jvar
    b(j1)=y(j1)

```

```

10   continue

      j3=0
      do 12 j1=1,jvar
          j4=indx(j1)
          sum=b(j4)
          b(j4)=b(j1)
          if (j3 .ne.0) then
              do 11 j2=j3 ,j1-1
                  sum=sum-a(j1 ,j2)*b(j2)
11          continue
              else if (abs(sum).ne.0.d00) then
                  j3=j1
              endif
              b(j1)=sum
12   continue

      do 14 j1=jvar ,1,-1
          sum=b(j1)
          do 13 j2=j1+1,jvar
              sum=sum-a(j1 ,j2)*b(j2)
13   continue
          b(j1)=sum/a(j1 ,j1)
14   continue

      do 15 j1=1,jvar
          x(j1)=b(j1)
15   continue

      return

      END

```

```

SUBROUTINE ludcmp(m,a,jvar,indx,d,ierr)
c *****
c Given an NxN matrix M with physical dimension jvar,
c this routine creates the LU decomposition of a rowwise
c permutation of M and outputs this as A.
c Indx is an output vector which records
c the row permutation and d is for parity.

integer    jvar
integer    indx(jvar),NMAX, ierr
real*8     d, TINY
complex*16 a(jvar,jvar), m(jvar,jvar)

parameter (NMAX=500,TINY=1.0e-20)

integer    i,imax,j,k
complex*16 cvalue, sum
real*8     aamax, value, vv(NMAX)

intrinsic abs

ierr=0

do 8 i=1,jvar
  do 9 j=1, jvar
    a(i,j)=m(i,j)
9  continue
8  continue

d=1.0d00
do 12 i=1,jvar
  aamax=0.0d00
  do 11 j=1,jvar
    if (abs(a(i,j)).gt.aamax) aamax=abs(a(i,j))

```

```
11      continue
      if (aamax.eq.0.0d00)then
        print*, 'singular matrix in ludcmp'
        ierr=1
        return
      end if
      vv(i)=1.0d00/aamax
12      continue

      do 19 j=1,jvar
        do 14 i=1,j-1
          sum=a(i,j)
          do 13 k=1,i-1
            sum=sum-a(i,k)*a(k,j)
13          continue
          a(i,j)=sum
14          continue

          aamax=0.
          do 16 i=j,jvar
            sum=a(i,j)
            do 15 k=1,j-1
              sum=sum-a(i,k)*a(k,j)
15          continue
            a(i,j)=sum
            value=vv(i)*abs(sum)
            if (value.ge.aamax) then
              imax=i
              aamax=value
            endif
16          continue

          if (j.ne.imax)then
            do 17 k=1,jvar
              cvalue=a(imax,k)
```

```
        a(imax,k)=a(j,k)
        a(j,k)=cvalue
17      continue

        d=-d
        vv(imax)=vv(j)
      endif
      indx(j)=imax
      if(abs(a(j,j)).eq.0.0d00) a(j,j)=TINY
      if(j.ne.jvar) then
        cvalue=1.0d00/a(j,j)
        do 18 i=j+1,jvar
          a(i,j)=a(i,j)*cvalue
18      continue

        endif
19      continue
      return
    END
```

C (C) Copr. 1986-92 Numerical Recipes Software !-13D8u2.